WARWICK
THE UNIVERSITY OF WARWICK

A Thesis Submitted for the Degree of PhD at the University of Warwick

Permanent WRAP URL:
http://wrap.warwick.ac.uk/132890

Copyright and reuse:
This thesis is made available online and is protected by original copyright.
Please scroll down to view the document itself.
Please refer to the repository record for this item for information to help you to cite it.
Our policy information is available from the repository home page.

For more information, please contact the WRAP Team at: wrap@warwick.ac.uk

warwick.ac.uk/lib-publications

SURFACE EXAFS (EXTENDED X-RAY ABSORPTION FINE STRUCTURE) STUDIES OF ADSORBATES ON SURFACES

Simon Ainsworth

A THESIS SUBMITTED TO THE DEPARTMENT OF PHYSICS, UNIVERSITY OF WARWICK, FOR THE QUALIFICATION OF PhD, FEBURARY 1985

Work for this thesis was carried out from October 1981 to November 1984 in the Department of physics, University of Warwick, and at the Synchrotron Radiation Source at the Science and Engineering Research Council's Daresbury Laboratory.

REPRODUCED
FROM THE
BEST
AVAILABLE
COPY

SUMMARY

This thesis describes detailed SEXAFS studies of iodine adsorption onto Ni(100), and some preliminary chlorine-Cu(111) studies. The main conclusions are as follows:-

The standard analysis technique (ie the method of deducing atomic structural information from measures of X-ray absorption coefficients) - the Fourier filtering approach - has potential problems. For short range spectra, a second shell can 'frequency' modulate the main oscillation giving incorrect phase shifts and bond lengths. Large ΔE_o's compensating for erroneous phase shifts produce Δr_1 errors up to 0.1 Å. A bond length derivation is not the weighted mean of two contributing bond lengths. A Fourier transform modulus is only a 'frequency' spectrum; discretion is needed in relating this to a radial distribution function and 'Ramsauer-Townsend effects' which should rarely be observed. A multi-shell modelling approach is useful for SEXAFS analyses. A surface NiI_2 structure is confirmed as being a slice of bulk NiI_2 on Ni(100); for $\theta = {}^1/_2$ I-Ni(100), adatoms lie in hollow sites; for $\theta = {}^3/_8$ and ${}^1/_3$, they lie in hollow, bridge, or some mixture of such sites. The I-Ni bond length remains 2.78 Å. The accuracy limitation of higher shell distances set by the single ΔE_o optimisation is not problematic, since generally the nearest shell dominates. There is no difference in I-Ni chemical bonding throughout the coverages; charge transfer after excitation causes large ΔE_o's.

Experimental problems limited the quality of Cl-Cu SEXAFS spectra, but some results could be obtained: For $\theta = {}^1/_3$, Cl adatoms lie in hollows, Cl-Cu = 2.39 (± 0.03)Å; for $\theta = 0.45$, adatoms lie in mixed co-ordination sites, bond length 2.33 (± 0.05)Å, similar to the 2.34 Å in bulk CuCl. A spline is a better estimation of the atomic absorption background, μ_o; polynomials can produce significant bond length errors.

Finally, the deduced structures are compared with present understandings of surface chemical bonding.

CONTENTS

LIST OF CONTENTS

Continued

Continued

Continued

Continued

GLOSSARY OF TERMS

θ: A definition of the coverage of an adlayer, being the number of adsorbate atoms divided by the number of substrate atoms in the top layer per unit area.

{100}: Any plane of the same geometrical arrangement of atoms as the (100) plane as defined by the Miller indices.

<100>: A set of directions within a crystal structure.

LMM: Notation for Auger electron spectroscopy, this example being the interatomic decay of an electron from the M shell to a hole in the L shell, an LMM Auger electron being ejected from the M shell of the atom.

λ: The wavelength of an X-ray, usually in units of Å (10^{-10} m).

$\lambda(k)$: The wavelength of an electron, this being a function of its waverector $k(\text{Å}^{-1})$.

λ^{imfp}: The inelastic mean free path of an electron; units of Å.

$h\nu$: The energy of an X-ray photon, the frequency being ν.

μ: X-ray absorption coefficient.

μ_o: X-ray absorption coefficient of isolated atoms, ie containing no EXAFS.

σ_a': X-ray scattering cross-section per atom.

$\chi(k)$: The extended X-ray absorption-fine structure (EXAFS) as a function of the photo-electron wave-vector.

N_j: The number of atoms in the j^{th} shell around the central absorbing atom.

N_j^*: The effective number of backscattering atoms; varies with the orientation of the sample to the electric vector $\hat{\underline{e}}$, of the plane-polarised X-ray beam, differently for K and L_I edges and for L_{II} and L_{III} edges.

α_i: The angle between $\hat{\underline{\epsilon}}$ and the radial vector joining the central atom to the i^{th} backscattering atom.

ℓ: The angular mementum of a partial wave used to describe the photo-electron.

σ: The amplitude of thermal vibration, or the displacement of an atom from the average position of similar atoms due to static disorder, (Å).

$2\sigma^2$: The Debye-Waller factor ($Å^2$).

$A(k)$: The amplitude of a single shell EXAFS as a function of k; in part proportional to the number of backscattering atoms.

$\theta(k)$: The phase function, ie the phase angle (as a continuous function) of the EXAFS as a function of the photo-electron wave-vector.

$\Phi(k)$: The total atomic phase shifts, (ie twice a central atomic phase shift plus a backscattering phase shift) involved in the EXAFS process.

$\delta(k)$: The phase shift of the photo-electron wave on leaving or re-entering the potential of the central atom.

$\psi(k)$: Phase shift on backscattering.

$F(k)$: The backscattering factor.

E_o: The point in energy space, of an X-ray absorption spectrum, at which k would equal $0Å^{-1}$, several eV from the absorption edge.

radial distribution function: A complete description of the local environment around a central atom, ie shells of neighbours at certain distances containing a number of atoms of a certain element; for EXAFS purposes only atoms within a radial distance, r, of 5 Å are important.

N(r): A shell representation of the radial distribution function.

F(R) / |FT|: The modulus Fourier transform of an EXAFS spectrum, which represents the 'frequency' spectrum, ie the amplitudes of the R-values contained in the EXAFS; this is, in principle, related to the radial distribution function.

R: $R = 2r + \frac{\Phi(k)}{k}$, such that removal of the atomic phase shifts and division of R by 2, yields r.

CAI: The name given to the central iodine atomic phase shift, $\delta(k)^{\ell=0-13}$, derived from a bulk NiI_2 L_{III} spectrum (834) in the multi-shell modelling approach.

BSN: $\psi(k)^{\ell=0-13}$ for a nickel backscatterer.

BSI: $\psi(k)^{\ell=0 \text{ to } 13}$, I backscattering phase shift.

EXOUTBO 1, 2: Alternative phase shifts derived from a different bulk NiI_2 spectrum (833).

AFAC: The amplitude factor used in the EXAFS computations.

VPI: The constant imaginary potential for the photo-electron in EXAFS calculations.

PHSCL: $\delta(k)^{\ell=0 \text{ to } 13}$ for a chlorine central atom, obtained from the K-edge EXAFS of bulk CuCl

EXOUTA 1: $\psi(k)^{\ell=0-13}$ for a copper backscatterer obtained from the K-edge EXAFS of bulk CuCl.

EXOUTA 2: $\psi(k)^{\ell=0-13}$ for a chlorine backscatterer obtained from the K-edge EXAFS of bulk CuCl.

LIST OF DIAGRAMS

Continued

Continued

Continued

Continued

Continued

LIST OF TABLES

ACKNOWLEDGEMENTS

The author would like to thank his supervisor at Warwick University, Dr Phil Woodruff, particularly for many stimulating discussions on data analysis and for his critical reading and advice on the presentation of this thesis. I would also like to thank all those involved in commissioning and helping to run the SEXAFS machine at Daresbury, and those involved in obtaining the experimental data presented in this thesis particularly Dr R G Jones, now at Nottingham University. My appreciation also extends to the Science and Engineering Research Council for the provision of a research studentship grant, to British Petroleum for their contribution to the funding of my research, and to Dr Richard Joyner and Dr Len Hazell for organising an interesting research project at the BP research centre, Sunbury on Thames. Lastly I would like to thank the typists at AWRE, Aldermaston, for their assistance.

DECLARATIONS AND LIST OF PUBLICATIONS

The author would like to state that the data analyses and conclusions presented in this thesis are based upon his own research work, whereas the collection of SEXAFS Spectra was largely the work of others in a team effort.

Material presented elsewhere include:-

1. 'A surface EXAFS study of a surface iodide phase on Ni(100)'
   Surface Science 152/153 (1985) p 443
   R G Jones, S Ainsworth, M D Crapper, C Somerton, D P Woodruff (Warwich University),
   R S Brooks, J C Campuzano, D A King, G M Lamble (Liverpool University),
   M Prutton (York University)
   - this author's main contribution being the single shell analyses.
2. 'Multiple Bondlengths and short data ranges in SEXAFS and EXAFS'
   Solid State Communications 56 (1985) p 461
   S Ainsworth and D P Woodruff.

To be published in Surface Science, hopefully in 1986:-

3. 'A SEXAFS study of several surface phases of iodine adsorption on Ni(100), I: Multi-shell simulation analysis'
   R G Jones, S Ainsworth, M D Crapper, C Somerton, D P Woodruff
   - this author's contribution being the multi-shell analyses.
4. 'II: The breakdown of Fourier filtering single shell analysis'
   Same authors ; S Ainsworth's contribution being the initial demonstration and explanation of the failure of the Fourier-filtering analyses of these SEXAFS spectra.

CHAPTER 1

INTRODUCTION TO SURFACE SCIENCE

1.01: OVERVIEW

Surface EXAFS is a particular application of the technique of EXAFS (extended X-ray absorption fine structure) which is generally applied to the study of bulk materials. SEXAFS is used to obtain the geometrical arrangement of atoms on a surface, in particular to obtain the local environment(s) around all those atoms of one chosen element. 'Tuning' the SEXAFS measurement to an atomic type within an adsorbate molecule (molecule of a foreign substance bonded to the surface of an impermeable solid) - enables one to obtain a determination of the environment of the adsorbate molecule, ie, the number of substrate atoms to which it is 'bonded', and the interatomic separation of the adsorbate-substrate atoms involved in the bond.

This chapter briefly discusses the motivation for surface science: it is hoped that studying the nature of solid surfaces and of the reactions of surfaces with gaseous molecules [1-4] will lead to a better understanding of such processes as oxidation, corrosion and catalysis. It is also necessary to explain how simple surfaces can be prepared and characterised; the types of experiments that can be done to study the chemical reactivities of these surfaces to various adsorbate molecules; and the ways in which the resulting adsorbate-substrate structures can be deduced. Some of the techniques of surface science and of UHV (ultra high vacuum) technology are therefore described.

1.02: INTRODUCTION TO SURFACE SCIENCE

The aim of surface science is to obtain an understanding of the fundamental physics underlying such important processes as oxidation, corrosion and the chemical reactions at solid surfaces occurring during heterogeneous catalysis, and to aid the developments of surface treatments to prevent the corrosion of metals and improve the performance of mechanical components, and to improve catalytic materials.

In the real world oxidation of metals occurs at room temperature and pressure, there being an oxide layer of up to 1 um in thickness, when the metal surface can be regarded as un-corroded, whereas in surface science experiments the conditions are those of ultra high vacuum (gas pressures below 10^{-10} mbar) and the materials studied are often confined to one monolayer or less coverage on clean single crystal surfaces. The disparity is even greater when one considers catalysis in which the gas phases are at very high pressures (many atmospheres) and the reactions occur at high temperatures. However, the fundamental microscopic processes of atoms or molecules sticking to clean surfaces, leading to the formation of a monolayer, must occur initially in the macroscopic processes described above and are likely to determine the eventual outcome of such large scale occurrences.

In order to study the initial adsorption of atoms, UHV conditions are needed so that it takes many hours for the adsorption of contamimant gases in the vacuum chamber to form a single monolayer at which point the surface is far from 'clean'. After the preparation of a clean surface there is this time available within which an amount

of gas (the adsorption of which is to be studied) can be leaked into the chamber to form a monolayer or less coverage and the resulting chemisorbed layer can be studied - if multilayers exist then the interesting adsorbate-substrate interface is inaccessible to the probes available to surface science.

Consider as an example catalytic reforming which is an important process in oil refining for the production of high octane fuel needed by high compression spark ignition engines. The heterogeneous catalyst typically consists of a complex mixture of elements, the physical make up having a large surface-to-volume ratio to provide many adsorption sites for the reactants. A catalyst for example, might consist of finely powdered graphite (the substrate), with islands of platinum metal (the active element) about 15Å in size containing sodium atoms (the promoter) in concentrations around 10 parts per million. The exact structure of such materials, their adsorption and reaction sites, and the effect of the promoter in determining the catalytic activity, selectivity and lifetime have remained to a large extent uncertain [5]. In recent years surface science has begun to elucidate the fundamental processes that occur in catalysis [6], by studying adsorption on to single crystals both in UHV [7, 8], and in reaction chambers [9], such that the effects of steps on a surface consisting of terraces and steps [10], and of promoters [11-14], are beginning to be understood.

1.03 SINGLE CRYSTAL PLANES

Bulk metals normally exist in the polycrystalline form, such that a slice through such a material forms a surface that contains many different atomic arrangements. The electronic band structures and chemical bonding properties are very hard to predict, although some understanding has been gained from studying the adsorption of gases on to these surfaces. In order to simplify the situation and hence make it easier to understand more, single crystal low index faces (for example the set of planes $\{100\}$, having the same atomic arrangements as the (100) plane, 100 being the Miller indices $[15]$) are mainly used in surface science. Such simple surfaces rarely occur in practical processes, an exception being in some catalysts consisting of very small metal particles (containing less than 100 atoms), which with the appropriate heat treatment can consist of a small number of flat planes of the same atomic arrangements as in low index crystal faces.

Two important metals in catalysis are nickel and platinum - transition metals having fcc (face centred cubic) structures, such that a simple termination of this bulk arrangement yields the surfaces shown in Figure 1.01. It can be seen that each family of crystal planes has a distinct geometrical arrangement of atoms, containing different adsorption sites, such that the planes may have widely differing chemical reactivities to various adsorbate molecules. For example, an adsorbate atom that bonds most readily to 5 metal atoms would have the largest sticking factor for adsorption on to a $\{110\}$ type of plane, assuming that it was small enough to drop into an available trough where it could have 5 equidistant substrate nearest neighbours.

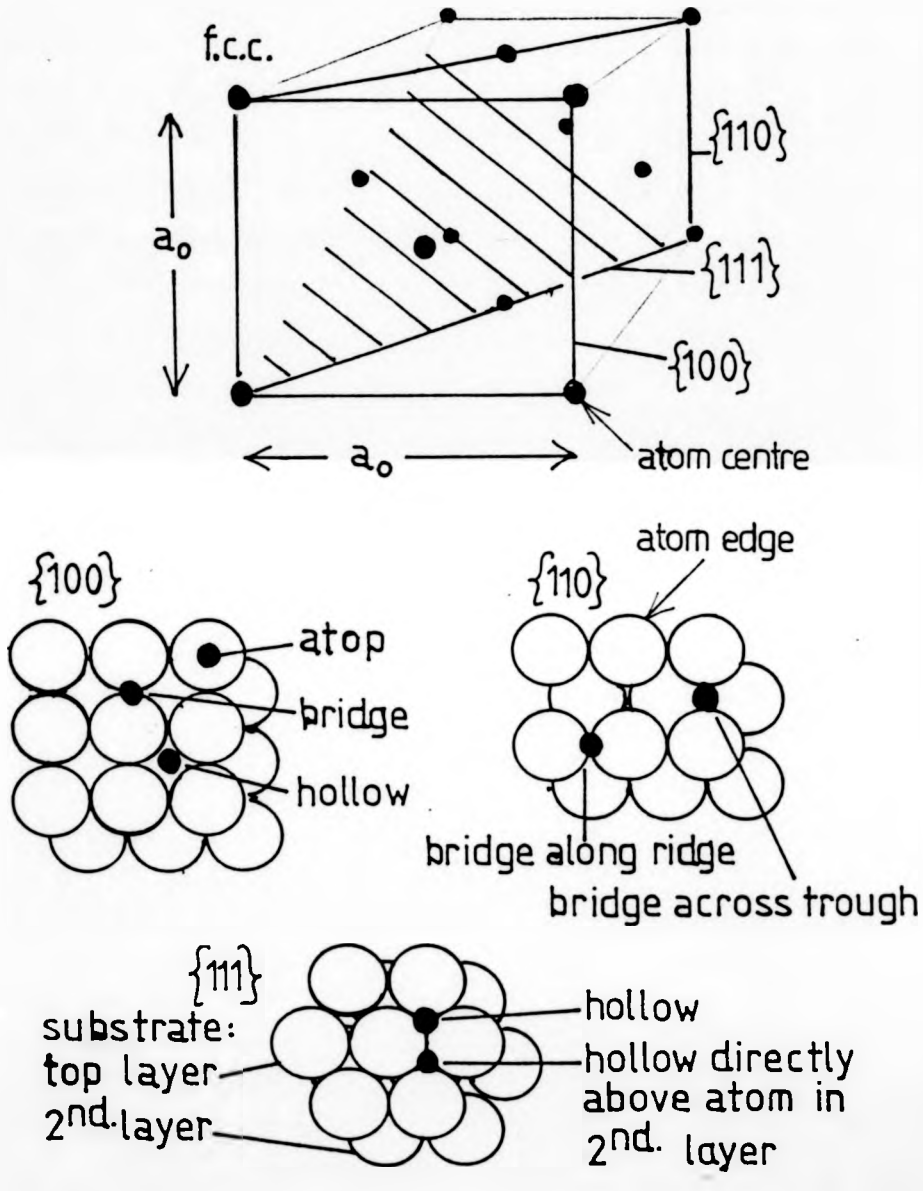

Fig. 1·01 : Face centred cubic structure, atomic planes, and adsorption sites.

Other adsorbate atoms or molecules would have very different chemisorption characteristics. In practice, even for these simple low index faces, complex calculations are needed to calculate their electronic structures such as the positions and directions of electron orbitals ('dangling bonds') available to form chemical bonds with impinging adsorbate molecules [16, 17], and hence to predict their chemical reactivities. Experimental measurements of adsorption processes can be used to test these forecasts, enabling the theory to be refined if necessary.

There are, however, a number of processes that may occur in the surfaces formed by terminations of the bulk structure. The disparity of forces on the top atomic layer (all the atoms that were on one side of this layer in the bulk have been removed) may cause a relaxation, i.e. a change in the layer spacing, to occur. It is not easy even to predict in which direction this movement will be - one theory argues that the absence of atoms on one side removes an attractive force in that direction, such that the top layer contracts towards the remaining bulk; and indeed data has been analysed and found to show a contraction of the layer spacing of up to 10% [18, 19]. For the surfaces consisting of low index planes of fcc solids, only the {111} planes have the atoms most closely packed in 2 dimensions - hexagonally close packed. Some {100} and {110} surfaces may therefore have a tendency to reconstruct to minimise the surface energy. For example, Pt {100} has been shown to reconstruct, the top atoms lying in a slightly compressed and buckled hcp layer [20].

Pt (110) is also known to reconstruct as do some other surface planes of fcc and bcc (body centred cubic) metals [20], hexagonal layers being a common form, but other models having been proposed[21].

1.04 ADSORPTION AND ADLAYER GROWTH

Adsorption - the accumulation of gas molecules on to a solid surface forming a thin film - can occur when a flux of gas molecules collides with a surface, this flux coming from the gaseous pressure or from a chemical or an evaporation source. Other processes that can occur include specular reflection, inelastic scattering, or adsoprtion followed by desorption [1]. The fraction of gas molecules or atoms that adsorb to the surface defines the sticking factor (which therefore ranges from 0 to 1), which varies between various surfaces and various adsorbates.

The adsorption of gases by charcoal was observed by C W Scheele in 1773 and by Abbé F Pontana in 1777,[22]. In 1915, Langmuir suggested that adsorption was similar to chemical combination[23], there being points on a crystal surface which can hold one atom or molecule, leading to a maximum coverage one molecule thick. In the early stages, a fraction θ of the surface is covered, such that the rate of adsorption is proportional to$(1-\theta)$.

The adsorption process is illustrated in Figure 1.02(a), and is explained below. An inert gas atom such as Xe approaching some surface with a kinetic energy $E_K(1)$ will 'hit' the surface at which point(2) it may be accommodated - energy being transferred to lattice vibrations (ie phonons), or to electronic excitations - the atom then lying in a bound state(3). For such physi-sorbed states there is no charge transfer between the atom or molecule and the surface, the binding energy being typically 0.25 eV being due to weak Van der Waals bonding.

Pt (110) is also known to reconstruct as do some other surface planes of fcc and bcc (body centred cubic) metals [20], hexagonal layers being a common form, but other models having been proposed[21].

1.04 ADSORPTION AND ADLAYER GROWTH

Adsorption - the accumulation of gas molecules on to a solid surface forming a thin film - can occur when a flux of gas molecules collides with a surface, this flux coming from the gaseous pressure or from a chemical or an evaporation source. Other processes that can occur include specular reflection, inelastic scattering, or adsoprtion followed by desorption [1]. The fraction of gas molecules or atoms that adsorb to the surface defines the sticking factor (which therefore ranges from 0 to 1), which varies between various surfaces and various adsorbates.

The adsorption of gases by charcoal was observed by C W Scheele in 1773 and by Abbé F Fontana in 1777,[22]. In 1915, Langmuir suggested that adsorption was similar to chemical combination[23], there being points on a crystal surface which can hold one atom or molecule, leading to a maximum coverage one molecule thick. In the early stages, a fraction θ of the surface is covered, such that the rate of adsorption is proportional to$(1-\theta)$.

The adsorption process is illustrated in Figure 1.02(a), and is explained below. An inert gas atom such as Xe approaching some surface with a kinetic energy $E_K(1)$ will 'hit' the surface at which point(2) it may be accommodated - energy being transferred to lattice vibrations (ie phonons), or to electronic excitations - the atom then lying in a bound state(3). For such physi-sorbed states there is no charge transfer between the atom or molecule and the surface, the binding energy being typically 0.25 eV being due to weak Van der Waals bonding.

Fig.1·02 : Adsorption (a,b) : potential energies
(c) : image charge model

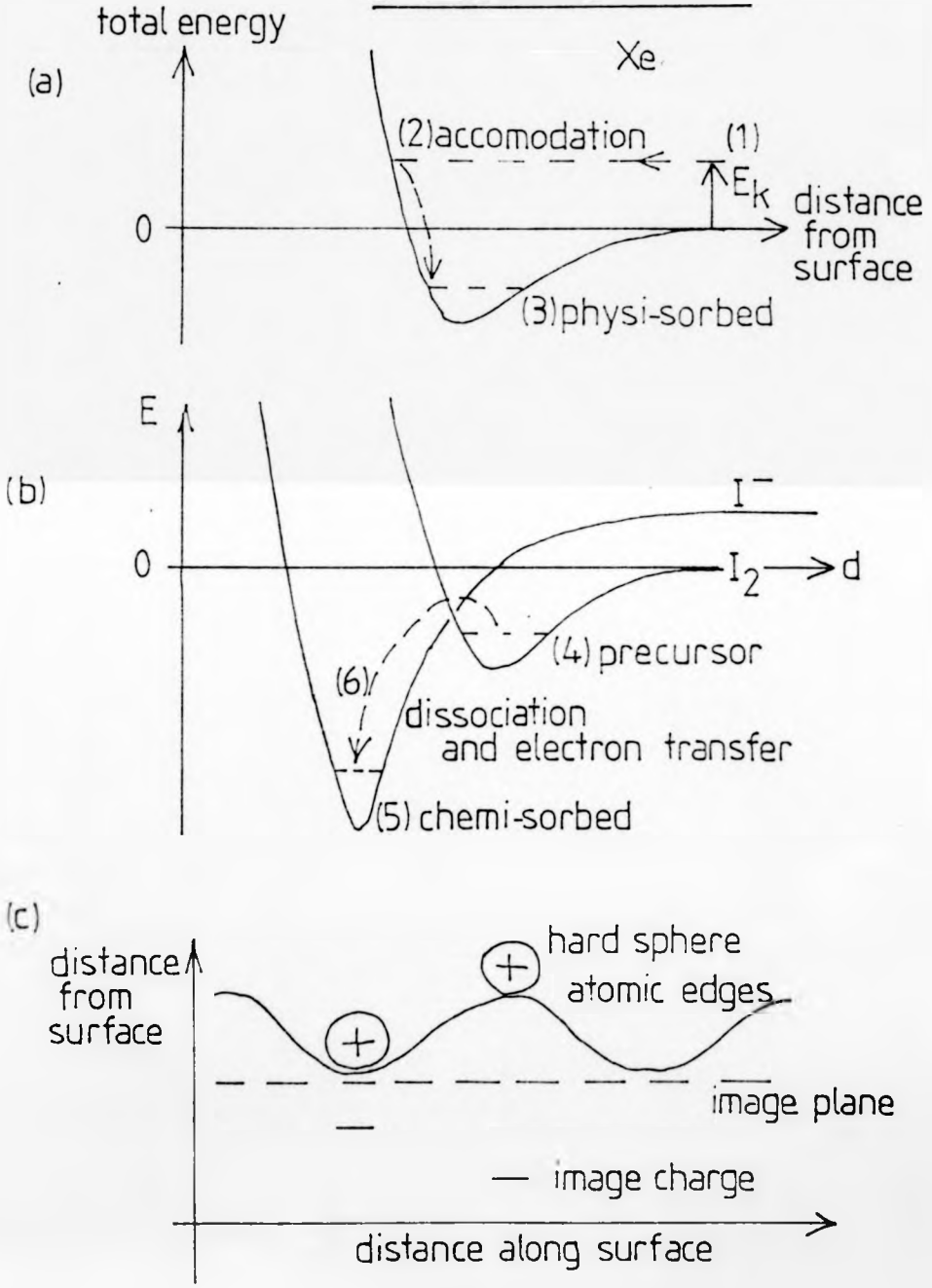

Other atoms or molecules may reach a chemisorbed state as illustrated in Figure 1.02(b). An iodine molecule for example could reside in a precursor state[4] where it is physisorbed. It can be seen that an iodine ion, I^-, can reside in a much deeper potential well (5), nearer to the surface. A dissociation of the iodine molecule accompanied by an electron transfer from the surface could therefore lead to this chemisorbed state. In general positive or negative ions can be found, the bond being either ionic or covalent, with binding energies up to 8 eV (for oxygen on tungsten, 8.4 eV, [1]). The molecule has to surmount the potential barrier (6) which may be above or below the line of zero total energy, in order to reach the chemisorbed state, and this may be achieved by vibrational or some other input of energy.

The particular adsorption site adopted by the atom is generally that of lowest energy. Once adsorbed that atom may be able to diffuse along the surface (see Fig.1.02(c)) although since the activation energy for diffusion is typically 0.5 eV [1] this process is restricted at room temperature ($k_BT \approx 0.03$ eV) spending most of its time where the total energy is minimised.

For the example of a positively charged adatom on a metal surface, the bonding can be considered as being due to the mutual attraction of this ion and its image charge as shown in Fig.1.02(c). The separation of the two charges equidistant on opposite sides of the image plane, can be minimised, and hence the binding energy maximised, by the adion 'falling down' into the 'lowest' available site. In most cases such a site would be where the co-ordination number (the number of substrate atoms that the adatom is in contact with) is maximised. Here the overlap of the electron charge density of the Fermi sea (which decays exponentially, being effectively zero 1 atomic distance

beyond the image plane [24]), with the positive ion is maximised.

For other surfaces it may be more meaningful to consider the spatial orientation of 'dangling bonds' or electron orbitals [16]. This technique has proved very useful in showing that adatoms are often likely to bond at the steps where there are dangling bonds, rather than on the terraces, of stepped surfaces [17].

The bonding of adsorbate atoms can be studied experimentally using techniques such as angle resolved ultra-violet spectroscopy which can determine the orientations of the bond orbitals, and core level shifts via X-ray photo-electron spectroscopy which determines the binding energy which is sensitive to the chemical environment. Measurements of the changes in the work function of a surfaces as a function of the adsorbate coverage, can give useful information on the charge state of the adlayer.

The adlayer growth process depends upon the initial adsorption sites and the relative sizes of the substrate and adsorbate atoms, which can be considered as hard spheres having fairly well defined atomic, metallic, covalent or ionic radii. Metal adatoms of similar size to metallic substrate atoms tend to fall into sites such that an outward growth of the bulk structure occurs - expitaxial growth - the absorbate having perfect registry with the substrate [1,2]. Usually for simple gas molecules [3], and for similar sized or smaller adatoms, a coherent growth, occurs, the overlayer having the same 2-D lattice parameters as the substrate. For larger adatoms the result may be for the overlayers to consist of the same geometrical structure as the top layer of the substrate but with twice the atomic

spacings, or it may be an incommensurate overlayer, for example hexagonally close packed on a rectangular substrate mesh.

A large number of adsorbate-substrate systems have been studied experimentally and explained theoretically, notably halogens on transition metals [25], and alkali metals on transition metals, [26, 27]. A variety of techniques - X-ray and electron energy analysis, Auger spectroscopy, SIMS (secondary ion mass spectroscopy) [4] - have been applied, LEED (low energy electron diffraction) being particularly important for structural derivations [26 - 29].

1.05 CRYSTAL PREPARATION AND THE UHV (ULTRA-HIGH VACUUM) CHAMBER

A single crystal surface can be obtained by cutting through a single crystal (usually by spark erosion) at the required angle, and checking the alignment to $\frac{1}{2}^{\circ}$ accuracy by photographing the Laue X-ray diffraction pattern [30]. This is followed by polishing with decreasing sizes of abrasive papers and pastes down to micrometer size, and possibly electrochemical polishing to remove the mechanically damaged top atomic layers.

Once inside the vacuum chamber, mounted on the crystal manipulator, the crystal can be cleaned by bombarding its surface with inert gas ions (usually argon), typically a 100 μA beam current of 2 keV energy ions for $\frac{1}{2}$ hr. The surface can then be annealed by heating the crystal to around 500°C which can be achieved by an electron bombardment of around 50 mA from a heated filament mounted close behind the crystal, the voltage between the two being typically 1 kV. This procedure is repeated for several cycles until the surface is 'clean' - those bulk

Fig. 1·03 : SEXAFS UHV chamber at Daresbury

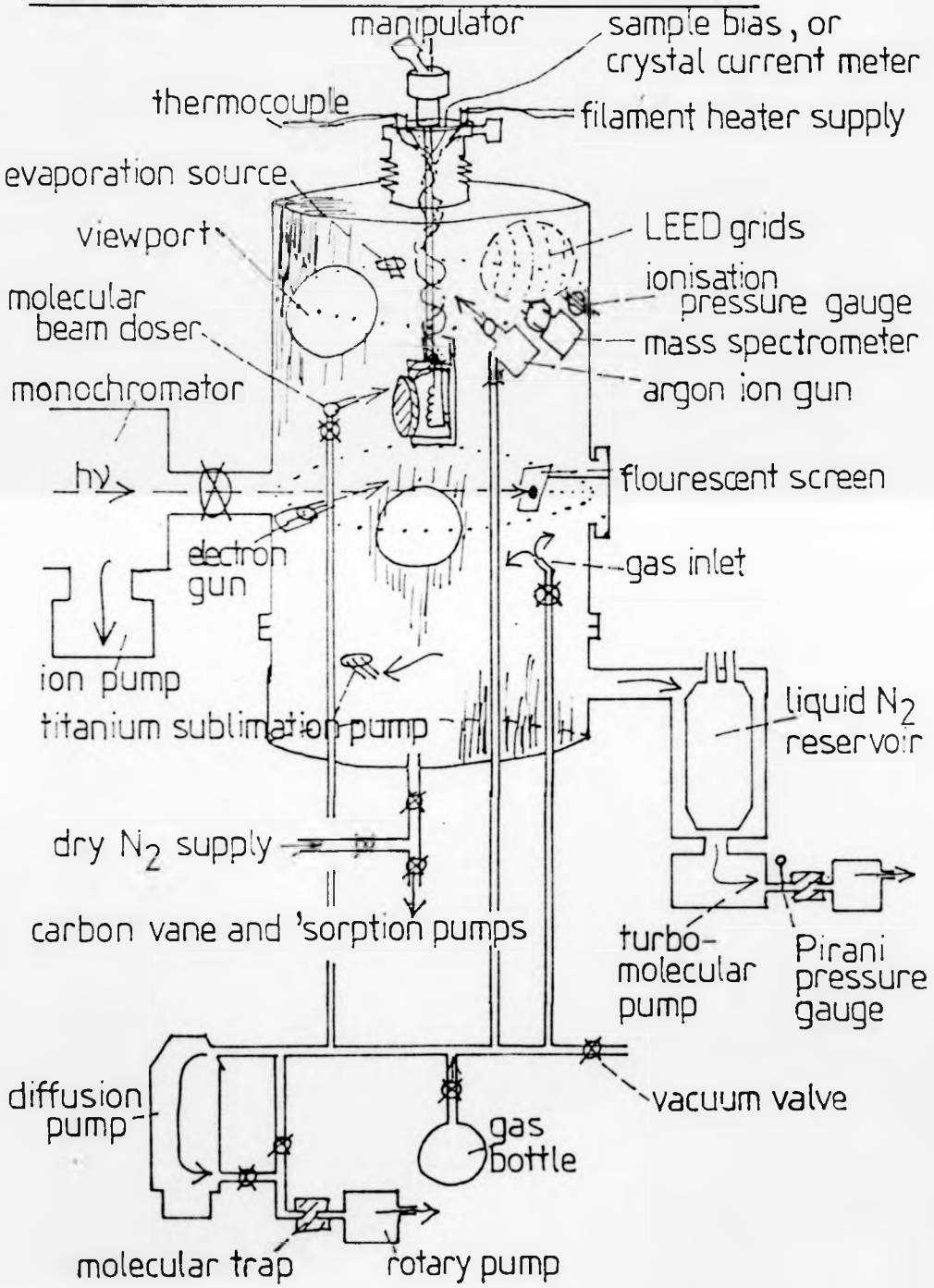

contaminants that precipitate out on to the surface during heating and cooling, will have been removed, and other surface impurities may have diffused into the bulk.

In practice UHV (ultra high vacuum) conditions of less than 10^{-10} torr (1 torr = 1.33 mbar) can be routinely obtained by roughing out the vacuum chamber using a rotary pump for example, and then using this pump to back a diffusion or turbo-molecular pump, which in conjunction with an ionization and a titanium sublimation pump, can achieve a base pressure of around 10^{-7} torr. The system then needs to be baked to 200°C to remove most of the water vapour, which would otherwise slowly desorb from the chamber walls, keeping the pressure high for many hours. After cooling, a final base pressure of 10^{-10} to 10^{-11} torr can be obtained. The chamber used for SEXAFS measurements at Daresbury is shown in Fig.1.03.

1.06 AES (AUGER ELECTRON SPECTROSCOPY) AND SURFACE CHEMICAL COMPOSITION

The Auger process consists of a core hole (which may have been created by a primary electron or by an X-ray photon colliding with the bound electron) being filled by an electron making the transition from an outer shell, an Auger electron being emitted from the atom to conserve energy. An example of such a process is shown in Fig.1.04. The kinetic energy of an Auger electron is a characteristic of the atomic energy levels; for the example shown in Fig.1.04 the kinetic energy is approximately given by Eqn. 1.01.

$$K E_{Auger} \approx B E_{L\ shell} - 2 B E_{M\ shell} \quad (1.01)$$

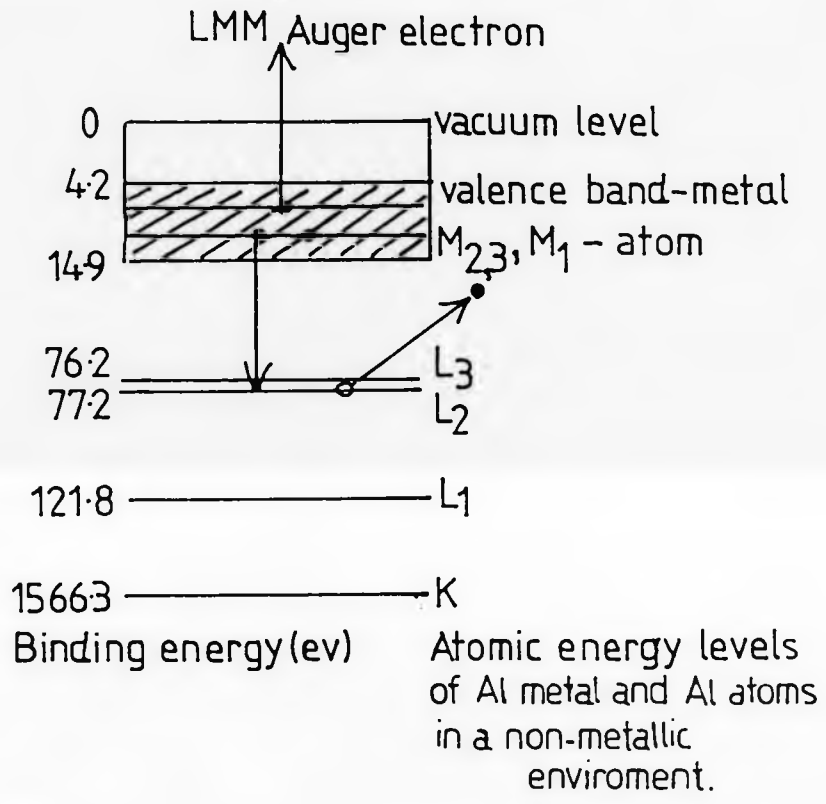

Fig.1·04: An example of the Auger process.

A more accurate calculation needs to include the relaxation effects. Since the escape depths from solids of electrons of such kinetic energies as produced by Auger processes are of the order of a few atomic layers, AES (Auger electron spectroscopy) is widely used for the chemical analysis of solid surfaces [31 - 33].

A typical AES experimental arrangement is shown in Fig.1.05. An electron gun, consisting of a heated filament at a negative potential of around 3 kV and of focussing tubes at similar voltages, provides typically a 1 μA beam of high energy electrons hitting the crystal over an area approximately 1 mm^2. These primary electrons penetrate several atomic layers into the solid, loosing energy as they undergo inelastic collisions with bound electrons, which are caused to move through the solid, in turn producing more low energy 'secondary' electrons. The fraction of electrons that happen to be travelling towards the surface can emerge into the vacuum, such that the energy distribution of electrons coming from the solid contains a large peak at low energy - see Fig.1.06. The elastic peak, which in this example is at 3 keV, results from elastic scattering of the primary electrons. Atoms that have been ionised can relax (after a time period that it effectively instantaneous in the macroscopic world, but quite long for interatomic transitions) from their excited state via the Auger process - for K-shell ionisation, decay via the emission of a fluorescent X-ray dominates for medium and high atomic number elements, ie Z>30; but for decay of an L-shell ionisation, the Auger process has the highest probability for all except the heaviest elements, Z>90. Auger peaks can be seen as small features on a large background - see Fig.1.06. In practice the electron energy spectrum is measured as described below.

Fig. 1·05 : AES - Experimental set up

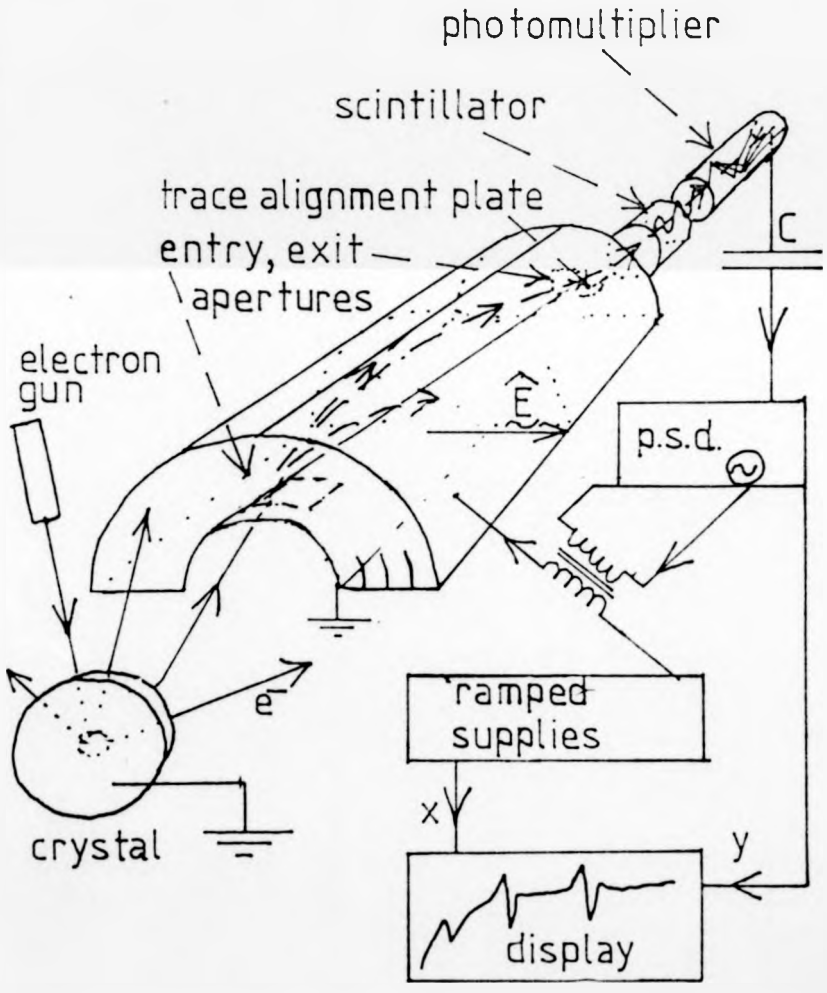

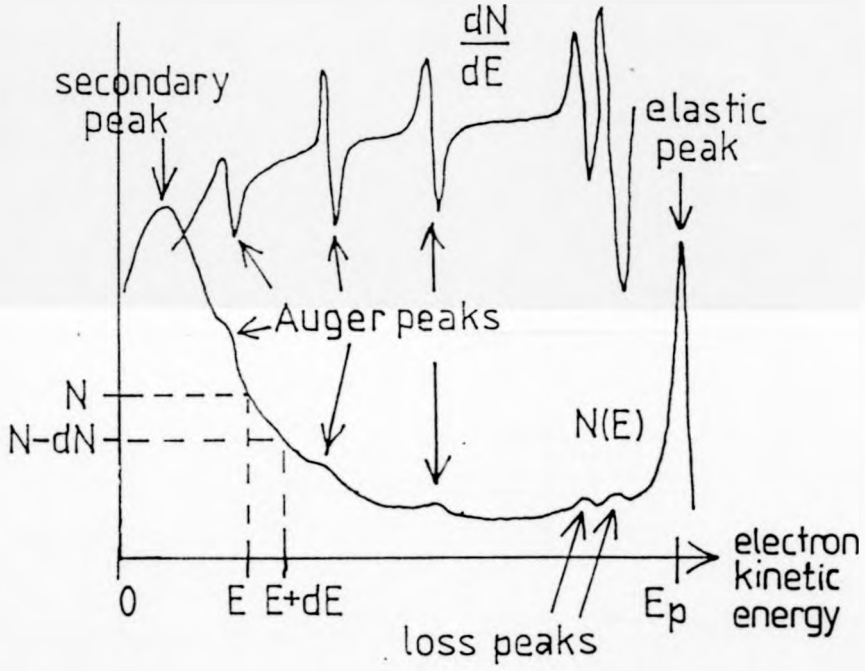

Fig. 1·06: Example of Auger spectra.

The hemi CMA (cylindrical mirror analyser) as shown in Fig.1.05, consists of two hemi-cylindrical plates, the outer plate being at a large negative voltage, for example 2 kV, such that there is a radial electric field in the region between the plates, the inner of the two being at earth potential and the field being confined and shielded by a mu-metal shield. Electrons entering the hemi CMA (it is more usual for a full CMA to be used) in a trajectory within a small solid angle, can pass through the CMA if they have a kinetic energy within a range determined by the deflection voltage, the geometry of the system, and the width of the exit aperture. Such electrons are then deflected by the trace alignment plate at a large negative potential, eg - 3 kV, on to a scintillator which is itself biased at around + 5 kV to accelerate the electrons which loose their energy as they collide with the atoms of the scintillator material which decay from their excited states via light emission. In this particular arrangement the 'signal' of light leaves the vacuum chamber through a small window at this point, a photo-multiplier tube being used to collect and amplify this signal. The light falls on to the photo-multiplier cathode, which is typically at a voltage of around - 1 kV, producing photo-electrons, which are accelerated on to the next dynode, at a less negative voltage, hitting the metal surface at glancing incidence producing a large number of ejected electrons, ie achieving a multiplication in the number of electrons. This proceeds until the electrons reach the anode, in this case charging a capacitor which is connected to earth through a leakage resistance.

A measure of the drain current through this resistor is proportional to the rate of arrival (averaged over the time constant of the system) of electrons having that particular kinetic energy determined by the CMA plate voltages. If these voltages are ramped from say zero to - 2 kV over a time of a few minutes, then a spectral distribution can be displayed on a chart recorder, the x-sweep being controlled by the plate voltages, the y - deflection being proportional to the drain current. In this way a spectrum, N(E), similar to that shown in Fig.1.06 can be obtained.

For small signals it is often useful to replace the scintillator and photo-multiplier with a channeltron electron multiplier inside the vacuum chamber, and to use pulse counting (although both arrangements can operate in either analogue or digital modes) where an electron arriving at the collector produces a pulse of electrical current at its output, enabling the elctronics to record directly the number of electrons passing through the CMA, hence N(E).

In general, the Auger peaks on the N(E) spectrum are small features which may be obscured by noise, introduced by the electronics or of a statistical nature. A method commonly employed to enhance the detection of Auger peaks is to use a modulation technique employing a psd (phase sensitive detector), sometimes called a lock-in amplifier. This device can be used to supply a sinusoidal electrical signal of typically 1 V peak-to-peak amplitude, and approximately 18 kHz frequency, which is connected through a transformer to the CMA plate voltages (see Fig.1.05). This modulation of the electron detection

energy causes a variation in the detected signal at the same frequency, the amplitude of which is proportional to the gradient of N(E) at the particular E value. For example, in Fig.1.06, if the detection energy varies from E to E+dE, then the detector signal oscillates between N-dN and N. For the arrangement shown in Fig.1.05 the photo-multiplier output is capacitatively coupled to the input of the psd, this device effectively rejecting all frequencies other than a band around 18 kHz, its output being a displayable voltage proportional to the amplitude of the 18 kHz frequency component. This voltage is used as the y-input of the chart recorder whose x-input is controlled by the ramped supplies, the result being a dN/dE spectrum, which as can be seen in Fig.1.06, enhances the clarity of the peaks.

1.07 SURFACE STRUCTURE, LEED (LOW ENERGY ELECTRON DIFFRACTION), AND SEXAFS (SURFACE EXTENDED X-RAY ABSORPTION FINE STRUCTURE)

The established technique for determining the structure of a bulk (usually crystalline) material is X-ray diffraction, in which a beam of X-rays ($\lambda \approx 10\text{Å}$) penetrates deeply into the solid, being absorbed and scattered by atomic core electrons in the process. A number of diffracted beams of significant intensity are formed, the direction and intensity of each being determined by the geometrical structure of the solid. Because of the small scattering factors involved there is negligible probability of an X-ray undergoing more than one scattering event before it leaves the solid or before it is absorbed by the solid, thus kinematic theory is sufficient to describe the process.

Like X-rays, a beam of electrons can be characterised by a wavelength, using the de Broglie momentum equation - eqn. 1.02.

$$h\lambda = mv \quad , \quad v = \text{velocity} \qquad \ldots (1.02)$$

λ is a function of the beam energy or voltage as in eqn 1.03.

$$\lambda = \sqrt{\frac{150}{V}} \qquad \text{units: Å, volts} \qquad \ldots (1.03)$$

At a potential of 100 V the wavelength being 1.2Å [3], ie of the order of atomic dimensions. If a beam of low energy electrons ($\lesssim$ 100 V) is incident upon a solid surface then the large electron scattering factors prevent the beam from penetrating more than a few atomic layers into the solid, and the top atomic layer contributes a large fraction of the total scattering of electrons from the solid back into the vacuum. It is the observation of the direction and intensity of these diffracted beams that can determine the structure of the top atomic layers [2, 30].

To a first approximation, scattering occurs entirely from the top atomic layer as shown in Fig.1.07 (a), where the wave-vector specifies the direction and energy of the incident beam. Two reflected beams, k_1 and k_2, are shown in the diagram; whether or not these beams have significant intensity depends on whether they contain components that are in phase with each other, ie is dependent on the directions of the beams and the geometrical arrangement of the scattering points. The symmetry of the diffraction pattern reflects that of the surface structure, thus for this example, a pattern of spots forming a rectangular mesh would be seen on intercepting and displaying the diffracted beams (see Fig.1.07 (b)).

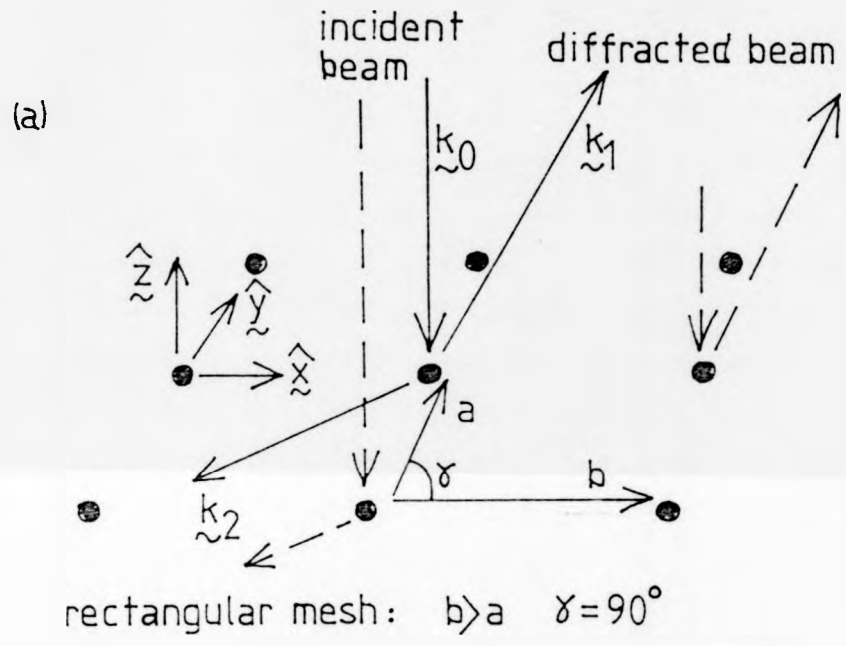

Fig.1·07: LEED, kinematic theory
(a): diffraction from a plane of atoms
(b): LEED pattern has same symmetry

In reality, multiple scattering occurs such that a dynamical theory is needed for a complete description of LEED, and more atomic layers are involved as illustrated in Fig.1.08. Whilst multiple scattering does not affect the symmetry and the spot positions of the LEED pattern, it does affect the spot intensity. A structure has therefore to be determined as follows:

(i) Make a guess as to the structure, based upon the symmetry of the LEED pattern, for a clean surface, or for an adsorbate covered surface assuming the most likely adsorption sites.

(ii) Calculate the LEED pattern that would be produced by this structure using a sufficiently high number of multiple scattering events.

(iii) Compare theory with experiment.

(iv) Refine the structure until an agreement is reached.

In general, if a good fit can be achieved then it is very likely that the structure is correct; problems only arise when it is only possible to achieve a number of poor fits for a variety of guessed structures, when the structural derivation remains somewhat uncertain. The calculations and measurements that are compared are those which are sensitive to the structure, such as:

(i) The intensity of a diffracted beam as a function of the primary beam energy.

(ii) The intensity of a reflected beam as the crystal is rotated about the surface normal.

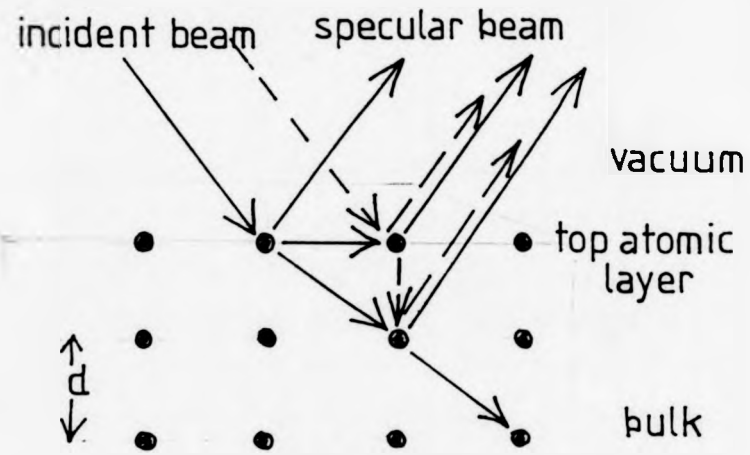

Fig.1·08: LEED-dynamic model, including multiple scattering and several atomic planes.

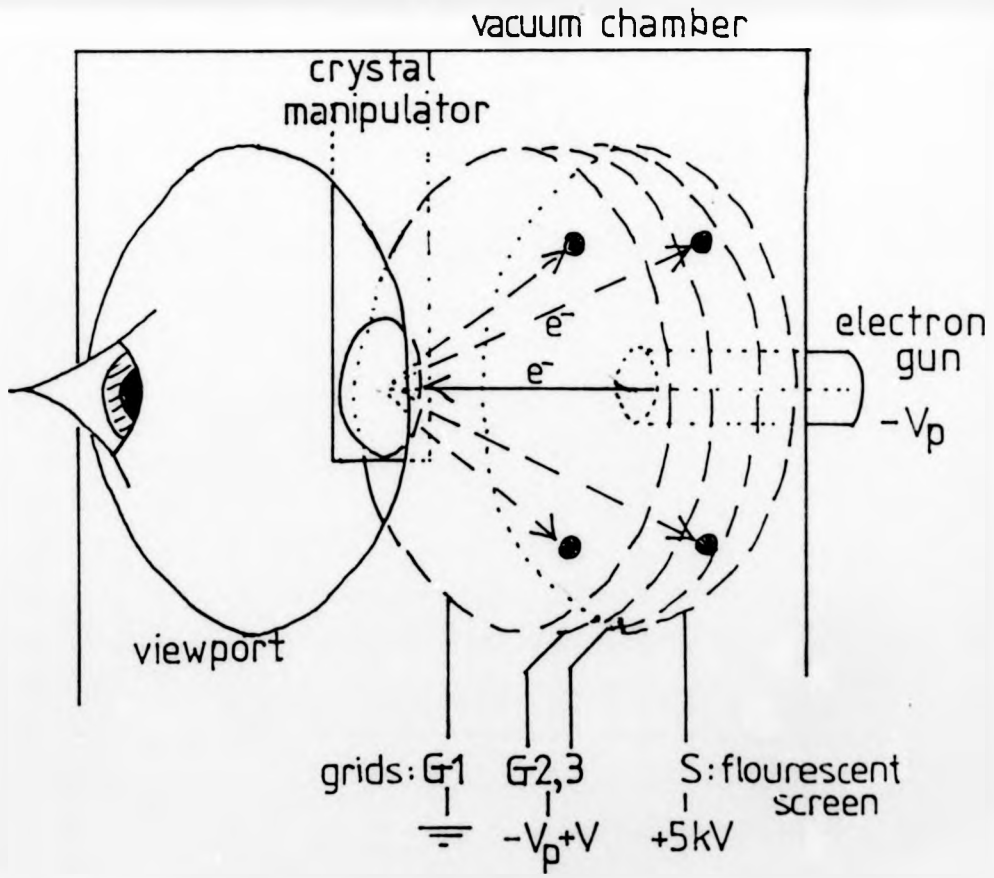

Fig. 1·09: LEED Experimental arrangement

A typical experimental arrangement for producing a LEED pattern is shown in Fig.1.09. The primary beam of electrons is derived from an electron gun, the beam striking the crystal, usually at normal incidence, after passing through apertures in the hemispherical grids and screen. The spot size of the electrons hitting the crystal surface is of the order of 1 mm x 1 mm, the crystal being mounted on a manipulator to allow translation in three perpendicular directions, and rotations. The LEED grids consist of an outer grid that is earthed (as is the crystal) to produce a field free region such that the electron beams travel in straight lines with no alteration of their energy. Most electrons pass through the grid which is made of very fine wire. The next two grids which are also largely transparent can be biased to repel those electrons below a certain energy, allowing the passage of the elastically scattered electrons that constitute the LEED pattern, but rejecting lower energy secondary electrons that give rise to a fairly isotropic background. Finally, the electrons are accelerated on to the phosphor screen biased at around +5 kV, to produce visible light at the points of impact.

In order to get a good LEED pattern, a single surface structure should be predominant over the area being probed by the electron beam, although this surface need not be ordered over the whole area 1 mm x 1 mm. The only requirement is that long range order exist over the transfer width or coherence zone [3], which is of the order of 100Å x 100Å, since the intensities in the diffracted beams from such well-ordered areas are very much greater than the intensity of the background arising from the disordered areas.

The simplest application of LEED is a routine method to indicate an ordered surface, when sharp spots and low background should be observed. The study of clean single crystal metal surfaces for example, has been limited mainly to LEED, in which dynamical (multiple scattering) calculations for postulated structures are compared with the experimental results [20]. Often a large number of structures have to be postulated, sometimes with the result that more than one gives a reasonable fit to the experimental data [21].

In some cases, very small amounts of adsorbate (below the detectibility of AES) cause a reconstruction of the surface causing a change in the LEED pattern. In such cases the technique of LEED is therefore very sensitive to the surface cleanliness. LEED is used for structural studies of adsorption [26, 28], in which the determination of the adsorbate-substrate layer spacing can be accurate to $\pm$ 0.1Å [29], provided occurrences such as multiple coincidences [34] are not present.

Unlike LEED, SEXAFS can be applied to systems lacking any long range order. In general, an analytical procedure can be used to obtain the local environment(s) of these atoms that have the X-ray absorption edge whose fine structure is being measured, removing the necessity for time consuming model calculations that require large computing capacities. In SEXAFS analyses, the adsorption site can often be reliably determined [35, 36], and the bond lengths can be derived to an accuracy of $\pm$ 0.01Å with exceptionally good data [37], although it

is rare for results to be quoted to an accuracy of $\pm$ 0.02Å [35, 38], typical accuracies being $\pm$ 0.03Å [36], and for data posing certain problems in the analyses errors are usually quoted to around $\pm$ 0.05Å [39, 40]. Thus, small changes in bondlengths of around 0.05Å which are chemically significant can, in principle, be detected by SEXAFS but not by LEED.

1.08 REFERENCES

1. M Prutton 'Surface Physics' Clarendon Press 1975

2. J G Dash 'Films on Solid Surfaces' Academic Press 1975

3. F C Tompkins 'Chemisorption of Gases on Metals' Academic Press '78

4. G C Allen and R K Wild, CEGB Research, Jan '81, p 12.
'Probing the secrets of solid surfaces'.

5. S R Tennison, Chemistry in Britain 17 (11) Nov '81 p 536
'Recent advances in catalytic reforming'

6. J J McCarroll, Surface Science 53, '75, p 297
'Surface Physics and Catalysis'

7. N Freyer, G Pirug, H P Bonzel, Surf Science 126, 1983, p 487
'C(1s) spectroscopy of hydrocarbons adsorbed on Pt(111)'.

8. M Surman, S R Bare, P Hofmann, D A King, Surf. Sci 126, '83, p 349
Direct Characterisation of a catalytic surface reaction step - benzene-deuterium exchange on Pt {110}'

9. W Hasse, H-L Günter, M Henzler, Surf. Sci 126, '83, p 479
'Study of self hydrogenation of ethene on clean Ni (111)'

10. K Christmann and G Ertl, Surf. Sci 60, '76, p 365
'Interaction of hydrogen with Pt (111): the role of atomic steps'.

11. C T Cambell, D W Goodman, Surf. Sci 123, '82, p 413
'A surface science investigation of the role of potassium promoters in nickel catalysts for CO hydrogenation'.

12. M P Kiskinova, Surf. Sci 111, '81, p 584
'CO Adsorption on Alkali Metal covered Ni (100)'.

13. N D Long, Phys.Rev.B4 (12), Dec '71, p 4234
'Theory of work function changes induced by alkali adsorption'.

14. C Pirug, H P Bonzel, G Boden, Surf.Sci 122, '82, p 1
'The adsorption of potassium on Pt (111) and its effect on oxygen adsorption'.

15. C Kittel, 'Introduction To Solid State Physics', 5th edn. '76, John Wiley & Sons.

16. R P Messmer, S K Knudson, K H Johnson, J B Diamond, C Y Yang, Phys Rev B13 (4) Feb '76, p 1396
'Molecular orbital studies of transition and noble-metal clusters by the self-consistent-field-Xα scattered wave method'.

17. A C Balazs and K H Johnson
Surf. Sci 114, '82, p 197
'Molecular-orbital models for the catalytic activity and selectivity of co-ordinateively unsaturated platinum surfaces and complexes.

18. W T Moore, S J White, D C Frost, K A R Mitchell
Surf. Sci 116, '82, p 253
'LEED crystallographic studies of the (311) surface of nickel. I. Structural analysis'.

19. J E Demuth, P M Marcus, D W Jepsen, Phys.Rev. B11 (4), 15 Feb '77, p 1460
'Analysis of low-energy-electron-diffraction intensity spectra for (001), (110), and (111) nickel'.

20. M A Van Hove, R J Koestner, P C Stair, J P Biberian, L L Kesmodel, I Bartoš, G A Somorjai
Surf. Sci 103, '81, p 189 and p 218
'The surface reconstructions of the (100) crystal faces of iridium platinum and gold'
I Experimental observations and possible structural models
II Structural determination by LEED intensity analysis'

21. J P Biberian, Surf.Sci 97, '80, p 257
'An alternative model of the reconstructed (100) surfaces of gold, platinum, and iridium'.

22. C L Mantell, 'Adsorption', second edition, McCraw-Hill, 1951, Chapter 2: Theories of adsorption.

23. Langmuir, Journal of the American Chemical Society : 38 (1916) p 2267; 39 (1917) p 1883; 40 (1918) p 1361.

24. G A Somorjai 'Principles of Surface Chemistry' Prentice Hall ('72) Chapter 4: 'Electrical Properties of Surfaces'.

25. D Bullet, Vacuum 31 (10 - 12) p 445, 1981 'Surface electronic structure calculations for Na and Cl adsorbates on Cu'.

26. R L Gerlack, T N Rhodin, Surf Sci 17, '69, p 32 : 'Structure analysis for alkali metal adsorption on single crystal nickel surfaces'.

27. R L Gerlack, T N Rhodin, Surf Sci 19 '70, p 403 : 'Binding and charge transfer associated with alkali metal adsorption on single crystal nickel surfaces'.

28. S Anderson, J B Pendry, J Phys. C6, '73, p 601 : "LEED intensity measurements and surface structures: The dynamical approach'.

29. K A R Mitchell, Surf Sci 100, '80, p 225 'On the bond lengths reported for chemisorption on metal surfaces'.

30. F Jona, J Phys. C11 ('78), p 4271
'LEED crystallography review article'.

31. D Chattarji 'The Theory of Auger Transitions'
Academic Press ('76) Chapter 8:
"AES and its appliation to surface science'.

32. J T Grant, Applications of Surface Science 13 ('82) p 35
"Surface Analysis with AES'.

33. 'Handbook of AES', 2nd edition, Physical Electronics Industries Inc.
L E Davies, N C MacDonald, P W Palmberg, G E Riach, R E Weber.

34. S Anderson and J B Pendry, Solid State Communications 16 ('75) p 563
'Multiple Coincidences in surface structure determinations'.

35. S Brennan, J Stöhr, R Jaeger, Phys.Rev. B24 (8) p 4871, Oct '81.
'Structure determination of C(2x2)S on Ni(100) using polarisation dependent SEXAFS'.

36. J Stöhr, R Jaeger, T Kendelewicz,
Physical Review Letters 49 (2), July '82, p 142
'Structure of p(2x2) Oxygen on Ni(100): a SEXAFS study'.

37. J Stöhr, Stanford Synchroton Radiation Laboratory Report 80/07 Dec '80
'EXAFS and SEXAFS: Principles, Analysis and Applications'.

38. Sean Michael Brennan, SSRL Report 82/03 June '82
'SEXAFS of sulphur on nickel'.

39. J Stöhr, L I Johansson, S Brennan, M Hecht, J N Miller
Phys. Rev. B22 (8) Oct '80 p 4052
'SEXAFS study of oxygen interaction with Al(111) surfaces'

40. J Stöhr, R Jaeger, G Rossi, T Kendelewicz, I Lindau
Surf. Sci 134 ('83) p 813
'Structure of the Ag on Si(111) 7x7 interface by means of surface EXAFS'.

CHAPTER 2

EXAFS-THEORY

2.1 Overview

In this chapter the phenomenon of the extended X-ray absorption fine structure is described, and the derivations of the EXAFS equations are outlined. Firstly the X-ray absorption coefficients are defined by reference to a simple transmission experiment in which X-rays are shone through a thin layer of solid, the reduction in beam intensity being due to X-ray absorption by the material. At an absorption edge the X-ray energy is exactly equal to the binding energy of a core electron, and the absorption coefficient is seen to rise rapidly at this energy. As the energy of the X-ray is increased, the absorption coefficient falls, and contains small oscillations up to an X-ray energy 1000 eV above the edge - this is the extended X-ray absorption fine structure - (EXAFS).

A simple model is presented to explain how the EXAFS is caused by the backscattering of photo-electrons, produced in the absorption process, from atoms neighbouring the central absorbing atom. Derivations of the two EXAFS equations for the fine structures above K and L_I edges, and above L_{II}, and L_{III} edges are briefly described, and reference given to fuller theoretical explanations.

The terms appearing in the EXAFS equations are explained - the atomic phase shifts, the electron backscattering factors, and the Debye-Waller factors (ie the thermal vibration, or the lattice disorder of the atomic positions). The simple theoretical explanation in terms of single scattering theory is validated by reference to the inelastic electron mean free paths within solids, and to the electron scattering factors. Since the EXAFS originates from the effect of the local invironment around the absorbing atom, radial distribution functions around central atoms are described.

2.2 The Absorption of X-rays by Matter

If a beam of X-rays[1] impinges upon solid matter, a number of processes can occur[2], leading to a reduction in the beam intensity, and a change in the relative intensities at different wavelengths. For a single wavelength, an X-ray absorption coefficient can be defined from the reduction in the intensity caused by a given thickness of matter, as illustrated in Figure 2.1, and stated in equation 2.1. The linear absorption coefficient, μ_l, is useful in determining the thickness of a material needed to absorb most of the X-rays, this being approximately $1/\mu_l$, typically of the order of a few micrometers[3]. More physically general coefficients are the mass absorption coefficients, μ_m, which are well documented[4, 5], and the atomic absorption coefficients, μ_a, which for a given atom has been shown[6] to be the sum of two terms, namely absorption and scattering, as stated in equation 2.2.

$$\mu_a = CZ^4 \lambda^3 + \sigma_a(Z, \lambda) \qquad \ldots (2.2)$$

The scattering term, σ_a, represents X-rays that are deflected in direction by the atomic core electrons. For wavelenths, λ, greater than 0.5Å, this term is approximately independent of λ, and increases linearly with the atomic number, Z; it is much smaller than the absorption term (sometimes referred to as the fluorescence term), except for very small λ and/or for the lightest elements. The fluorescence term represents an X-ray being 'absorbed' by an atom, thus ceasing to exist, and in the process ejecting a tightly bound inner electron, a photo-electron of kinetic energy, E_K, being roughly equal to the difference between the X-ray energy, $h\nu$, and the binding energy, E_B, as stated in equation 2.3.

$$E_K \approx h\nu - E_B \qquad \ldots (2.3)$$

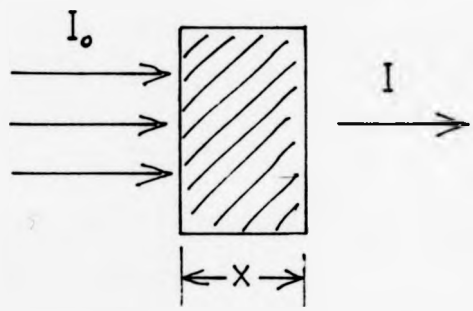

$$I = I_o e^{-\mu_l x} \quad \ldots\ldots (2{\cdot}01)$$

μ_l = linear absorption coefficient (m^{-1})

Fig. 2·01: Reduction in X-ray intensity due to absorption by matter.

The core hole left by the photo-electron is filled by an outer electron of the same atom, with a fluorescent X-ray being emitted, or more probably for K-levels of elements of atomic number less than 30 and for L_{III}-levels of elements Z < 90, accompanied by the emission of an Auger electron.

The absorption coefficient falls as $(h\lambda)^{-3}$, with the constant C (equation 2.2) depending on the element and the inter-absorption edge region, until the X-ray energy reaches that needed to excite electrons from the next deepest shell, at which point the absorption coefficient rises - the absorption edge - and the falls again as the same function of energy, but with a different constant of proportionality. Figure 2.2 illustrates the X-ray absorption process and shows the absorption coefficient as a function of $h\lambda$ for two elements. Extrapolation of the pre-edge function for chlorine, in the diagram, shows that above an absorption edge, the total absorption is made up of two components: firstly, in this case, the excitation of electrons from the K-level, and secondly the absorption due to less tightly bound electrons, forming a background.

2.3 The Absorption Edge

As pointed out by Kossel[7] in 1920, a rapid rise in the absorption of an X-ray occurs when its energy is sufficient to promote a core electron to the first empty atomic state, these empty states having energies determined by the effective central atomic charge, which is then (Z + 1). The exact energy of the absorption edge is defined as the inflection point in this initial rise. If these final states are bound, then to cause ionization a greater X-ray energy is needed (as illustrated in Figure 2.3(b)) and in general the absorption edge can vary in energy position by up to several electron volts from the ionisation threshold. In this example of the K-edge of argon, an electron from the 1S level is first excited to the lowest 4p level where it remains bound to the atom. In

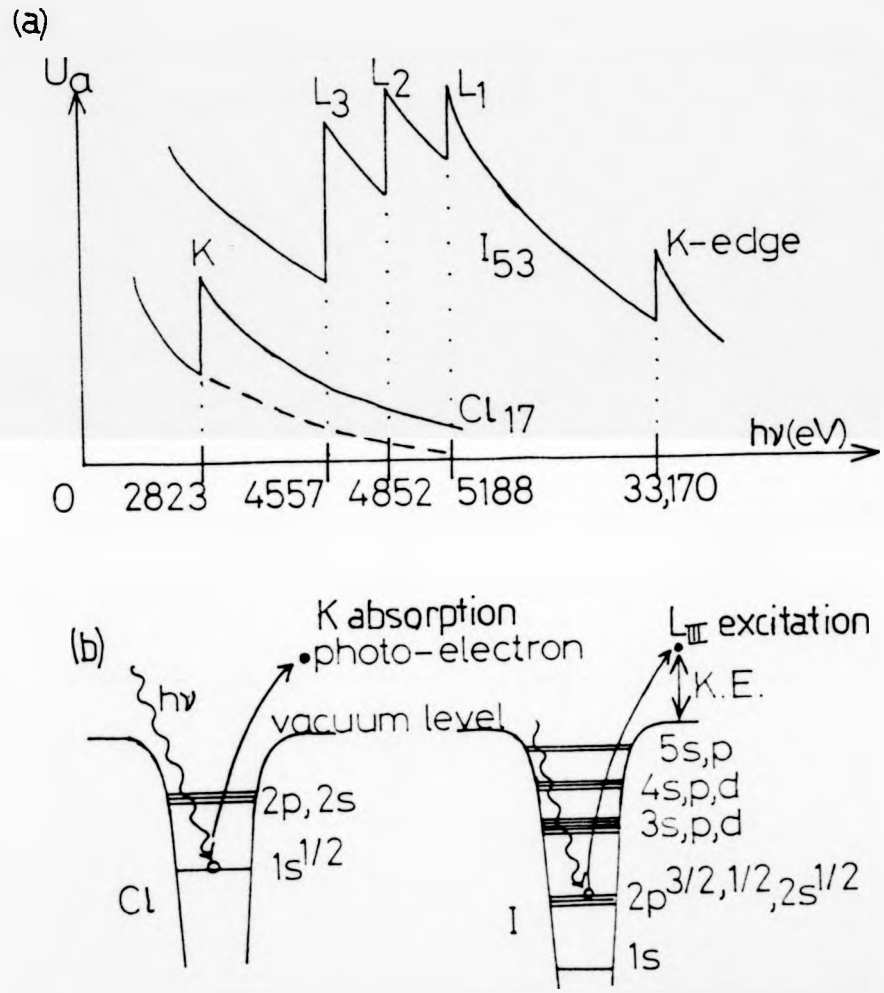

Fig. 2·02 : (a): Atomic X-ray absorption coefficients
(b): Energy level diagrams

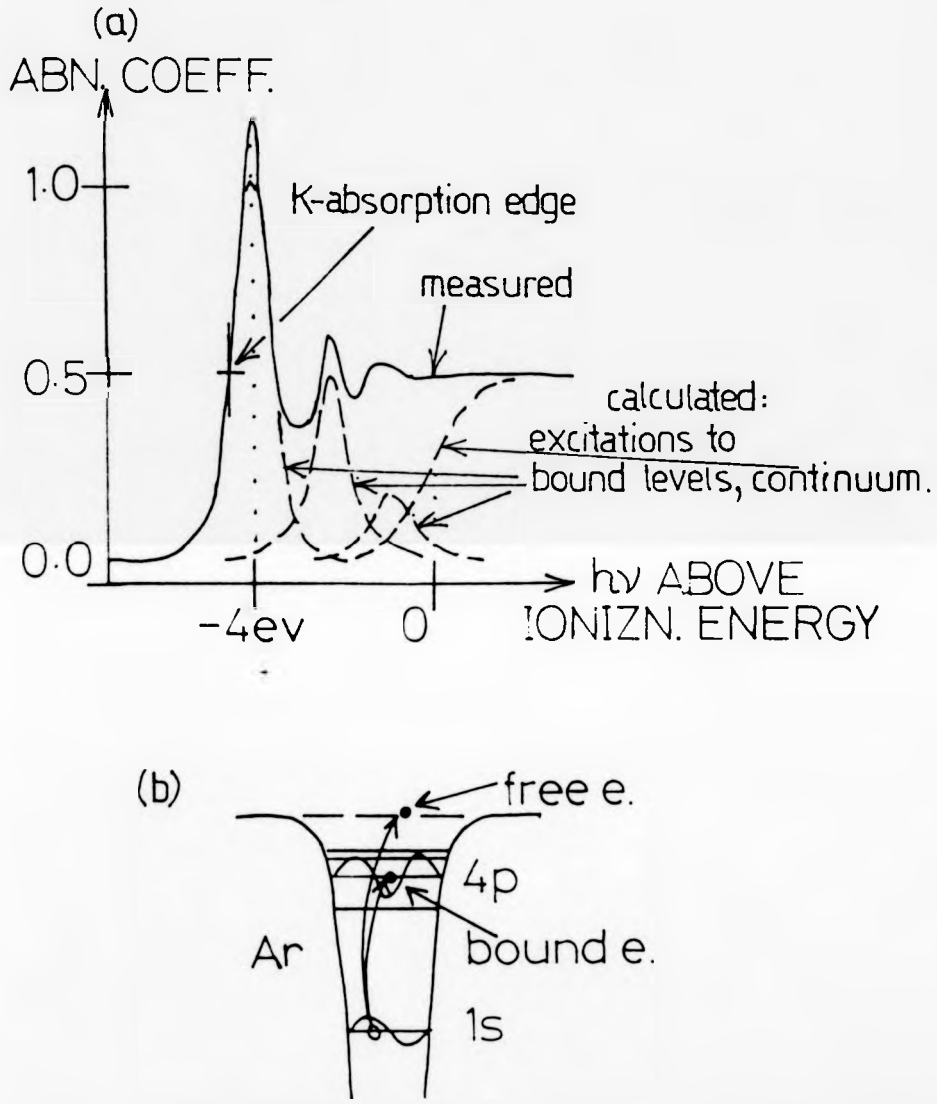

Fig. 2·03: Explanation of Argon absorption edge

order to create a free electron the X-ray needs to have another 4 eV of energy and at this ionization threshold a step increase in the absorption coefficient is observed. The total (as measured) absorption coefficient can be explained by the sum of the absorption lines and the step edge, each broadened by a gaussian-type function, as shown in Figure 2.3(a).

The occurence of a sharp 'white line' followed by oscillations spread over a few electron volts and then a roughly level value is typical of absorption edges, the structure arising from a variety of effects, depending upon the edge, the atomic type, and the chemical environment.

2.4 The Extended X-ray Absorption Fine Structure (EXAFS)

In the 1930's, using low power X-ray tubes, dispersive Bragg spectrometers and photographic films, research workers observed oscillations on the high energy side of absorption edges extending for up to 1000 eV above the edge, and having a magnitude of up to 10% of the edge jump. Theories, notably that of Kronig[8], decided on a short rather than on a long range order effect. The advent of synchrotron radiation sources[6] and new technology in the 1970's enabled acurate experiments to be performed, which provided stimuli to refine the theory, which is now well understood[9-12], such that EXAFS can now be used as a structural probe[12, 13].

That the EXAFS is due to nearby atoms affecting the absorption of X-rays by a central atom, can be seen by comparing the absorption coefficients above the K-edges of Krypton (which has no nearby atoms in its monatomic gas form) and of bromine (existing as diatomic molecules, in which each absorbing atom has an accompanying partner), as shown in Figure 2.4.

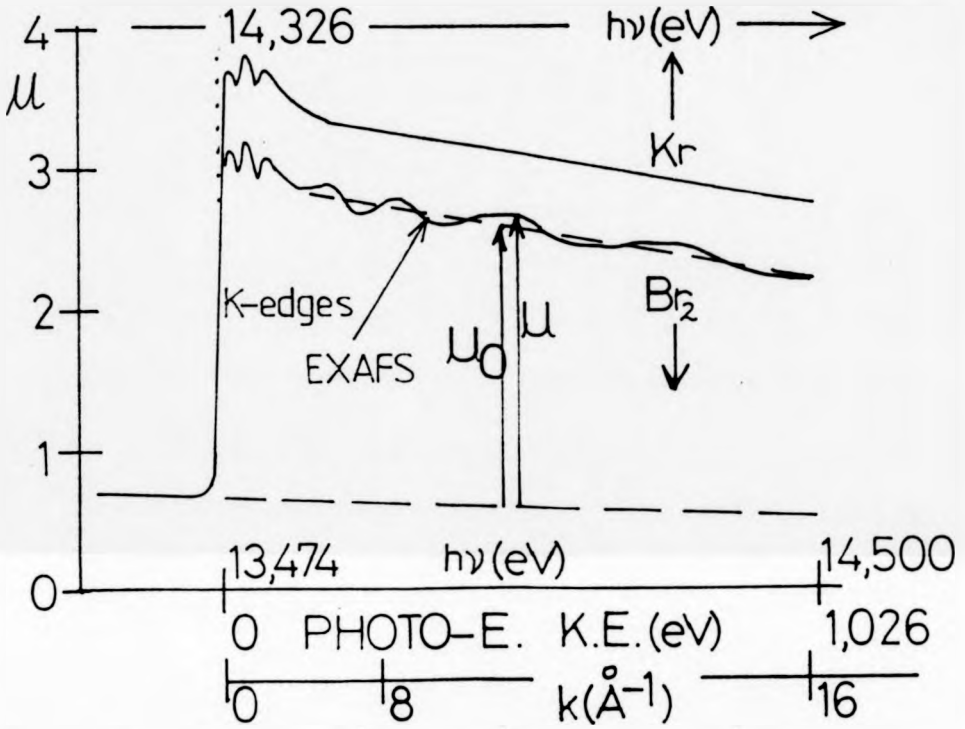

Fig 2·04 : X-ray absorption coefficients of bromine and krypton.

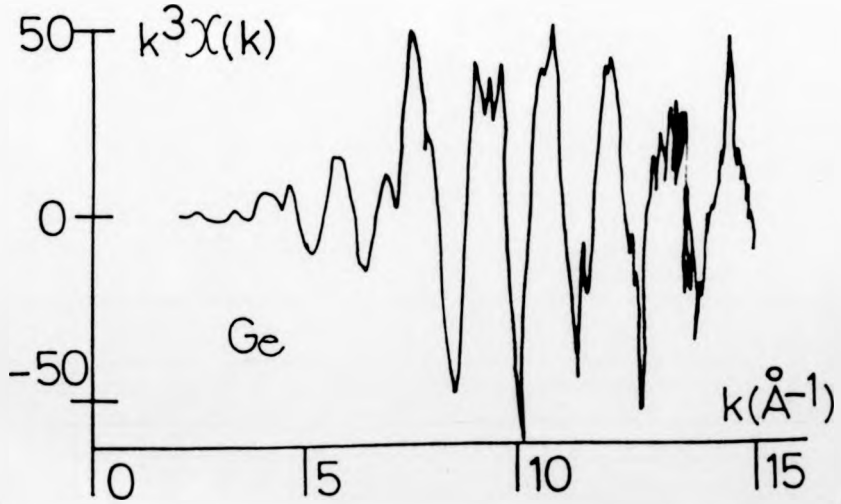

Fig. 2·05 : EXAFS of powdered crystalline germanium, [14].

The EXAFS function, usually given the symbol χ, is defined (equation 2.4) in terms of the absorption coefficient, μ, for the material and of the absorption coefficient, μ_o, that would be observed for single isolated atoms, as illustrated in Figure 2.4.

$$\chi(h\nu) = \frac{\mu(h\nu) - \mu_o(h\nu)}{\mu_o(h\nu)} \qquad \ldots (2.4)$$

Conversion from a function of X-ray energy, $h\nu$, to a function of photo-electron wave-vector, k, is via equation 2.5, (the energy of the photo-electron), requiring a knowledge of the E_o point

$$\frac{\hbar^2 k^2}{2m_e} = h\nu - E_o \qquad \ldots (2.5$$

For E_o (approximately equal to the binding energy of the core electron) and $h\nu$ in electron-volts, and k in inverse angstroms, Å^{-1}, this equivalence is given by equation 2.6

$$k = 0.51231\sqrt{h\nu - E_o} \qquad \ldots (2.6)$$

The EXAFS function is usually quoted as a function of k, as in equation 2.7:

$$\chi(k) = \frac{\Delta\mu(k)}{\mu_o(k)} \qquad \ldots (2.7)$$

This fine structure is usually multiplied by k, k^2, or k^3, to bring the oscillations to approximately the same amplitude over the full k-range, as shown in Figure 2.5, the example here being the EXAFS of crystalline germanium.

2.5 A Simple Model to Explain EXAFS

The main, roughly sinusoidal, oscillation in Figure 2.5, can be understood as a modulation of the absorption coefficient that passes through a series of constructive and destructive interferences as the X-ray

energy increases. From a quantum mechanical viewpoint, the outgoing photo-electron wave created in the absorption process, is partially backscattered by neighbouring atoms, to return to the central atom either in or out of phase with the outgoing wave, and thus increasing or reducing its effective amplitude. Physically, this results in a higher or lower probability of the photo-electron being created for a single atom within the X-ray flux, and this is observable as a higher or lower absorption coefficient for a large number of atoms. Two examples of the process are shown in Figure 2.6. The wavelength of the photo-electron, depends on its energy which depends on the X-ray energy, $h\nu$. The total phase difference between the outgoing and backscattered photo-electron waves depends upon this wavelength, λ, and upon the distance travelled, $2r$, (where r is the interatomic spacing), neglecting any other phase-shifts. The period of the EXAFS oscillation in k-space, therefore depends upon twice the interatomic distance. The extent of photo-electron backscattering is fairly weak, such that the amplitude of the modulation is typically between 1% and 10% of the amplitude of the absorption coefficient. The amplitude of the EXAFS modulation varies in its average magnitude and as a function of k, depending upon the number and the elemental-type of the backscattering atoms.

2.6 Theoretical Calculations of the EXAFS Equations

To determine the X-ray absorption coefficient, it is necessary to calculate the probability, P, of an X-ray being absorbed by an atom, using the Golden rule[9-12], as in equation 2.8:

$$P \alpha \sum_f \left| \langle f \left| \hat{\underset{\sim}{\xi}} . \hat{\underset{\sim}{p}} \right| i \rangle \right|^2 \delta(E_i + h\nu - E_f) \qquad \ldots (2.8)$$

The initial state, $|i\rangle$, is the bound electron in its core level of energy, E_i; the final state, $|f\rangle$, is the core hole and photo-electron propagating with $\underset{\sim}{k}$, of energy, E_f; $\hat{\underset{\sim}{\xi}}$ is the electric field vector of the X-ray; $\hat{\underset{\sim}{p}}$ is the electron momentum operator; the total probability for the

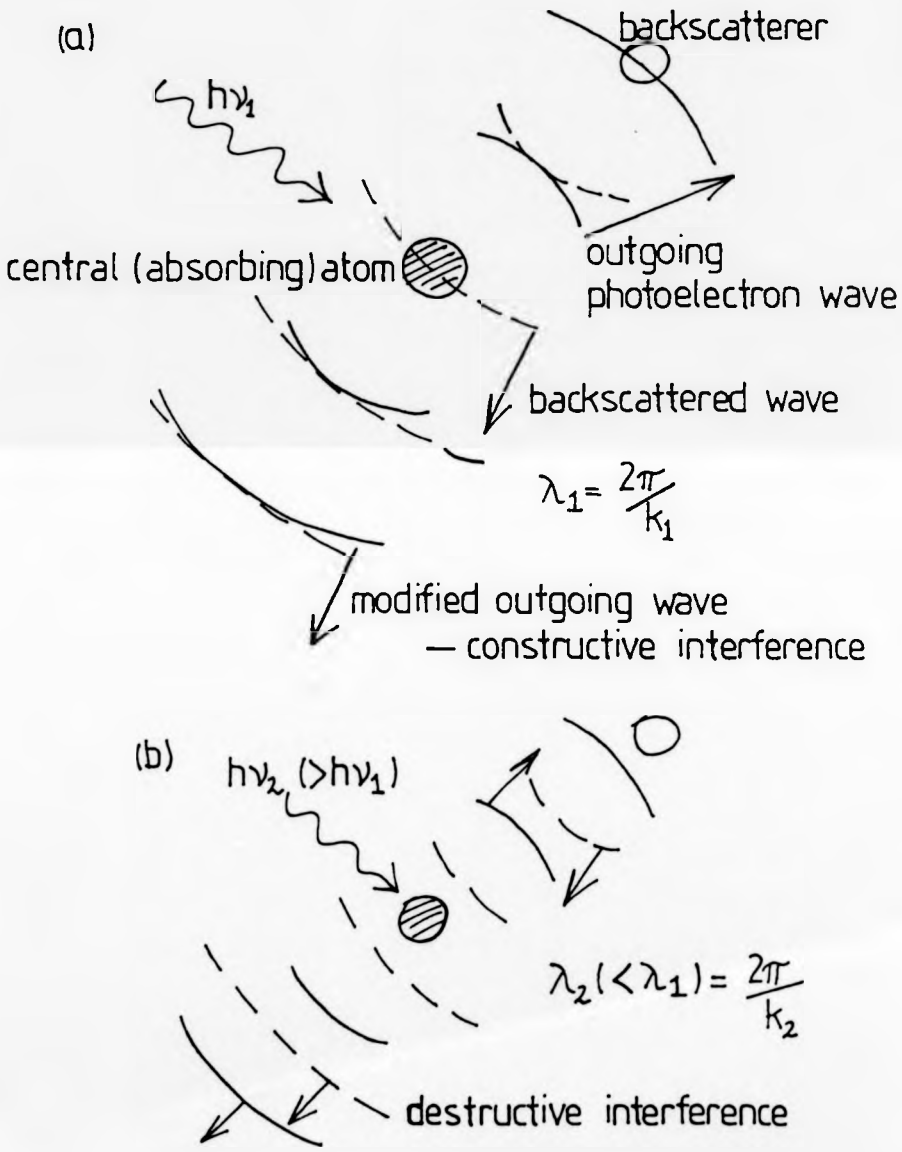

Fig. 2·06 : EXAFS illustration : as the X-ray energy increases, photo-electron emission changes from enhanced (a) to (b) reduced rate.

excitation of an electron from a particular core-level is the sum over all the possible final states, maintaining energy conservation as required by the delta function.

For an isolated atom, the final state is just an outgoing photo-electron wave, and the absorption coefficient is observed to be a smoothly decaying fuction above the threshold. If there are nearby atoms, then this outgoing wave is diffracted by them, giving rise to incoming waves that modify the final state, thus altering the absorption coefficient, (probability P), via the matrix element, $\left|\langle f|\hat{\underline{\epsilon}}.\hat{\underline{p}}|i\rangle\right|^2$.

The calculation of the absorption fine structure, requires a calculation of the probability of photo-electron emission in the particular direction of a neighbouring atom; of the phase-shifts encountered by the photo-electron as it leaves the attractive potential of the central atom, as it travels to the backscattering atom, is backscattered, and returns to the central atom; and of the backscattering factor; the calculation including such terms as the inelastic electron mean free path, and the Debye-Waller factors, which reduce the EXAFS amplitude.

The fine structures above K and L_I absorption edges, for which the electron initially resides in an S-state (l=o), and must therefore be excited into a p-state (l=1), since the dipole process requires $|\Delta l| = 1$ on the absorption of a photon, are given by equations 2.9-2.11,(9-11).

$$\chi(k) = -\sum_j^{\text{shells}} \frac{N_j^* F_j(k)}{kr_j^2} \sin(2kr_j + \phi_j(k)) e^{-2\sigma_j^2 k^2} e^{-2r_j/\lambda(k)} \quad \ldots (2.9)$$

$$N^* = 3 \sum_i^{\text{atoms}} \cos^2\alpha_i \quad \ldots (2.10)$$

$$\phi_j(k) = 2\delta^{l=1}(k) + \psi_j(k) \quad \ldots (2.11)$$

The total EXAFS function is a sum of the individual contributions from each shell of atoms, containing one element, all at the same distance from the central atom. The distance of such a shell is r_j, containing an effective number of backscattering atoms N_j^*, each with

backscattering factor $F_j(k)$, the Debye-Waller factor being $2\sigma_j^2$, and the total atomic phase shifts experienced by the photo-electron on returning to the central atom being $\phi_j(k)$. Also in equation 2.9, $\lambda(k)$ is the inelastic electron mean-free path.

Usually in SEXAFS work a plane polarised X-ray beam is used and the effective number of backscattering atoms, N^*, depends on the directions of the atoms relative to the electric vector, $\hat{\xi}$. N^* is greatly enhanced if the backscattering atoms lie in the same direction from the absorbing atom as the electric vector, since photo-electron emission in this direction is strongly favoured. The effective number of backscattering atoms in a shell is given by equation 2.10[12], where α_i is the angle between the vector from the central atom to the i^{th} atom in the shell, and the electric vector. In polycrystalline samples, the effective number averages out to be equal to the number of atoms in any shell.

The total atomic phase shift is the sum of twice the central atomic phase shift and of the backscattering atomic phase-shift, as stated in equation 2.11.

For the EXAFS functions above L_{II} and L_{III} edges, the general expression is given in equation 2.12-2.15[15]:

$$\chi(k) = \sum_j^{\text{shells}} \frac{F_j(k)\, N_j}{kr_j^2} \left| \frac{B(\alpha,k) + C(\alpha,k) + D(\alpha,k)}{|M_{21}|^2 + \frac{|M_{01}|^2}{2}} \right|_j e^{-2\sigma_j k^2} e^{-2r_j/\lambda(k)} \qquad \ldots (2.12)$$

$$\text{where } B(\alpha,k)_i = \frac{1 + 3\cos^2\alpha_i}{2} |M_{21}|^2 \sin(2kr + 2\delta_1^{l=2}(k) + \psi(k)) \qquad \ldots (2.13)$$

$$C(\alpha,k)_i = \frac{|M_{01}|^2}{2} \sin(2kr + 2\delta_1^{l=0}(k) + \psi(k)) \qquad \ldots (2.14)$$

$$D(\alpha,k)_i = M_{01} M_{21}(1 - 3\cos^2\alpha_i) \sin(2kr + \delta_1^{l=2}(k) + \delta_1^{l=0}(k) + \psi(k)) \qquad \ldots (2.15)$$

This complicated expression results from the fact that excitation from an initial p-state can result in either a d- or an s- final state. The $|M_{o1}|^2$ term (equation 2.14) represents an s- final state where l=o; $|M_{21}|^2 \gg |M_{o1}|^2$, such that this term can be neglected. The 'cross term', $|M_{o1}||M_{21}|$, requires an average estimation of the central atomic phase-shift, as in equation 2.15, but in most circumstances this term is also negligible; in particular it vanishes on angular integration for a polycrystalline material. This leaves just the d- final state term (equation 2.13), which is always dominant, given by equations 2.16-2.18. Only in certain circumstances, do the full equations need to be rigorously applied[16].

$$\chi(k) \approx \sum_j^{\text{shells}} \frac{F_j(k)\, N_j^*(k)}{kr_j^2} \sin(2kr_j + \phi_j^{(2)}(k))\, e^{-2\sigma_j^2 k^2}\, e^{-2r_j/\lambda(k)} \qquad \ldots (2.16)$$

$$\phi^{(2)}(k) = 2\delta_1^2(k) + \psi(k) \qquad \ldots (2.17)$$

$$N^* = {}^1/_2 \sum_j^{\text{atoms}} (1 + 3\cos^2\alpha_i) \qquad \ldots (2.18)$$

A useful approximation is to express the EXAFS in terms of only the l=2 phase-shift, but to account for the cross term by including the effect of this contribution in the effective number of atoms, by modifying equation 2.18 to equation 2.19:

$$N^* = \sum_i (0.5 + c) + (1.5 - 3c)\cos^2\alpha_i \qquad \ldots (2.19)$$

Since $\frac{|M_{21}|}{|M_{o1}|} \approx 5$, [15], $c \approx 0.2$ leading to equation 2.20:

$$N^* = \sum_i 0.7 + 0.9\cos^2\alpha_i \qquad \ldots (2.20)$$

Unlike the EXAFS spectra taken from K or L_I edges which show a large amplitude variation as a function of the angle of incidence of the polarised X-ray beam relative to the orientation of the crystal surface

(equation 2.9), EXAFS spectra from L_{II} or L_{III} edges vary only slightly in amplitude as can be seen by the approximately equal isotopic and anisotopic terms in equation 2.20.

2.7 The Atomic Phase-Shifts and Backscattering Factors

The procedure for calculating the atomic phase-shifts is briefly described below and this serves to illustrate the process that causes these phase-shifts to occur. Firstly the electron charge density around the atom of interest is calculated using the Hartree-Fock wave functions tabulated by Clementi-Roetti[17], from which the local Fermi energy and momentum are determined via the Thomas-Fermi description of the atom. A complex potential, accounting for the exchange and correlation effects, and depending upon the kinetic energy of the incoming electron, is constructed and is added to the electrostatic potential. Finally the atomic phase-shifts are derived.

As the photo-electron is created in the X-ray absorption process, it needs to escape from the attractive potential of the central, now ionized, atom. It is the effect of this potential that causes the phase-shift of the photo-electron wave. For low-k photo-electrons, the outer electrons of the singly ionized atom of atomic number Z, can relax inwards, thus shielding the core hole, in a much shorter time than that for the photo-electron to escape the potential[18]. Hence the central atomic phase-shift can be calculated using the electronic energy levels of a (Z + 1) ion, in which the missing electron is from the outermost shell[19], or those of a (Z + 1) atom using the equivalent core approximation[20].

For high-k values, relaxation cannot occur in the time for the photo-electron to leave, hence it is necessary to consider the completely unrelaxed Z ion.

Various calculations have been made by theoreticians, using variations of the above parameters, but the resulting phase-shifts can always be made to match each other by a variation in the E_o value of only a few eV. Basically this means that the assumptions made concerning the energy levels are not critical.

It should be pointed out that an extra $\pi/2$ radians appears in the phase-shifts[21], resulting from a '$-i$' factor for the outgoing photo-electron wave, which is necessary to set the phase-shift equal to zero in the absense of a potential[11]. This results in the EXAFS being described by a '-sin' rather than a 'cos' function of the total phase-shifts.

The atomic backscattering factor, $F(k)$, can be determined from the individual l- components of the backscattering phase-shifts ψ_L (using the spherical harmonic expansion method)[21], as given in equation 2.21:

$$F(k) = \frac{1}{2ik} \sum_{l=0}^{\infty} (2l + 1)\left[e^{2i\psi_L} - 1\right]\left[-1\right]^L \qquad \ldots (2.21)$$

Calculations of atomic phase-shifts and backscattering factors have been extended to heavier atoms, using Herman-Skillman wave functions, by Teo and Lee[15], being given for nearly one half of the atoms in the Periodic Table, those values that are not given can be derived by interpolation. Some examples of phase-shifts and factors are given in Figures 2.7, 2.8 and 2.9. There are trends as functions of the atomic number and other parameters. The central atomic phase-shifts are steeper (having a larger negative gradient as a function of k) for heavier atoms, for larger positive central atomic charge, and for lower photo-electron l-value (Figure 2.7). By comparison the backscattering phase-shifts have much less variation in value over the same k-range; those of heavier atoms contain more variations in gradient, as shown in Figure 2.08.

Fig. 2·07:

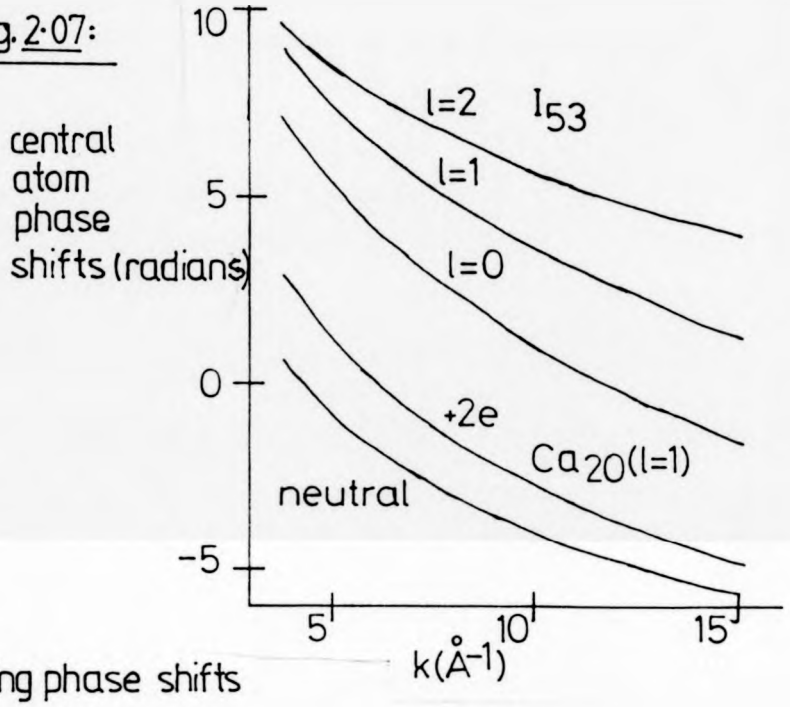

Fig. 2·08:
backscattering phase shifts (radians)

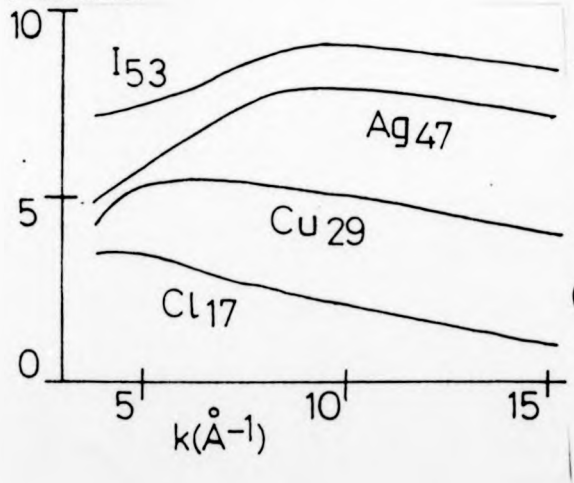

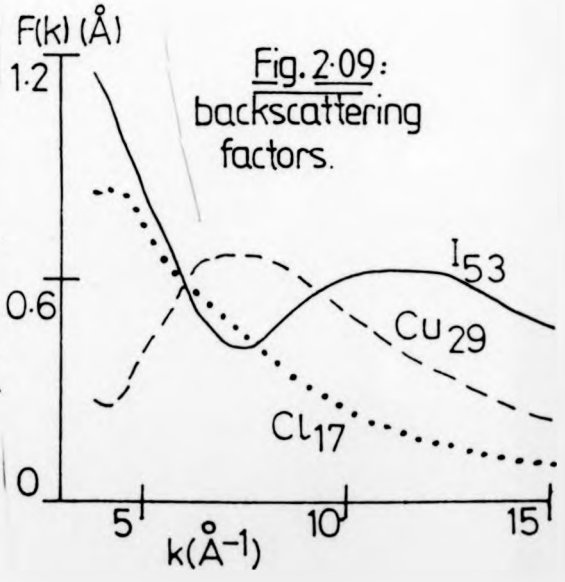

Fig. 2·09:
backscattering factors.

The backscattering factors (ie amplitudes) become larger for heavier atoms and show more structure as a function of k than those factors for the lighter atoms - as one scans upwards through the Periodic Table, maxima appear and move to lower k-values as illustrated in Figure 2.9.

As mentioned above the phase-shifts can be understood by the effect of a potential upon the phase of an outgoing (or incoming) photo-electron wave, and strictly speaking an attractive potential causes a negative phase-shift, and a repulsive potential causes a positive phase-shift[21]. However, the phase-shifts are arbitary to $\pm 2\pi n$ radians, where n = 0, 1, 2.... For example a phase-shift of -1 radian produces exactly the same effect as a phase-shift of 5.3 rads, 11.6 radians, etc.

2.8 Electron Scattering Factors, the Inelastic Electron Mean Free Path and the Application of Single Scattering Theory to EXAFS

The angular variation of the electron scattering factors, and the variation of the inelastic mean free path as functions of the electron kinetic energy enable the EXAFS phenomenon to be adequately described by single (rather than multiple) scattering theory, for photo-electron kinetic energies ranging from around 30 eV up to 1000 eV.

For kinetic energies of less than 30 eV, the inelastic mean free path, λ^{imfp} (the average distance that an electron can travel through a solid before suffering an inelastic collision, in which kinetic energy is lost) can be very large compared to atomic dimensions, as shown in the Universal curve[22-24] - Figure 2.10. Also, the electron scattering factors for angles around 45^{o}-135^{o} are significant at these low energies (Figure 2.11), such that multiple scattering events in which each electron travels a large distance and undergoes many near-90^{o} scattering events

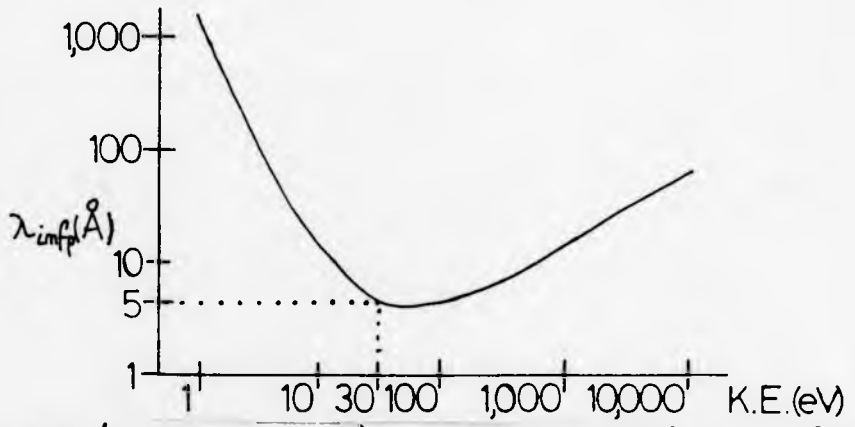

Fig. 2·10 : 'Universal curve' of electron inelastic mean free path through elemental solids

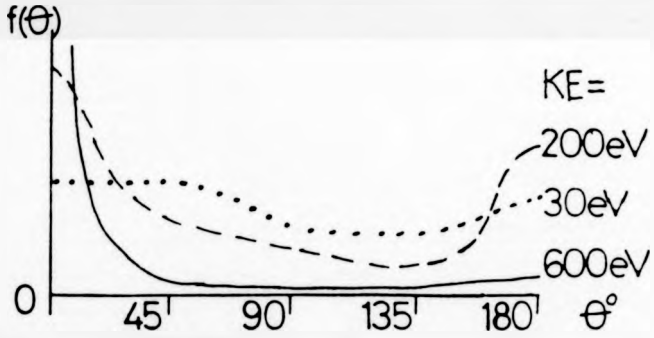

Fig. 2·11 : Angular variation of electron scattering factors

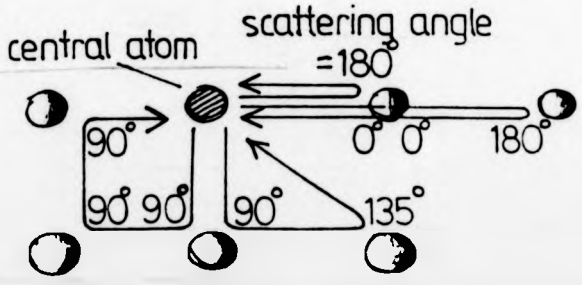

Fig. 2·12 : Possible scattering paths for electrons

before returning to the central atom (see Figure 2.12), can have significant probabilities of occurence compared to single scattering events in which the electron travels a shorter total distance, and is scattered only once, its vectorial direction being altered by 180^{o}.

For higher kinetic energies, λ^{imfp} is small (at 1000 eV kinetic energy it is only $20\mathring{A}$) and the electron scattering factors, $f(\theta)$, for angles 45^{o}-135^{o} and thereabouts, are much smaller than $f(180^{o})$ ie the backscattering factor, sometimes written as $f(k, \pi)$ since the factor is a function of k. This means that only single scattering is important, enabling the EXAFS to be described by the simple forms of equations 2.8 and 2.12.

An exception to this rule is where an atom of a distant shell lies directly behind one in an inner shell, as is the case in metallic copper[13], where the contribution to the EXAFS amplitude of this distant shell is enhanced, the apparent atomic phase-shifts involved in scattering form this shell are anomalous, and hence a determination of the distance of this shell would be unreliable if one attempted to analyse the EXAFS being unaware of these occurrences.

However, even if multiple scattering events are significant, then since they consist of large path length events, their EXAFS components are oscillations having small periods in k-space, such that they affect attempts to determine the distances of shells at similar large distances, but do not cause any problems with the determination of the distance of the first shell of neighbouring atoms. Typically in SEXAFS work, the available k-range of the data is small, and the signal-to-noise ratio is relatively poor, such that it is not possible to identify shells other than the nearest one.

2.9 Debye-Waller Factors, and Radial Distribution Functions

The observable EXAFS originates from a sum of the fine structures from all the atoms involved in the absorption process, each of which, at a given point in time, has a slightly different local environment. This may be due to lattice disorder or to the thermal vibration of atoms about their central positions. These effects serve to reduce the amplitude of the EXAFS - if the disorder was complete, then no EXAFS would be present (in practice, even for materials such as glasses, the first nearest neighbour distance is often fairly well defined by the bond length, such that the EXAFS is observable).

Strictly speaking the EXAFS should be calculated using the appropriate radial distribution function about the central atom[25], as in equation 2.22, where $p(r_j)$ is the probability that the j^{th} atom is at the radial distance r_j.

$$\chi(k) \propto \int_{r=0}^{\infty} \sin(2kr_j + \phi_j(k))\, p(r_j)\, dr_j \qquad \ldots (2.22)$$

If the atomic neighbour is in thermal vibration, or if the lattice disorder consists of a gaussian distribution about the average position, then the radial distribution probability is given by equation 2.23:

$$p(r_j) = \frac{1}{(2\pi)^{1/2}\sigma_j} e^{-(r - R_j)^2/2\sigma_j^2} \qquad \ldots (2.23)$$

This equation (ie 2.23) shows that the atoms are positioned roughly at distances, R_j; a given atom typically varying from such an average distance by the root-mean-square deviation, σ_j. The equation is valid for $\sigma_j \ll R_j$, which is generally true, since σ_j typically has a value around 0.07Å[27].

The EXAFS can then be expressed in a simplified form, as in equation 2.24:

$$\chi(k) \propto \sum_{\text{shells}}^{j} \sin (2 k r_j + \phi_j(k)) \, e^{-2 \sigma_j^2 k^2} \qquad \ldots (2.24)$$

The use of this equation (ie 2.24) simplifies the calculation, or the description, of the EXAFS, and requires only that one calculates the EXAFS from a given shell of atoms, assuming a fixed distance, and then reduces the amplitude of this function, according to the $e^{-2 \sigma_j^2 k^2}$ term. The total EXAFS is simply the sum of the contributions from the nearest shells - remember that the amplitudes fall rapidly with increasing radial distance due to the $1/r_j^2$ and $e^{-2 r_j/\lambda(k)}$ terms, not listed in equations 2.22-2.24.

The Debye-Waller factor for a given shell is the value $2\sigma^2$. Typical values are $2\sigma_1^2 \approx 0.01$ Å^2, and $2\sigma_j^2 \approx 0.03$ Å^2 ($j = 2, 3....$) for room temperature thermal vibration. The first shell of atomic neighbours contain those atoms to which the central atom is chemically bonded hence there is a correlation in the thermal vibrations of these atoms (two atoms that are strongly bonded together tend to vibrate synchronously such that the bond length remains fairly constant) giving rise to the smaller Debye-Waller factor for the first shell compared to those of the more distant shells (uncorrelated vibration),[17, 26].

The use of the simplified equation (2.24) in preference to the general equation (2.22), when the approximations stated above are not valid, can lead to errors in an EXAFS analysis as has been pointed out by Eisenberger and Brown[28] and by Lee et al[13]. One unfortunate consequence of this effect is that an EXAFS analysis can lead to the prediction of a bond length contraction as the temperature of the material increases ! The true bond length is that which would be obtained from an

analysis of the EXAFS taken from the solid at absolute zero temperature. As the temperature is increased the radial distribution function of an atomic shell changes from a delta function to a broader assymetric function, with a tail extending from the high-r side - this results from the atomic vibration to the low-r direction about the average-r value, being suppressed by the hard sphere repulsion of atoms brought close together, there being no such restriction on the movement to higher r-values. A very narrow peak in the radial distribution function produces an EXAFS spectrum that consists of an oscillation in k-space having a single well defined period (strictly speaking the non-linearity of the atomic phase-shifts causes this period to be a function of k), and an analysis of this data proves to be fairly straightforward. A broad peak in r-space, by contrast, gives rise to an EXAFS spectrum that contains oscillations of widely varying periodicities. An analysis by a Fourier transform type method of a limited k-range of data (low k data is never available, and high k data is often not available) can lead to an erroneous answer as to the shell distance. In particular for a thermally broadened assymetric peak, the analysis can lead to a bond length deduction that is too small.

The assymetry in the near-gaussian radial-distribution-function peak can be produced by effects other than thermal vibration, such as the presence of another shell of atoms at a slightly different distance, and this could also lead to erroneous results in an EXAFS analysis.

2.10 References

1 Strictly speaking, X-rays are produced in the relaxation of an electon to a vacancy in a core level, the energy varying from 275 eV for soft, up to 8 keV for hard X-rays. Aluminium and magnesium are commonly used as target anodes, the 'K-radiation' produced having energy, $h\nu \approx 1.3$ keV.

Electromagnetic radiations of these energies, produced by other processes such as synchrotron radiation, are indistinquishable from X-rays and are commonly referred to as X-rays.

2. G L Clark 'Applied X-rays'.
International Series in Pure and Applied Physics, 4th Edition, 1955:
Chapter 8: Absorption and Scattering of X-rays.

3. W J Veigele, Atomic Data Tables 5, (1973), p51:
- For $h\nu \approx 1$ keV, $^1/\mu \approx 2{,}000$ A.

4. A H Compton and S K Allison, 'X-rays in theory and experiment'.
2nd edition 1935:
Appendix IX: Mean values of mass absorption coefficients of elements.

5. B E Warren, 'X-ray diffraction', Addison-Wesley, 1969:
Appendix III: Mass absorption coefficients, μ_m, of the elements (Z = 1 to 83) for a selection of wavelengths.

6. L V Azaroff, 'X-ray Spectroscopy'
International Series in Pure and Applied Physics, McGraw-Hill, 1974:
Chapter 6: X-ray absorption spectra
Chapter 7: Synchrotron radiation and applications.

7. W Kossel, 'Zum Bau der Röntgenspektren', Z Physik 1 p 119 (1920).

8. R L Kronig, Z Physik 70 p 317 (1931), and 75 p 191 and p 468 (1932):
Zue Theorie der Feinstruktur in Röntgenabsorption-spektren' parts I, II and III.

9. E A Stern, Physical Review B10(8), October 1974, p 3027:
'Theory of EXAFS'.

10. C A Ashley and S Doniach, Phys Rev B11(4), February 1975, p 1279:
'Theory of EXAFS in crystalline solids'.

11. P A Lee and J B Pendry, Phys Rev B11(8), April 1975, p 2795:
'Theory of EXAFS'.

12. P A Lee, Phys Rev B13(12), June 1976, p 5261:
'Possibility of adsorbate position determination using final-state interference effects'.

13. P A Lee, P H Citrin, P Eisenberger and B M Kinca d,
Reviews of Modern Physics, volume 53, number 4, part 1, October 1981, p 769:
'ECAGS-strengths and limitations as a structural tool'.

14. P Eisenberger and B M Kincaid, Science 200(4349), June 1978, p 1441:
'EXAFS: New Horisons in Structure Determinations'.

15. Boon Keng Teo and P A Lee, Journal of American Chemical Society, 101(11), May 1979, p 2815:
'Ab initial calculations of amplitude and phase functions for EXAFS spectroscopy'.

16. J Stöhr and R Jaeger, Phys Rev B27(8), April 1983, p 5146:
'Polarisation-dependent phase and amplitude interference effects in $L_{2,3}$ surface EXAFS'.

17. P A Lee and G Beni, Phys Rev B15(6), March 1977, p 2862:
'New method for calculation of atomic phase-shifts: application to EXAFS in molecules and crystals'.

18. G E Laramore, Phys Rev A24(4), October 1981, p 1904:
'Effect of screening charge transfer on EXAFS phase-shifts: model calculations for excitation of 1s level in Br_2 molecule'.

19. C Noguera, D Spanjaard and J Friedel, J Phys F(metal Physics)9(6), 1979, p 1189:
'Dynamic screening of core hole: Semiclassical model'.

20. D A Shirley, Chemical Physics Letters 16(2), October 1972, p 220.
'Effect of atomic and extra-atomic relaxation on atomic binding energies'.

21. L I Schiff, 'Quantum Mechanics', International Student Edition, 1955:
Chapter V:Continuous Eigenvalues: Collision Theory.

22. M P Seah and W A Dench, National Physical Laboratory report (Chem 82), April 1978:
'Quantitative electron spectroscopy of surfaces - a standard data base for electron inelastic mean free paths in solids'.

23. Powell, Surface Science 44(74) p 29.

24. I Lindau and W E Spicer, Journal of Electron Spectroscopy 3(1974) p 409

25. P J Orders and C S Fadley, Phys Rev B27(2), Jan 1983, p 781:
'Single cluster calculations and Fourier-transform analyses of normal photo-electron diffraction'.

26. E A Stern, D E Sayers and F W Lytle, Phys Rev B11(12), June 1975, p 4836:
'EXAFS technique III: Determination of physical parameters'.

27. C Kittel 'Introduction to Solid State Physics', 5th edition Wiley, 1976
- Debye temperature of a solid is typically, $\theta_D \approx 400$ K.
- Nickel = 450 K, Copper = 343 K.

The Debye-Waller factor can be calculated as follows:-

In simple harmonic motion, the force F on the atom is inversely proportional to its displacement x, from its equilibrium position, the constant k, being the force constant:

$$F = -kx \qquad (a)$$

The motion is therefore an oscillation of amplitude x_o, and angular frequency, ω_D- the Debye frequency:

$$x = x_o \sin \omega_D t \qquad (b)$$

Using Newtons third law, it can be shown that:

$$w_D = \sqrt{k/m} \qquad (c)$$

The amount of energy cotnained within the oscillation depends on the Debye temperature:

$$^1/_2 k x_o^2 = k_B \theta_D \qquad (d)$$

this being 1 quantum ie $^1/_2 k x_o^2 = \hbar\omega_D$ (e)

Such that, from (d) and (e) it can be shown that:

$$\omega_D = \frac{k_B \theta_D}{\hbar} \qquad (f)$$

From (d), the amplitude is: $x_o = \sqrt{\frac{2 k_B \theta_D}{k}}$ (g)

which on substituting values from equations (c) and (f), gives:

$$x_o = \frac{1}{\hbar}\sqrt{\frac{2}{m \theta_D k_B}} \qquad (h)$$

Substituting $\theta_D \approx 400$ K, $m \approx 60 \times m_p$ (proton mass = $1{\cdot}7.10^{-27}$ kg), $\hbar = 1{\cdot}1.10^{-34}$ J_s, and $k_B = 1{\cdot}4.\ 10^{-23}$ J K^{-1} (Boltzmann constant) gives

$$x_o \approx 0.07\text{Å}$$

28. P Eisenberger and G S Brown, Solid State Communications 29, (1979), p 481:
'Study of disordered system by EXAFS: limitations.'

CHAPTER 3:

SEXAFS: DATA COLLECTION

3.01 Overview

In this chapter, the typical procedure is described for the experimental collection of an EXAFS spectrum of atoms lying near the surface of solid. The measurements involved in data collection at the SRS (synchrotron radiation source) at the SERC (Science and Engineering Research Council) DL (Daresbury Laboratory) are detailed, but the chapter also serves as a general outline of SEXAFS data collection

The necessity of synchrotron radiation is explained by the requirements of a wide range of X-ray energies, with a selected increment having a very high intensity. The production and characteristics of synchrotron radiation are described, along with the optical components constituting the beam line, that are necessary to produce a small spot of intense monochromatic X-rays at the sample surface: namely, the filters for the removal of low energy scattered X-rays, the premirror for focussing and high energy rejection, and the monochromator for the wavelength selection.

An outline is given of the measurements required to monitor the X-ray absorption coefficient of surface rather than bulk atoms, and to obtain SEXAFS spectra of useful quality.

Finally, a description is given of the computer control of the various components used to vary the X-ray energy, and to simultaneously collect and process signals.

3.02 The Synchrotron Radiation Source at the Daresbury Laboratory

In order to use EXAFS as a structural technique, it is first necessary to obtain some measure of the X-ray absorption coefficient of the material under investigation, as a function of the X-ray energy extending above an absorption edge of an element contained within the material, the local environment(s) around the atoms of that element to be determined on an analysis of the data. It is therefore necessary to have an X-ray source that can be tuned to a starting energy around 50 eV below the absorption edge of interest, that can be ramped in approximately 1 eV increments, and that can finish at an energy, several hundred

eV above the edge. If the appropriate measurements are made at each energy, then a spectrum can be obtained. In surface EXAFS work, measurements of the absorption coefficient are typically made from around one monolayer (or less) of absorbates on a crystal surface of an approximate size 10 mm x 10 mm, and in order to get an appreciable signal, a very intense X-ray beam is required, having a spot size at the sample surface of a few mm^2 - see Figure 3.01.

The SRS shown in Figure 3.02 satisfies these requirements, providing an X-ray beam that is plane-polarised, which is particularly useful for a number of surface science experiments. Electrons are injected into the storage ring in a series of bunches, there being 160 of these when the ring is full at which point the circulating electron current is around 200 mA. The energy of these electrons is increased to up to 2 GeV at which point they are relativistic, ie travelling at near to the speed of light. Around the ring are 1 dipole magnets arranged such that the electrons are bent into circular paths during which time synchrotron radiation is emitted. As the electrons loose energy in this process, their energy is maintained by radio frequency (rf) radiation being fed into the ring via rf cavities. Collisions with residual gas molecules cause electrons to scatter and to be lost from the circulating beam, such that a gas pressure below 10^{-9} torr is required for a beam lifetime (the time taken for the beam current to fall to approximately half of its initial values) of greater than 8 hours. As far as all the SEXAFS work described in this thesis is concerned, the radiation source appears to be continuous in time, ie the bursts of radiation from the electron bunches occur at a frequency far too high to be resolvable with the instrumentation used. The intensity of the radiation does fall off as the electron beam current decays.

Each source of radiation is approximately 7mm (horizontal) by 0.7 mm (vertical) in size, the radiation being peaked in the forward direction tangential to the electron path, the angular width of such a source being of the order 1 mrad in the vertical direction and 10 mrad in the horizontal plane. The SEXAFS instrumentation is positioned on beam line 6.3 at the SRS[1] (the X-ray

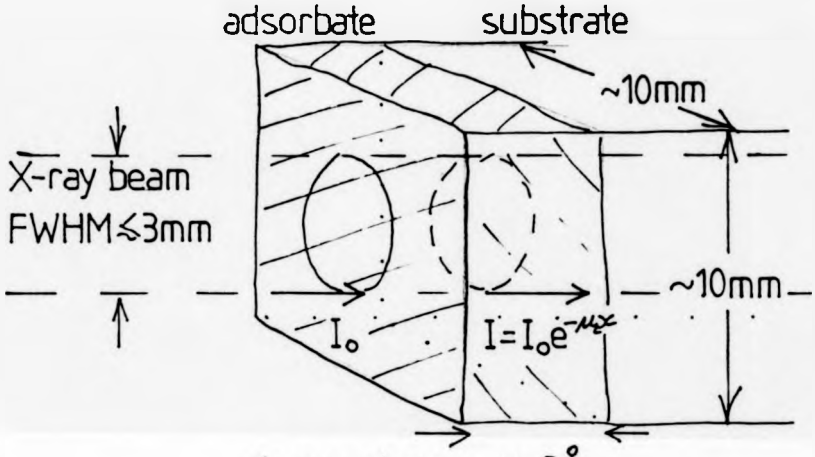

From $I=Ie^{-\mu_l x}$ it can be shown that $\frac{I_o-I}{I_o} \approx \mu_l x$

Since $\mu_l \approx 10^5 m^{-1}$ ($\frac{1}{\mu_l} \approx 10\mu m$) : $I_o - I \approx 3.10^{-5} I_o$

If a signal:noise of 10^4 is required,
then 10^8 counts are needed, ($N \approx \sqrt{S}$)

If the counting time is 1s,
then the count rate must be $I_o - I = 10^8$ photons s^{-1}
such that I_o needs to be $\sim 3.10^{12}$ photons s^{-1}

Fig. 3.01 : SEXAFS work needs an intense X-ray beam.

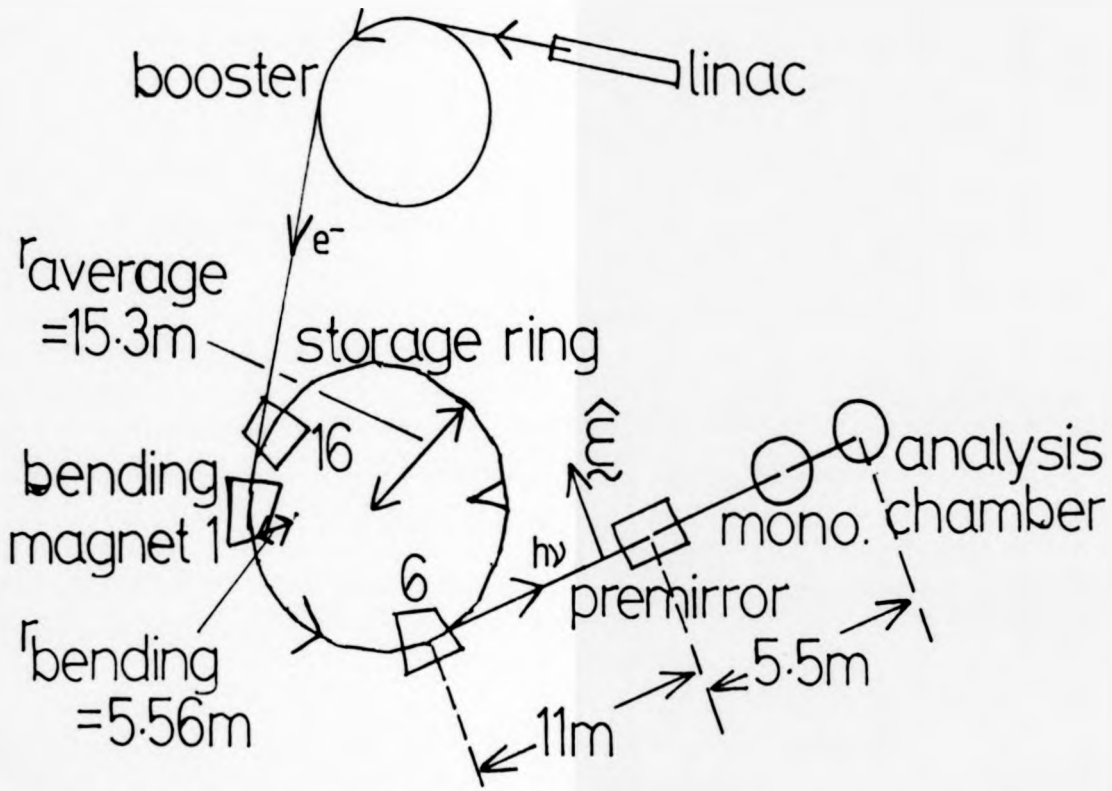

Fig. 3·02: Daresbury SRS and SEXAFS beamline.

beam travelling down beam line 6 is split into 3 components by the use of mirrors intersecting parts of the beam), the horizontal acceptance having been reduced to less than 10 mrad to reduce the spherical aberration produced by the pre-mirror. For an X-ray travelling along the plane of the electron orbit, the polarization is entirely parallel to this plane, ie. the electric vector lies in the horizontal plane. For more diverging X-rays lying above or below the electron orbit plane, the perperdicular component of the polarization becomes more significant, but even if all the vertical divergence of ± 1 mrad is collected and utilized, the total X-ray beam is still about 75% plane polarised.

The intensity of the synchrotron radiation as a function of the wavelength can be calculated from first principles[2], a characteristic wavelength, λ_c in units of Å, being defined by equation 3.01[3], where R is the radius of the electron path within the magnetic field of the bending magnets in metres, E is the electron kinetic energy in GeV, and B the field in tesla(T):

$$\lambda_c = \frac{5.6R}{E^3} = \frac{18.6}{BE^2} \qquad \ldots (3.01)$$

At wavelengths shorter than λ_c, the intensity falls off sharply, such that at $\lambda_c/4$, there is no longer a significant flux. At higher wavelengths the intensity falls off gradually. For the working parameters at the SRS, The intensity spectrum is shown in Figure 3.03, the maximum intensity being in the X-ray region. It can be seen from Figure 3.03, that a fall in the electron kinetic energy from 2 GeV to 1.8 GeV causes an almost complete loss in intensity of X-rays of wavelengths less than 1 Å, and a significant reduction in the flux at 10 Å. These are the enegies of the X-rays needed for SEXAFS work, the X-ray energy, $h\nu$ and wavelength, λ, being related by equation 3.02, h being Planck's constant, and c, the speed of light:

$$h\nu = \frac{hc}{\lambda} \text{ or } h\nu(eV) = \frac{12399}{\lambda(\text{Å})} \qquad \ldots (3.02)$$

3.03 The SEXAFS Beamline, Filters and Pre-mirror at DL

The X-ray beam used for surface EXAFS work at the SRS, first passes through one of a variety of filters: a thin slice of beryllium (having a K

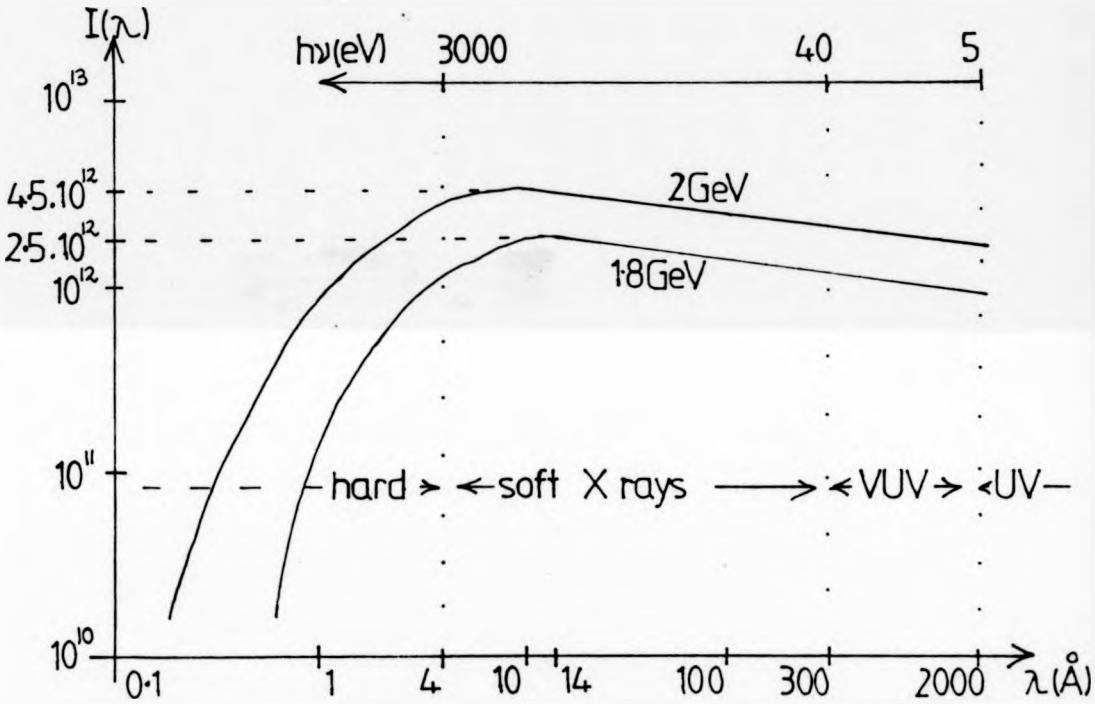

Fig. 3·03 : Synchrotron radiation intensity (photons per second per horizontal mradian per 100mA electron current per 0·1% bandwidth) spectra produced by dipole bending magnets (radius = 5·56m) for 2 electron energies.

absorption edge at 111 eV), a few hundred angströms of carbon (*K*-edge at 284 eV), or 0.75 μm thick aluminium (*K*-edge at 1560 eV and $L_{I,\ II,\ III}$ edges at 118, 74 and 73 eV respectively). These filters serve to absorb the visible light, ultra-violet, and in the case of aluminium the low energy X-rays; the high energy X-rays pass through virtually unattenuated. This removal of unwanted wavelengths serves to improve the signal-to-noise of the data collected.

The X-ray beam then falls at glancing incidence onto a pre-mirror, as shown in Figure 3.04, which serves two purposes, namely a focussing of the diverging X-rays to a spot at the crystal surface, and a removal of high energy X-rays from the beam, ie a high energy cut-off. Focussing in the horizontal plane is achieved by the mirror being curved by the appropriate amount, and the much smaller divergence in the vertical direction is corrected by bending the mirror slightly along its length (see Figure 3.04(a)), the radius of curvature being as large as 50 m. The mirror acts in the double focussing mode such that the image size is (in principle) 3.5 mm x 0.35 mm.

A movable mask is situated before the pre-mirror, and can be used to reduce the spot size of the X-ray beam on the mirror which serves to reduce the heat load upon the mirror, and to improve the focussing at the crystal.

The quartz mirror is coated with a surface layer of gold as shown in Figure 3.04(b). The refractive index of gold is less than unity (the phase velocity of X-rays in this material is higher that it is in vacuum), such that the angle of refraction, ψ, is larger than the angle of incidence, Φ, as predicted by Snell's law: refractive index = $\sin \Phi / \sin \psi$. For a sufficiently large Φ, ψ becomes 90^{o}, and total external reflection is achieved.

The refractive index varies with the X-ray energy, such that the amount by which it is less than unity is greatest for the lowest energy. This means that for a higher X-ray energy, a smaller glancing angle, θ, is needed to get total external reflection. Alternatively, at a given angle of incidence, there is a critical energy, below which X-rays are totally reflected, and above which they are transmitted (and partly reflected).

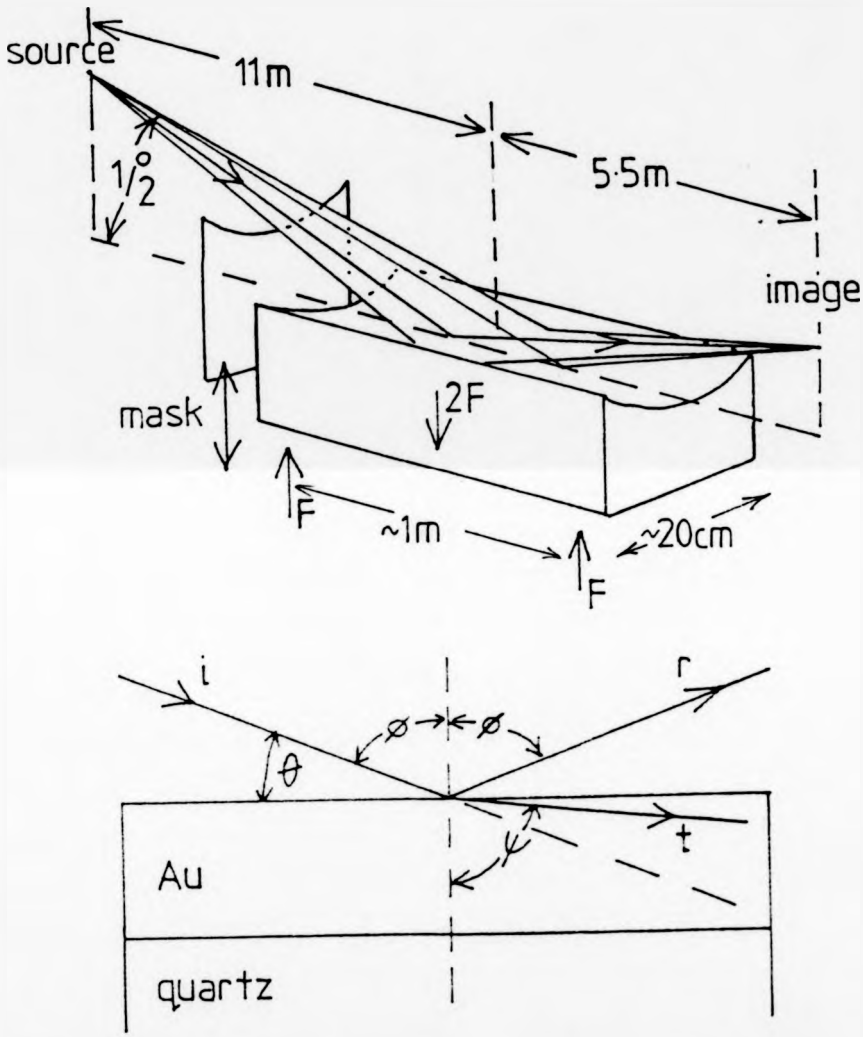

Fig. 3·04 : (a) : X-ray focussing by premirror
(b) : transmitted (refracted), reflected and incident X-ray beams.

The critical angle θ_c, for the wavelength, $\lambda(\mathring{A})$, is given by equation 3.03[2], in which n is the number of electrons per unit volume (cm^3), e is the electronic charge, 1.6 $10^{-19}C$, m_e is the electron mass (kg), c the velocity of light, 3.10^8 ms^{-1}:

$$\sin \theta_c = \frac{n e^2}{\pi m_e c^2} \lambda \qquad \ldots (3.03)$$

For gold (which has a high n valve), an energy cut-off at 10 keV can be achieved by setting the angle of incidence, θ, to be $^1/_2{}^o$ - this is the arrangement at the SRS.

3.04 The X-ray Monochrmator at Daresbury

A particular energy can be extracted from the continuum X-ray beam, by utilizing Bragg reflection from crystals, as shown in Figure 3.05(a). For an X-ray beam incident at the glancing angle θ, upon a set of reflecting atomic planes, the spacing of which is the distance, d, the reflected specular beam contains the wavelength, λ, given by the Bragg equation - equation 3.04.

$$2d \sin \theta = n\lambda \text{ or } h\nu = n \frac{hc}{2d \sin \theta} \qquad \ldots (3.04)$$

According to this equation (ie 3.04), the fundamental energy (n=1) is accompanied by a set of higher energy harmonics (n = 2, 3...).

The crystal monochromator at the SRS is a commonly used double crystal arrangement as shown in Figure 3.05(b). The first crystal is rotated to select the required energy in the reflected beam, and the second crystal is rotated to the same angle and moved to intersect the monochromatic beam (plus harmonics) and reflect this towards the analysis chamber. Both incoming and outgoing beams are travelling horizontally, there being a downwards displacment of 20 mm in the process. There are three pairs of crystals available for use within the SEXAFS monochromator at Daresbury, namely silicon, cut such that (111) planes lie parallel to the surface, and Ge (111), and Ge(220). The X-ray energies that can be selected by these crystals, depends upon the interplanar spacing, and the angular range available, which at present is limited to $\theta = 13.5^o$ to $\theta = 72$. The

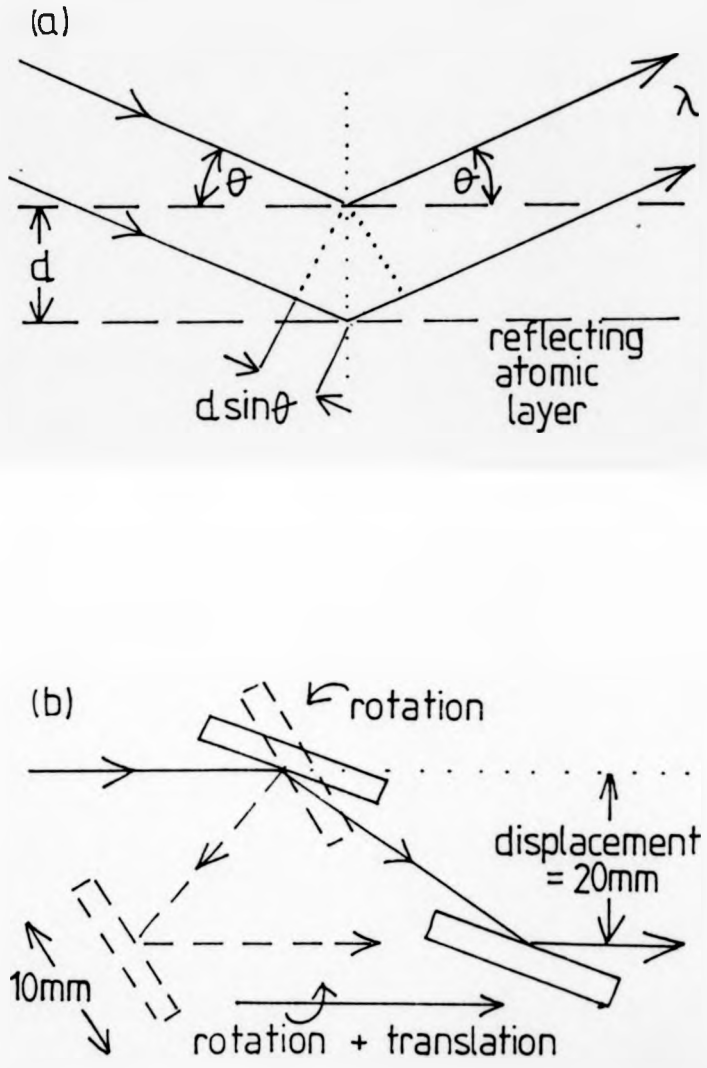

Fig. 3·05 : (a) : Bragg reflected X-ray beam
(b) : Double crystal monochromator

characteristics are given in Table 3.01. For example, the Ge (220) set to reflect an X-ray energy of 3523 eV, also reflect the X-rays of energy 7046 eV, and although the intensity of these present in the beam is much smaller due to the nature of the synchrotron radiation, the reflected intensity at the centre of the Bragg peak can be significant, since their reflection is confined to a smaller angular spread than that of the first order X-rays. The third harmonic from such an arrangement, ie 10,569 eV, is not present in the incident beam because of the high energy cut-off of the pre-mirror.

When being used, the first crystal of the monochromator is subjected to the full X-ray flux, and can become up to 300^{o}C hotter than the second crystal, as is common in such monochromators[4]. This causes the lattice to expand, such that the top crystal needs to be rocked around the angle (as calculated from the room temperature 2d-spacing), until a reflection of the required X-ray energy is obtained, at which point such an X-ray can reflect from the bottom crystal and be detected. Since only about 1% of the intensity of a particular energy is Bragg reflected[4], the second crystal is not heated appreciately; also the actual intensity of X-rays in the small energy range selected by the monochromator is much less than that given in Figure 3.03.

The energy resolution of the monochromator is largely determined by the entry and exit slits which can be closed to reduce the angular acceptance of the crystals to the incoming beam, and the angular divergence of the outgoing beam. For example, with Ge (111) crystals set to $\theta = 24.56^{o}$, such that $(h\nu)^{1} = 4557$ eV, an X-ray of energy $(h\nu)^{1} = 4547$ eV, but entering at an angle 1 mrad from the horizontal can also pass through the monochromator, exiting at a 1 mrad divergence. Thus, for the slits set at 1 mrad, this implies an energy resolution of $\sim$ 10 eV. In practice the pre-mirror mask and collimators reduce the observed resolution to 2 eV, such that the resolving power, ie $E/\Delta E$, is of the order of 2,000. Since it is required to collect a spectrum of the X-ray absorption coefficient as a function of the X-ray energy, with a resolution of features several eV wide, this is adequate for SEXAFS work.

Table 3·01: Daresbury monochromator characteristics.

crystal plane	2d spacing (Å)	X-rays (eV)	harmonics
Si{111}	6·271	2075–8453	1, 3, 5....
Ge{111}	6·533	1992–8115	
Ge{220}	4·000	3523–13250*	1,2,3,4....

* Attainable upper energy=10000eV due to premirror cut-off

For a Bragg reflection from a crystal, the peak intensity is at the angle of reflection equal to the angle of incidence, Φ_i, and the intensity falls away at smaller and larger angles, such that the reflection has an angular width of the order of $\Delta\Phi$ as shown in Figure 3.06(a). A detailed calculation from perfect crystal theory[5], for a thick crystal with negligible absorption (ie perfect reflection) shows that the diffracted beam has a uniform intensity over the angular range (θ_o - S) radians to (θ_o + S) radians, θ_o being the centre of the reflected beam, S being given by equation 3.05.

$$S = \frac{q\lambda}{2\pi d \cos\theta} \qquad \ldots (3.05)$$

In this equation (3.05), q is the amount of reflection from a single atomic plane, these being spaced apart by the distance d (in units of Å, λ also being in these units), and is given in equation 3.06:

$$q = \frac{e^2}{M_e c^2} \frac{M\lambda f(2\theta)}{\sin\theta} \qquad \ldots (3.06)$$

In equation 3.06, M is the number of atoms per unit surface area, being equivalent to Nd where N is the number per unit volume; and f(2θ) is the atomic X-ray scattering factor for the beam reflected at an angle θ from the surface plane, the angular change in direction upon scattering being 2θ.

Applying such a theory shows that the full-width-half-maximum (FWHM) of the peak is 2.12s, such that for $\lambda \sim 1.5$Å, this corresponds to ~ 0.04 mrad[5].

However, even for a negligibly absorbing crystal, the penetration depth is limited by the diffraction process to around 9,000Å[5], such that the Scherrer equation (which is really only valid for crystals of dimensions less than or of the order of 1,000Å) gives a better estimation of the width of the peak - see equation 3.07.

$$FWHM = \frac{0.94\ \lambda}{L \cos\theta} \qquad \ldots (3.07)$$

This equation (3.07) gives the FWHM in radians as a function of the X-ray wavelength, λ, the penetration depth L, both in angstroms, and the

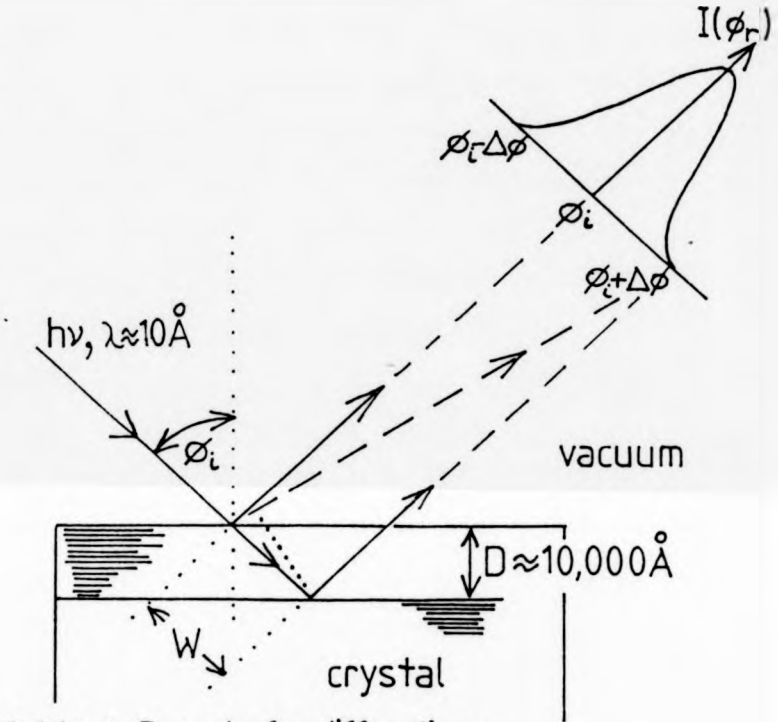

Fig. 3·06 (a) : Fraunhofer diffraction :
$\Delta\phi \approx \lambda/W \approx 1$ mrad

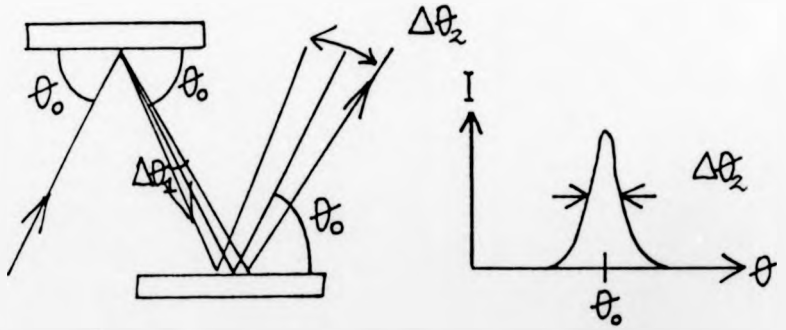

(b): Beam divergence produced by double reflection.

scattering angle, Θ. This gives the FWHM to be approximatley 1.5 mrad for $\lambda \simeq 10\text{Å}$, in agreement with the estimation shown in Figure 3.06(a).

Figure 3.06(b) shows that double reflection broadens the peak even further.

The introduction of a divergence into the beam upon the reflections from the crystal surfaces, and the non-perfect convergence of the beam from the monochromator, mean that in practice to get a resolution of around 2 eV, apertures are needed to reduce the spot size at the sample to 5 mm x 1 mm, the intensity then being approximately 10^{13} photons s^{-1} $Å^{-1}$ at $\lambda = 10\text{Å}$, for the storage ring operating at 2 GeV and 100 mA[6].

Another point to note in the layout of the beam line at the SRS is that the pre-mirror and the monochromator are orientated such that the main component of the electric vector of the X-rays that lies in the horizontal plane, lies along their surfaces, thus enhancing the reflection of this polarization component, in preference to the unwanted vertical field component. This serves[4] to provide a beam at the sample surface that for all practical purposes can be considered as being perfectly plane polarized, the electric vector being horizontal.

3.05 The Detection Methods Used in Bulk EXAFS Work

Having explained the need for a tunable high-intensity X-ray source for the collection of an EXAFS spectrum of a material, and before explaining some of the procedures necessary for surface EXAFS, the measurements needed to obtain a bulk EXAFS spectrum are now outlined.

For bulk EXAFS, the local environment(s) around those atoms of an element that makes up a large percentage of the chemical composition of the sample, can be determined by performing a transmission experiment (see Figure 2.01). The X-ray energy is scanned through an absorption edge of the element of

interest, the best choice of edge being such that there are no edges of other elements within an energy range of several hundred eV. The intensities of the X-ray beam before (I_o) and after passing through the sample of thickness x, give the absorption coefficient, according to equation 3.08.

$$\mu(h\nu) = \frac{1}{x} \ln\left[\frac{I_o(h\nu)}{I(h\nu)}\right] \qquad \ldots (3.08)$$

In order to maximise the accuracy of such a measurement[2,7], I should be around one half the value of I_o, which sets the required thickness of the sample to 0.1 - 1 μm[8].

For the determination of the local structure(s) around atoms of a minor elemental constituent, there is only a small increase in the total X-ray absorption at an energy corresponding to an absorption edge of this element, due to the large background absorption of the other atomic types. The amplitude of the EXAFS is therefore a small fraction of the total absorption coefficient, and the EXAFS may not even be visible if the measurement of the absorption coefficient has a large statistical uncertainty.

A measurement that is specific to the atoms of interest is needed, for example, the detection of the fluorescent X-rays[7]. A typical experimental set-up is shown in Figure 3.07, the sampling depth being dependent on the X-ray escape depth (which is of the order of many tens of thousands of atomic layers, such that this is a bulk technique), and the signal-to-noise ratio of the measurement being dependent upon such parameters as the detector energy resolution, and the relative amounts of fluorescent and inelastically scattered X-rays that pass through the discrimination of the detector.

3.06 Surface Sensitive Techniques for SEXAFS - Total, Partial and Auger Electron Yields

In a transmission experiment the X-ray absorption of a single monolayer of adsorbate atoms, would be negligible compared to that of the many thousands of atomic layers constituting the bulk of the substrate. If it were possible to measure the absorption coefficient of only the atoms near the surface, then it could be possible to deduce the geometrical environment of these atoms via an

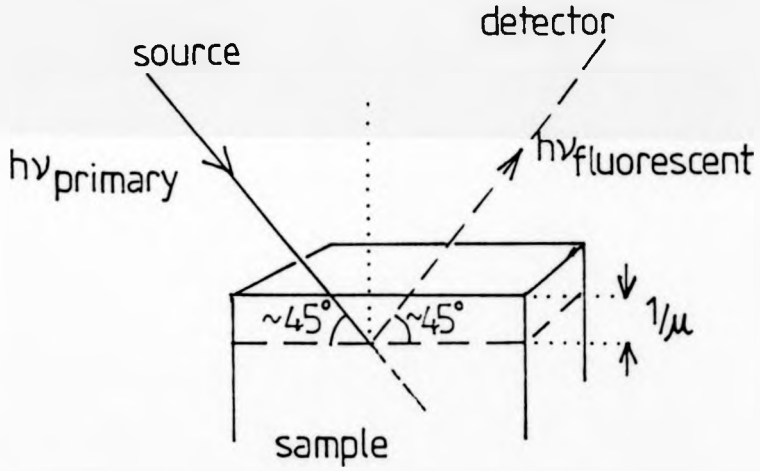

Fig. 3·07: EXAFS measurement via flourescent X-rays

analysis of the EXAFS. This can be done by utilising the fact that the escape depths of electrons are of the order of atomic dimensions.

Consider, as example, a monolayer of chlorine on a copper substrate, it being wished to determine the environment(s) around central chlorine atoms. When X-rays are incident upon such a surface[9], (Figure 3.08(a)), they are absorbed, producing pboto-, Auger, and secondary electrons, such that at one particular X-ray energy, the energy distribution of the electrons being ejected from the solid constitutes a spectrum[8], as shown in Figure 3.08(b). In this example, the X-ray energy is $h\nu$ = 3323 eV, this being 500 eV above the K-edge of chlorine and hence the region where the EXAFS would be observed. The photo-electrons ejected from the K-shell of chlorine have at this point an energy just less than 500 eV as they emerge into the vacuum, and constitute a peak (A in Figure 3.08(b)) that can be seen in the electron energy spectrum. The most obvious method of measuring the EXAFS above the chlorine K absorption edge would be to measure the size of this peak, requiring that the detection energy of the analyser be swept such that it remains equal to the photo-electron energy ie ($h\nu$ - 2823 eV). However, there are two problems.

Firstly, a detector set to count the number of electrons with the particular energy of those electrons in peak A would also count all the electrons constituing the large background-B in Figure 3.08(b). These electrons are produced from photo-ejected valence and less lightly bound core electrons (for example, the photo-electrons from the copper L_I level at a binding energy of 1096 eV, would have an initial kinetic energy of 2227 eV at this particular X-ray energy), and from Auger electrons, originating at depths up to 100Å, and loosing energy and creating secondary electrons as some travel towards the vacuum. This background is very much larger than the photo-electron peak (this peak being much exagerated in Figure 3.08(b)), and the background level falls steeply with the electron energy, such that the small functuations in the photo-electron intensity are obscured.

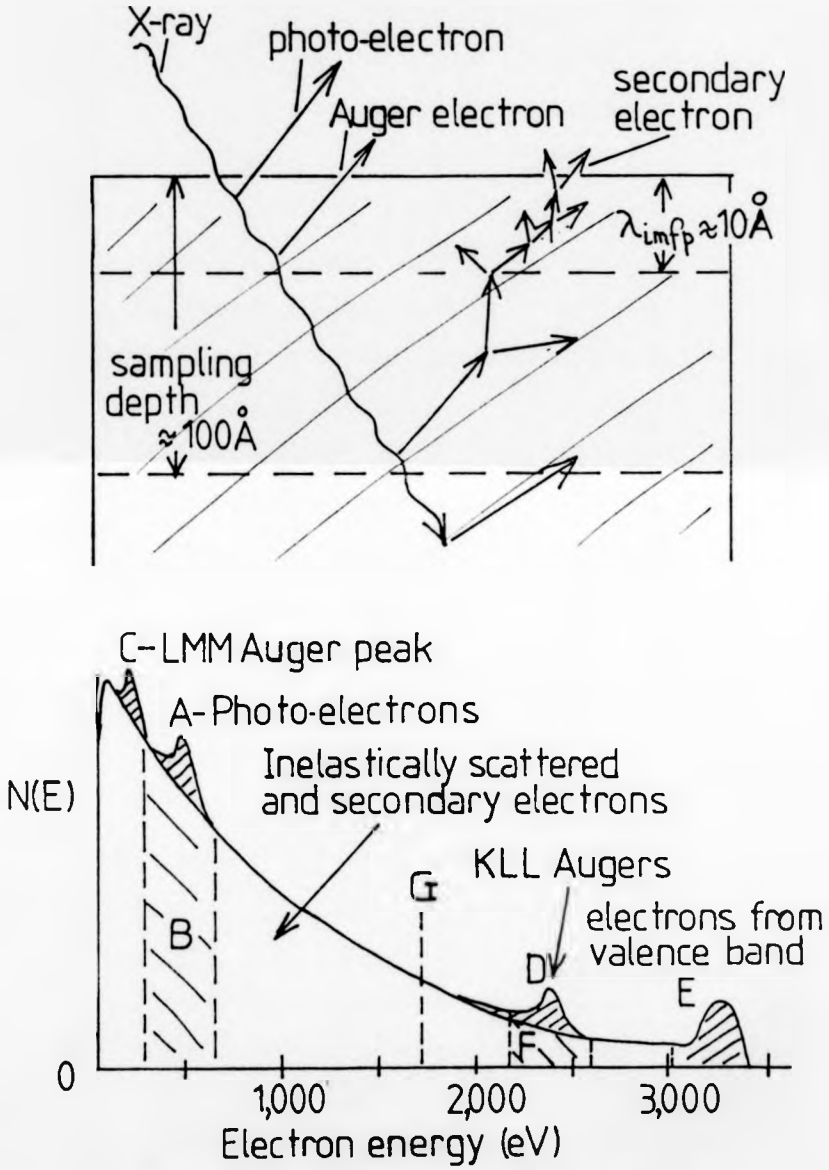

Fig. 3·08 (a) Emerging electrons caused by X-ray absorption (b) Electron energy spectrum.

Secondly, for single crystals, the intensity of electrons reaching the detector at a fixed geometry , tends to vary with electron energy due to diffraction effects[10, 11] more so than due to EXAFS. One way of eliminating such effects is to detect electrons emitted from chlorine atoms near the surface at fixed energy. The high energy chlorine KLL-Auger electrons have a fixed energy of 2383 eV, originating from an L electron falling to fill a core hole (most probably created by the X-ray beam) in the K-shell, a second L electron being emitted in the Auger process. A measurement of such an Auger peak (peak D in Figure 3.08(b)), is a direct measure of the rate of creation of core holes and hence of the X-ray absorption coefficient due to the K-shell of chlorine. The EXAFS can also be measured via a lower energy Auger peak (eg, C, in Figure 3.08(b)). The advantages in measuring at the energy of high energy Auger electrons[12] are that the background (F) is fairly small, compared to that below the low energy Auger peak (C), and that these low energy Augers have originated from a larger chain of events following the X-ray absorption.

The electrons in peak E of Figure 3.08(b) have been ejected from the valence levels of atoms at depths up to the electron mean free path, $\lambda^{imfp} \approx 10\text{Å}$, at these electron energies. For atoms at greater depths, such electrons loose energy and create low energy secondaries which constitute the background level, which as one looks at lower electron energies becomes larger, and represents the X-ray absorption coefficient of atoms down to increasing depths. A measurement of all the electrons above a certain energy, such as the point G in Figure 3.08(b) - the partial yield - is often used in SEXAFS work[13, 14], combining high count rates with surface sensitivity.

The highest count rates can be achieved by detecting all the electrons (the current being dominated by the low energy electrons) - the total yield - which samples a depth of around 100Å. Total electron yield has been shown to be proportional to the bulk X-ray absorption coefficient for soft[15] and hard[16] X-ray regions, and often gives good signal-noise for SEXAFS[17].

As the energy cut-off of the partial yield is increased, the surface sensitivity is improved, so that the EXAFS representative of atoms in the bulk or on the surface can be obtained[18].

3.07 Experimental Measurements of the Electron Yields and the Crystal Current, and the Normalisation to the X-ray Intensity

A typical experimental set-up at the SRS for obtaining a spectrum of values of the X-ray absorption coefficient as a function of the X-ray energy, of the atoms near the surface of a sample, is shown in Figure 3.09.

The approximately horizontal monochromatic X-ray beam from the monochromator, passes through a 99% transmittance tungsten mesh (the mesh size being very much less than the beam area to prevent fluctuations in signal as the beam position varies) from which photo-electrons are ejected. The mesh is connected to earth through a pico-ammeter, and the emission of electrons registers as a drain current. Such a current (typically of the order of 10^{-10}A) is converted to a voltage which can be used in the feedback loop to optimise the X-ray intensity as the top crystal of the monochromator is rocked around the Bragg peak. The signal from this mesh can also serve as a measure of the X-ray intensity from the synchrotron, beam line and monochromator as shown in Figure 3.10(c).

Figure 3.10 shows the measurements taken to obtain the EXAFS above the caesium L_{III} edge at 5012 eV, the X-ray energy being scanned from 4800 eV to 5370 eV. Since tungsten has no electron energy levels between the binding energies of 2820 eV and 10,205 eV, its X-ray absorption coefficient around 5000 eV is a smoothly decaying function - the three large dips in Figure 3.10(c) are monochromator 'glitches' - at these energies multiple reflections occur between the crystal planes, reducing the X-ray intensity.

It is important to accurately measure the X-ray intensity at each point simultaneously with the measurement of the signal from the sample, if a correct measure of the absorption coefficient is to be obtained. This can be seen by considering the plot of the crystal drain current (equivalent to the total

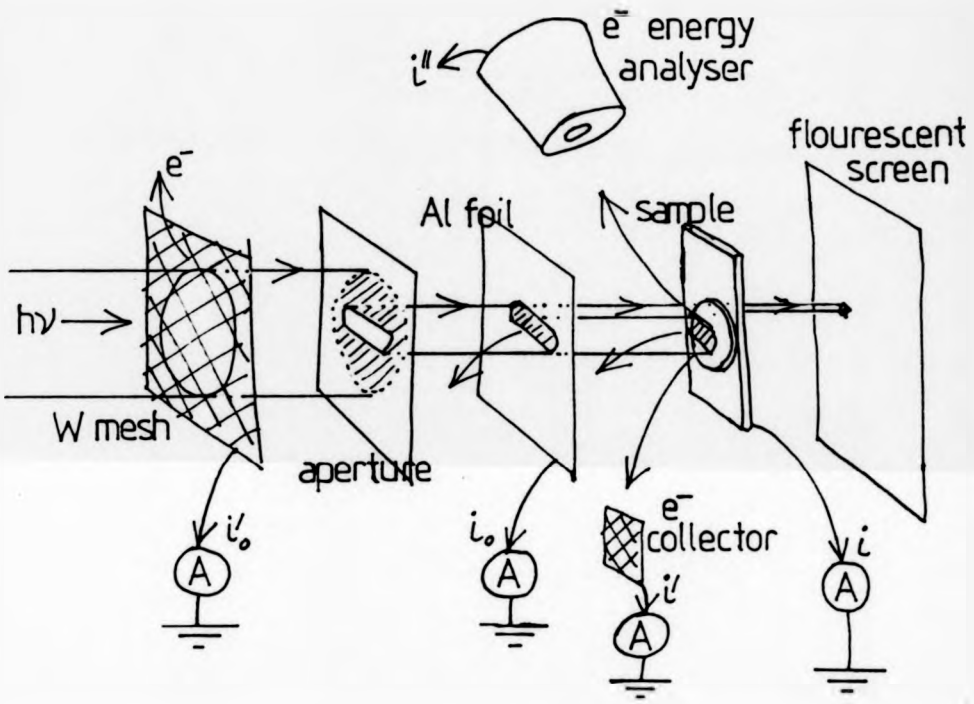

For measures of the X-ray absorption coefficients of atoms down to increasing depths in the sample, the Auger(i''), partial(i'' or i'), or secondary (i') e^- yield , or the crystal current (i) must be divided by a reference signal — i_o or i'_o.

Fig. 3·09 : Layout of beam monitors and sample measurements for SEXAFS.

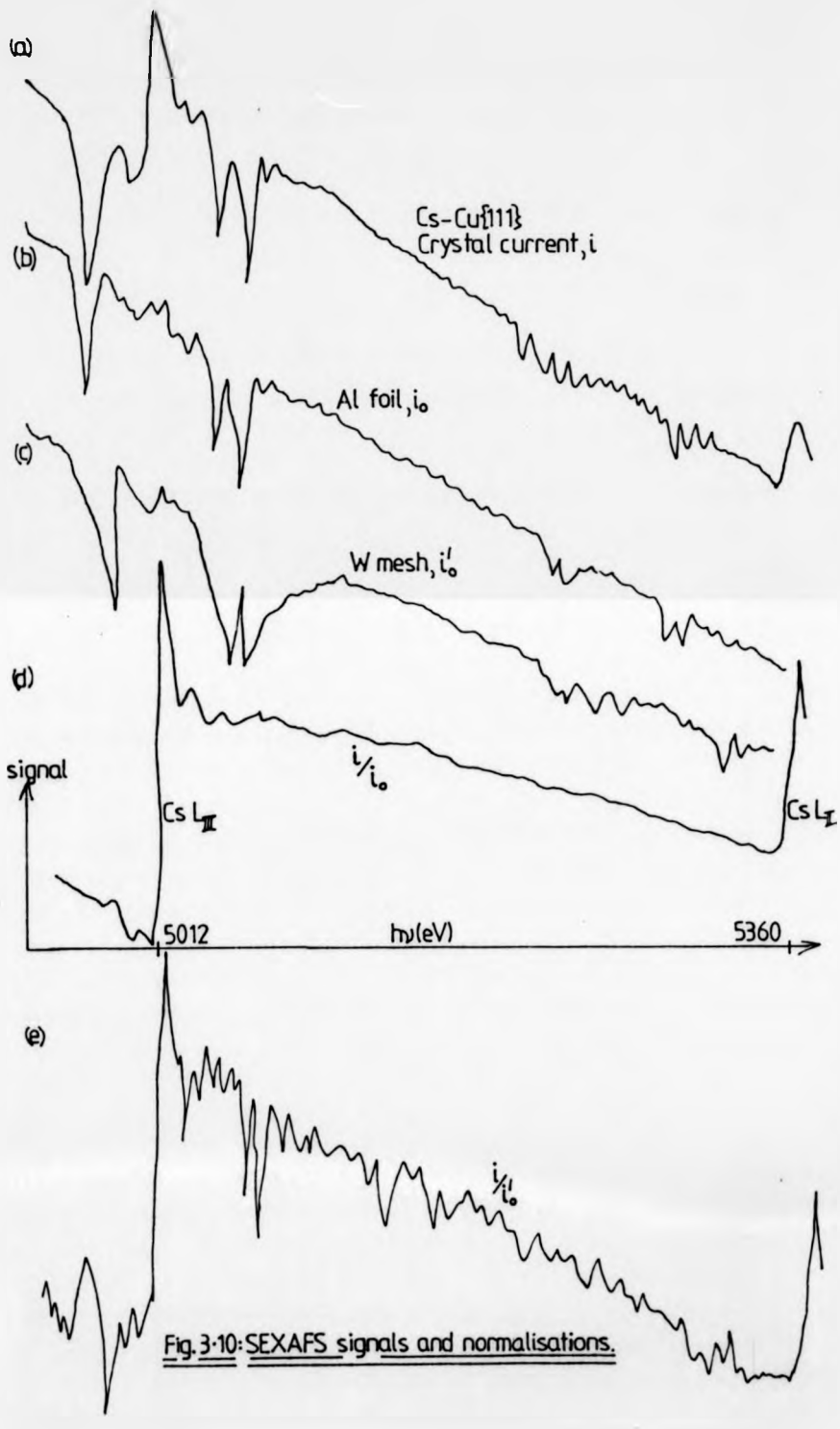

Fig. 3·10: SEXAFS signals and normalisations.

electron yield) versus the X-ray energy - Figure 3.10(a) - which in itself is rather useless. If this signal (which is a spectrum of values of the X-ray induced electron yield, integrated over a time of a few seconds at each X-ray energy increment) is divided by the tungsten mesh reference signal, then the edge jumps become more clearly apparent - Figure 3.10(e), although the monochromator glitches and some of the random point-to-point scatter in the X-ray intensity, have not been correctly normalised out. The reason for this is that the tungsten mesh is not monitoring exactly the same X-rays as are incident upon the sample, (see Figure 3.09) and the intensity and wavelength distributions across the beam are not homogeneous. The only way to monitor the X-rays that hit the crystal sample is to use a mesh or foil after the aperture (used to reduce the beam cross-section to a size smaller than the crystal face). For the experiments to measure the caesium L_{III} EXAFS, a thin aluminium foil (96% transmitting at around 5,000 eV X-ray energy) was found to give a satisfactory reference signal, as can be seen in Figure 3.10(b and d).

An important function of the aperture is to keep the X-ray spot in a constant position on the sample during the time taken to collect an EXAFS spectrum (~ 2 hours), during which time the electron beam in the storage ring is decaying, and the optical components in the beam line may be heating cooling, causing the X-ray beam trajectory to vary. It was found to be important to ensure that all the collimated X-ray beam hit only the crystal under study. If any part of the beam hit the crystal holder or 'spilled off' the manipulator, then poor normalisation results. A fluorescent screen is situated behind the sample (Figure 3.09) to observe any X-ray missing the crystal. In practice, the alignment of the pre-mirror and of the monochromator, to give a horizontal X-ray beam onto the sample, at all X-ray energies and for all storage ring conditions, was found to be a very critical parameter in the performance of the SEXAFS set-up.

3.08 Signal-to-noise Considerations

In this section the need for an exceptionally high signal-to-noise ratio is explained, and an outline is given of the ways in which potential sources of data corruption can be overcome.

The detection method that produces the clearest EXAFS should be used. Recent studies of one third of a monolayer of chlorine on Cu(111), at Daresbury, gave an edge jump of just 2% of the background level (see Figure 3.11(b)) when monitoring the chlorine K-edge EXAFS via the total electron yield (which is derived from the one-third monolayer of chlorine, plus about 50 atomic layers of copper). Monitoring electrons of energies around the Cl KLL Auger region produced an edge jump of 30%, and the LMM Auger electrons gave a jump of 17%, but in both cases the EXAFS oscillations were less clear, despite the improved surface sensitivity, due to the low count rates when using the CHA (concentric hemisphere analyser).

Any measurement is accompanied by an uncertainty (for N counts the standard deviation is $\sqrt{N}$), such that a spectrum of measurements of the X-ray absorption coefficient appears to be 'noisy', ie there are large random changes from one energy datum to the next - such fluctuations tend to obscure the true variations in μ, ie the edge and the EXAFS. For surface EXAFS the problem is acute when the edge and the EXAFS are small compared to the background, since the 'noise' is proportional to the total signal; for bulk EXAFS the problems are not as great.

Consider Figure 3.11(a), showing the K-edge EXAFS of bulk CuCl. The μ value (in arbitrary units) increases from 0.01 to 1.0 at the edge, ie the edge: background ratio is 100%. EXAFS oscillations are typically 1% of the edge in amplitude, in this case 1% of 1.0 ie 0.01. If the statistical fluctuation is only 0.1% of the measurement, ie 0.1% of 1.0 = 0.001, then the EXAFS amplitude compared to the 'noise' amplitude is 0.01: 0.001 ie 10, such than this spectrum shows the EXAFS clearly. Now consider Figure 3.11(b), for only one third of a monolayer of chlorine on copper . The edge jump is 0.1, ie 2% of the background

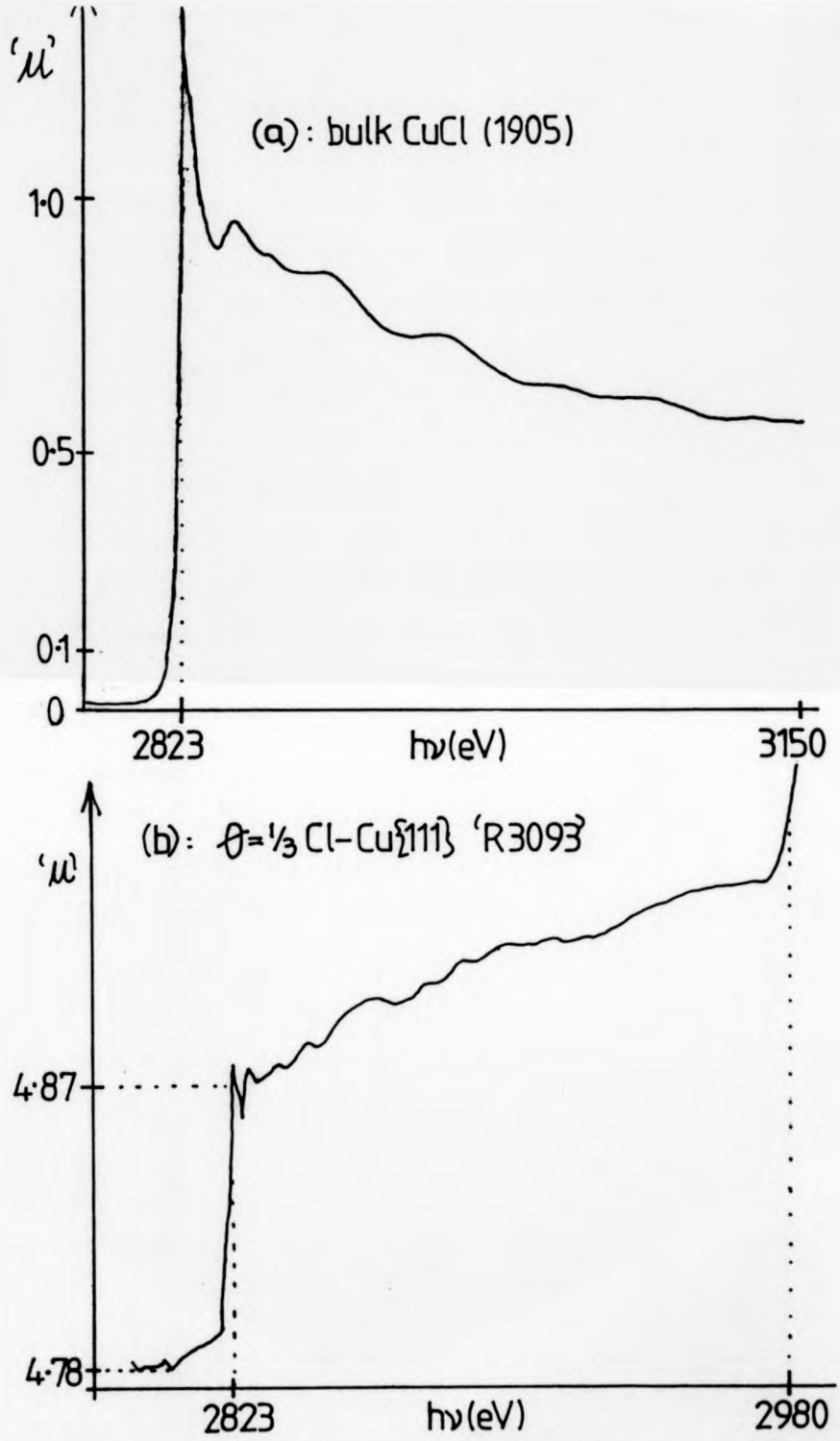

Fig. 3·11: Signal:noise ratios in SEXAFS and EXAFS spectra.

(4.78), the EXAFS oscillations have an amplitude of 0.001 (ie 1% of 0.1), whereas the statistical 'noise' is 0.005 (0.1% of 4.87), such that the signal (EXAFS): noise ratio is only 1:5. For this surface EXAFS spectrum, the edge is clearly discernable, but the EXAFS is not. In order to get a 'signal: noise' ratio of 10 (as for the bulk CuCl spectrum), 2500 separately measured spectra would have to be added together, to 'integrate out' the noise (2500 counts improves the signal to noise by 50 times); alternatively, the 'noise' would need to be reduced to 0.002% of the total signal (0.002% of 4.87 is approximately 0.0001, compared to the 0.001 EXAFS), enabling one scan to produce a clear spectrum.

It is clearly of great importance, therefore, that the normalisation procedure, described in the previous section :(3.07), and illustrated in Figure 3.10, be extremely accurate. One potential problem is the varying presence of higher energy harmonics in the 'monochromatic' X-ray flux. Figure 3.12(a) shows that whilst the total energy contained within the third harmonic peak is much less that the integral of the intensity of the fundamental X-ray energy, the intensities at the centre of the Bragg peak can be comparible. Consider the Cl K-edge EXAFS being measured using an aluminium foil as a beam monitor. If the monochromator normally moves to a position such as 'X' in Figure 3.12(a), then only X-rays of energy $h\nu_1$ are present. Such an energy might be 3000 eV, such that the $I(h\nu_1)$ and $I_O(h\nu_1)$ signals are derived from the chlorine and aluminium absorption coefficients at 3000 eV, as shown in Figure 3.12(b) and (c). If, however, the monochromator positions itself at an angle giving rise to the point 'y' in Figure 3.12(a), then third order X-rays are reflected, causing the signal from the sample to be effectively unchanged ($I(3\ h\nu_1) \ll I(h\nu_1)$; Figure 3.12(b)), whereas that from the monitor is approximately doubled ($I_O(3\ h\nu_1) \approx I(h\nu_1)$; Figure 3.12(c)), causing the 'false' measurement 'y' in Figure 3.12(d). Over a whole spectrum, the amount of third order at each energy datum , varies randomly, causing the apparent noise to increase.

Whilst fluctuations in the currents measured, can be integrated out by counting for longer times, only multiple scanning, (ie adding together spectra)

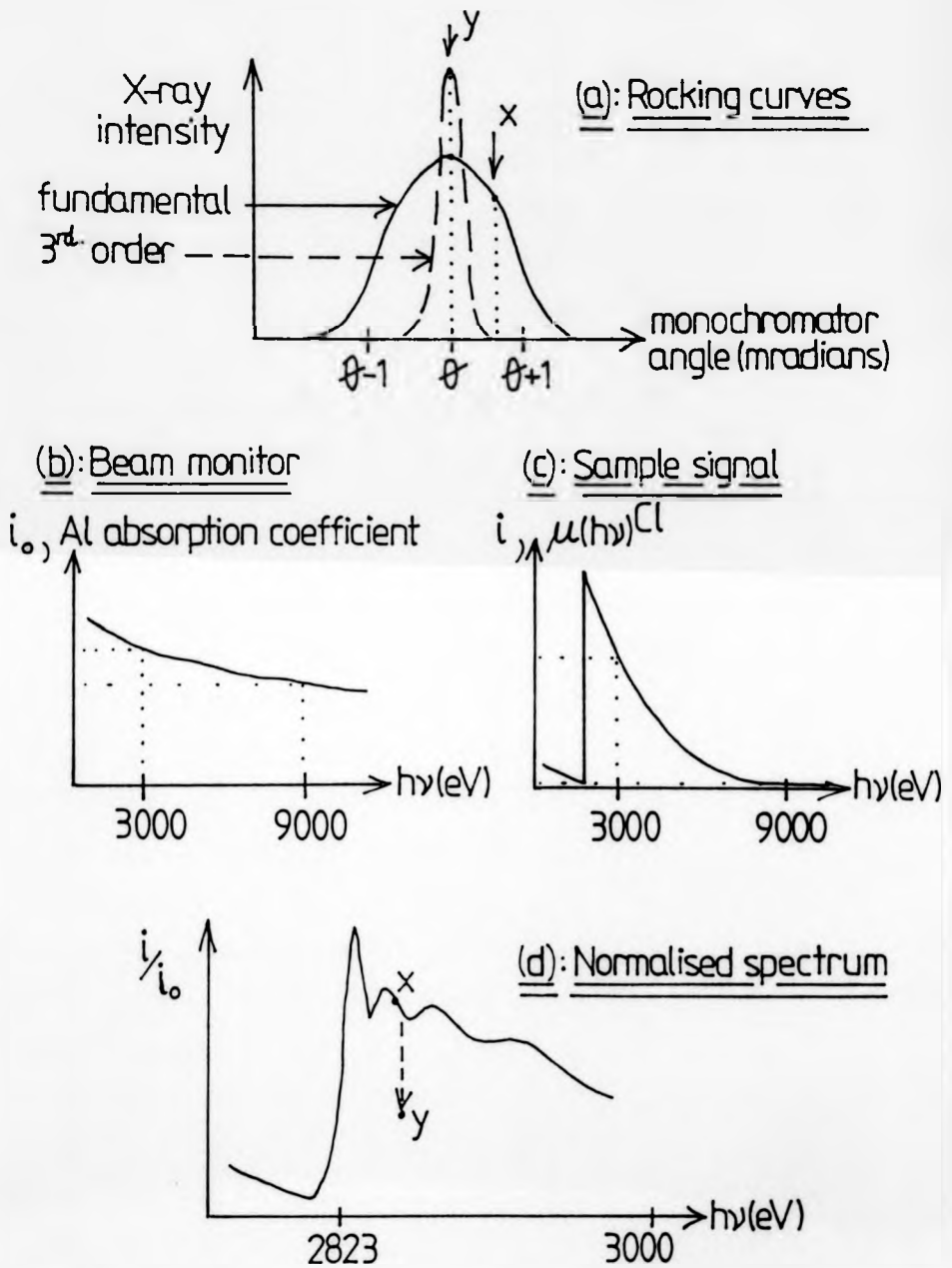

Fig. 3·12: Apparent noise introduced by 3rd harmonic X-rays.

can remove the 'noise' introduced by the third order effect described above, and the errors introduced by the monochromator moving to a slightly incorrect energy. When the monochromator does move to an incorrect angular setting (by a random amount), a measurement of μ at this actual energy is interpreted as being the absorption coefficient at the expected energy - this 'smears out' any features in the spectrum that are narrower than the energy resolution of the monochromotor. Using an electron analyser of a given electron energy resolution, for example, when monitoring the Auger yield, in no way affects the X-ray energy resolution of the spectrum.

3.09 Sample Preparation and Analysis Chamber and Computer Control

The UHV chamber for the crystal preparation and characterisation by LEED and AES, shown in Figure 1.03, is also used for the SEXAFS data collection, the crystal simply having to be moved down to the 'SEXAFS' level see Figure 3.13(a). X-rays enter the chamber via a vacuum tube leading to the monochromator, and are absorbed by the crystal, producing electrons of various energies, some of which are emitted in a variety of directions. The electron current flowing from earth to the crystal - the crystal current - is equivalent to the total electron yield, and can be measured by a Keithley current-to-voltage amplifier (capable of measuring 10^{-12}A). Biasing the sample positive can, in principle, enable the partial electron yield to be measured at a selectable energy cut-off. A secondary electron detector can similarly be used to monitor the total or partial electron yield (over a limted angular range). The CHA can be used to monitor an Auger or partial yield.

The crystal can be rotated about a vertical axis in order to vary the X-ray incidence angle from 90^{o} to approximately 30^{o} (see Figure 3.13(b)), the limit of the glancing angle being reached when the diameter of the crystal presented to the X-ray beam becomes equal to the diameter of the beam itself. The azimuthal orientation is varied by rotating the crystal about a horizontal axis

Fig.3·13: Crystal at SEXAFS level in analysis chamber

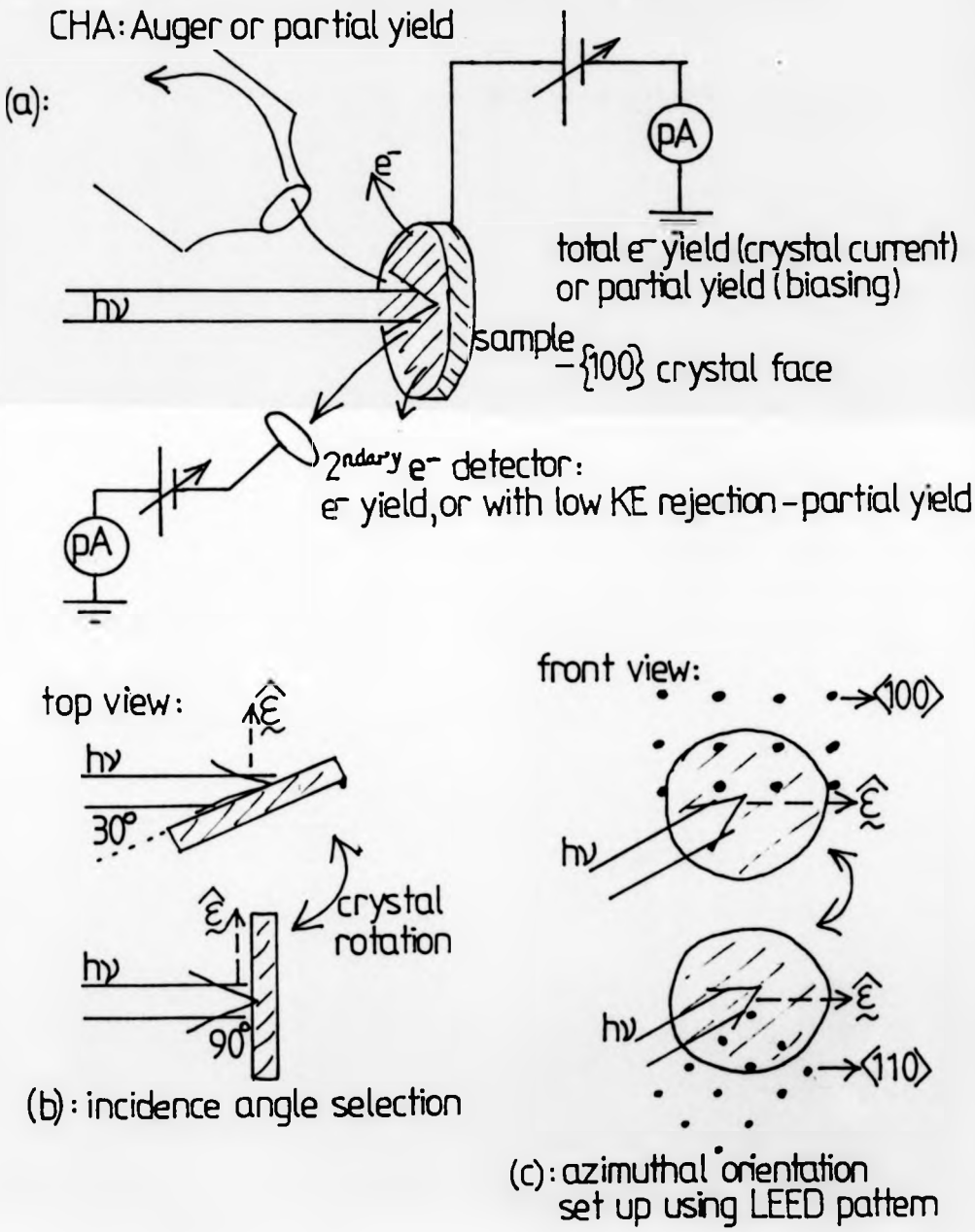

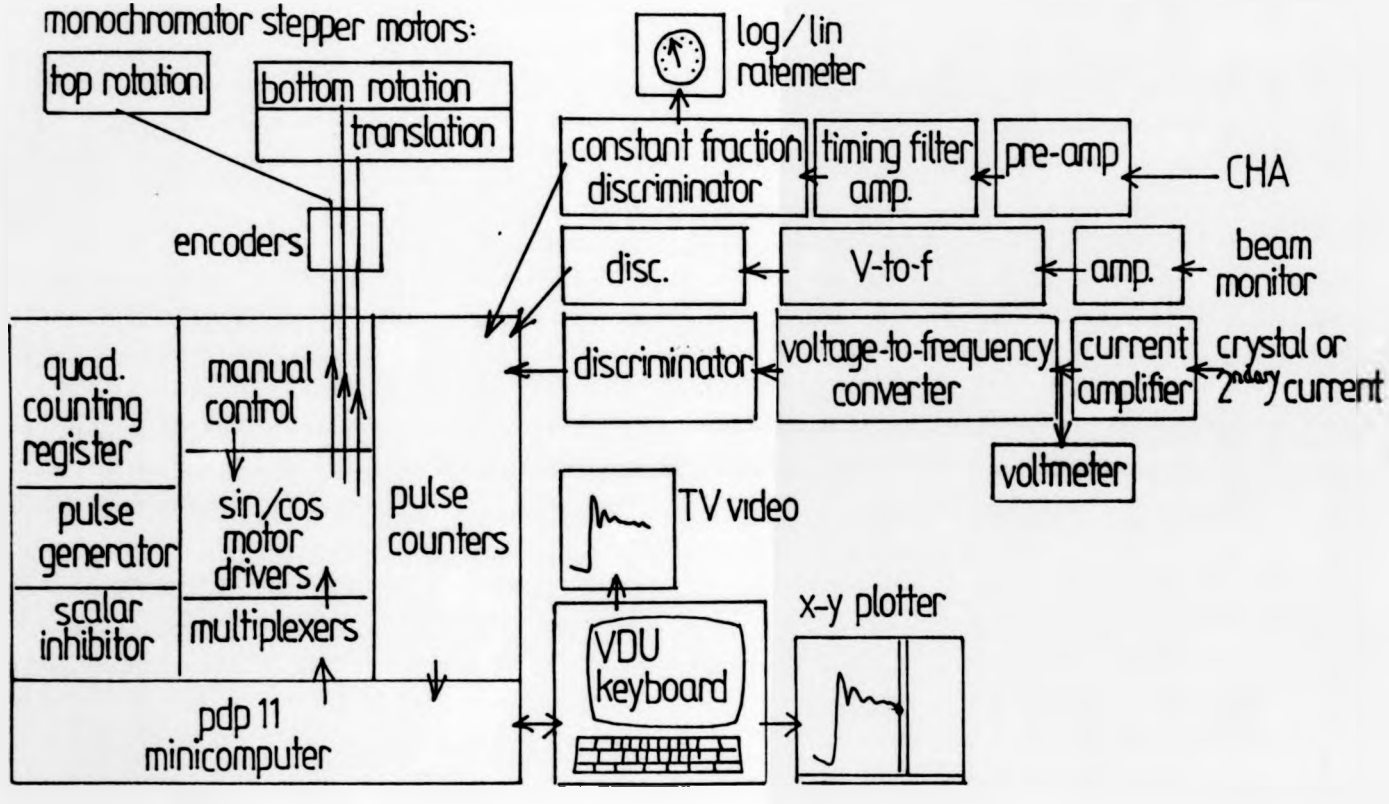

Fig.3.14: SEXAFS computer controlled data collection system.

normal to its surface, as shown in Figure 3.13(c) - in practice the LEED pattern needs to be checked with the crystal at the 'upper level', and it must then be carefully moved down to the 'lower level'.

Data collection is controlled by a pdp 11 minicomputer which is interfaced via Camac Crates to the experimental equipment - see Figure 3.14. Information such as start, finish and incremental X-ray energies, monochromator crystal type, and counting time is entered at the keyboard, and the computer automatically moves the monochromator crystals to the appropriate positions, maximises the X-ray flux, and processes all the signals required for the SEXAFS spectrum. It typically takes a few seconds to move to a new energy, and allow the instruments to stabilise and a few seconds are spent collecting signals before moving to the next energy, thus for a spectrum consisting of 450 points at 1 eV increments, it takes of the order of a couple of hours.

3.10 References

1. K R Lea and I H Munro, 'The Synchrotron Radiation Source at Daresbury Laboratory' published 1980
   available from The Librarian, DL, SERC, Warnington, WA4 4AD.

2. L I Azaroff, 'X-ray Spectroscopy'
   1974, International Series in Pure and Applied Physics, McGraw-Hill
   Chapter 7: Synchrotron Radiation and Applications
   Chapter 3: Grating spectrometers and their application in emission spectroscopy.
   Chapter 6: X-ray absorption spectra.

3. Design Study for a Dedicated Source of Synchrotron Radiation
   DL/SRF/R2
   Daresbury Laboratory.

4. Z Hussain, E Umbach, D A Shirley, J Stöhr and J Feldhaus
Nuclear Instruments and Methods 195 (82) p 115
'Performance and application of double crystal monochromator in energy region 800 ≤ hν ≤ 4500 eV'.

5. B E Warren, 'X-ray Diffraction', Adison-Wesley, 1969:
Chapter 14: Perfect Crystal Theory
Chapter 13: Diffraction by Imperfect Crystals.

6. A Jackson and K R Lea
Synchrotron Radiation, appendix to Daresbury annual report, 1982/83/
Daresbury Laboratory.

7. P A Lee, P H Citrin, P Eisenberger and B M Kincaid
Reviews of Modern Physics 53(4, 1) October 1981, p 769
II B: Signal-to-noise evaluation of different detection techniques.

8. A Bianconi, Applications of Surface of Science 6(1980) p 392:
'Surface X-ray Absorption Spectroscopy: SEXAFS and SXANES'.

9. J Stöhr 'EXAFS and Surface EXAFS: Principles, Analysis and Applications'.
Stanford Synchrotron Radiation Laboratory, Report 80/07, December 1980.

10. P A Lee, Phys Rev B13(12), June 1976, p 5261
'Possibility of absorbate position determination using final state inteference effects'
- discusses the necessity to angularly integrate the electron yeild.

11. P J Orders and C S Fadley, Phys Rev B27(2). January 1983, p 781:
'Single-scattering cluster calculations and Fourier-Transform analyses of Normal Photo-electron Diffraction.

12. S Brennan, J Stöhr and R Jaeger, Phys Rev B24(8). October 1981, p 4871:
'Structure determination of c(2x2) S — Ni(100) using polarization-dependent SEXAFS'.
-Sulphur KLL Auger electrons detected by an analyser set to 2100 eV with a 30 eV window.

13. A Puschmann and J Hasse, Surf Sci 144 (1984) p 559:
'Surface EXAFS of the (2x1) oxygen adlayer on Ag(110)'
-SEXAFS monitored using partial yield, retardation voltage = 450 V.

14. J Stöhr, T Jaeger and T Kendelewicz, Physical Review Letters 49(2), July 1982, p 142:
'Structure of p(2x2) and c(2x2) Oxygen on Ni(100): A SEXAFS study'.
- Partial yield, retardation = 350 V.

15. W Gudat and C Kunz, Phys Rev Lett 29(3), July 1972, p 169
'Close similarity between photo-electron yield and absorption spectra in soft X-ray range;

16 G Martens, P Rabe, N Schwentner and A Werner, Journal of Physics C11 (1978) p 3125:
'EXAFS in photo-electron yield spectra and optimisation of photon glancing angle'.

17. J Stöhr, L I Johansson, S Brennan, M Hecht and J N Miller, Phys Rev B22(8), October 1980, p 4052. 'SEXAFS Study of oxygen interaction with Al(111) surfaces'.

18. A Bianconi and R Z Bachrach, Phys Rev Lett 42(2), January 1979, p 104: 'Al surface relaxation using SEXAFS'.

CHAPTER 4:

THE ADSORBATE-SUBSTRATE SYSTEMS STUDIED

4.01 OVERVIEW

Analyseable SEXAFS spectra are available for a variety of structures fomed by the dissociative adsorption of iodine gas molecules onto Ni(100), and chlorine molecules onto Cu(111), namely:-

(i) A surface nickel iodide on Ni(100).

(ii) C(2 x 2) I-Ni(100), at an iodine coverage of $\theta = {}^{1}/_{2}$.

(iii) C(2 x 8) I-Ni(100), $\theta = {}^{3}/_{8}$.

(iv) (2 x 3) I-Ni(100), $\theta = {}^{1}/_{3}$.

(v) ($\sqrt{3}$ x $\sqrt{3}$) R30° Cl-Cu(111) at a chlorine coverage, $\theta = {}^{1}/_{3}$.

(vi) (6 $\sqrt{3}$ x 6 $\sqrt{3}$) R30° Cl-Cu(111), $\theta = 0.45$.

SEXAFS spectra have also been measured from bulk nickel iodide (NiI_2) and bulk copper (I) chloride (CuCl) acting as reference compounds.

In this chapter, descriptions are given of the procedures used in forming the above surface structures, and for preparing the bulk compounds in forms that are suitable for SEXAFS measurements.

The geometrical structures that have been postulated on the basis of LEED and other studies, are described, and the corresponding radial distribution functions appropriate to central iodine and chlorine atoms are calculated, and some implications for the SEXAFS spectra are considered.

4.02 The Surface Structures Formed by the Adsorption of Iodine onto Ni(100)

Molecular iodine adsorbs onto a single crystal Ni(100) surface (the (100) surface of a face centred cubic element is shown in Figure 1.01) to form a variety of structures depending on the partial

pressure of iodine vapour, and on the temperature of the nickel substrate - see Figure 4.01[1]. Heating or cooling can cause a variety of phase transformations.

With the iodine pressure at 2.10^{-7} mbar, and the crystal at room temperature (<340 K), dissociative adsorption occurs, such that a C(2 x 2) layer of adatoms is formed after an exposure of 45 Langmuirs (1 Langmuir = 1.33 10^{-6} mbars.s.). On heating, the LEED pattern is seen to contract in one dimension, being given by the general equation 4.01.

$$\begin{vmatrix} 1 & 1/\tan\alpha \\ -1 & 1/\tan\alpha \end{vmatrix} \quad \alpha \neq 45^{o} \qquad \ldots (4.01)$$

The explanation of this is that on heating, some iodine atoms desorp, and the remaining iodine adatoms expand in 1-D, in a < 100 > direction along the Ni{100} surface. The C(2 x 2) room temperature overlayer corresponds to a coverage, $\theta = 1/2$, at which point $\alpha = 45^{o}$. At 550 K (10 mV above room temperature measured by a chromel-alumel thermocouple), $\theta = 3/8$ and $\alpha = 37^{o}$ corresponding to a C(2 x 8) LEED pattern, and at 725 K ('17 mV') $\theta = 1/3$ and $\alpha = 34^{o}$ such that the LEED pattern is (2 x 3). At coverages between the above mentioned commensurate structures, the LEED pattern is ill defined. Three real space structures corresponding to C(2 x 2), C(2 x 8) and (2 x 3) LEED patterns are shown in Figure 4.02. These correspond to a postulated hollow adsorption site in the C(2 x 2) structure, but since the LEED pattern is sensitive only to the adlayer symmetry, bridge, atop, or indeed any non-symmetric adsorption site could be possible.

Above 800 K, the adlayer becomes disordered (long range order is lost); desorption is only complete above 1000 K, this temperature being comparable with the sublimation temperature of nickel iodide, which is 1020 K[2].

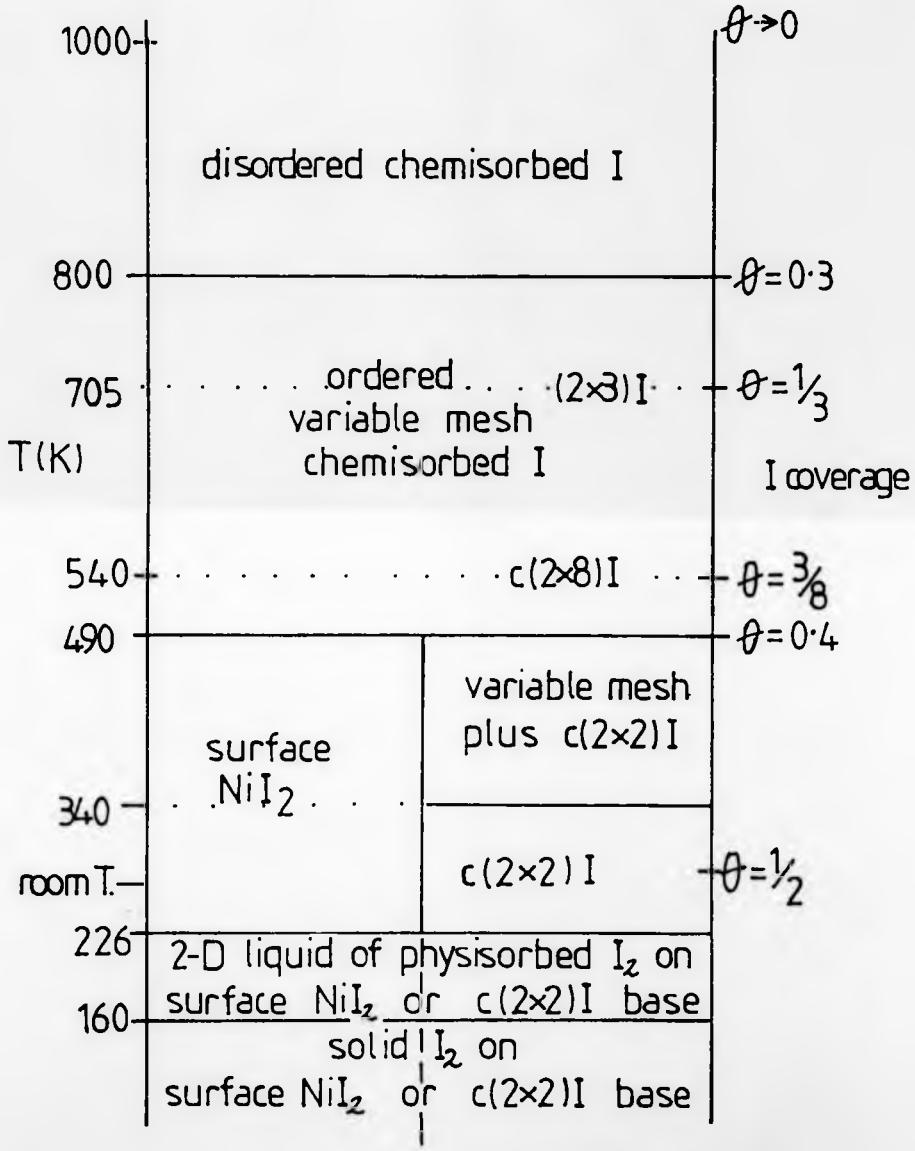

Fig. 4·01 : Surface structures on Ni{100} formed by the adsorption of I_2, coverage being a function of temperature.

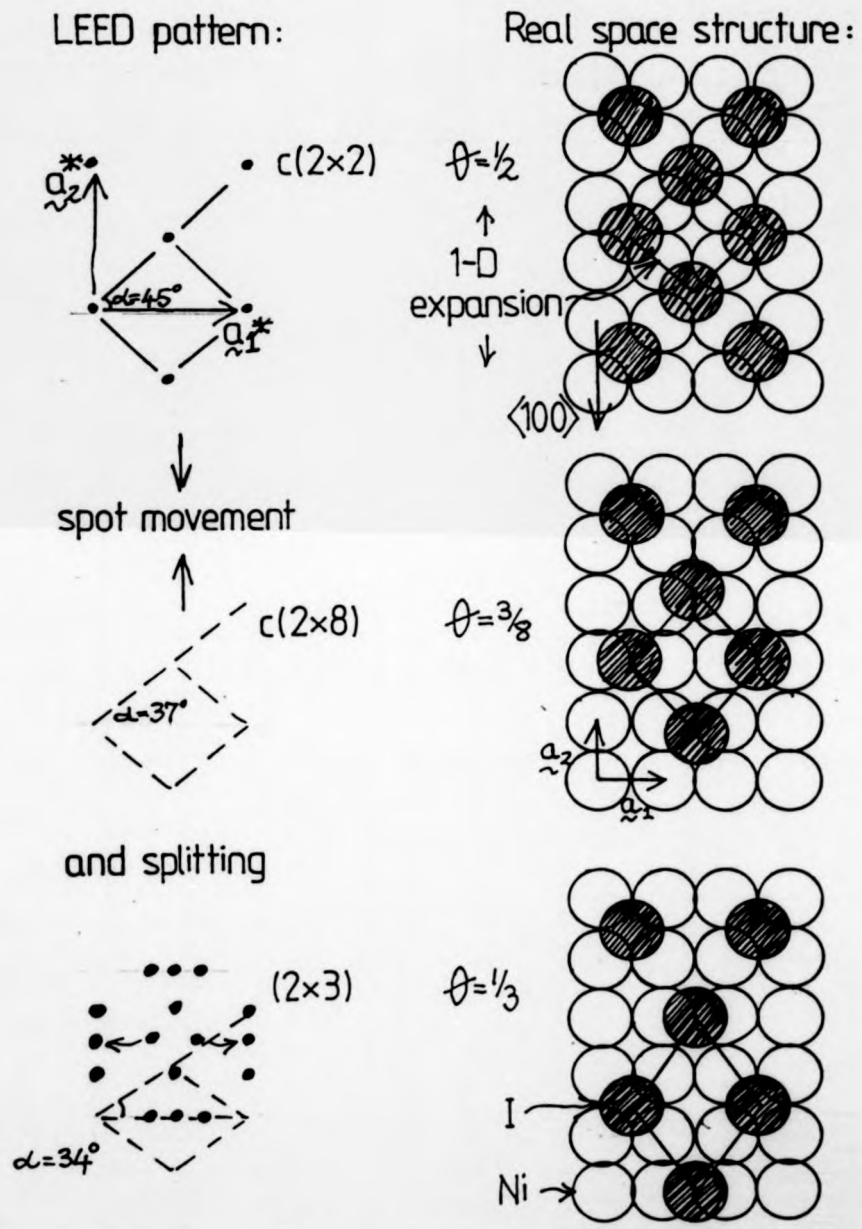

Fig.4·02 : LEED patterns and 3 possible I-Ni{100} structures.

If the crystal at a temperature in the range 370-1000 K, is exposed to iodine vapour at a pressure of 10^{-6} mbar, and cooled whilst maintaining this high iodine pressure, then a surface iodide structure results. This structure has been shown to consist of a single sandwich of I, Ni, and I layers of atoms, arranged almost as they are in bulk nickel iodide (Figure 4.03[3]) - the hexagon defining such a structure being slightly distorted ($\beta \approx 61^{o}$, rather than 60^{o}), and expanded (the dimensions of each side by ~ 4% larger than in the bulk nickel iodide) - lying on the undistorted Ni(100) face[3] - Figure 4.04[4]. This surface nickel iodide structure is stable at room temperature, and on heating above 490 K, iodine molecules begin to desorb such that the same set of structures are formed as when starting from the C(2 x 2) overlayer.

The transition to lower coverage iodine overlayers is reversible; for example with the crystal at a temperature of 450 K and the iodine vapour pressure at 5.10^{-5} Nm^{-2}, the coverage increases back to $\theta = 0.4$.

Below 160 K, and after long exposures of iodine (0.1 Nm^{-2} seconds), solid iodine in the molecular form, grows on top of either the C(2 x 2) or the surface iodide layers - this condensed iodine desorbs when the pressure is reduced to 10^{-6} Nm^{-2} and the crystal is heated to 185 K, leaving a physisorbed iodine layer that itself desorbs at 226 K.

Similar overlayer structures, formed by the dissociative adsorption of halogen molecules onto transition metal surfaces, followed by the growth of a 'corrosion' layer, with molecular adsorption onto this layer, have been observed - bromine on silver for example[5].

Thermal desorption studies have yielded some clues as to the nature of the surface chemical bondings present in the iodine-nickel

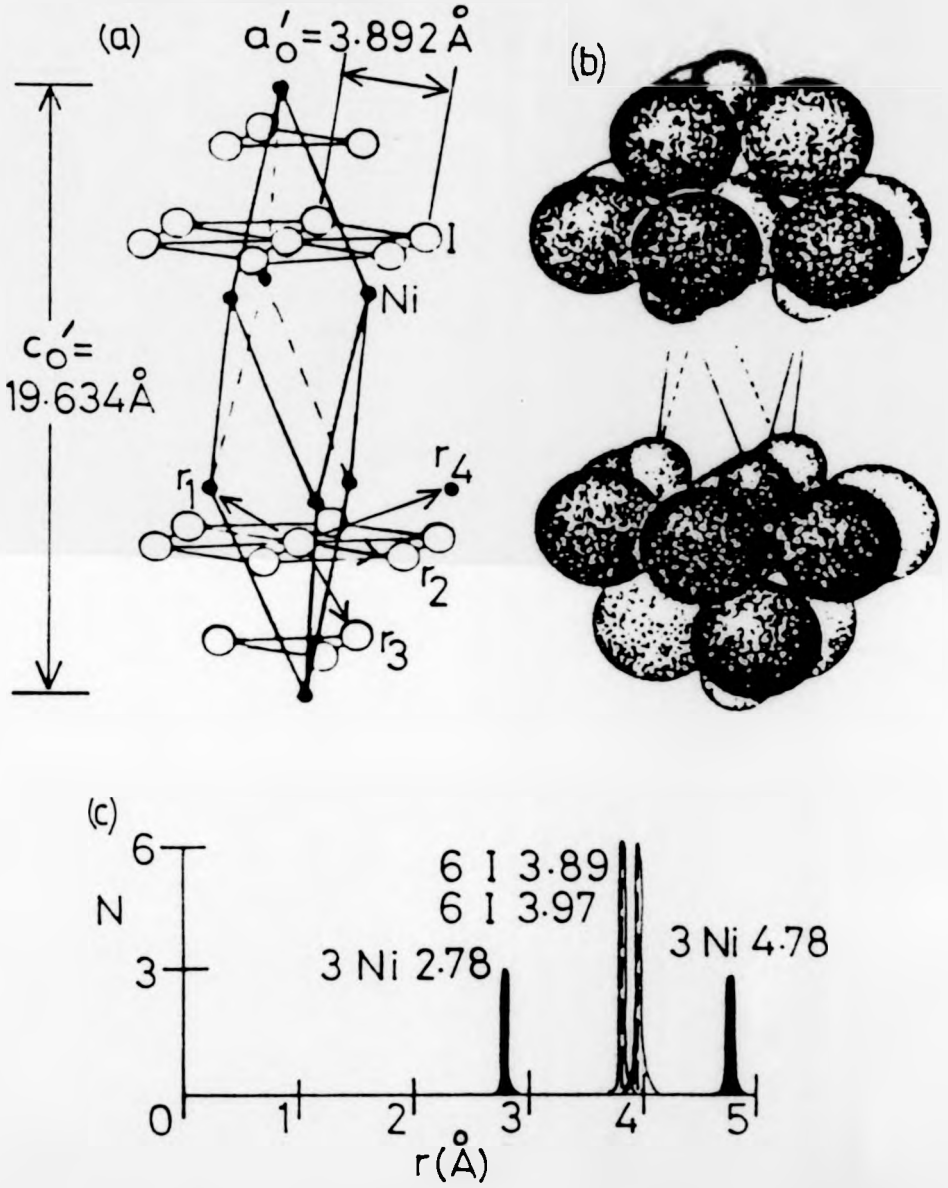

Fig. 4·03: Bulk NiI_2 structure
(a): unit rhombohedron
(b): hard sphere representation
(c): central iodine radial distribution function

Fig. 4·04: Surface NiI_2–Ni{100} structure deduced by LEED and AES.

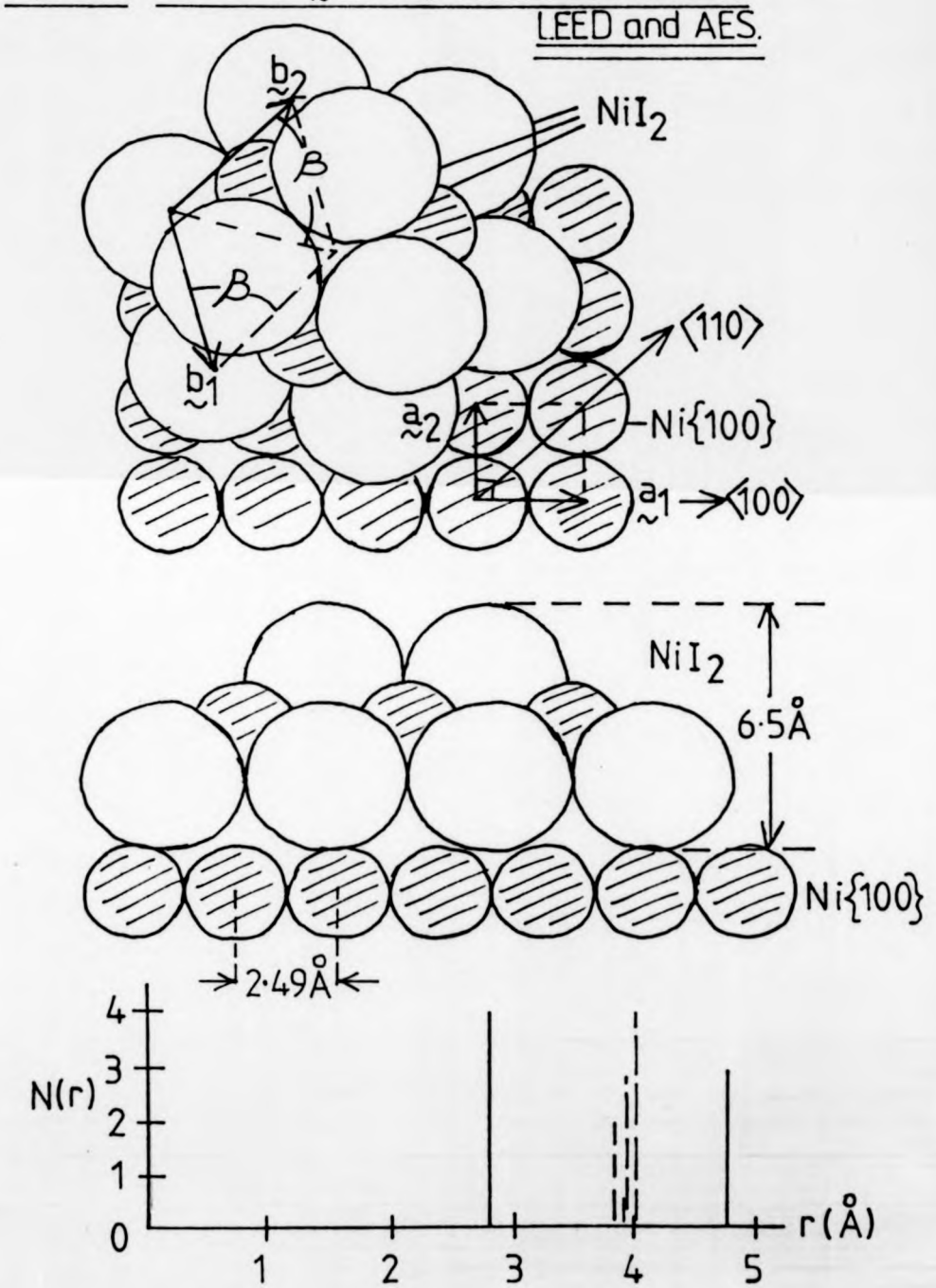

structures. On heating the C(2 x 2) iodine overlayer, the iodine does not all desorb at a well defined temperature, but instead desorbs gradually as the temperature is raised, the remaining iodine expanding in one dimension. This suggests that the total binding energy of the iodine increases as the iodine coverage is reduced. If there is a repulsive force between the iodine adatoms (obviously smaller in magnitude than the attractive force between each iodine adatom and the nickel metal, since the iodine atoms remain bound to the surface at room temperature) that increases as the adatoms are stacked closer together, then this could explain the observed decrease in the total binding energy as the iodine coverage is increased. The iodine-nickel bond is only partially ionic - the small work function changes observed on iodine adsorption suggest that each iodine atom has a charge of approximately - 0.1 e ($e = 1.6\ 10^{-19}$ C). This would produce a 'through-space' repulsive force between the iodine adatoms, that would increase as their separation was reduced. This force would be a dipole-dipole repulsion between one iodine adatom and its accompanying image charge, and the adjacent dipole, and the charges would also be screened by the conduction electrons of the metal, reducing this repulsive force to less than that requred to explain the observed changes in the total binding energy as measured by the thermal desorption study. However, there could be another repulsive force present. Electrons are required for the I-Ni(100) bonds, such that if more adatoms are stacked into a given area, then there is a 'competition' for the available bonding electrons, and if there is a shortage of bonding electrons then each bond is weakened. On expansion, the I-Ni(100) bond can become stronger, thus increasing the total binding energy - since such a process is favoured, it appears as an apparant I-I repulsion, - the 'through-metal' repulsion. Core level shift measurements[6], have been unable to

determine the changes in the total binding energy of the iodine atoms as a function of their coverage, due to final state changes, causing the through space interaction to be concealed; the through-metal repulsion having been estimated, and a calculation showing that it could explain around a half of the binding energy reduction as the iodine coverage increases from $\theta = 0.33$ to $\theta = 0.5$, the other half therefore arising from the through-space screened dipole–dipole repulsion. It should be noted that quite different explanations of similar binding energy variations with coverage have been put forward[5].

4.03 Predictions of the EXAFS Spectra from the likely I-Ni(100) Surface Structures

The EXAFS above the iodine L_{III} edge, depends upon the local environment(s) of all the iodine atoms that are situated in the region from which the X-ray absorption coefficient is being measured. To determine the structure of one of the iodine coverages, it is necessary to postulate a structure that is consistent with the LEED pattern and/or other available measurements; to guess an adsorption site (or number of sites) using the available knowledge of adsorption sites in similar adsorbate—substrate systems; to calculate the local structures around each uniquely situated iodine atom; to calculate the EXAFS from such a radial distribution function of atomic neighbours; and to compare this with the experimentally measured surface EXAFS spectrum.

The EXAFS above the I L_{III} edge for bulk nickel iodide (Figure 4.03) can be predicted as follows. Because of the systematic arragement of atoms within the crystal structure[3], a given iodine atom has the same arrangement of neighbouring atoms as all the other iodine atoms. This radial distribution function consists of 3 nickel nearest neighbours (to which the central iodine atom can be regarded

as being bonded) each at a distance of 2.78 Å (one example of an I–Ni vector is labelled r_1 in Figure 4.03). The next nearest atomic neighbours are 6 iodine atoms in the same hexagonal–close–packed layer as the central iodine atom, at 3.89 Å, followed by 6 iodine atoms at the slightly larger distance of 3.97 Å (3 of these are in an iodine hcp layer above, the other 3 in the layer below). The only other atoms within a 5 Å radius are 3 nickel atoms at 4.78 Å (see Figure 4.03(c)).

The bulk nickel iodide sample from which the measurements described in this thesis were taken, was a compressed powder, consisting of many small polycrystalline particles, each aligned randomly at a variety of orientations to the electric vector of the plane–polarized X–ray beam. The effective number of backscattering atoms per shell is therefore equal to the number of atoms in each shell. The EXAFS consists of a superposition of oscillations in k–space, each having a period characteristic of the backscattering shell from which it results, as well as the atomic phase shifts involved. For bulk nickel iodide there would be a main oscillation resulting from the nearest nickel shell, and an oscillation of smaller amplitude and smaller period in k–space due to the 12 iodine atoms at an average distance of 3.93 Å(the contributions to the EXAFS from the two iodine shells, differing in distance by only 0.08 Å could only be resolved if a very large k–range of EXAFS were considered). Even though there are four times as many atoms in this shell compared to the nearest shell, and despite the fact that iodine is a heavier atom than nickel, and hence a stronger photo–electron backscatterer, the EXAFS would be dominated by the nearest shell. This strong fall off in EXAFS amplitude with distance is due to the inverse square law decay of the photo–electron wave, the small inelastic mean free path (~ 4 Å), and the higher Debye–Waller factors

for all shells other than the nearest. A simple calcualtion[7] shows that the contribution from the iodine shell would have about one half of the amplitude of that of the nickel shell, the total EXAFS effectively consisting of the superpostion of just these two oscillations.

With hindsight it can be seen that nickel iodide is an unfortunate choice of model compound, when applying the Fourier-filtering single-shell analysis method to determine the I-Ni distance precisely, since this technique requires that the central iodine and the backscattering nickel atomic phase shifts be obtained as functions of k, very precisely, and hence the presence of the iodine central atom/iodine backscattering atom oscillation in the total EXAFS is unwanted. However, for a fuller structural analysis using a multi-shell modelling method, the strong influence of the iodine backscattering shell to the total EXAFS, is useful as it enables the iodine backscattering atomic phase shifts to be obtained with some reliability.

Now consider the EXAFS resulting form the iodine atoms contained within the surface iodide structure. One point worth mentioning is that iodine is a good adsorbate to study because of its high atomic mass and hence its high X-ray absorption, helping to make the 'signal' component of the X-ray absorption that comes from the few atomic layers of the adsorbate and that contains the EXAFS, significant in comparison to the 'background' absorption by the substrate, that varies smoothly over the energy range of the X-rays. (This signal:background ratio also depends on the surface sensitivity of the detection method.) The EXAFS should appear very similar to that from bulk nickel iodide, except for a few differences.

The relative contribution to the EXAFS from the nearest iodine shell compared to the nearest nickel shell, would be smaller,

since each central iodine atom has 4 nickel and 9 iodine neighbours. The amplitude of the EXAFS caused by backscattering from the iodine atoms in the same hcp plane as the central iodine atom, would vary with the angle of incidence of the plane-polarized X-ray beam upon the layered crystalline surface structure (possibly enabling any differences in the iodine spacing in-plane and between-planes to be resolvable).

The C(2 x 2) LEED pattern determines the $\Theta = {}^{1}/_{2}$ room temperature structure to consist of an overlayer containing iodine atoms in a square mesh of side $\sqrt{2}$ times larger than that of the square mesh of the Ni(100) substrate top layer, and rotated 45^{o} relative to the nickel mesh. The adsorption site is not determined, although by analogy with other halogen adsorbates on single crystal metal surfaces, the hollow site is most likely, two other possible sites being bridge and atop.

The hollow-site structure is shown in Figure 4.05(a), each iodine being bonded to four nickel atoms. For bridge and atop sites, the co-ordination numbers are two and one respectively, hence the EXAFS amplitude should give an indication of the adsorption site. The variation of the EXAFS amplitude as a function of the incidence angle of the X-ray beam, should be particularly useful in the site determination - for the atop site, the amplitude should increase dramatically as the electric vector sweeps from lying parallel to the surface to lying along the surface normal, whereas for the hollow site, the change would be hardly noticeable. The radial distribution functions for iodine atoms in bridge and atop sites are very

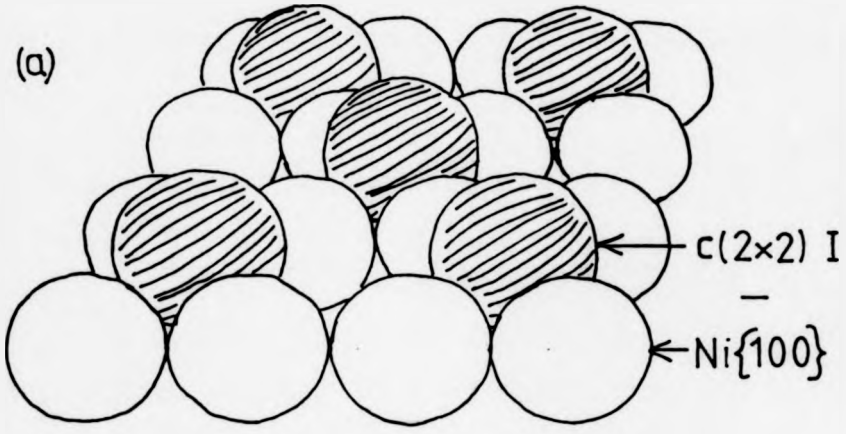

I atoms in hollow sites

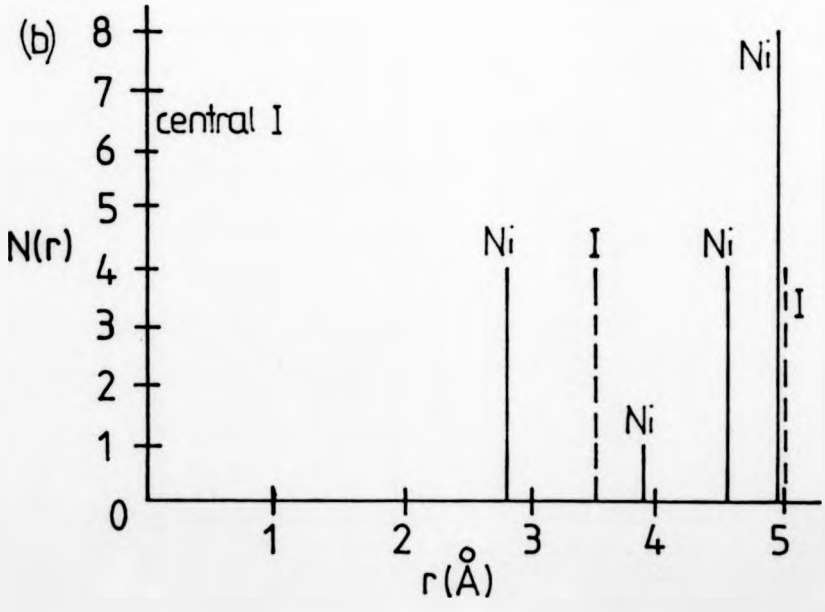

Fig. 4·05 : c(2×2)I-Ni{100} structure for hollow adatom sites.
(a) : I atoms drawn smaller than actual size for clarity.

different from that for the hollow site shown in Figure 4.05(b), and such differences should show up in the relative contributions of the higher shells to the total EXAFS, such contributions also varying differently as functions of the crystal orientation relative to the X-ray beam.

With reasonable SEXAFS data it should be possible to determine the adsorption site and to get an accurate measure of the I-Ni bond length .

At $\theta = {}^{3}/_{8}$, the halogen net is in coincidence with that of the substrate, forming a C(2 x 8) LEED pattern. One possible structure is shown in Figure 4.06, based upon a one-dimensional expansion of the C(2 x 2) overlayer in one <100> direction, such that one third of the atoms lie in hollow sites, and the remaining two-thirds lie near to bridge sites, assuming that the iodine-iodine spacings are maximised (subject to the constraints of equation 4.01).

Such assymetrical sites would greatly affect the EXAFS. For data from $k \approx 4$ Å^{-1} to $k \approx 8$ Å^{-1}, each peak in the Fourier transform modulus due to a single shell of atoms, is broadened by an amount, $\Delta R \approx 0.5$ Å. For hollow, bridge or atop sites, the second shells of nickel atoms lie at distances, $r > 3.7$ Å, such that there is negligible overlap with the main peak, due to $r \approx 2.8$ Å. For the postulated C(2 x 8) structure, however, the second nickel peak lies at $r \approx 3.4$ ($\pm$ 0.5)Å, which would overlap with the main peak at 2.8 ($\pm$ 0.5)Å. This would cause problems with the filtering-out of the main peak, which is necessary to obtain the phase function, and would therefore show up as a broad assymetrical peak in the Fourier transform, and as a phase function with a large amount of curvature, causing problems with an accurate determination of the I-Ni bond length, when using the Fourier-filtering single shell analysis method.

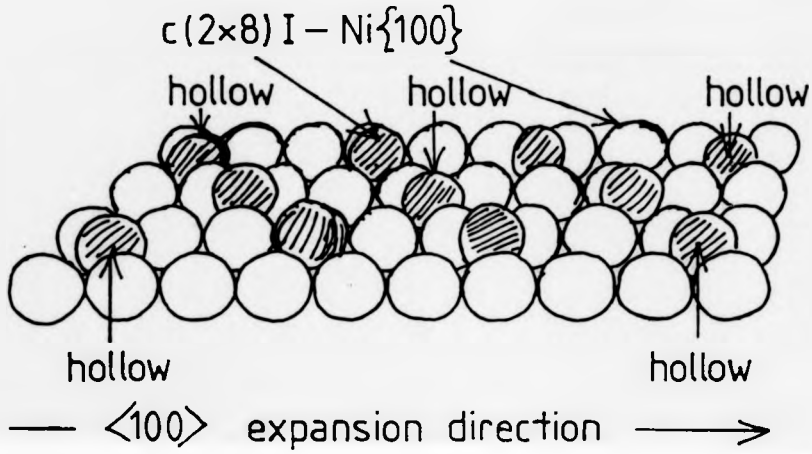

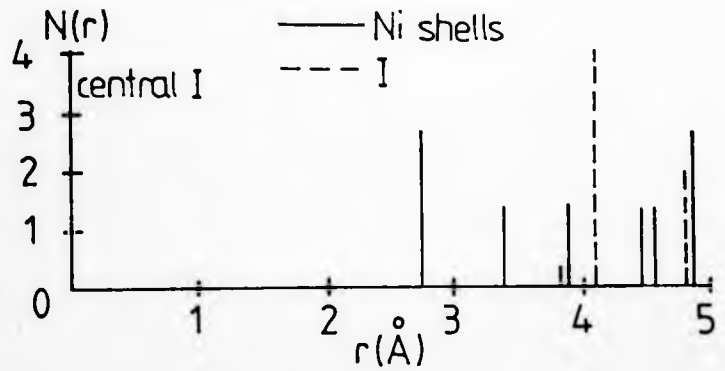

Fig. 4·06: (a): Postulated $\theta = 3/8$ c(2×8)I-Ni{100} structure.
(b): Average radial distribution function

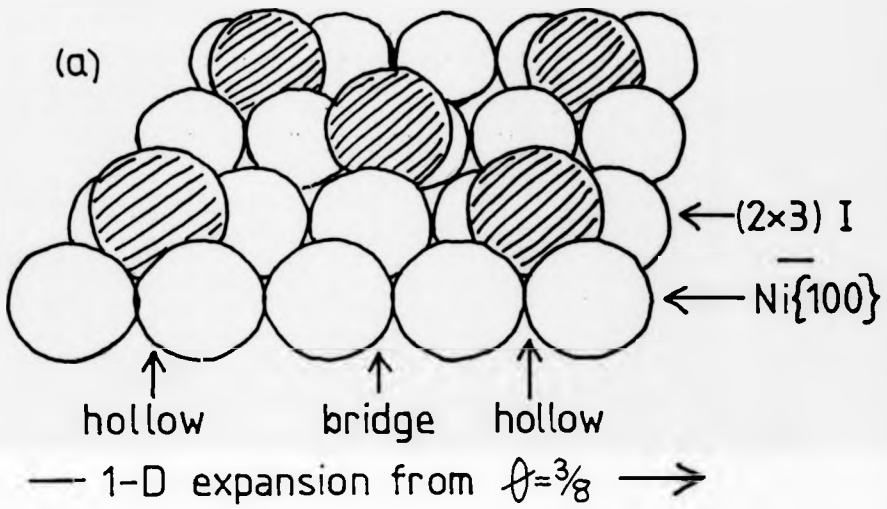

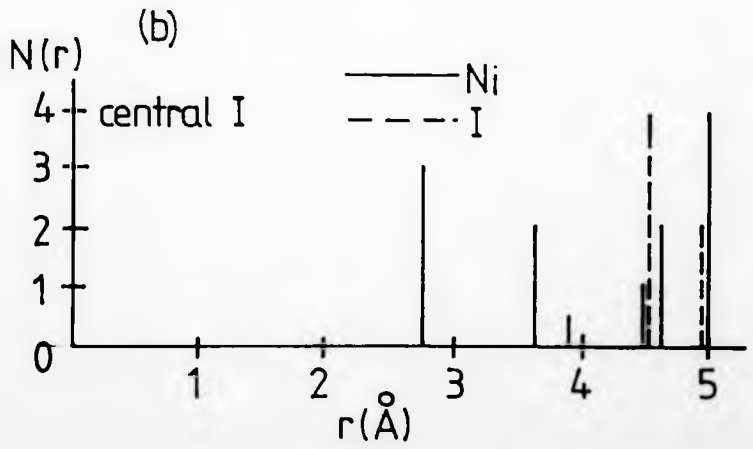

Fig. 4·07: Postulated $\theta=1/3$ (2×3)I–Ni{100} structure
(b): Average I enviroment – bridge and hollow sites

At $\Theta = {}^{1}/_{3}$, a well defined structure can be observed, being characterised by a (2 x 3) LEED pattern; at lower coverages the iodine atoms disperse into an incommensurate hcp overlayer. Starting with a $\Theta = {}^{1}/_{2}$ overlayer with the iodine atoms in hollows, a one-dimensional expansion along a <100> vector, produces the $\Theta = {}^{1}/_{3}$ overlayer shown in Figure 4.07, at which point half the adatoms are in hollows and half in bridge sites; exactly the same structure is reached from bridge sites, but starting with atop sites, the $\Theta = {}^{1}/_{3}$ structure would consist of equal numbers of iodine atoms in atop and bridge sites. It should be possible to get some idea of the average effective coordination number from analyses of SEXAFS spectra, perhaps taken at various angles of incidence of the X-ray beam, and it should also be possible to get a value for the average I-Ni bond length.

4.04 The Surface Structures Formed by the Adsorption of Chlorine onto a Cu(111) Surface and Bulk CuCl

Chlorine molecules adsorb dissociatively onto Cu(111) (see Figure 1.01), the resulting Cl-Cu chemical bond being predominantly covalent in nature[8, 9], such that the chlorine adatoms have approximately their atomic radii, forming a stable coverage at $\Theta = 0.33$, at whiich point a $(\sqrt{3} \times \sqrt{3})R30^{o}$ LEED pattern can be observed. Further chlorine adsorption causes a compression of this hexagonal close packed overlayer, such that in general the overlayer is incommensurate with the substrate (111) surface, but passes through a series of well ordered phases[10], as the coverage increases, up to $\Theta = 0.45$, where a $(6\sqrt{3} \times 6\sqrt{3})R30^{o}$ LEED pattern can be seen. Figure 4.08 shows the LEED patterns.

For the C(2 x 2) Cl-Cu(100) adsorption system, the chlorine atoms have been shown to reside in the hollow adsorption sites, the Cl-Cu chemical bond length being 2.39 ($\pm$ 0.03)$\mathring{A}$[11, 12]. Using the

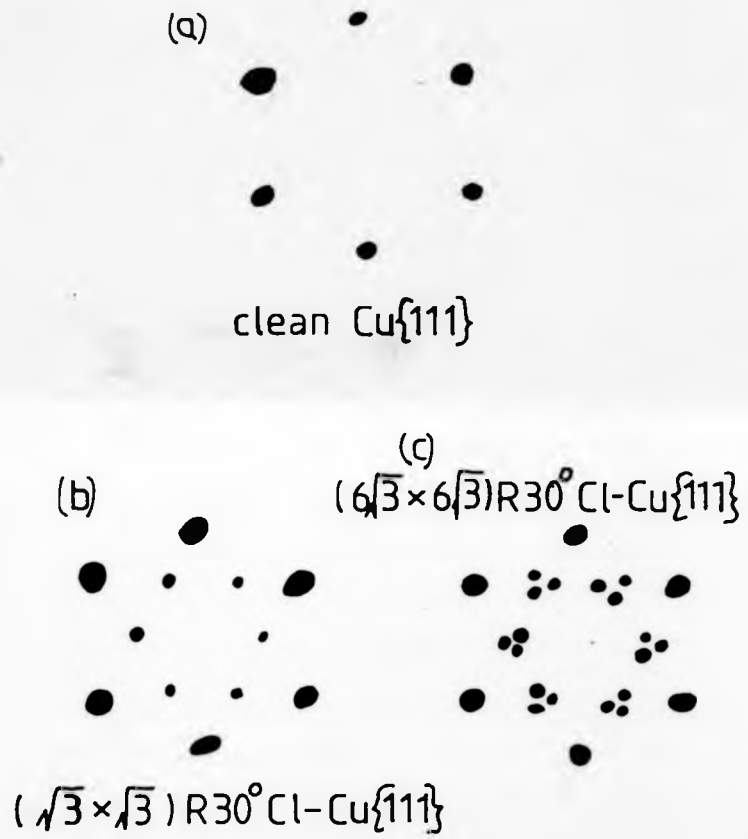

Fig. 4·08: LEED patterns - extra spots in (b) and (c) are due to electron scattering from Cl atoms.

analogy of the chlorine adatoms being in the adsorption site with the highest co-ordination number, then they would reside in the hollow sites on the Cu(111) surface, the ($\sqrt{3}$ x $\sqrt{3}$)R30^{o} Cl-Cu(111) structure then being as shown in Figure 4.09(a). The radial distribution function for a chlorine atom situated in such a structure is shown in Figure 4.09(b) - this local environment would be very different if each chlorine atom was in a bridge, an atop, or any other adsorption site, and this should enable the EXAFS to distinguish between these postulated sites.

A proposed real space structure corresponding to the ($6\sqrt{3}$ x $6\sqrt{3}$)R30^{o} LEED pattern and to Θ = 0.45, is shown in Figure 4.10(a)[10],. This structure can be thought of as being reached by compressing the Θ = 0.33 chlorine overlayer along two directions orientated at 60^{o} to each other as shown in Figure 4.10(a). At Θ = 0.45, the overlayer mesh is commensurate with that of the top layer of copper atoms, the unit cell of the chlorine atoms being a rhombus having sides $6\sqrt{3}$ times larger than those of the copper unit cell rhombus, and being rotated by 30^{o} relative to the substrate mesh. Since there are two other sets of compression directions, the surface would consist of domains of these three orientations, leading to the splitting of the overlayer LEED spots as is observed. (Figure 4.08(c)). (Other explanations such as double diffraction have been put forward to explain this LEED pattern.) At this coverage, the chlorine atoms must lie in a variety of adsorption sites, these being approximated by 2 hollow: 1 bridge: 1 atop - this is independent of the adsorption sites for the Θ = 0.33 overlayer, the predominance of chlorine atoms lying near hollows arises from the geometry of the hcp

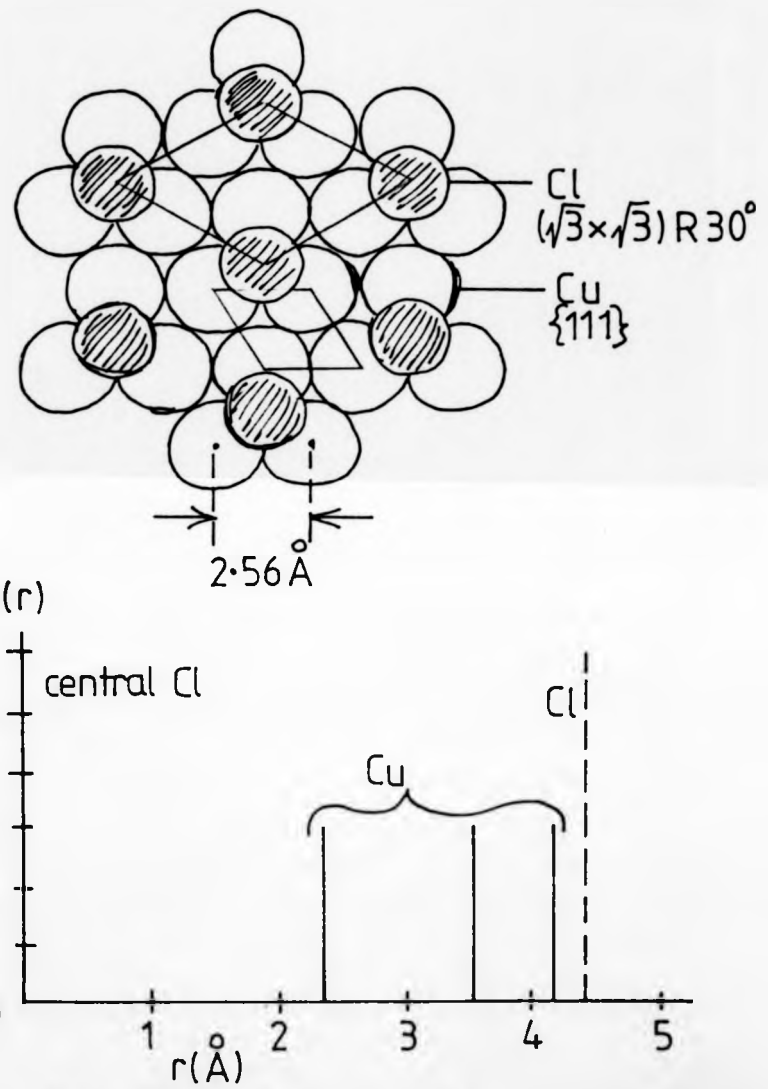

Fig. 4·09 : $\theta = 1/3$ $(\sqrt{3}\times\sqrt{3})R30°$ Cl-Cu{111}, assuming hollow adatom sites.

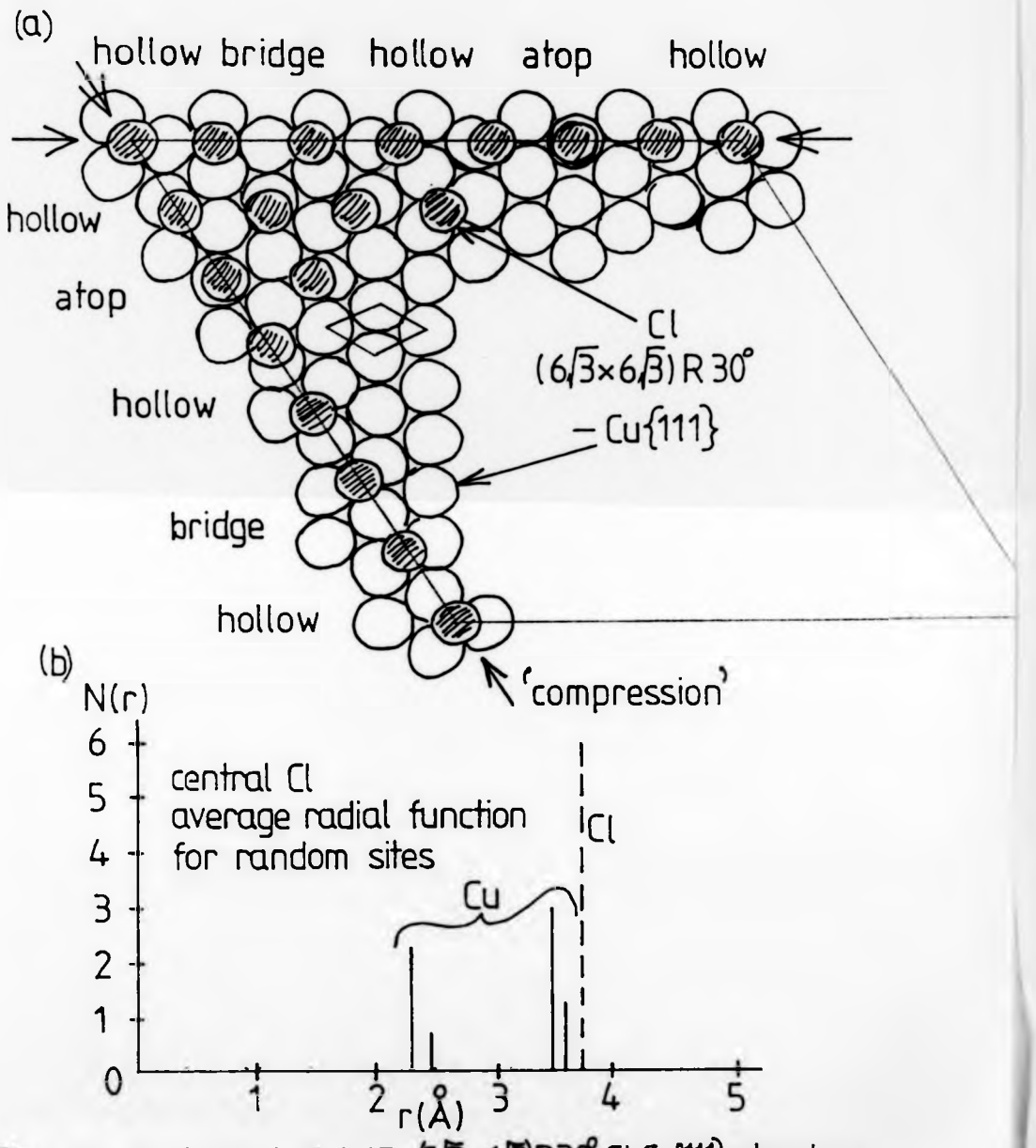

Fig. 4·10 : Postulated $\theta = 0{\cdot}45$ $(6\sqrt{3}\times 6\sqrt{3})R30°$ Cl-Cu{111} structure can be visualised - (a) - as being formed by a compression of the $\theta = \frac{1}{3}$ overlayer.

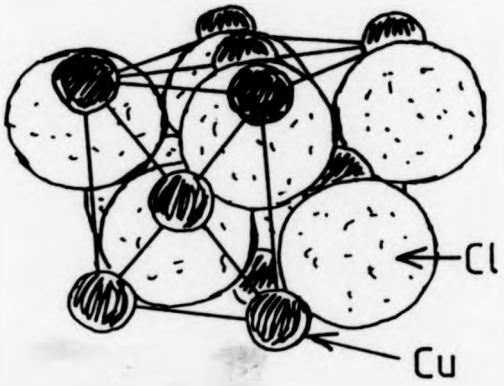

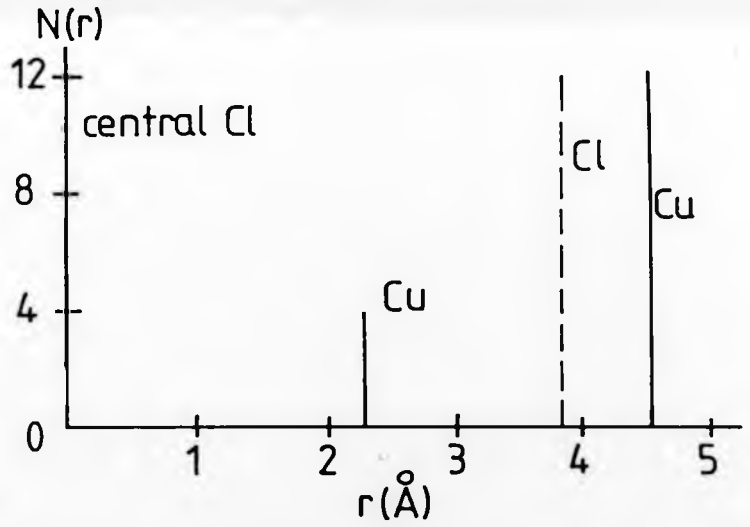

Fig. 4·11: Bulk CuCl structure

surface. The average radial distribution function for a central chlorine atom is shown in Figure 4.10(b); the average co-ordination number being 2.25 (there being 3 nearest neighbours for those atoms in hollow sites, 2 for bridges, and 1 for atop).

Bulk copper chloride(CuCl) having the structure shown in Figure 4.11[3], was used in the SEXAFS work as a reference compound, in order to determine the atomic phase shifts.

4.05 Sample Preparation

The two surface structures studied by SEXAFS, were prepared by exposing a clean Cu(111) surface in UHV, to a flux of chlorine molecules from an electrochemical source. LEED was used to check the cleanliness and ordering of the initial surface, and to observe the onset of the $(\sqrt{3} \times \sqrt{3})R30^{o}$ and of the $(6\sqrt{3} \times 6\sqrt{3})R30^{o}$ structures, the latter being formed by a longer exposure to chlorine molecules (- $^{1}/_{2}$ hour), it being possible to revert to the former by heating to 250°C; heating to 500°C caused a complete desorption of the chlorine adatoms, but at room temperature, both coverages remained stable for many hours.

The bulk copper chloride (CuCl) sample was prepared by compressing copper chloride powder into a disc shaped pellet, about 1 cm in diameter, and a few mm thick. This was mounted on the crystal manipulator and placed in the SEXAFS data collection chamber.

4.06 Information to be gained from SEXAFS Spectra of Cl-Cu(111)

It can be expected that the EXAFS from bulk CuCl, be dominated by a single oscillation resulting from the backscattering of the photo-electrons from the nearest shell of copper atoms; the second shell contains the much lighter chlorine atoms at a significantly larger distance, thus producing a smaller oscillation

of a smaller period in k-space. The Fourier transform modulus should therefore be dominated by a single peak at an R-value corresponding to the copper shell, which could be filtered out easily, allowing an accurate estimation of the sum of the central chlorine and backscattering copper atomic phase-shifts as functions of k.

This would give the potential for accurate determinations of the Cl-Cu bond lengths in the two surface structures studied, since the EXAFS spectra would predominantly arise from electron backscattering from copper atoms.

It should be possible to determine the adsorption site in the $\Theta = {}^{1}/_{3}$ overlayer - for a hollow site, the EXAFS would consist of a single oscillation of a large amplitude, each chlorine atom being co-ordinated to three copper atoms; for bridge and atop sites the main oscillation would be increasingly smaller in amplitude, and the effects of the next nearest copper shells would become more important.

It can be expected that such differences between sites would show up in the absolute EXAFS amplitude, and the EXAFS amplitude as a function of the angle of incidence of the plane-polarized X-ray beam.

Since electron scattering by chlorine atoms is a relatively small effect, little information of the Cl-Cl spacings could be extracted from the data analysis; this is not important since the chlorine overlayer structure is itself derived from the LEED pattern fairly reliably.

It can be anticipated that SEXAFS analyses could confirm the postulated $\Theta = 0.45$ structure, and determine the average Cl-Cu distance with good accuracy.

4.07 References

1. R G Jones and D P Woodruff, Vacuum 31 (10–12), 1981, p 411
'The adsorption of I_2 on Ni(100) studied by AES, LEED and thermal desorption'.

2. R F Rolsten 'Iodide Metals and Metal Iodides'
John Wiley and Sons, 1961, Chapter 8, section D: NiI_2.

3. R W G Wyckoff, 'Crystal Structures', volume 1, 2nd edition, 1965
Chapter 2: Structures of the Elements: II, a: cubic close packing, including metallic nickel and copper
p270: IV, c2: Cadmium chloride arrangement, including NiI_2
p108: III, c1: Zinc sulphide arrangement, including CuCl.

4. R G Jones, C F McConville, and D P Woodruff, Surf Sci 127 ('83), p 424
'Formation of a surface iodide on Ni(100) and adsorption of I_2 at low temperatures'.

5. C Benndorf and B Krüger, Surf Sci 151 ('85) p 271
'Adsorption and reaction of bromine with Ag(110)'.

6. C Somerton, C F McConville and D P Woodruff, Surf Sci 136 ('84) p 23
'Core level photoemission study of adsorption of iodine on Ni(100)'.

7. An estimation of the relative amplitudes of the contributions to the total EXAFS of bulk NiI_2, from the nearest nickel and iodine shells around a central iodine:

$$\frac{\text{Amplitude Ni}}{\text{Amplitude I}} \approx \frac{N(Ni)}{N(I)} \cdot \frac{F(k)Ni}{F(k)I} \cdot \frac{(r_I)^2}{(r_{Ni})^2} \cdot \frac{e^{-2r_{Ni}/\lambda}}{e^{-2r_I/\lambda}} \cdot \frac{e^{2\sigma_{Ni}^2 k^2}}{e^{-2\sigma_I^2 k^2}}$$

$$\approx \frac{3}{12} \cdot \frac{0.6\text{Å}}{0.6\text{Å}} \cdot \frac{15.4\text{Å}^2}{7.73\text{Å}^2} \cdot \frac{0.25}{0.14} \cdot \frac{0.70}{0.34} \qquad \text{for } k = 6\text{Å}^{-1},\ \lambda \approx 4\text{Å}.$$

$$\approx 0.25 \cdot 1 \cdot 2.0 \cdot 1.7 \cdot 2.1$$

$$\approx 1.8$$

8. D Westphal and A Goldmann, Surf Sci 131 ('83) p 113
'Chlorine adsorption on copper, II:
Photoemission from Cu(001) C(2 x 2) - Cl and
Cu(111) ($\sqrt{3}$ x 3)R30°-Cl'

9. Periodic Table of the Elements
Sargent-Welch Scientific Company, Illinois, USA,
catalogue number S-18806 side 2:
Chlorine atomic radius = 0.99 Å, ionic(-1) radius = 1.81 Å.
Pauling's electronegativities imply that the Cl-Cu bond is 26% ionic, suggesting a chlorine radius $\approx$ 1.20 Å.
In metallic copper, the atomic radius of copper is 1.28 Å.
Addition of these two values suggests a Cl-Cu bond length of approximately 2.48 Å for chlorine adatoms on the surface of metallic copper.

10. P J Goddard and R M Lambert, Surf Sci 67 ('77) p 180
'Adsorption-desorption properties and surface structural chemistry of chlorine on Cu(111) and Ag(111)'.

11. P H Citrin, D R Hamann, L F Mattheiss and J E Rowe, Phys Rev Lett 49(23), December 1982, p 1712
'Geometry and Electronic Structure of Cl on the Cu(001) surface'
A measurement of the Cl-Cu bond length is quoted as 2.37 (± 0.02)Å.

12. F Jona, D Westphal , A Goldmann and P M Marcus,
Journal of Physics C (Solid State Physics), 16, ('83), p.3001 :
'LEED structure determination of Cl on Cu (100)'.
Quotes the results:-

(i) Cu-Cl = 2.41(± 0.02)Å, deduced from the Cl-Cu layer separation of 1.60 (± 0.03)Å with chlorine adatoms residing in hollow sites.

(ii) The top Cu layer is slightly expanded compared to the bulk structure, such that the surface copper atoms have radii $\gtrsim$ 1.3Å.
Combination of these two results, suggests that the chlorine radius $\approx$ 1.1Å.

CHAPTER 5

DATA ANALYSIS BY THE FOURIER-FILTERING SINGLE-SHELL METHOD

5.01 OVERVIEW

This chapter describes the analysis method consisting of Fourier-filtering the EXAFS originating from a single-shell of atoms, which enables the atomic phase shifts to be obtained from a model compound, and the shell distance and number of backscatterers for an unknown compound[1]. For SEXAFS work, the limitations of the data are such that usually only the nearest shell is clearly visible in the Fourier transform, such that it is the bond length and co-ordination number that can be derived. Throughout most of the outline, I-Ni(100) datasets are used as examples, but the chapter also serves as a general description of the method applied to any SEXAFS data.

The main steps in the analysis procedure are:-

(i) background subtraction;

(ii) μo estimation;

(iii) Eo and ΔEo choices;

(iv) choice of multiplier: k, k^2 or k^3;

(v) Fourier transform;

(vi) windowing and inverse Fourier transform

(vii) phase function derivation;

(viii) determination of atomic phase shifts from model compound;

(ix) transfer of phase shifts to derive shell distance for unknown compound;

(x) amplitude functions to derive number of atoms in shell.

The typical reliability of an amplitude function, and hence the accuracy of the determination of the number of atoms in the backscattering shell, is generally accepted to be fairly poor. By contrast, exceptionally accurate shell distances are sometimes

reported, but it should be remembered that this accuracy is severely limited by a short k-range of the EXAFS, producing a large amount of curvature in the phase function.

5.02 Background Subtraction and μo Estimation

A typical SEXAFS spectrum is shown in Figure 5.01, this being the normalised electron yield from a bulk NiI_2 sample as a function of the X-ray energy around the iodine L_{III} absorption edge region. The spectrum is self-calibrated, ie the L_{III} and L_{II} edges are set to energies of 4557 and 4852 eV respectively and the energies of the other data points are obtained by linear interpolation and extrapolation (this is more accurate than relying on the monochromator angular settings).

It is first necessary to subtract the background absorption, to obtain a measure of the absorption due to the edge of interest. In this example, this is the L_{III} edge, but the procedure applies equally well to the K, L_I and L_{II} edges. The procedure adopted at Warwick University is to use a straight line (in energy space) that passes through the base of the edge jump, and that is parallel to the least-squares-fit straight line passing through the data points between $h\nu_{min}$ and $h\nu_{max}$ choosen to span the range of the EXAFS. Due to experimental factors the background is not a simple extrapolation of the pre-edge function, such that a straight line is a reasonable estimate.

The background subtracted absorption coefficient above the iodine L_{III} edge for bulk NiI_2 is shown in Figure 5.02.

At this point it is necessary to make an estimate of μ_o, the absorption coefficient of isolated atoms, therefore containing no EXAFS. This can be done by fitting a stiff spline[2] to the data. The stiffness parameter needs to be adjusted, such that the spline follows the broad curvature of the data without response to the EXAFS

REPRODUCED
FROM THE
BEST
AVAILABLE
COPY

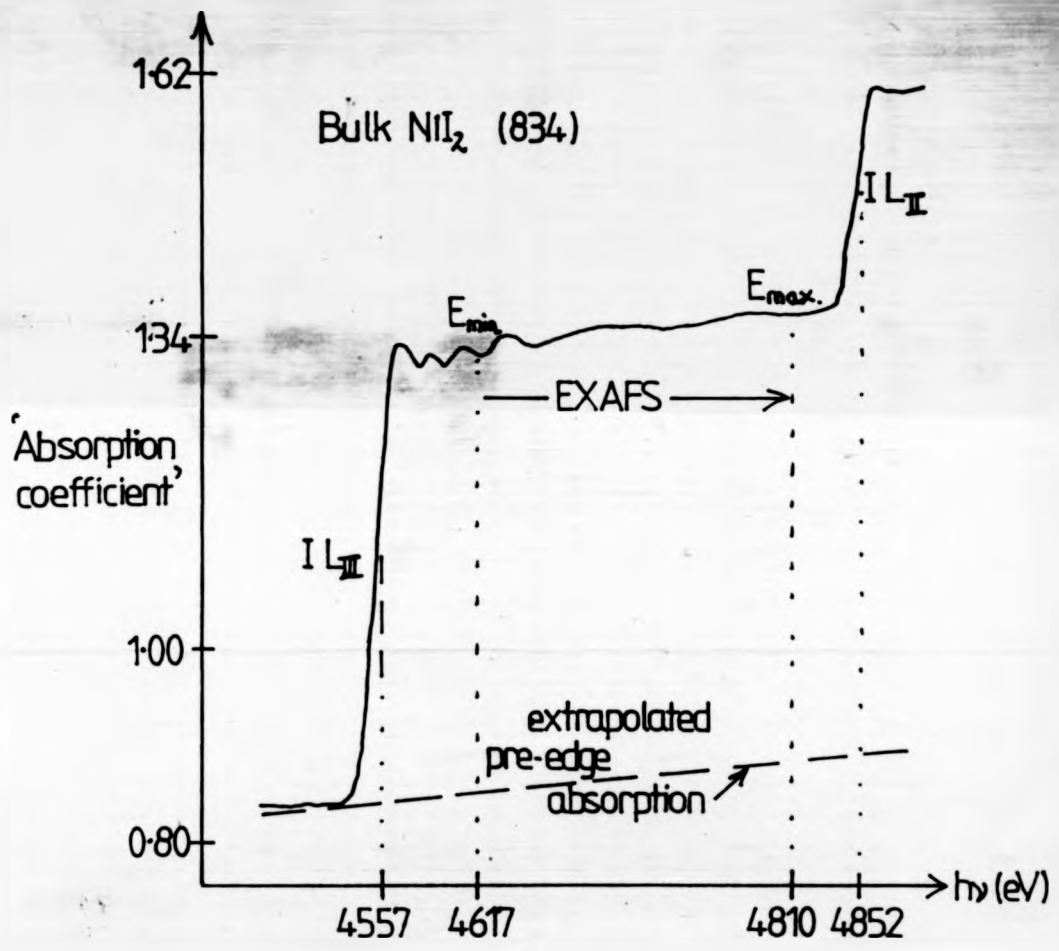

Fig. 5·01: A measure of the X-ray absorption coefficient over an energy range containing EXAFS.

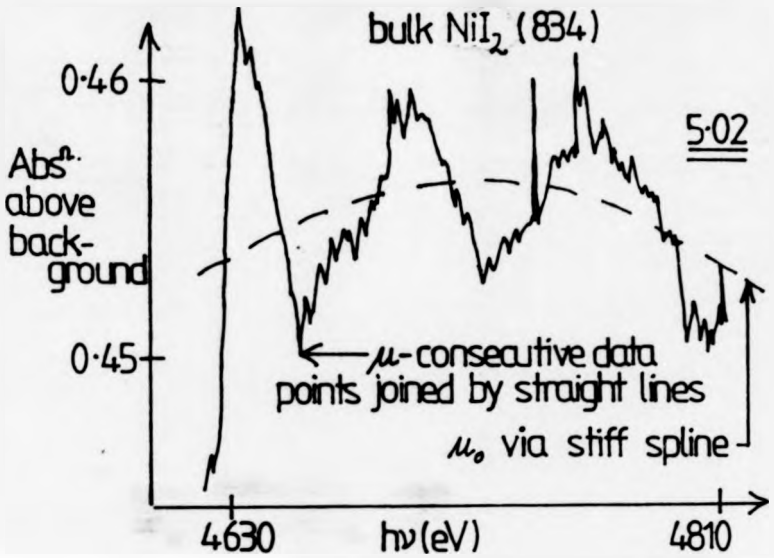

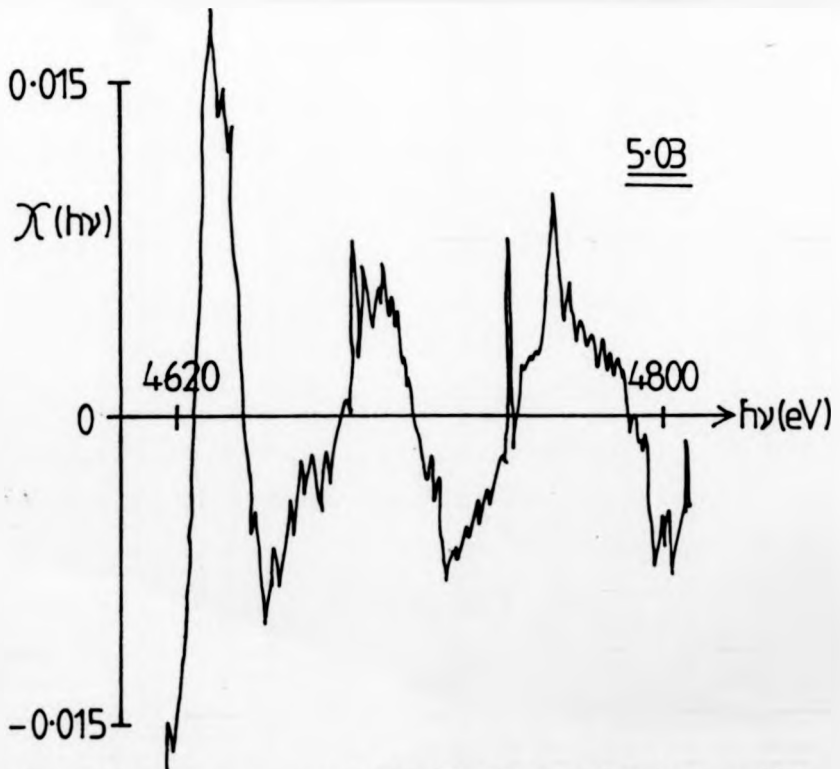

Figs. 5·02,3 : μ, μ_0 and the EXAFS as functions of $h\nu$.

oscillations, and therefore represents μo , as shown by the dashed line in Figure 5.02. The spline routine is described in more detail in section 8.05.

The fine structure is obtained from the calculation of $(\mu-\mu o)/\mu o$ at each energy datum. Inspection of this structure (for the example of NiI_2, see Figure 5.03), in particular a comparison of the relative extents of the positive and negative excursions, must be used to check on the validity of the μo estimation.

5.03 The Choice of Eo Required for the Conversion of $\chi(h\nu)$ to $\chi(k)$

In order to convert the EXAFS from a function of the X-ray energy into a function of the photo-electron energy, $(h\nu-Eo)$, or of the photo-electron wave-vector, k, it is necessary to identify the point in the spectrum at which k is equal to zero, ie the Eo value, as in equations 2.04 and 2.05. This point is within a few eV of the absorption edge. For the example described in Figure 2.03, this point is 4 eV above the absorption edge, since argon is a monatomic gas such that the photo-electron has to be excited to above the vacuum level in order to travel to a backscattering atomic neighbour.

For metals[3,4], and diatomic gases[5], the Eo point is E_F below the edge, E_F being the Fermi energy, typically a few eV. In such materials the onset of an increase in the X-ray absorption occurs when electrons are excited to the lowest energy level, which is that just above the Fermi level, but at this point the electrons have a translational kinetic energy of E_F within the inner potential. See Figure 5.04.

Tabulated binding energies are referenced to the Fermi level, so estimations of E_F are needed to reference the photo-electron energy to the correct point. For the example of the iodine L_{III} edge, the binding energy of the L_{III}level is known to be

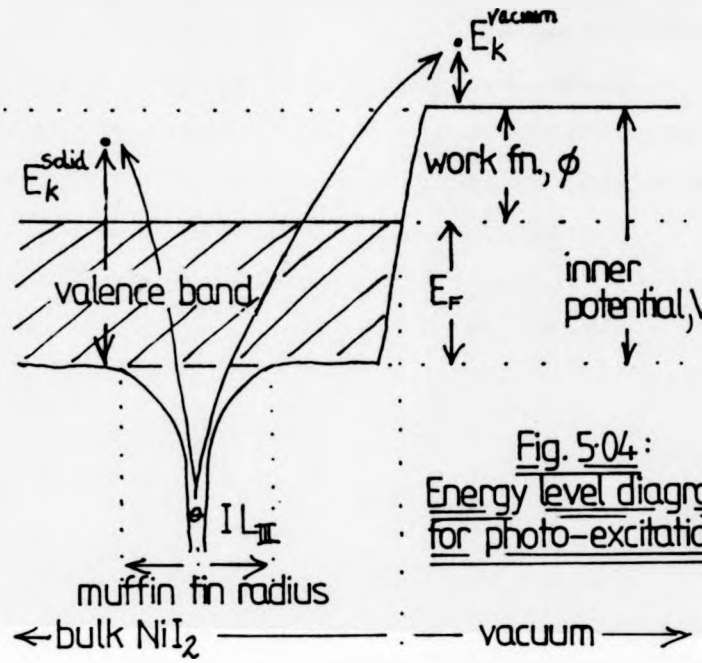

Fig. 5·04: Energy level diagram for photo-excitation

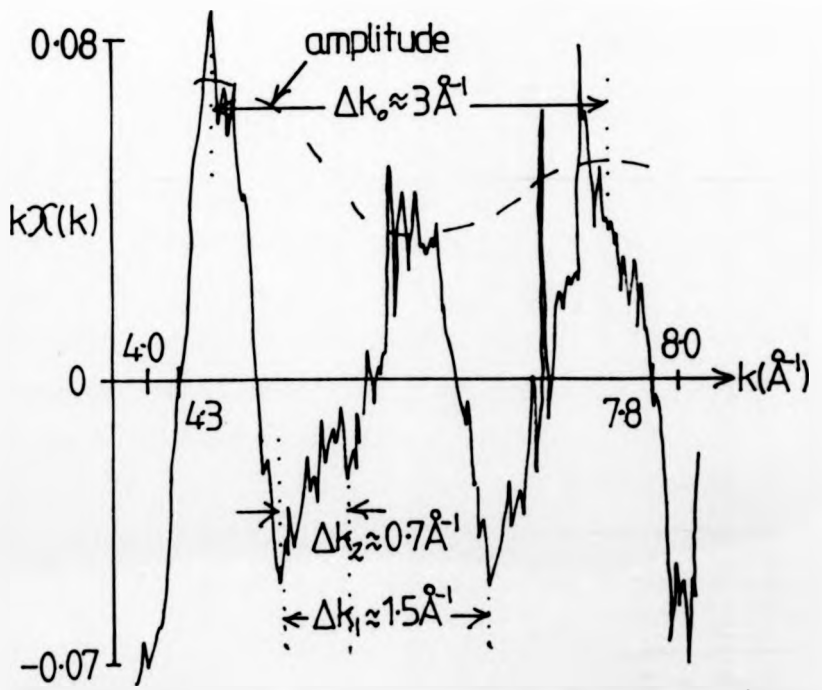

Fig. 5·05: Periodic oscillations in an EXAFS spectrum.

4557 eV[6], and E_F can be estimated to be around 4 eV[7], such that Eo = 4553 eV. However, unless there is a distinguishing feature in the absorption spectrum[8], there remains an uncertainty in Eo, so it is commonplace to treat it as a variable parameter[9]. This procedure is adopted in the examples given in this chapter; the methods by which Eo is selected, are explained in the appropriate section. When comparing EXAFS spectra of two similar compounds it is the difference in the Eo values, ie ΔEo, that is of greatest importance in deriving the difference in the bond length[10].

5.04 $k^n\chi(k)$; n = 0, 1, 2 or 3

In order to be able to see the EXAFS oscillations throughout the entire k-range of the spectrum, it is necessary to increase the amplitude of the high k data relative to that at low k, since the EXAFS amplitude falls off strongly as a function of k, due to the nature of the electron backscattering factors, the Debye-Waller term, and the $^1/k$ term in the EXAFS equation (see equation 2.08). In bulk EXAFS work, data is often available up to k ≈ 15 $\mathring{A}^{-1}$, such that multipliers of k^2 or k^3 are often employed. For surface EXAFS work the data is rarely so extensive. For the example of the iodine L_{III}-edge EXAFS, the onset of the L_{II}-edge, restricts the data to below k ≈ 8 $\mathring{A}^{-1}$, such that a multiplier of k^1 is sufficient to bring the three EXAFS peaks to roughly the same size - see Figure 5.05.

Some information can be obtained by looking at the EXAFS spectrum at this point. Central atomic phase shifts are known to be approximately linear functions of k, having significant negative gradients[11], backscattering phase shifts each have a much smaller variation in value over similar k-ranges. The sum of the atomic phase shifts for any pair of atoms, can therefore be approximated by a straight line in k-space of n gative gradient (typically around -0.6 radians/$\mathring{A}^{-1}$), as in equation 5.01.

$$\phi(k) \simeq a - bk;\ b \approx 0.6 \text{ radians/}\mathring{A}^{-1} \quad \ldots (5.01)$$

The EXAFS from a single shell of backscattering atoms, at a distance of r_i from the central absorbing atom, consists of a sinusoidal oscillation - equation 5.02 - with a period in k-space given by equation 5.03.

$$\chi_i(k) \propto \sin(2kr_i + \phi(k)) \equiv \sin\{k(2r_i - b) + a\} \quad \ldots (5.02)$$

$$\Delta k_i \approx \frac{2\pi}{(2r_i - b)} \quad \ldots (5.03)$$

The main oscillation in Figure 5.05, for example, results from backscattering from the nearest shell of nickel atoms around each iodine atom, within bulk NiI_2, and can be seen to have a period, $\Delta k_i = 1.5\ (\pm\ 0.5)\ \mathring{A}^{-1}$, and hence $R_i = (2r_i - b) = 4(\pm\ 1)\ \mathring{A}$.

For a model compound r_i is known, and the R_i value is necessary to obtain an estimate of b; for an unknown structure involving the same atomic pairs, r_i could then be derived from a measurement of R_i from the EXAFS of this unknown structure.

The R-value of an oscillation can be thought of as its 'frequency'. This notation may seem unfamiliar, but it is possible to Fourier transform the data in k-space to get a function F(R) - the 'frequency' spectrum; whereas usually a function in the time domain is Fourier transformed to get the frequency (measured in radians per second or Hertz); however, the mathematics is identical and the procedure is analogous.

It is necessary at this stage of the analysis, to separate out the components due to different shells enabling more precise measurements of their 'frequency' and amplitude to be made - each of these values containing information on the number and distance of atoms within each shell.

Looking at Figure 5.05, it can be anticipated that the Fourier transform would contain a large amplitude at the 'frequency'

of 4 Å, and would also contain significant 'frequency' components at 2Å (arising from the amplitude modulation, having period, $\Delta k_2 \approx 3$ Å^{-1}), at around 8 Å (arising from the amplitude modulation, having period, $\Delta k_1 \approx 0.75$ Å^{-1}, this being attributed to the iodine-iodine distance), and at higher 'frequencies' (resulting from the statistical fluctuations in the EXAFS measurements from one point to another). A significant peak in the modulus of the Fourier transform at 0Å, would indicate that the derived EXAFS function does not oscillate about the zero line, but is in fact offset (either to predominantly positive or negative regions), indicating that the μo estimation is unsatisfactory.

5.05 The Fourier Transform

A Fourier transform modulus is simply a plot of the amplitudes of the frequencies needed to build up an anharmonic waveform[12]. Any function, such as $\chi(k)$ can be built up from an infinite series of sine and cosine waves, of various (frequencies), as in equation 5.04.

$$\chi(k) = \frac{1}{\pi}\int_0^\infty A(R)\cos kR\,dR + \frac{1}{\pi}\int_0^\infty B(R)\sin kR\,dR \qquad \ldots (5.04)$$

where: $A(R) = \int_{-\infty}^{\infty} \chi(k)\cos kR\,dk$; THE FOURIER COSINE TRANSFORM ... (5.04a)

and: $B(R) = \int_{-\infty}^{\infty} \chi(k)\sin kR\,dk$; THE FOURIER SINE TRANSFORM ... (5.04b)

Alternatively, this Fourier analysis can be expressed in a complex representation as in equation 5.05:

$$\chi(k) = \frac{1}{2\pi}\int_{-\infty}^{\infty} F(R)\,e^{-ikR}dR \qquad \ldots (5.05)$$

where $F(R) = \int_{-\infty}^{\infty} \chi(k)\,e^{ikR}dk$; THE COMPLEX FOURIER TRANSFORM

With regard to an EXAFS $\chi(k)$, the 'radial function', F(R), is obtained by a Fourier transform, this complex function containing a real part, A(R), indicating the amplitudes of the cosine waves contained in $\chi(k)$, and an imaginary part, B(R), for the sine wave amplitudes. The modulus of F(R) gives the 'frequency'' spectrum, the variable R being equivalent to the variable (2r-b). See equation 5.06.

$$F(R) = A(R) + i\,B(R) \qquad \ldots (5.06)$$

$$|F(R)| = \sqrt{A(R)^2 + B(R)^2} \qquad \ldots (5.06a)$$

Since the EXAFS function is dependent upon sine terms, the sine transform should give the 'frequencies' of each oscillation, ie the R-values of the shells of atoms, the amplitudes of which are dependent upon a number of factors. However, an incorrect choice of Eo shifts the EXAFS in k-space, such that it can no longer be described by sine waves. For this reason the modulus of the complex Fourier transform is required, peaking at the R-values of the atomic shells (and at other 'frequencies' that are contained within the EXAFS). Only for the correct choice of Eo, does the imaginary component of the transform, peak at the same R-value as the modulus[13,14].

In order to eliminate misleading 'frequencies' being introduced, the Fourier transform should be performed from k_{min} to k_{max} values, where the EXAFS function is near zero - see Figure 5.05 for the example of a SEXAFS spectrum. For bulk EXAFS in which a large k-range is available, a better procedure is to multiply the EXAFS by a 'windowing function' that has an amplitude of unity near the centre of the data, decaying smoothly to zero at the ends of the data. The truncation method applied to the SEXAFS spectrum makes no

assumption as to the periodicities of the function to higher and lower k-ranges, but effectively sets the function to zero outside the range k_{min} to k_{max}, having the same effect as using a square multiplying function[15].

The Fourier transform algorithm (equation 5.07) applied to the data shown in Figure 5.05, produces a complex Fourier transform, the modulus and positive part of the imaginary component being shown in Figure 5.06.

$$F(R_i) = \sum_{j=2}^{n-1} k_j \chi(k_j)\, e^{-ik_jR_i}\, \frac{k_{j+1}-k_{j-1}}{2} \qquad \ldots (5.07)$$

Equation 5.07, is fundamentally the same as equation 5.05(a), a multiplying factor of k being applied.

The Fourier transform modulus needs to be interpreted with care. If the EXAFS data is of very good quality, ie extending over a large k-range (up to - 15 $\mathring{A}^{-1}$), having very little point-to-point scatter, and very good background subtraction and μo estimation, then the 'frequency' spectrum can be interpreted as being approximately equal to the radial distribution function of shells around the central absorbing atoms, multiplied by terms falling rapidly with radial distance.

In bulk EXAFS this is often valid - each peak can be attributed to a shell of atoms - if the R-value is halved it can be seen to be a few tenths of $\mathring{A}$ smaller than the r-value (the radial distance of the backscattering shell), this shift being due to the negative gradient in k-space of the atomic phase shifts. The amplitude of each peak falls rapidly with distance, such that for shells of r-values greater than around 5 $\mathring{A}$, their peaks are often smaller than the 'noise' peaks.

The relatively poor quality of data that can be obtained in surface EXAFS work, means that often only the first shell of atoms

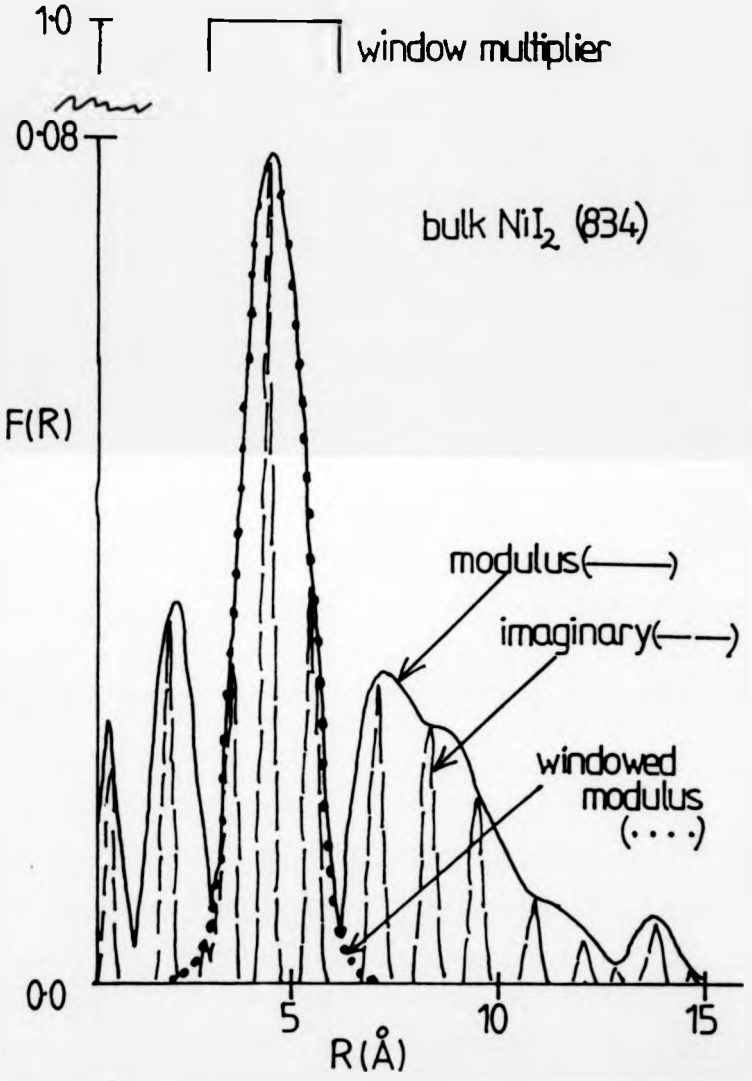

Fig.5-06: Fourier transform of an EXAFS spectrum.

gives rise to a clearly resolvable peak . For the example of bulk NiI_2, shown in Figure 5.06, this is the case. The main peak at $R \approx 4.4$ Å is due to the nickel neighbours at $r = 2.78$ Å[16]. Other peaks visible, include that at $R \approx 2.2$ Å being due to a side band of the main peak[12] and due to the amplitude modulation 'frequency' (see Figure 5.05); that at $R = 0$ Å due to the sharp truncation of the short data range, it being possible to minimise the amplitude of this peak by ensuring that the μo estimation produces equal positive and negative excursions in the EXAFS. Peaks at higher R-values in Figure 5.06 are due to the side bands of the main peak and to point-to-point deviations in the data, which to a large extent obscure the peaks due to more distant atomic shells, as is typical in SEXAFS data.

The large width in R-space of the main peak is mainly due to the short data range (such a k-range can be shown to produce a broadening of $\Delta R \approx 0.5$ Å[15]), which, along with the broadenings due to 'noise', imperfect background subtractions and the effects of more distant shells, is convoluted with the inherent width of the main peak, due to the non-linearity of the atomic phase shifts over the k-range of the data.

A general implication for SEXAFS analyses, is that for two shells to be clearly resolvable in the modulus Fourier transform of a spectrum up to $k \approx 10$ Å^{-1}, the radial distances need to differ by $\Delta r \approx 0.3 - 0.4$ Å[17].

The width of the main peak prevents an accurate determination of its position, authors typically quoting errors of ± 0.5 Å in R-space. This means that if the data is that of a model compound, then an accurate value of b (the gradient in k-space of the atomic phase shifts) cannot be obtained, and if the data is that of an unknown

compound, then an accurate determination of the bond length is not possible. For the example of bulk NiI_2, $R_1 \approx 4.4\ (\pm\ 0.3)\mathring{A}$. Further steps in the analysis procedure are therefore necessary, and are described below.

5.06 The Window Function and the Inverse Fourier Transform

Generally in surface EXAFS it is wished to obtain accurate information on the first shell of atoms, namely the bond length and the co-ordination number; for bulk EXAFS more distant shells may be resolvable. In either case, if a single peak in the modulus Fourier transform can be isolated, then the imaginary and real components of the Fourier transform within the range of this peak, can be used to generate the EXAFS from this single shell, (via an inverse Fourier transform) enabling accurate deductions to be made.

Multiplying the Fourier transform by a window function can be used to isolate a single shell. It is generally agreed that this function should have a value of unity over the R-range of the peak, decay rapidly but smoothly to zero at each side of the peak, and be symmetric, so as not to distort the peak[9]. In fact, the inverse Fourier transform can simply be applied to the R-range of the peak, which is equivalent to applying a square window function prior to the inverse transform procedure. There are no problems with inverse transforming a peak that does not decay to zero on each side - indeed an inverse transform of a complex function contained within a narrow square function, produces a nearly sinusoidal oscillation extending over a large k-range.

Consider as an example, bulk NiI_2 data. A suitable window function having a value of unity over an R-range of 1.5 Å, centred about the R-value of 4.4 Å, with a Gaussian decay to zero over 0.4 Å on each side[18, 19], is shown in Figure 5.06, where it can be seen that the 'windowed peak' is altered very little, whilst being separated from unwanted peaks.

The appearance of the windowed modulus (ie the Fourier transform modulus multiplied by the window function) serves only as an indication of how well the peak has been 'filtered out'. It is the complex function, that is in practice, multiplied by the window function, and back Fourier transformed, according to equation 5.08, in which $F'(R_i)$ is the windowed complex function, (in the bulk NiI_2 example being defined from 0.1 to 15.0 Å in increments of ΔR = 0.1 Å), $k_j \chi(k_j)$ being calculated, in this example, since an original multiplier of k^1 was used.

$$k_j \chi(k_j) = \frac{1}{\pi} \sum_{i=2}^{149} F'(R_i)\, e^{-i k_j R_i}\, \Delta R \qquad \ldots (5.08)$$

The reason for the '$1/\pi$' in equation 5.08, rather than the '$1/2\pi$' in equation 5.05, is because a factor of 2 is 'lost' in back transforming just the positive R data.

Using bulk NiI_2 as an example, the <u>complex</u> $k\chi(k)$, calculated for 150 k-values from 0.1 to 15.0 $Å^{-1}$ (increments of 0.1 $Å^{-1}$), is shown in Figure 5.07(a). The real part is the filtered EXAFS of the first shell of atoms (producing the main peak in the Fourier transform) - it is only strictly meaningful over the k-range of the original raw EXAFS data, in this case from k_{min} = 4.3 $Å^{-1}$ to k_{max} = 7.8 $Å^{-1}$. The modulus is gaussian in shape, its width in k-space depending inversely on the width of the windowed peak in R-sapce[12]. The maximum value of this 'amplitude function' gives an indication of the effective number of backscattering atoms in the filtered shell,

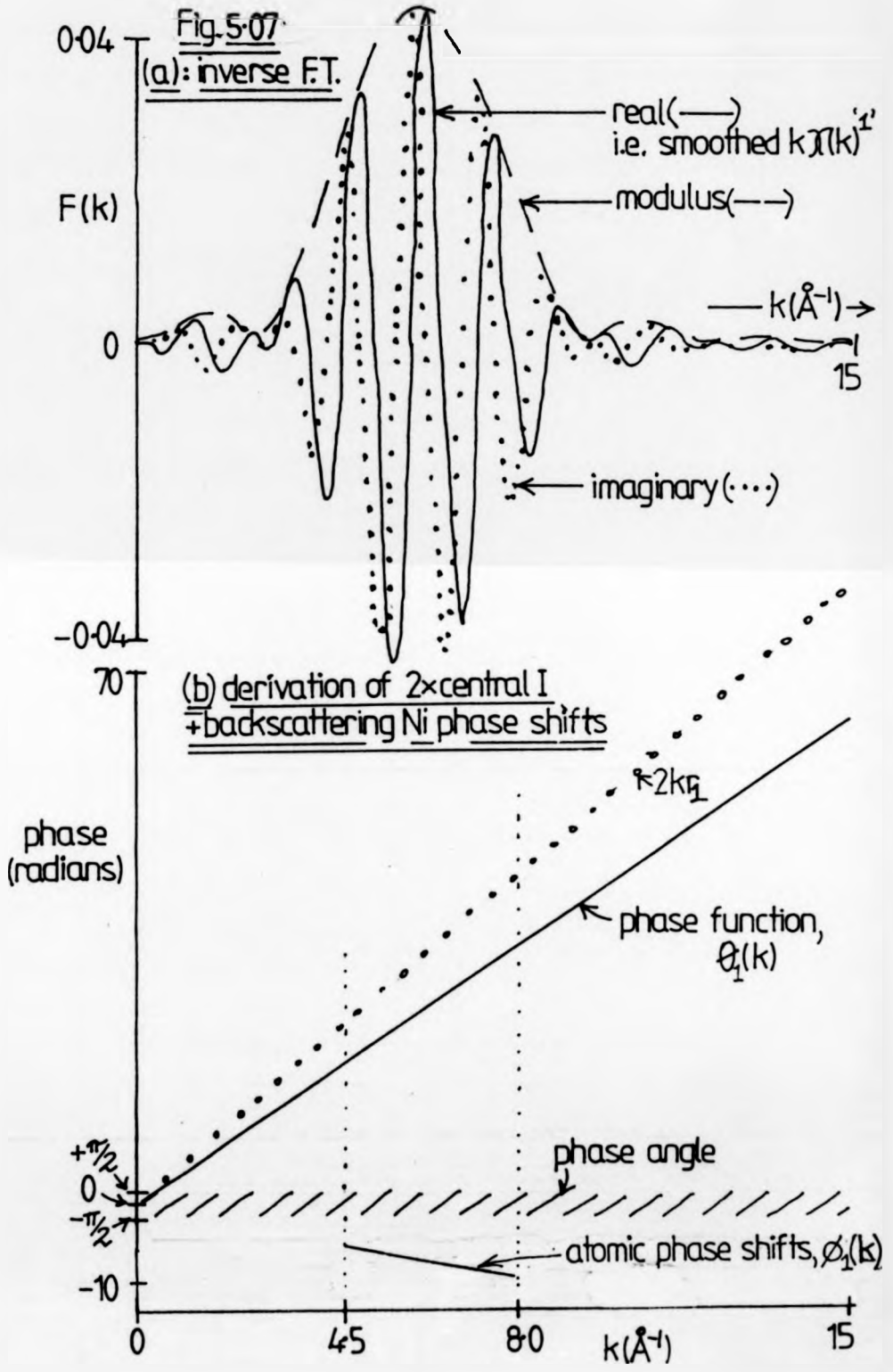
Fig. 5·07
(a): inverse F.T.
0·04
F(k)
0
-0·04
real(——)
i.e. smoothed k χ(k)
modulus(– –)
imaginary(···)
k(Å⁻¹)→
15
70
(b) derivation of 2×central I
+backscattering Ni phase shifts
phase
(radians)
+π/2
0
-π/2
-10
2kr₁
phase function,
θ₁(k)
phase angle
atomic phase shifts, ∅₁(k)
0
4·5
8·0
k(Å⁻¹)
15

but the actual value can differ from that predicted by theory, due to the extent of the data manipulation, and to the large number of parameters involved[20], respectively. Also shown in the figure is the imaginary part of the inverse transform, used in the calculation of the modulus, and also needed to calculate the 'phase function'.

5.07 The Phase Function

The filtered EXAFS of a single shell is a roughly sinusoidal oscillation in k-space, and can be defined by a phase function and an amplitude function. The phase angle of a sine wave varies from 0 to 2π radians over one period, and then repeats from 0 to 2π radians, etc. The phase function is defined to be continuous by the addition of 2π radians to the phase angle after each cycle, hence it is arbitrary to $\pm n\,2\pi$ where $n = 0, 1, 2....$.

In order to calculate a phase function from a complex inverse transform, the phase angle is first calculated using equation 5.09.

Phase angle, θ, of a complex function is given by:-

$$\tan\theta = \frac{\text{real}}{\text{imaginary}} \qquad \text{... (5.09)}$$

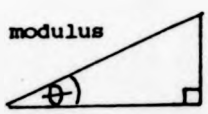

....COMPLEX FUNCTION

The phase angle $\theta(k)$ is calculated from the real and imaginary parts of $k\chi(k)$, (in general $k^n\chi(k)$), and it has a value between $-\pi/2$ and $+\pi/2$ radians, at each k value, since the tangent function is uniquely defined over this angular range.

To convert to a phase function, each time a calculation yields a phase angle that is approximately - $\pi/2$ radians, the previous k-value calculation having produced a value $\sim \pi/2$ radians, π radians is added to the phase angle. This produces a continuously increasing function that is arbitrary to $\pm n\pi$, n = 0, 1, 2....

Since $\chi_i(k) \propto \sin (2\ kr_i + \phi_i(k))$, $\phi_i(k)$ being the atomic phase shifts involved, the phase function is defined in equation 5.10.

$$\theta_i(k) = 2\ kr_i + \phi_i(k) \qquad \ldots (5.10)$$

The gradient of this phase function is given in equation 5.11, it being an acurate measure (typically errors being 0.04–0.10 $\mathring{A}$[10]) of the position in R-space of the main peak.

$$\frac{d\theta_i}{dk} = 2r_i + \frac{d\phi_i}{dk} = 2r_i - b_i \qquad \ldots (5.11)$$

If the phase function has been derived correctly, it should be the sum of the straight line, $2kr_i$ (a function in k-space depending only upon the bond length, r_i), and the very nearly linear term $\phi_i(k)$, having a negative gradient, (depending upon the atomic phase shifts). If this phase function shows a significant amount of curvature, then it is likely that this has been introduced in the windowing and back transforming procedure. The criteria of a straight phase function is useful in optimising the window function used[21]. A major source of error in this analysis procedure is that the window function always contains within it some effects due to other shells, point-to-point scatter within the 'frequency' range, and imperfect background subtractions (ie it is not possible to totally isolate the peak due to one shell), such that the phase function invariably has a larger curvature than is inherent from the non-linearity of the atomic phase shifts. As the window function is reduced in width (ie approaching a Delta function at one R-value),

the phase function becomes a straight line, but this procedure simply produces a result (ie an R-value) that is determined by the position of the window itself, which is clearly unsatisfactory. In practice an optimum width of the window function needs to be determined for the dataset under study.

For the EXAFS of a model compound[22], $2kr_i$ can be subtracted from the phase function (over the k-range for which it is meaningful) to yield the atomic phase shifts. Such a procedure is shown in Figure 5.07(b), for bulk NiI_2.

Having derived the phase function for an unknown compound, such atomic phase shifts can then be subtracted to yield the $2kr_i$ function, and hence determine the unknown bond length.

A full description of this atomic phase shift transfer is given in the next section.

5.08 Atomic Phase Shift Transferability and the Determination of Bond Lengths

The basic procedure of phase shift transferability is described below:-

Obtain	$2kr_i^{model} + \Phi_i(k)^{model}$	via the phase function of the EXAFS of the model compound.
Subtract	$- 2kr_i^{model}$	since r_i^{model} is known
to yield the atomic phase-shifts	$= \Phi_i(k)^{model}$	

Obtain $2kr_1^{unknown} + \phi_1(k)^{unknown}$ – the phase function of the EXAFS of the unknown structure.

transfer and subtract the $- \phi_1(k)^{model}$

to yield $= 2kr_1^{unknown}$ hence determine $r_1^{unknown}$

$$\underline{\text{if}}\ \phi_1(k)^{model} = \phi_1(k)^{unknown}$$

Unfortunately the atomic phase shifts are not, in general, the same in the model and the unknown compounds, since the local chemical environments (the bond nature) are likely to differ. However the atomic phase shifts can be made to appear equivalent by a shift in k-space of the EXAFS spectrum of the unknown structure, relative to that of the model, by a change in the energy zero, ΔE_o, of a few electron-volts. Such a procedure can determine r-values to accuracies of up to ± 0.01 Å[10], this being more accurate then the use of theoretical phase shifts which can introduce errors of up to 0.05 Å.

As an illustration of phase shift transerability, the fine structures were calculated for two geometrical structures of atoms around the same central atom, one being regarded as a model and the other as an 'unknown' structure. The model compound consists of a central calcium atom with neutral charge, the EXAFS being calculated using the appropriate central atomic phase shift[11], with a single backscattering shell of atoms at r = 4.0 Å, with the backscattering factor, F(k) = 5 Å, and the backscattering phase shift $\psi(k)$ = 0 radians. Since the backscattering phase shifts are known to be little affected by changes in chemistry (a fact that is important in LEED work) they can be regarded as directly transferable. The EXAFS

was truncated, Fourier transformed, windowed and inverse transformed, and the atomic phase shifts were derived, and could be seen to be the same as the inputted phase shifts - this illustrates that the data manipulation does not introduce significant errors.

The EXAFS of the 'unknown' structure - a central calcium atom having double positive charge (and hence a different atomic phase shift - see Figure 5.08(a)), with a shell at r = 4.1 Å, with F(k) = 5 $Å^{-1}$ and $\phi(k)$ = 0 radians - contain oscillations of a larger period in k-space at low k values, (Figure 5.08 (b)), due to the steeper central atom phase shift, compared to the 'model'.

A comparison of the positions of the main peaks in each of the Fourier transforms implies that the unknown r-value is approximately 4.0 Å which is incorrect. A subtraction of the simply transferred atomic phase shift (Figure 5.08(c)), shows that the subtraction is not complete (the intercept is not zero), and hence the gradient is not the bond length change.

However, if ΔE_o in equation 5.12 is allowed to vary until the intercept of the phase function difference becomes zero (or a multiple of π radians), then the atomic phase shifts have been effectively eliminated leaving a straight line, the gradient of which can be used to derive the 'unknown' r-value.

$$k_{new} = \sqrt{k_{original}^2 - \frac{2m_e \Delta E_o}{\hbar^2}} \quad \text{)} \quad \ldots (5.12)$$

ie $k_{(\Delta E_o)} = \sqrt{k^2 - 0.26\ \Delta E_o}$ k in Å, ΔE_o in eV)

In this example, the intercept is zero for ΔE_o = - 10.95 eV, (Figure 5.08(d)), indicating 'r-unknown' = 4.105 Å, which is in error by only 0.005 Å. Note in Figure 5.08(b), that the EXAFS for the

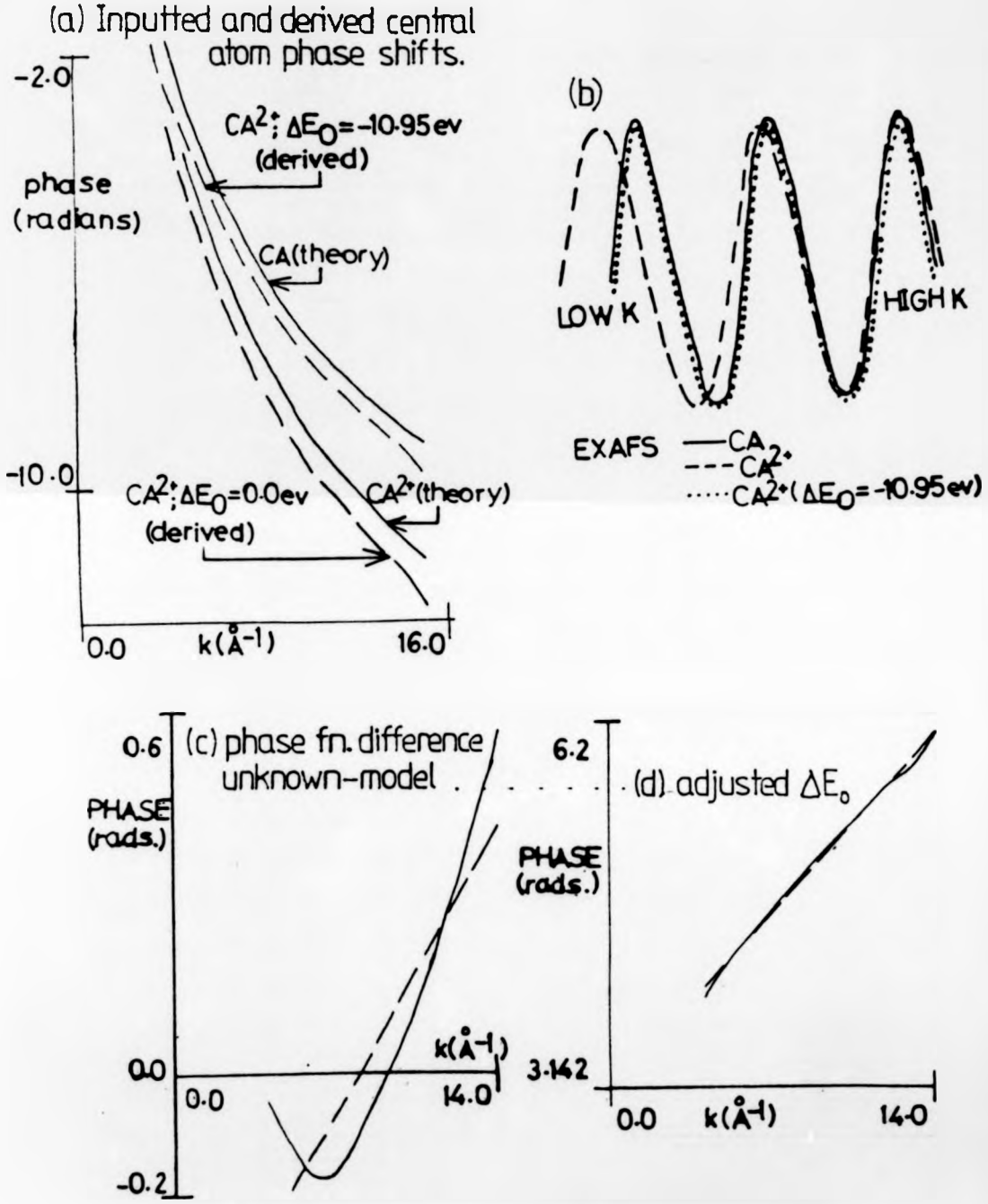

Fig. 5·08: Illustration of phase shift transferability.

'Ca^{2+} structure' appear as if they had been produced by a Ca^{o} central atomic phase shift; Figure 5.08(a) shows that the ΔEo of - 10.95 eV causes the Ca^{2+} phase shift to appear equivalent to that of a neutral central Ca atom.

Experimental data is shown in Figure 5.09 - the EXAFS of bulk NiI_2 in (a); the Fourier transform modulus, its windowed main peak, and the imaginary component (positive values only) in (b); the back transform of the single shell also in (a); and the difference between the phase function derived from this spectrum (data set number 833) and that of another bulk NiI_2 spectrum (834) in (c); this latter diagram shows that the difference between two spectra is small enough to suggest a potential accuracy of ± 0.01 Å in a bond length determination.

Such a determination is shown in Figure 5.10(c) which is a plot of the difference between the phase functions of bulk NiI_2 dataset 834 and surface NiI_2 - Ni{100} SEXAFS spectrum 794 (shown in Figure 5.10(a)). ΔEo has been adjusted to - 2.0 eV (ie the Eo point is 6 eV below the edge in the unknown structure, compared to 4 eV below for the model in order to make the least squares fit straight line, between k_{min} = 4.5 $Å^{-1}$ and k_{max} = 7.9 $Å^{-1}$ (ie the k-range over which the fine structures of both materials have been measured) have zero intercept, at which point the gradient is - 0.10 (± 0.02)Å indicating that Δr_i = - 0.05 (± 0.01)Å (ie in the surface nickel iodide structure, the average I-Ni bond length has a value of approximately 2.73 Å, compared to the value of 2.78 Å in bulk NiI_2 [23]).

In SEXAFS publications, the bond length determinations are typically quoted to accuracies of ± 0.02, ± 0.03 Å[24, 25], the above mentioned bulk NiI_2 and surface nickel iodide spectra seen to justify this assumption. Since the phase function difference is generally

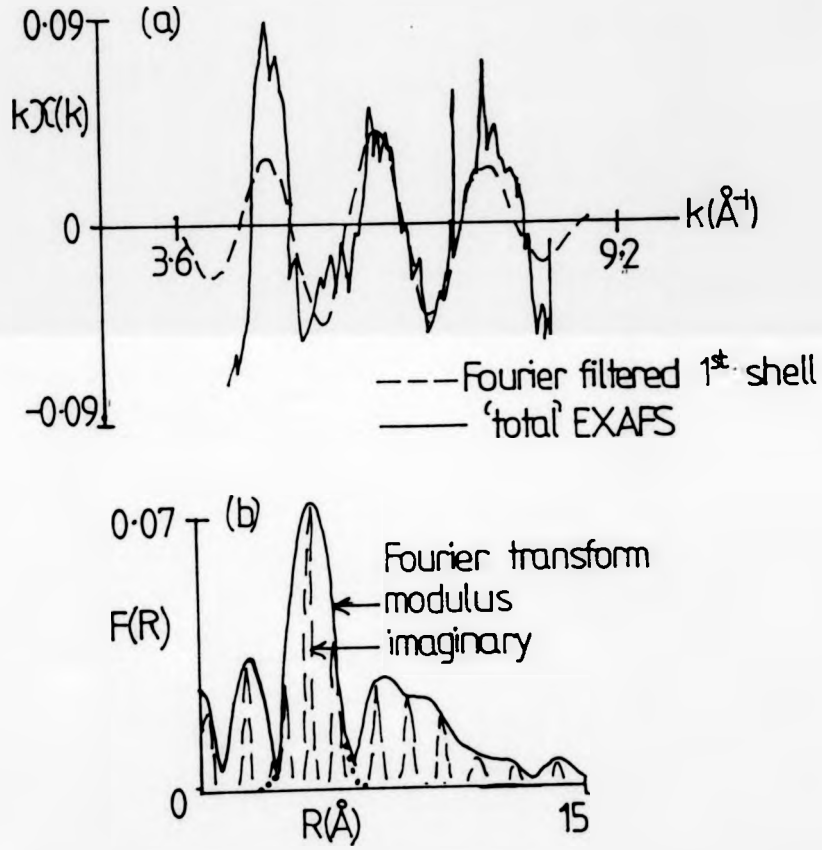

Fig. 5·09, (a,b): bulk NiI_2 dataset 833

Fig. 5·09 :
(c) : referenced to another bulk NiI_2 spectrum (834).

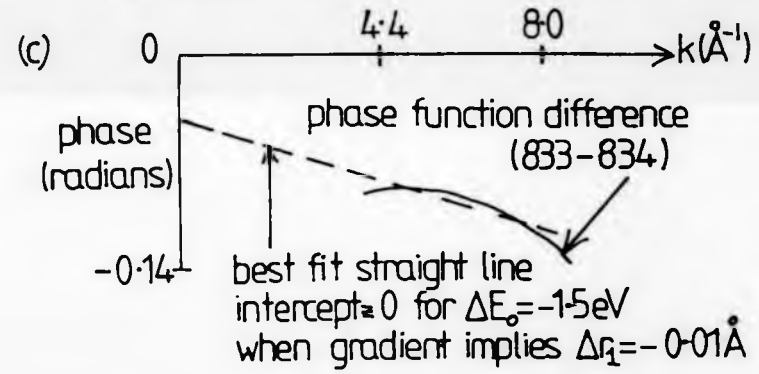

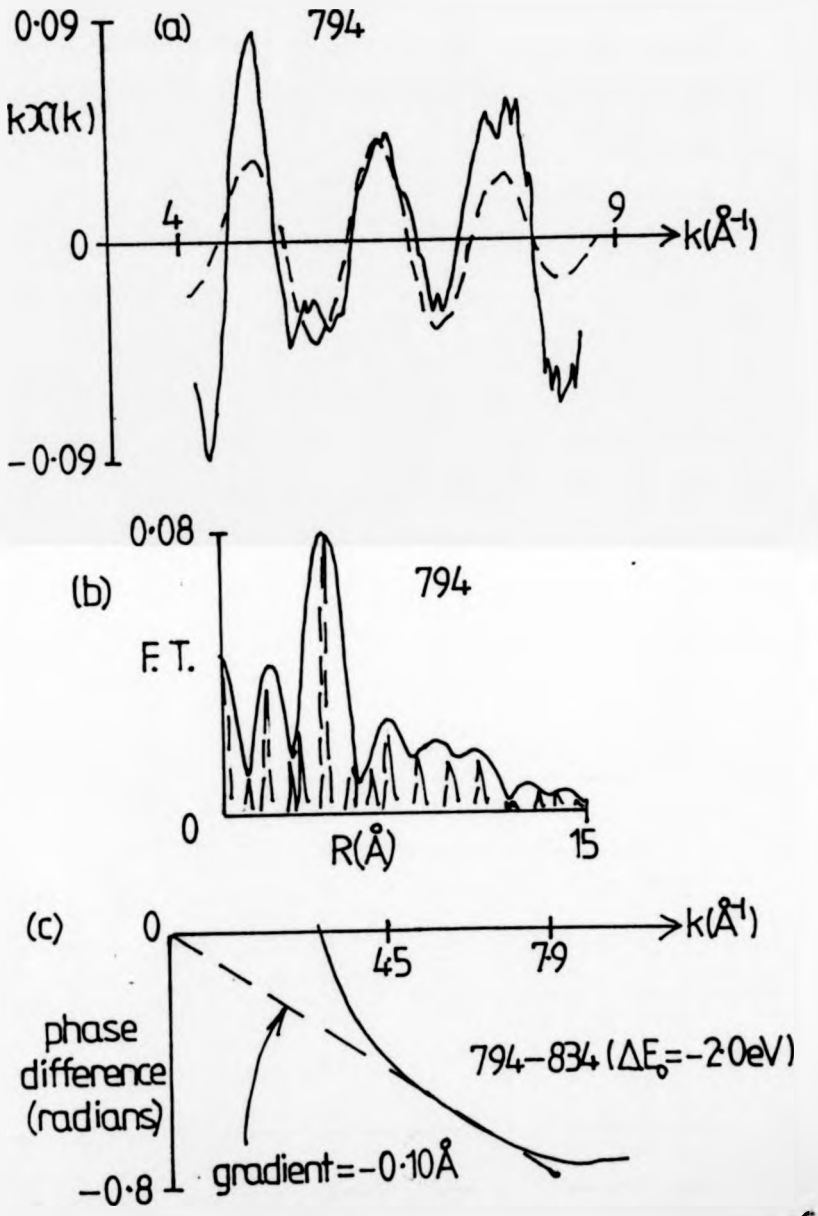

Fig. 5·10: Bond length derivation (I-Ni in surface NiI_x-Ni{100}).

parabolic in nature, the method of estimating the uncertainty of the gradient of the least squares fit straight line, by summing the residuals [9], is not valid. This method produces far too low an error[26] as it is only valid for random scatter about a straight line.

A far better method of estimating the uncertainty in the gradient is to fit a straight line to the whole of the k-range to get the best estimate, and to fit straight lines to the lowest half and to the highest half of the data range (there is some controversy as to whether low k or high k data is the most reliable), taking these two gradients as the two extremes of the possible answer, (these two lines clearly have non-zero intercept, but the re-optimisation of ΔE_o has only a minor effect on the r-value determination). For example, applying this method to a published phase function difference (Figure 16(a)[9]), produces a realistic uncertainty of $\pm$ 0.02 Å[27].

5.09 The Amplitude Function and the Determination of the Effective Coordination Number

The amplitude function is the modulus of the inverse Fourier transform, and should in principle be given by $A_1(k)$ in equation 5.13.

$$k\chi_i(k) = A_i(k) \sin(2kr_i + \phi_i(k))$$

where $$A_i(k) = \frac{N_i^*}{kr_i^2} F_i(k) e^{-2r_i/\lambda(k)} e^{-2\sigma_i^2 k^2} \quad \ldots (5.13)$$

However, due to the finite R-range included in the inverse transform, the amplitude function does not contain much of the variation with k as is expected from the $F_i(k)$ and other terms, and it can have an amplitude that differs from that calculated using equation 5.13 (assuming that parameters such as the inelastic electron mean free path can be estimated) by as much as 20%[20].

If a single peak is back transformed (as is the established procedure[24]), then the amplitude function can only be gaussian in nature[12], it being accepted that this causes a loss in the amplitude match between the raw and the filtered EXAFS[25]. This still enables an estimation of the value of N_i^* to be made, this being directly proportional to the maximum value of A(k). Due to the uncertainty of some of the terms in equation 5.13, it is often more useful to use the ratio of the amplitude maxima at two angles of incidence of the plane-polarised X-ray beam, to indicate the ratio of the effective co-ordination numbers, according to equation 5.14, which can be useful in determining the adsorption site, for instance. Even this equation is not strictly

$$\frac{A_i(k)^{\theta_1}_{max}}{A_i(k)^{\theta_2}_{max}} = \frac{N_i^{*\theta_1}}{N_i^{*\theta_2}} \qquad \ldots (5.14)$$

correct, as the effective Debye-Waller factors and the electron mean free path, can vary between angles of incidence, θ_1 and θ_2.

It is possible to get an indication of the atomic number of the atoms in the backscattering shell, by attempting to identify the F(k) function that is contained within A(k), the potential accuracy being $\Delta Z = \pm 5$[19], for high atomic numbers, where F(k) contains maxima and minima over the typical k-ranges involved. In order to do this, the window function must be wide enough to include the 'satellite' peaks around the main peak, that contain the 'frequency' information of the F(k) variation. The phase function extracted from such a back transformed spectrum is not linear and cannot therefore be used to obtain a measure of distance, unless a specialised method is applied[17].

A wide window can also be used to give a closer amplitude match between the raw and the Fourier-filtered EXAFS. Figure 5.11

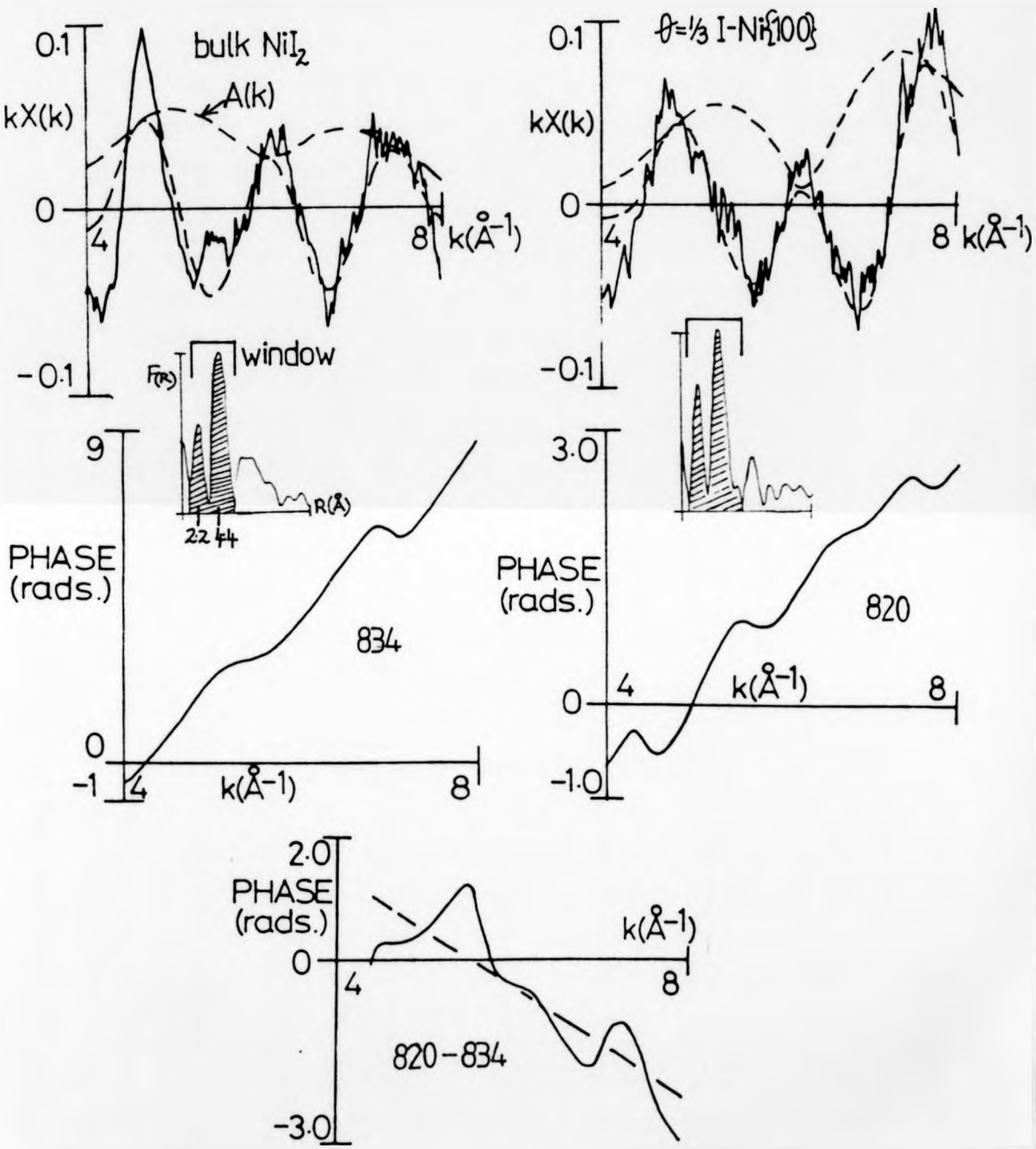

Fig. 5·11: Wide windows preserve A(k)'s but distort phase functions.

shows two such windows, including the low R-peak at R $\approx$ 2.2 Å, as well as the R $\approx$ 4.4 Å peak for the EXAFS spectra of bulk NiI_2 and a surface structure of iodine adsorbed onto Ni(100) ie (2 x 3) I-Ni(100). Whilst the derived amplitude function, A(k), can be seen to have the necessary structure to model the raw EXAFS, (in this case this is not due to the F(k) variation, but is due in part to the effects of the higher shells) the phase functions, and in particular the difference between the phase functions (necessary for the determination of the I-Ni bond distance in the surface structure) are meaningless. As mentioned previously a suitably narrow window around the peak of interest is therefore required for distance determinations.

5.10 References

1. D E Sayers, E A Stern, F W Lytle Phys Rev Lett 27(18), Nov '71, p 1204
   'New technique for investigating noncrystalline structures: Fourier analysis of EXAFS'

2. The program to perform the spline estimation of μo is called TEXAN 1 on the GEC computer in the physics dept, Warwick University. It is based upon a program outlined by M Prutton to remove 'noise' from an Auger spectrum.

3. E A Stern, D E Sayers, F W Lytle Phys Rev B11(12) June '75 p 4836
   'EXAFS technique III: Determination of physical parameters'.

4. A Bianconi, R Z Bachrach Phys Rev Lett 42(2) Jan '79 p 104
   'Aluminium surface relaxation using SEXAFS'.

5. G E Laramore Phys Rev A 24(4) Oct '81 p 1904
'Effect of screening charge transfer on EXAFS phase shift: model calculations for excitation of 1s level in Br_2 molecule'.

6. Electron binding energies for ESCA*
* after K Siegbahn
VG Scientific, East Grinstead, Sussex.

7. C Kittel (Introduction to Solid State Physics) 5th edition Wiley
The Fermi energy for copper is given as 7 eV (p 154), that of nickel is slightly less than this

8. L V Azaroff, X-ray spectroscopy, '74, International series in pure and applied physics,
McCraw-Hill, chapter 6: X-ray absorption spectra.

9. P A Lee, P H Citrin, P Eisenberger, B M Kincaid
Reviews of Modern Physics 53(4,1) Oct '81 p 769
'EXAFS - its strengths and limitations as a structural tool'

10. B A Bunker, E A Stern, Phys Rev B27(2), Jan '83, p 1017
'Phase factor in EXAFS'

11. Boon-Keng Teo and P A Lee, Journal of the American Chemical Society, 101: 11, May '79, p 2815:
'Ab Initio Calculations of Amplitude and Phase Functions for EXAFS Spectroscopy'.

12. E Hecht and A Zajac, 'Optics', Addison-Wesley, '79 :
Chapter 7: The Superposition of Waves
Chpater 11: Fourier Optics.

13. P A Lee and G Beni, Phys Rev B15(6), March '77 p 2862 :
'New method for calculation of atomic phase shifts: application to EXAFS in molecules and crystals'.

14. Strictly speaking, the EXAFS function is described by sine waves if the atomic phase shifts at k = 0 $Å^{-1}$ are equivalent to 0 radians.

$\chi(k)$ is proportional to $\sin\{2kr+\phi(k)\}$

$\therefore \chi(k) \propto \sin\{(2r-b)k+a\}$; since $\phi(k)=2\delta(k)+\Delta(k) \approx a-bk$

$\propto \sin\{(2r-b)k\}$ if $a=0$

but: $\propto -\cos\{(2r-b)k\}$ if $a=\pi/2$ radians

If this is not the case (ie if a is not equivalent to 0 radians), then the atomic phase shifts should be removed first, in order for this procedure[12] on the choice of Eo to be valid. Alternatively, it can be argued that adjusting Eo until the imaginary and modulus Fourier transform peaks align at the same R-values, sets b to be zero, which is the physically correct situation.

15. P J Orders and C S Fadley, Phys Rev B27(2), Jan '83 p 781 :
'Single-scattering cluster calculations and Fourier transform analyses of normal photo-electron diffraction'.

16. The displacement of this peak is larger than predicted:

$2r \simeq 2 \times 2.8$ Å $\simeq 5.6$ Å.

$b \simeq -0.6$ Å

∴ expect peak at $\simeq 5.0$ Å in R-space.
This has important implications, and is discussed in later chapters.

17. G Martens, P Rabe, N Schwentner, A Werner, Phys Rev Lett 39(22), Nov '77, p 1411 :
'EXAFS beats: new method to determine differences in bond lengths'

18. S M Brennan, Stanford Synchrotron Radiation Laboratory, report 82/03, June '82.
'SEXAFS of sulphur on nickel'.

19. J Stöhr, Stanford Synchrotron Radiation Laboratory, report 80/07, Dec '80,
'EXAFS and SEXAFS: principles, analysis and applications'.

20. E A Stern, B A Bunker, S M Heald, Phys Rev B21(12), June '80, p 5521 :
'Many body effects on EXAFS amplitudes'.

21. This criterion is basically the same as that of ensuring that the analysis produces a distance determination for an unknown compound that does not vary with the k- value, as explained by:

S Brennan, J Stöhr, R Jaeger, Phys Rev B24(8), Oct '81, p 4871

'Structure determination of C(2x2) S-Ni(100) using polarization dependent SEXAFS'.

22. A model compound is one whose structure is known, most usually having been derived from X-ray diffraction. Many structures including that of bulk NiI_2 are given in the text:

R W G Wyckoff, 'Crystal Structures', 2nd edition, volume 1, 1965.

23. This procedure is basically the same as that set out in section 5·08. A direct subtraction of the phase functions is:-

$$2kr_i^{unknown} + \phi_i(k)^{unknown}$$

$$-\left\{2kr_i^{model} + \phi_i(k)^{model}\right\}$$

$= 2k(r_i^{unknown} - r_i^{model})$ when ΔE_o has been adjusted to make $\phi_i(k)^{unknown} \approx \phi_i(k)^{model}$

Such that the gradient of this plot in k-space is:-

gradient $= 2\Delta r_i$

24. J Stöhr, R Jaeger, T Kendelewicz, Phys Rev Lett 49(2), July '82, p 142
'Structure of p(2 x 2) and c(2 x 2) Oxygen on Ni(100): A SEXAFS Study'.

25. P H Citrin. P Eisenberger, R C Hewitt, Surf Sci 89, 1979, p 28
'SEXAFS studies of iodine adsorbed on single crystal substrates'.

26. Lee et al[9] calculate an error in the bond length of ±0·002Å by summing the squares of the deviations (Figure 17 [9]), but realising that this is unrealistic, quote a final error of ± 0.01 Å.

27. Straight line fits to the whole, low, and high k data ranges (Figure 16(a)[9]) produce the more realistic answer of $\Delta r_1 = -\ 0.11(\pm\ 0.02)$Å, ie a bond length contraction of 0.11 Å, the uncertainty being ± 0.02 Å.

CHAPTER 6

RESULTS OF THE FOURIER-FILTERING SINGLE-SHELL ANALYSIS METHOD, APPLIED TO THE I-Ni(100) STRUCTURES

6.01 Overview

In this chapter, an outline is given of the results of the Fourier-filtering single-shell analyses of the SEXAFS spectra taken from surface structures formed by the adsorption of iodine onto Ni(100), using bulk nickel iodide as a reference compound. The results consist of: accurate I-Ni bond length determinations for all of the structures studied except c(2x8) I-Ni(100); some indications of trends in chemistry as the iodine coverage varies; the identification of the iodine atomic adsorption site in the c(2x2) structure as being hollow or bridge; and rough estimations of the co-ordination numbers for iodine atoms in each of the other structures.

The second half of the chapter consists of a critical appraisal of the validity of the analysis method for these particular SEXAFS spectra, and identifies a problem - the strong interference of the iodine-iodine component of the EXAFS, particularly in the bulk and surface nickel iodide structures, causes the Fourier transform of the limited data range to be unable to correctly separate out the 'frequency' of the main iodine-nickel component which in turn causes incorrect atomic phase shifts to be derived, and incorrect bond lengths to be obtained. Explanations are given of these effects, including the errors in derived bond lengths that can be introduced when large ΔE_o shifts are required.

Published SEXAFS studies of iodine overlayers are reviewed, and found to be unaffected by the problems described for the I-Ni work. Some questions are raised, however, on the interpretations of the Fourier transform moduli, particularly with regard to the 'Ramsauer-Townsend effect'. One imporant conclusion is that the 'Ramsauer-Townsend effect' will rarely be observed in SEXAFS studies, due to data limitations.

6.02 X-ray Absorption Coefficient of Bulk NiI, and I-Ni(100) Structures

Figure 6.01 shows the measurements of the X-ray absorption coefficients of a number of structures, extending over the X-ray energies, from the iodine L_{III} edge at 4557 eV, to the iodine L_{II} edge at 4852 eV. These measurments were made around the summer of 1983 at Daresbury, in each case using the Ge(111) monochromator crystals, with the total electron yield being measured by a current meter attached to a detector close to the sample position, this being referenced to the yield from a gold coated tungsten mesh.

In Figure 6.01 the spectra are normalised to the L_{III} edge jumps - the edge jump: background ratio was seen to consistently decrease as the iodine coverage was reduced.

In each spectrum there are two distinct regions. From the L_{III} edge up to a photo-electron energy of about 70 eV, there is the NEXAFS (near edge X-ray absorption fine structure) which is caused by multiple scattering of the outgoing photo-electron wave giving rise to a complicated intensity modulation, that serves as a 'fingerprint' of the local chemical environment of the central atom. For the bulk and surface nickel iodide spectra, the near edge structures are very similar; for each of the other absorbate layers, the structure is distinctly different. For sufficiently high photo-electron energies, single backscattering becomes predominant, such that the fine structure on the absorption coefficient consists of oscillations that are periodic in k-space - the EXAFS region. In Figure 6.01, the EXAFS oscillations can be seen to be obscured by the iodine L_{II} edge at 4852 eV, such that only three maxima can be seen in each spectrum.

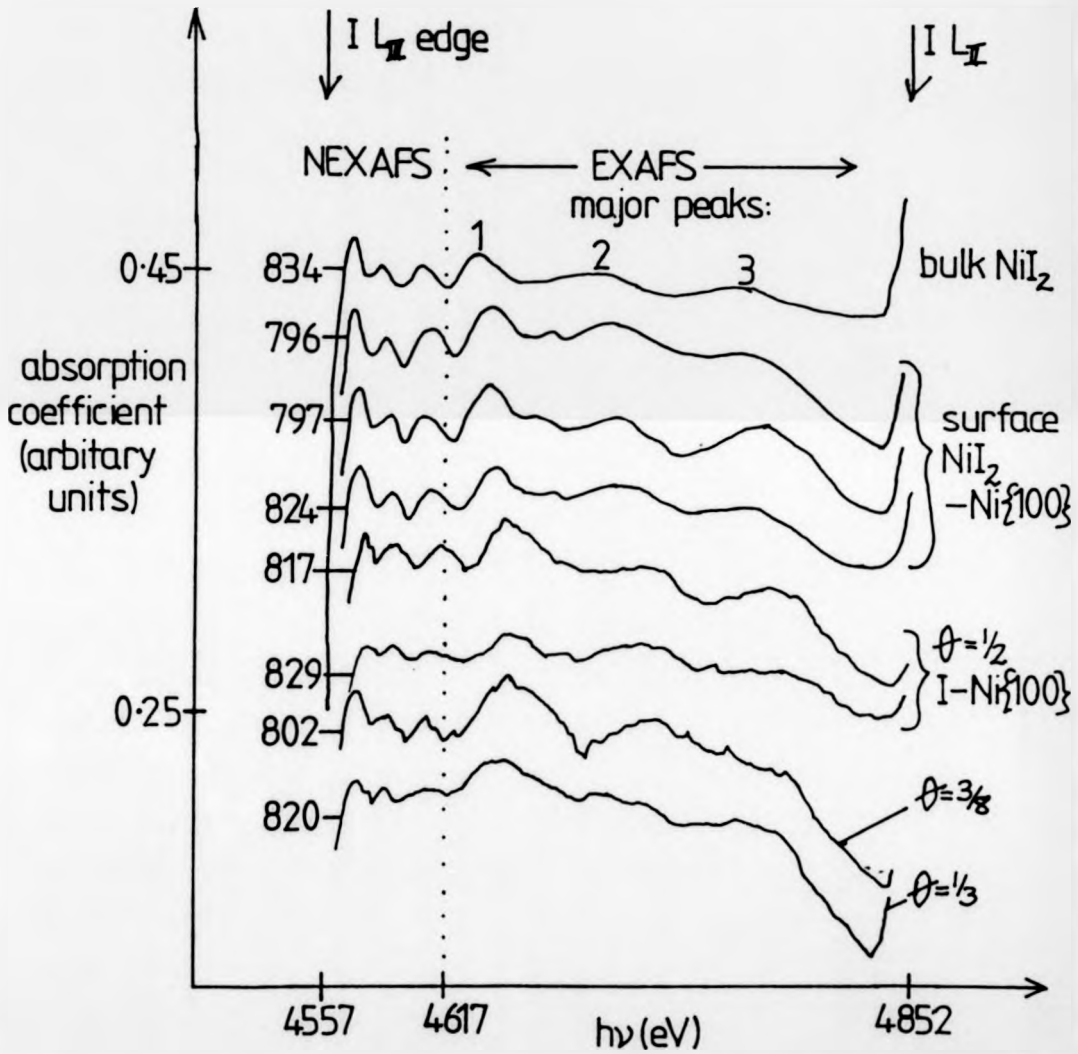

Fig. 6·01 : X-ray absorption coefficients (I L_{III} - I L_{II} range) of I-Ni structures, normalised to the L_{III} edge jumps.

For sample orientations, see Table 6·01.

It appears, for example, that the surface nickel iodide structure contains smaller I-Ni bond lengths than bulk NiI_2, since the EXAFS maxima occur at higher energies and their periodicity is larger. Of course it is difficult to make any quantitative assumptions from the data in this form.

6.03 Results of the Fourier-Filtering Single-Shell Analysis Method

The results of the analysis method as described in chapter 5, are given in Table 6.01, and a sample of results are shown in Figures 6.02 to 6.08. The bulk NiI_2 data set 834 is used as the reference spectrum, the phase function of this spectrum being subtracted from those of the other spectra to determine the Δr_1 values (ie the changes in the I-Ni bond lengths), the ΔE_o's being adjusted as required.

The I-Ni bond length in the surface nickel iodide can be seen to be 0.05 Å shorter than 2.78 Å, this being determined with good acuracy (± 0.01 Å) requiring only a small ΔE_o shift (between 0 and - 3 eV). The $\theta = 1/2$, and $\theta = 1/3$ iodine overlayers appear to have similar shortened I-Ni distances, much larger ΔE_o's (around + 7 eV) being required to compensate for the differences in the atomic phase shifts present in these structures and in the reference compound. For the c(2x8) I-Ni(100) structures, the bond length appears to be even shorter, but there is a large error associated with this conclusion - looking at Figure 6.07 this is not surprising - Figure 6.07(a) shows that the EXAFS spectrum does not look quite as desired, (b) shows that the main peak at - 4.4 Å is not easily separable[1,2], particularly from the lower R peak at - 2.2 Å, it therefore not being surprising that the phase function contains a significant amount of distortion as can be seen in (c). One point worthy of comment, is that in each of the spectra, except those of

I-Ni sample	SEXAFS spectrum	E_o point (eV) relative to edge	$r_2/\Delta r_2$ (Å)	Amplitude
bulk NiI_2				
$\hat{\underline{\varepsilon}}$ at 45° to sample	834	4 below (i.e. 4553eV)	2·78	0·04
"	833	5·5 below	−0·01 (±0·01)	0·04
surface NiI_2–Ni{100}				
⟨100⟩ horizontal, $\hat{\underline{\varepsilon}}$ at 45°	823	4·3 below	−0·04 (±0·02)	0·05
" " " "	824	6 below	−0·05 (±0·01)	0·05
" " " 90°	794	4·3 below	−0·05 (±0·01)	0·05
" " " "	796	5 below	−0·06 (±0·01)	0·04
⟨111⟩ " " 90°	797	6 below	−0·05 (±0·01)	0·08
" " " "	798	7·3 below	−0·05 (±0·01)	0·09
average		$\Delta E_o = -1·5 (\pm 1·0)$	−0·05 (±0·01)	
$\theta = \frac{1}{2}$ c(2×2) I–Ni{100}				
⟨100⟩ horiz^{l}, $\hat{\underline{\varepsilon}}$ at 45°	829	2 above	−0·06 (±0·02)	0·07
" "	830	6 above	−0·05 (±0·03)	0·08
" "	831	at edge	−0·07 (±0·01)	0·09
" 90°	817	3 above	−0·05 (±0·02)	0·06
average		$\Delta E_o = +7·0 (\pm 2·0)$	−0·06 (±0·01)	
$\theta = \frac{3}{8}$ c(2×8) I–Ni{100}				
⟨100⟩ horiz^{l}, $\hat{\underline{\varepsilon}}$ at 90°	802	6 above	−0·09 (±0·08)	0·07
" "	803	6 above	−0·09 (±0·07)	0·05
" "	811	at edge	−0·12 (±0·04)	0·08
average		$\Delta E_o = +8·0 (\pm 3·0)$	−0·10 (±0·02)	0·07 (±0·02)
$\theta = \frac{1}{3}$ (2×3) I–Ni{100}				
⟨100⟩ horiz^{l}, $\hat{\underline{\varepsilon}}$ at 90°	820	2 above	−0·04 (±0·01)	0·04
" "	821	5 above	−0·05 (±0·04)	0·03
average		$\Delta E_o = +7·5 (\pm 1·5)$	−0·05 (±0·01)	0·035 (±0·005)

Note: changes in the E_o point and the I–Ni bond length are quoted relative to the reference compound bulk NiI_2 (SEXAFS spectrum 834)

Table 6·01: Fourier-filtered single shell results for I–Ni structures

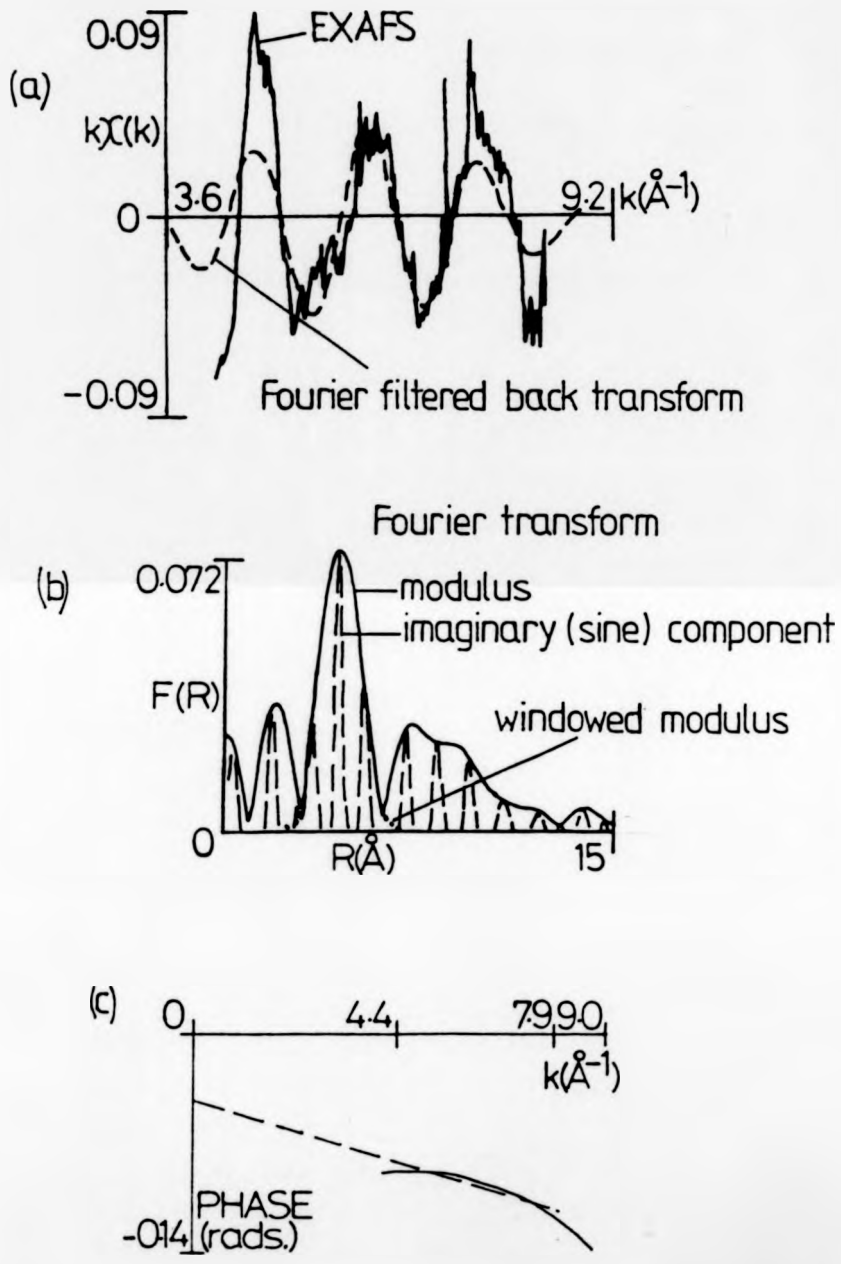

Fig. 6·02: (a) EXAFS and (b) Fourier transforms of bulk NiI_2 dataset 834; (c) phase function difference 833-834.

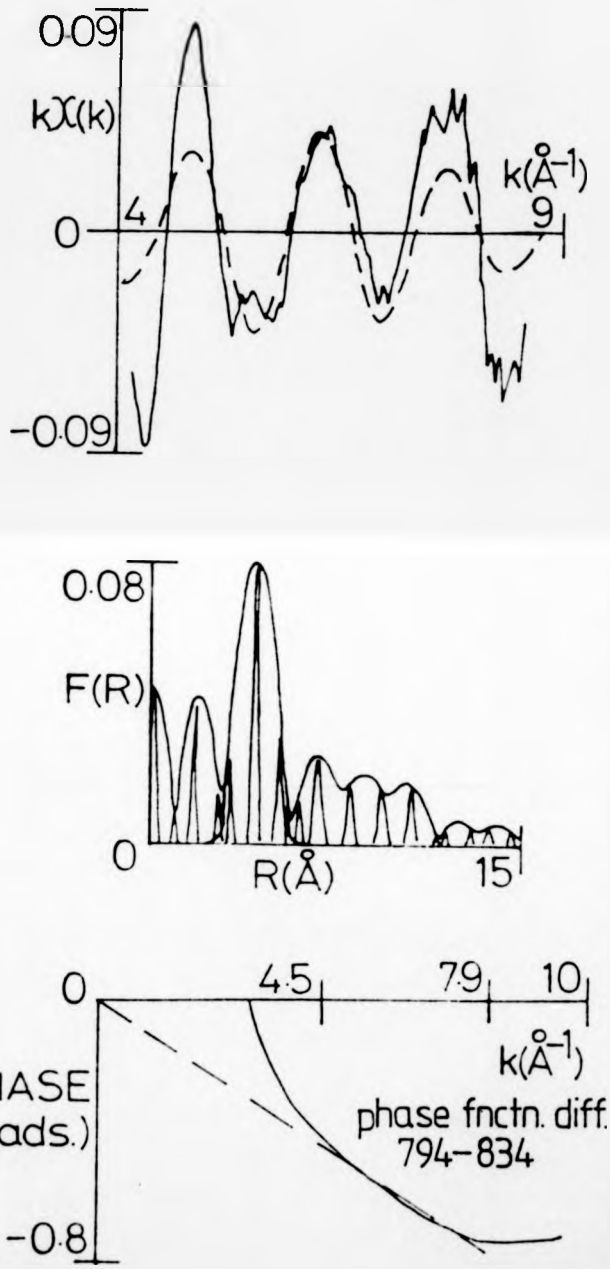

Fig. 6·03 : Surface NiI_2–Ni{100} spectrum 794.

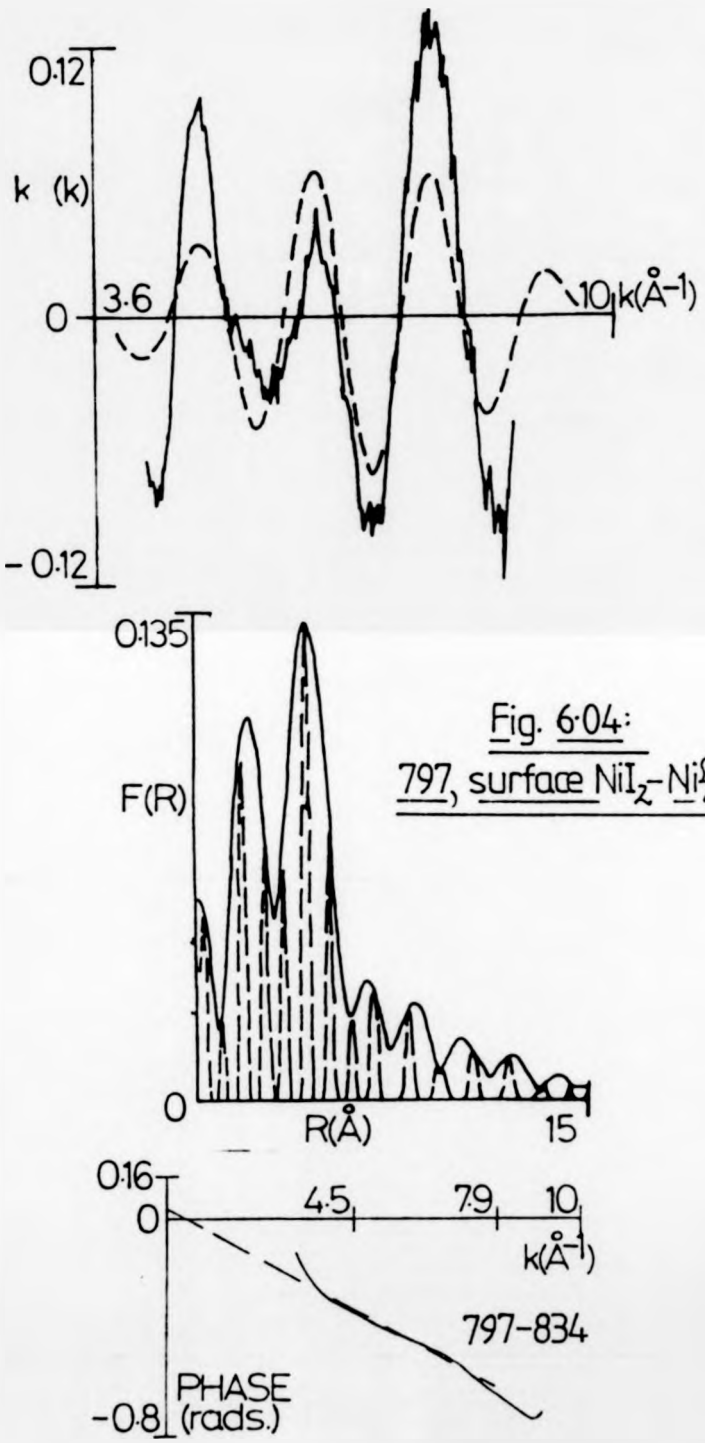

Fig. 6·04:
797, surface NiI_2-Ni{100}

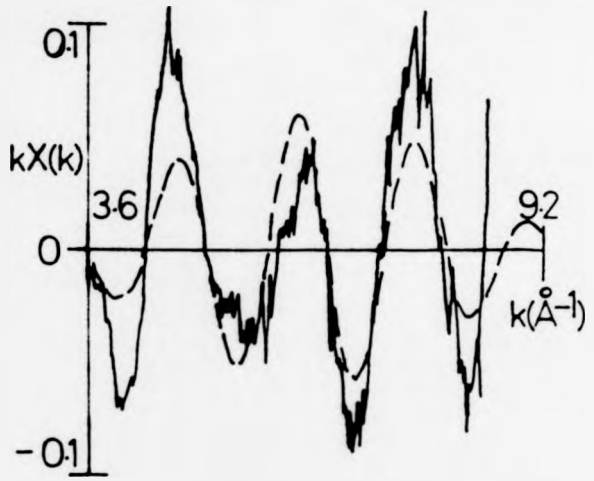

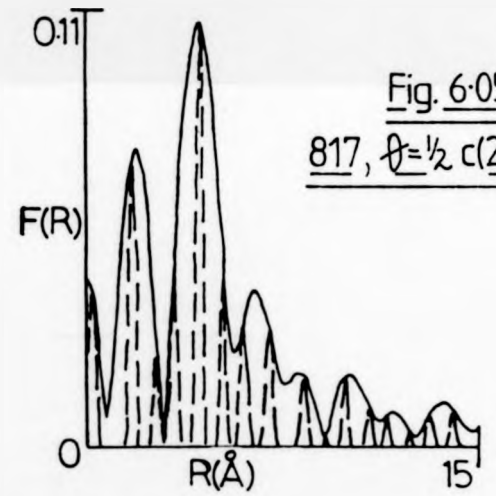

Fig. 6·05:
817, θ=½ c(2×2)I-Ni{100}

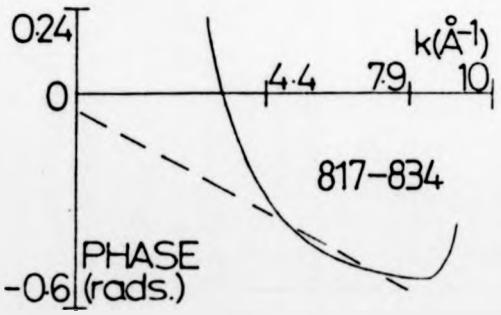

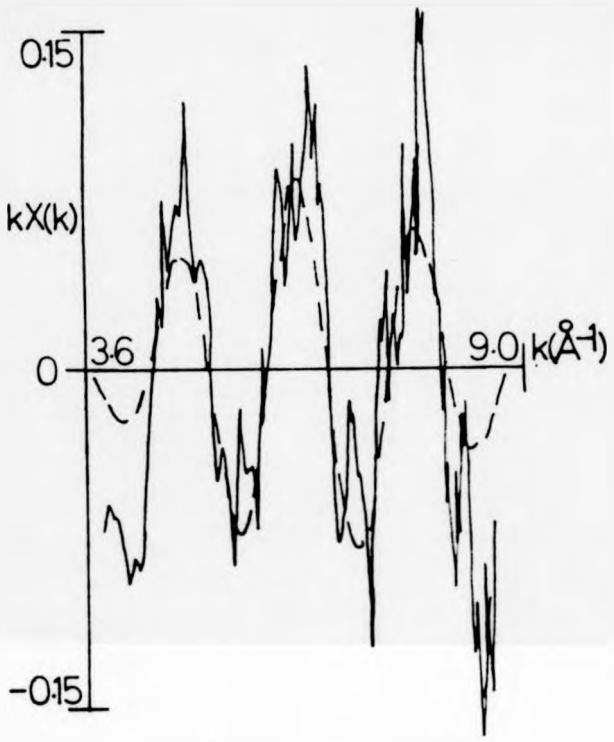

Fig. 6·06: 831, $\theta = \frac{1}{2}$ I–Ni{100}

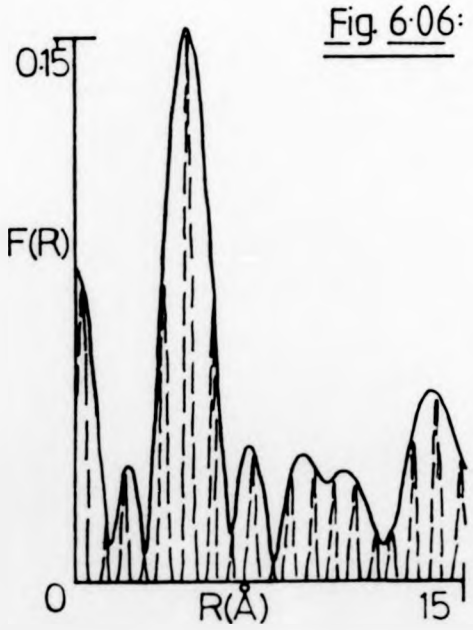

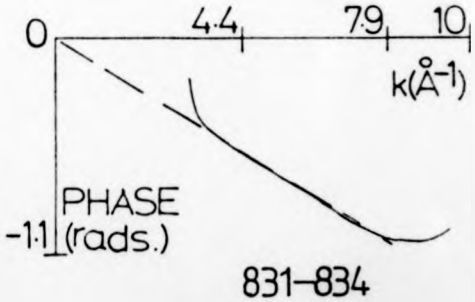

831–834

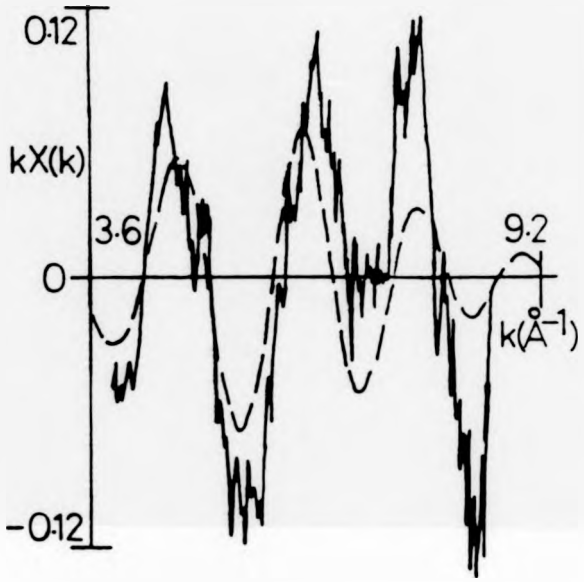

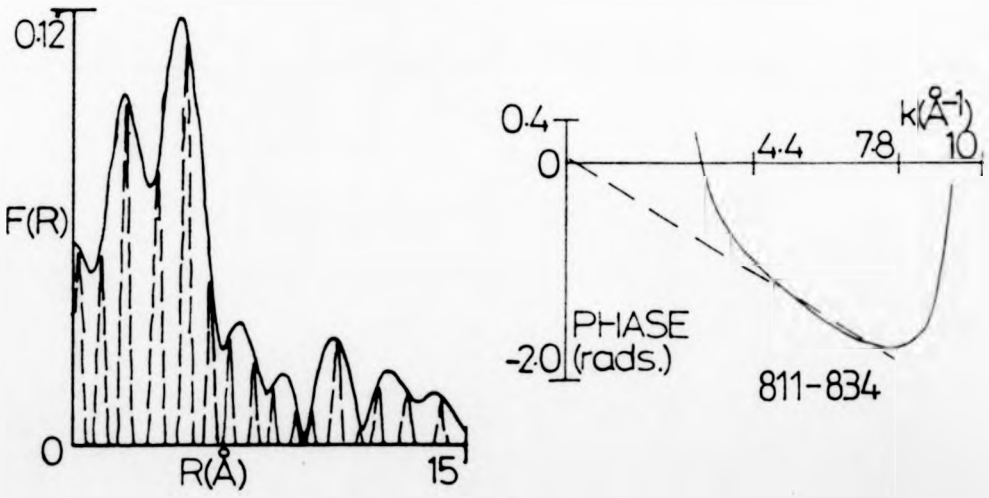

Fig. 6·07: 811, $\theta = 3/8$ c(2×8) I-Ni{100}

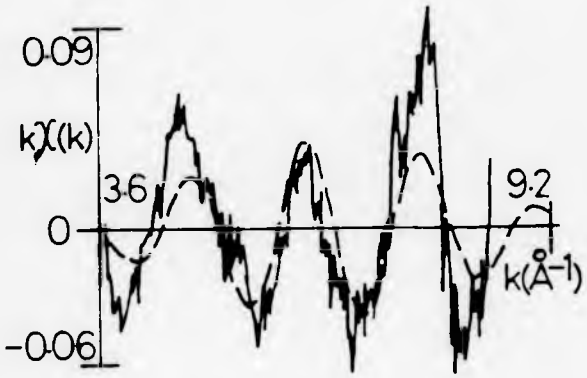

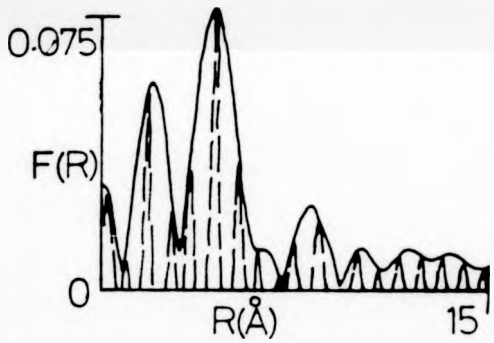

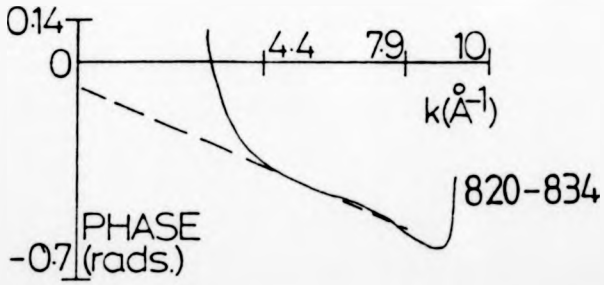

Fig. 6·08: 820, $\theta = 1/3$ (2×3) I-Ni{100}

the $\theta = {}^{3}/_{8}$ coverage, the imaginary component and the Fourier transform contain maxima that coincide at R - 4.4 Å, indicating that the Eo's are roughly correct. Since the phase function of the $\theta = {}^{3}/_{8}$ structure is so uncertain, it is not surprising that an incorrect Eo is obtained from an analysis method that demands that the intercept of the difference between phase functions be effectively zero radians.

The maximum value of the amplitude function indicates the effective number of nearest nickel atoms, ie the effective co-ordination number of the central iodine atom, for each spectrum. For bulk NiI_2, the maximum value of A(k), (ie the filtered $k\chi(k)$ due to the nearest shell of atoms) is 0.04, it being known that each iodine atom has three nickel nearest neighbours in this crystalline structure. Without going into too much detail covering the angular dependences, the effective co-ordination numbers are by comparison found to be 4 for the surface nickel iodide structure (as expected - see Figure 4.04), and 6, 4.5 and 3 for the $\theta = {}^{1}/_{2}$, $\theta = {}^{3}/_{8}$ and $\theta = {}^{1}/_{3}$ overlayers (this being not inconsistent with the postulation that the iodine adatoms all lie in hollow sites on the Ni{100} surface for $\theta = {}^{1}/_{2}$, but as the adatoms expand in a ‹100› direction some must pass over bridge sites as the coverage falls).

The $\theta = {}^{1}/_{2}$ overlayer has a c(2x2) LEED pattern, such that all the iodine adatoms lie in the same adsorption site, this being likely to be the hollow, the bridge, or the atop site. The dependence of the filtered EXAFS amplitude upon the angle of the X-ray electric vector relative to the surface orientation, can be used to test the validity of each of these postulated sites. Figure 6.09 shows the calculation of the ratios of the effective co-ordination numbers of iodine adatoms in each of the three sites, for the two X-ray incidences that were used during the collection of the SEXAFS

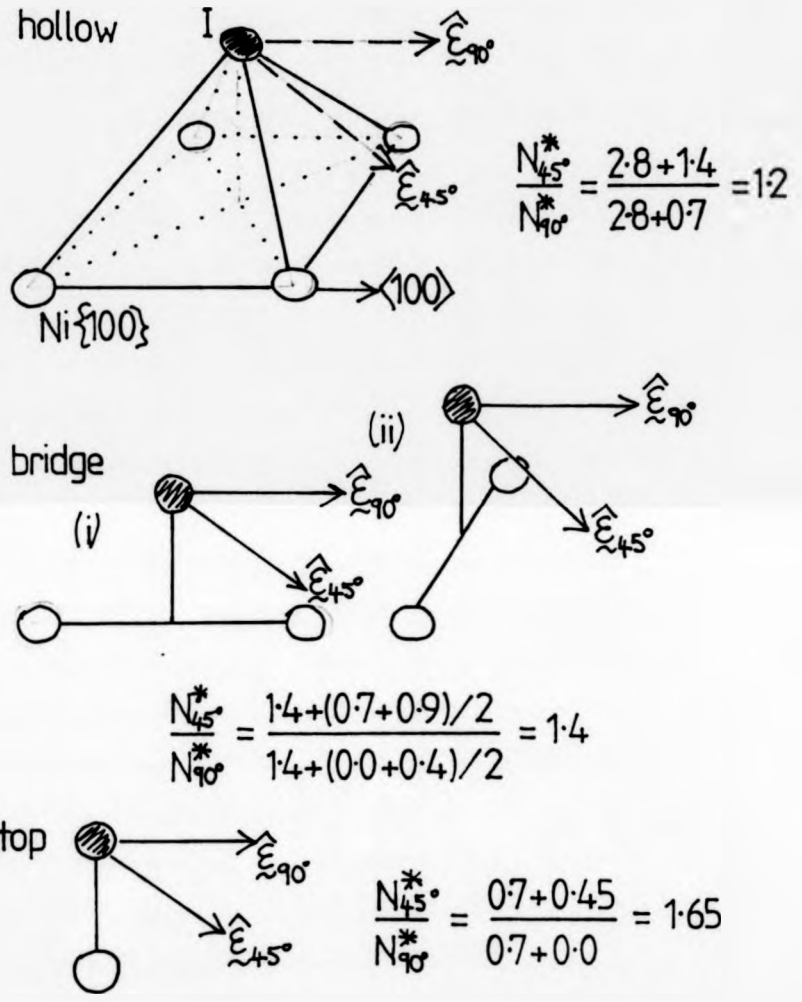

Fig. 6·09 : Effective coordination numbers as functions of I–Ni{100} orientation to X-ray beam for 3 sites.

spectra. The approximate expression of equation 2.20 is used, giving N^*45^o/N^*90^o = 1.2, 1.4 and 1.65 for the hollow, bridge, and atop sites, The observed ratio of the EXAFS amplitudes $A_1(k)^{max}{}_{45^o}/A_1(k)^{max}{}_{90^o}$ = 1.3 (± 0.2) is therefore unable to distinguish between the hollow and bridge sites, but does rule out the atop site.

In order to get a more definitive answer, more results are needed at normal incidence, and the glancing incidence needs to be reduced (say to 30^o or even 20^o if possible) in order to produce a greater variation in the amplitude - the L_{III} edge EXAFS has an amplitude that is largely isotropic.

Although the accuracy of a typical result appears to be around ± 0.02 Å for the bond length determination, this being backed up by the statistical differences between the spectra of each structure, there are some features that cause concern. The large discrepancy between the total EXAFS and the filtered first-shell EXAFS, in the amplitude of the first maxima in the spectra for bulk and surface nickel iodides (Figures 6.02-6.04(a)), implies that another shell of atoms makes a significant contribution to the total EXAFS. Also, the position of the main peak at R ≈ 4.4 Å (giving rise to atomic phase shifts having a gradient in k-space of - 1.2 Å, from the model compound in which $2r_1$ = 5.6 Å), cannot be explained, since the atomic phase shifts from a central iodine atom and a backscattering nickel atom are thought[3] to have a gradient of - 0.6 Å in k-space, which should give a peak at R ≈ 5.0 Å.

6.04 Discussion, Modelling and the 'RAMSAUER-TOWNSEND EFFECT'

For the SEXAFS datasets of the NiI_2 and I-Ni(100) structures, the main peaks in the Fourier transforms are situated around R ≈ 4.4 Å, and since r_1 ≈ 2.8 Å, this suggests that the atomic phase shifts have gradients in k-space around - 1.2 Å, in conflict

with theoretical calculations of twice central iodine plus backscattering nickel atomic phase shifts having a gradient of -0.7 Å over the same k-range[3], such phase shifts being used in EXAFS analyses with reasonable reliability[4].

In order to ascertain the reasons for the discrepancy in the experimentally derived atomic phase shifts a modelling procedure was pursued. The EXAFS can be theoretically calculated, starting with a radial distribution function around a central atom, and using theoretical phase shifts, backscattering factors, Debye-Waller factors, and electron inelastic mean free paths. For bulk nickel iodide, the local environment of each iodine atom can be adequately described by the four shells listed in Table 6.02.

TABLE 6.02 - RADIAL DISTRIBUTION FUNCTION FOR CENTRAL I ATOM IN BULK NiI$_2$

SHELL	1:3 Ni ATOMS at	2.78 Å, with DEBYE-WALLER FACTOR, $2\sigma^2$ =	0.01 Å^2
	2:6 I	3.89	0.03
	3:6 I	3.97	0.03
	4:3 Ni	4.78	0.03

The Debye-Waller factors are available from measurements of the temperature dependence of EXAFS amplitudes and from X-ray diffraction work[5-7]. The inelastic mean free path of the photo-electron can be approximated by $\lambda(\text{Å}) \approx k(\text{Å}^{-1})$[8], and theoretically calculated phase shifts and backscattering factors are available[3]. The calculated EXAFS is shown in Figure 6.10(a), the multiplier being k^3 because of the long k-range, and a ΔE_o of + 10.0 eV being used to shift the EXAFS downwards in k-space (equation 5.12) such that the region

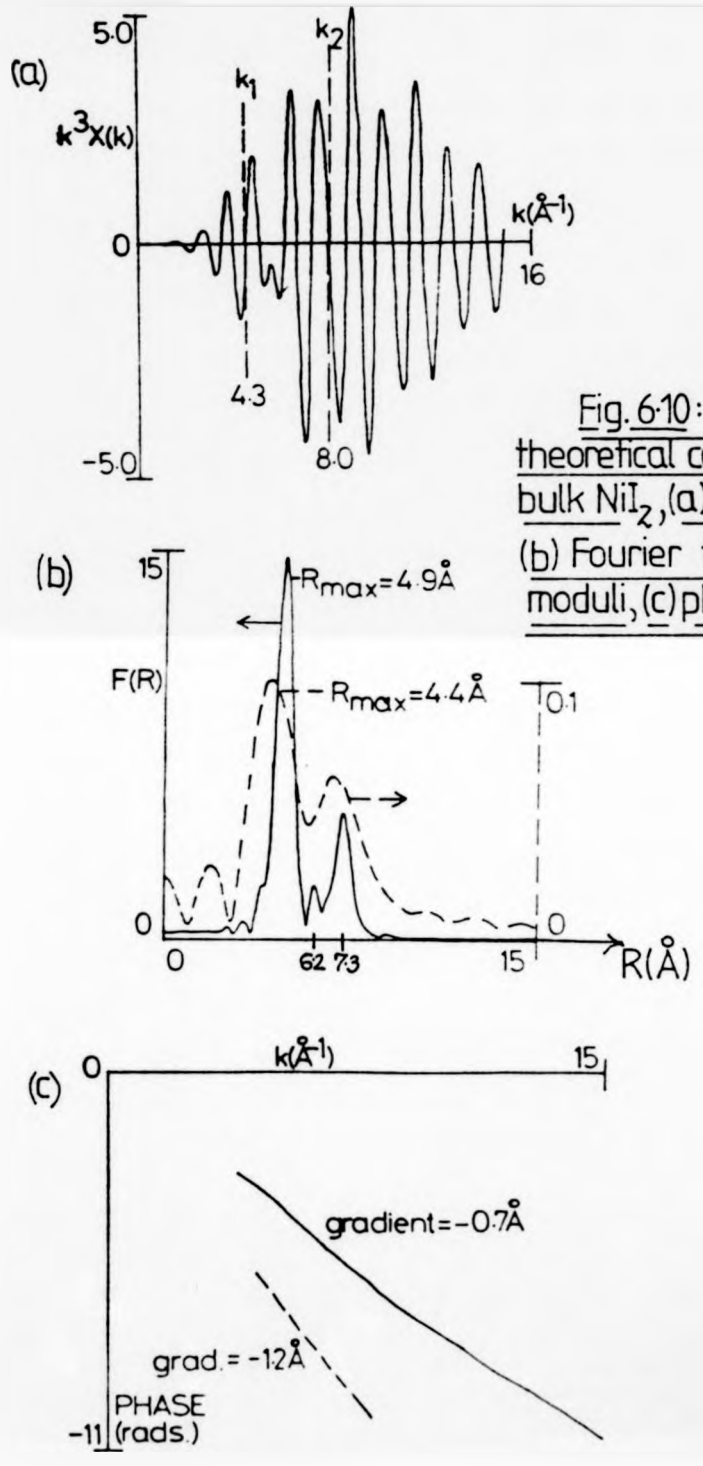

Fig. 6·10: theoretical calculations for bulk NiI_2, (a) EXAFS, (b) Fourier transform moduli, (c) phase functions.

k = 4.3 to 8.0 $\AA^{-1}$ matches an experimental spectrum quite closely (Figure 6.02(a) for example) - this ΔE_o accounts for the errors in the calculated phase shifts, due to the plane wave approximation[9].

The Fourier transform modulus of the whole k-range of $k^3 X(k)$, is shown as the solid line in Figure 6.10(b), closely resembling the radial distribution function - the largest peak at $R \approx 4.9$ $\AA$ is due to the nearest nickel atoms, and that at $R \approx 7.3$ $\AA$ is due to the twelve iodine atoms around $r \approx 3.93$ $\AA$ (the distances 3.89 and 3.97 $\AA$ are not resolved). The iodine peak is accompanied by a 'satellite' peak at a lower R-value of 6.2 $\AA$, the occurrence of this peak can be explained as follows. The I-I EXAFS component between k = 5 and 10 $\AA^{-1}$, has a 'frequency' corresponding to the 2r value of 7.86 $\AA$ plus the gradient of the atomic phase shifts (approximately - 0.08 $\AA$ over this k-range; see Figures 2.07 and 2.08), predicting a peak around $R \approx 7.78$ $\AA$. Between 10 and 15 $\AA^{-1}$, the I-I EXAFS has a markedly different 'frequency', because of the different gradient of the atomic pahse shifts, mainly arising from the iodine backscatterer; Figures 2.07 and 2.08 show that this gradient has an average value of - 0.46 $\AA$, predicting a peak at 7.40 $\AA$. These two peaks are observed at lower R-values in Figure 6.10(b) because of the ΔE_o value. The highest R peak is the largest in magnitude because the I-I EXAFS has the largest amplitude between 5 and 10 $\AA^{-1}$; the multiplier of k^3 being required to make the lower R peak of significant size, because the EXAFS amplitude decays rapidly at high k values.

When the EXAFS shown in Figure 6.10(a) is truncated at 10 $\AA^{-1}$, and the data below this k value included in the Fourier transform, the iodine satellite peak is not present. This suggests that for SEXAFS studies in which the data ranges are generally fairly limited, such satellite peaks will rarely be observed, even for

medium-to-high atomic number backscatters. These peaks are often referred to as 'Ramsauer-Townsend peaks', as they are thought to arise due to the presence of minima in the backscattering factor, F(k), similar to the very low electron scattering factors observed in the Ramsauer-Townsend effect[10]. The mechanism of this is explained in the next section, after an explanation of amplitude modulation.

Returning to the main nickel peak - the inverse Fourier transform of this peak at R $\simeq$ 4.9 Å, (a window being applied from R = 3 Å to R = 5.8 Å) produces a phase function and hence the atomic phase shifts shown as the solid line in Figure 5.10(c), the gradient being - 0.7 Å.

A Fourier transform of k^3 X(k) for $k = 4.3 - 8.0$ Å^{-1}, at which points the value is zero, (this being the data range available in a measured spectrum), produces the modulus shown as the dashed line in Figure 6.10(b). The poor resolution causes both the iodine and nickel peaks to be broadened by $\Delta R \simeq \pm 1$ Å, such that they are only just resolvable from each other, the nickel peak being centred about R $\simeq$ 4.4 Å (as observed for experimental data) having been displaced downwards by 0.5 Å in R-space from its anticipated position. Atomic phase shifts derived from this peak have a gradient of - 1.2 Å (the dashed line in Figure 6.10(c)). The discrepancy in the R-values of the main peak, and in the atomic phase shifts, can be understood in terms of amplitude and frequency modulation.

6.05 Amplitude and Frequency Modulation, and the 'Frequency' Spectrum

The fact that Fourier transforms of different k-ranges can yield different frequency components, can be understood in terms of amplitude and frequency modulation[11]. Two sine waves of equal amplitude but different 'frequencies' R_1 and R_2, add to give a single

sine wave of 'frequency', $R_{average} = (R_1 + R_2)/2$, whose amplitude is modulated over the period of $4\pi/|R_2-R_1|$ in k-space - see equation 6.01 and Figure 6.11.

$$X(k) = \sin kR_1 + \sin kR_2 = 2 \sin\left[k\left[\frac{R_1 + R_2}{2}\right]\right]\cos\left[k\left[\frac{R_2 - R_1}{2}\right]\right] \quad \ldots (6.01)$$

A Fourier transform of a k-range that is large enough to include one or more 'beats', yields the two 'frequencies' R_1 and R_2, whereas a transform of a k-range much smaller than one beat, yields the average 'frequency', $(R_1 + R_2)/2$ - in this case, it is the amplitude modulation that contains information on the frequency components.

If the second sine wave has a smaller amplitude, then it has the effect of modulating both the amplitude and <u>frequency</u> of the main sine wave, as has been reported in relation to EXAFS work[12], and can be shown analytically[13]. If this interfering sine wave has a much higher 'frequency', then it just adds a high frequency oscillation to that of the main frequency. With regard to EXAFS, this main oscillation may be due to an effective bond length, R = 3.0 Å, with a second shell of atoms providing the interfering R = 10 Å term, as in equation 6.02:

$$X(k) = \sin 3\,k + {}^1/_2 \sin 10\,k \quad \ldots (6.02)$$

The EXAFS defined by equation 6.02 is plotted in Figure 6.12(a), the Fourier transform modulus of the whole (0 to 15 $Å^{-1}$) and a limited (2.0 to 7.5 $Å^{-1}$) k-range, being able to correctly determine the frequency components - see Figure 6.12(b). That second shells of atoms rarely cause problems in the R-value determinations in EXAFS work can be understood by the small beat period: in this ecample the k-range necessary to yield the correct 'frequencies' is approximately

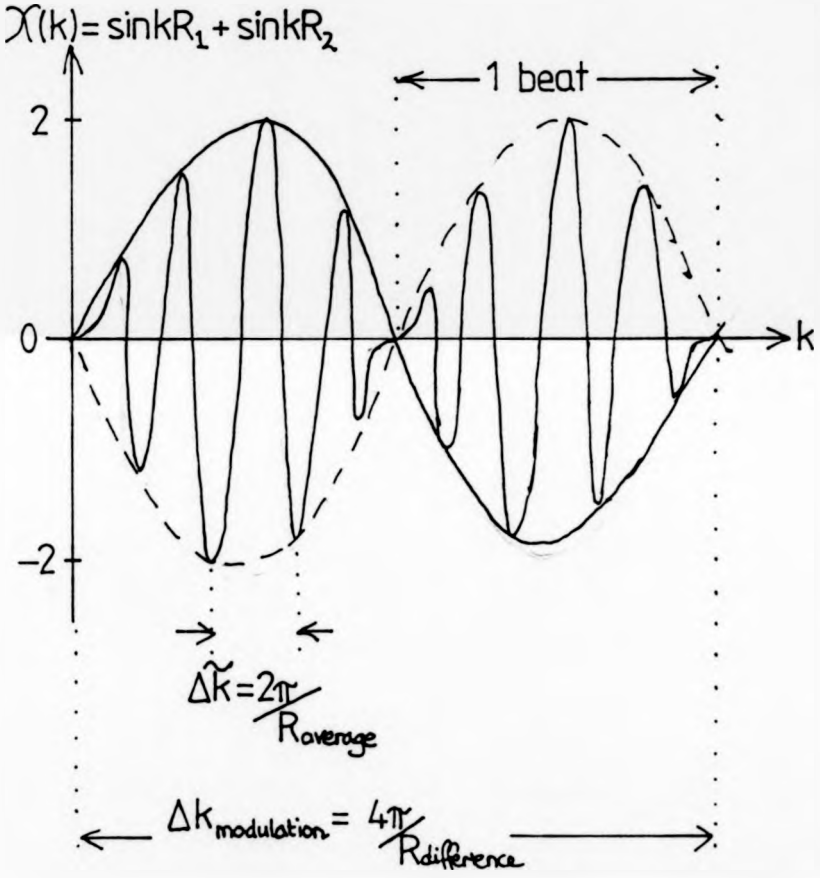

Fig. 6.11: Frequency and amplitude modulation for 2 sine waves of same amplitude but different frequency.

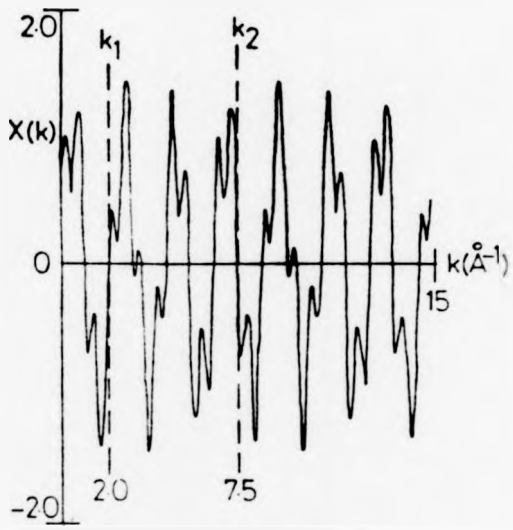

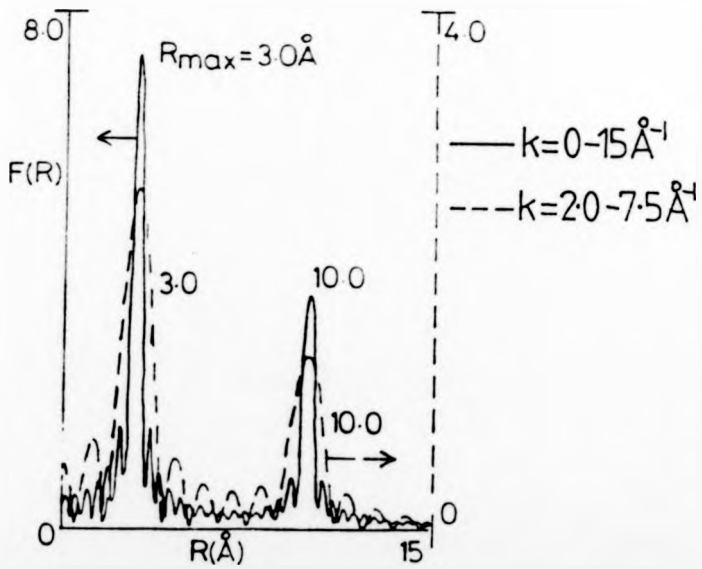

Fig. 6·12: (a): $\chi(k) = \sin 3k + \frac{1}{2}\sin 10k$
(b): Fourier transform moduli

$\frac{1}{2} \cdot \frac{4\pi}{(10 - 3)} \approx 1$ Å^{-1}, this being easily obtained.

For a second 'frequency' close to the main 'frequency', the beat period is much larger, hence for two similar bondlengths to be correctly resolved, a large k-range of the EXAFS needs to be included in the Fourier analysis. Consider a main R-value of 3.0 Å, with an interfering R = 3.33 Å term of half the magnitude, as in equation 6.03.

$$X(k) = \sin 3k + \tfrac{1}{2} \sin 3.33k \qquad \ldots (6.03)$$

The EXAFS is shown in Figure 6.13(a), the amplitude and frequncy modulations extend over a period of approximatley 20 Å^{-1}. The Fourier transform of the range from 0 to 15 Å^{-1}, is insufficient to correctly deduce the 'frequencies', the result being the main 'frequency' derived as R = 2.9 Å (the solid line in Figure 6.13(b) is the FT modulus). A transform from k = 6.0 to 11.8 Å^{-1} produces the main peak at R = 2.7 Å. The 'frequency' is clearly being modulated very significantly, the 'frequency' being smallest where the amplitude is a minimum. It has generally been thought that when two similar bondlengths contribute to the EXAFS, the measured bond length is a weighted average lying somewhere between the two[14]. In fact the situation is not quite so simple - when the interfering bond length lies at higher R, the main bondlength (as measured) shifts to lower R, and vice versa[13].

The iodine satellite peak in Figure 6.10(b) can be understood in terms of amplitude modulation. The iodine backscattering factor varies over the k-range from 5 to 15 Å^{-1}, with a period of $\sim$ 8 Å^{-1} (see Figure 2.09(b)), hence the I-I EXAFS component varies similarly in amplitude. In order to build up this amplitude modulation two beating frequencies are needed, which may explain why the Fourier transform yields the two R-values of 7.4 and

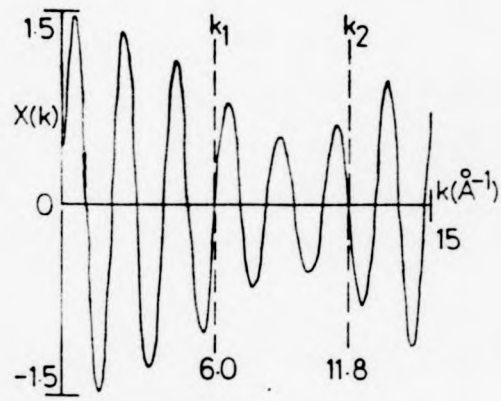

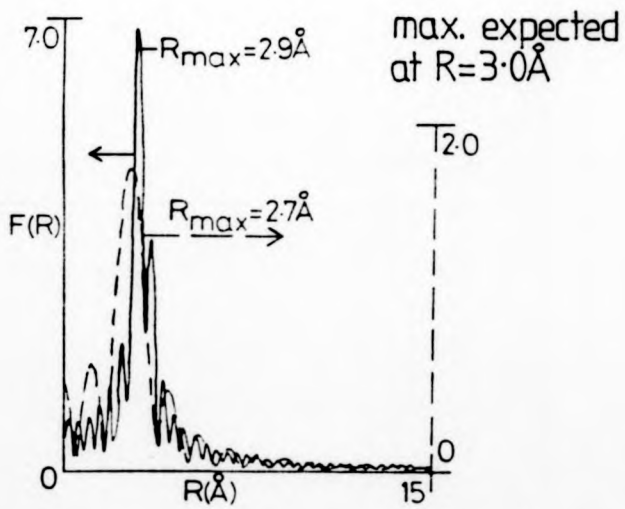

Fig. 6·13 : $\chi(k) = \sin 3k + \frac{1}{2}\sin 3{\cdot}33k$ and |FT|'s.

6.4 Å for a single iodine shell at r = 3.93 Å. Medium and high atomic number atoms have minima in their backscattering factors, such that satellite peaks are often expected on the basis of the 'Ramsauer-Townsend effect[15].

In conclusion, the Fourier transform simply yields the frequencies of the sine and cosine components contained within the k-range considered - care needs to be taken when trying to relate this to a radial distribution function and 'Ramsauer-Townsend effects'.

6.06 A Demonstration of the Fallibility of the Fourier-Filtering Analysis Method

From the EXAFS of the model compound, bulk nickel iodide, the main nickel peak is in an incorrect position in R-space, due to the interfering effect of the iodine shell and the short k-range included in the Fourier transform. Filtering out this shell, therefore yields incorrect atomic phase shifts, which are used in the analyses of structures of unknown bond lengths. To demonstrate the errors that can be introduced, theoretical calculations of EXAFS spectra were made, and these were analysed using the established procedure.

The model compound of bulk NiI_2 (Table 6.02) produces the EXAFS as shown by the dashed line in Figure 6.14(a) - this theoretical calculation showing good similarity to a spectra measured from bulk NiI_2 (eg, Figure 6.02(a)). An 'unknown' structure consisting also of three nickel atoms around the central iodine atom at the same r-value of 2.78 Å, but with no other shells within r = 5 Å, produces (calculating with the same Debye-Waller factor, λ_{imfp}, etc) the EXAFS, $k\chi(k)$, shown by the solid line in Figure 6.14(a), this being effectively due to a single shell.

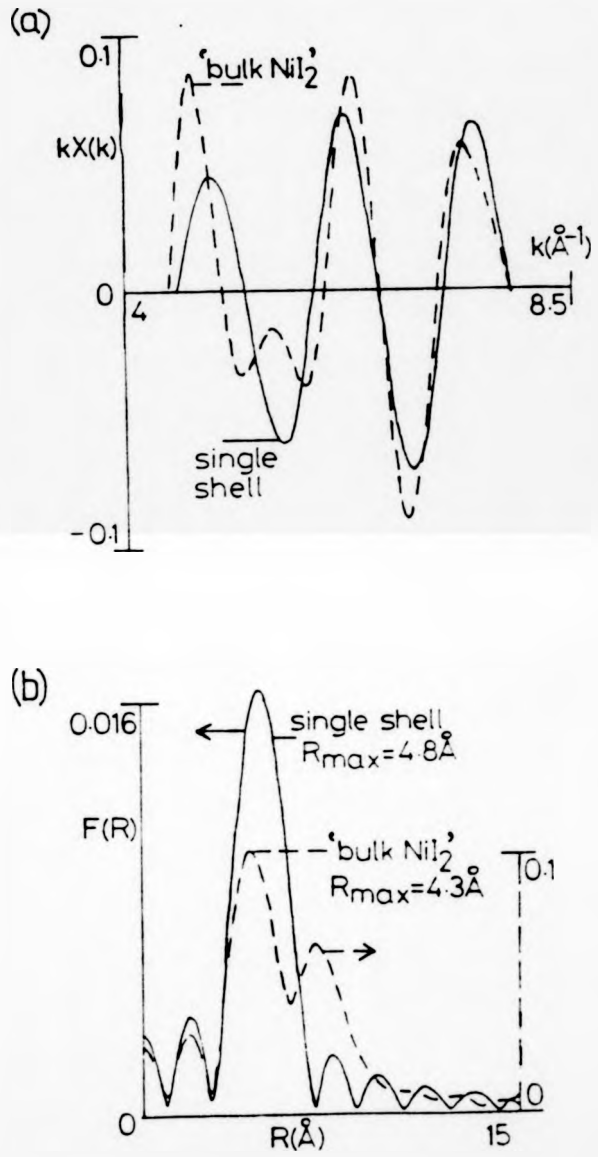

Fig. 6·14: Modelled EXAFS and |FT|'s

I-Ni distance = 2·78Å in both structures.

The Fourier transform moduli of the limited k-range of the two spectra, are shown in Figure 6.14(b). The single shell analysis method interprets the 0.5 Å difference in the R-values of the peaks as being due to the unknown compound having a bond length of r = 2.53 Å which is clearly incorrect by a significant amount: 0.25 Å. In practice, phase functions were derived from the Fourier-filtered EXAFS spectra of each compound and these were compared, enabling the Δr_1 value to be obtained to an accuracy of two decimal places (hundreths of angstroms).

It is important to check that the shifts in the positions of the main peaks of the surface NiI_2, and the c(2x2), c(2x8) and (2x3) overlayers, relative to that of bulk NiI_2, are due to real I-Ni bond length changes, or are due to differing interference effects from the different iodine shells in each of these structures (as postulated).

6.07 Analyses of Theoretically Calculated EXAFS Spectra of Postulated I-Ni(100) Structures; ΔE_o Problems

In order to check the validity of the derived I-Ni bond lengths for the various structures formed by the adsorption of iodine onto Ni(100), the EXAFS spectra were calculated, using postulated radial distribution functions and were analysed to see if the bond lengths could be correctly obtained.

For the surface nickel iodide structure (Figure 4.04), the appropriate radial distribution function is given in Table 6.03:

TABLE 6.03 - RADIAL DISTRIBUTION FUNCTION OF CENTRAL I IN SURFACE NiI_2-Ni(100)

4 Ni ATOMS at r_1 = 2.78 Å, $2\sigma_1^2$ = 0.01 Å^2		
9 I	3.93	0.03
3 Ni	4.78	0.03

The EXAFS was calculated from first principles, and found to match that of an experimental measurement (eg, Figure 6.03(a)) quite well. The Fourier transform modulus of the 'experimental' k-range was found to have a peak at R ≈ 4.5 Å - a full phase function analysis, derived a bond length 0.09 Å larger than the 2.78 Å of bulk nickel iodide. No variation in ΔEo was needed since both spectra were calculated from the same atomic phase shifts, ie ΔEo fixed at 11.0 eV, in equation 5.12.

Similar procedures were carried out for the c(2x2), c(2x8) and (2x3) I-Ni(100) overlayers containing the same I-Ni bond lengths of 2.78 Å, and the analyses produced the results shown in Table 6.04:

TABLE 6.04: RESULTS OF ANALYSES OF MODELLED EXAFS SPECTRA

STRUCTURE	COMMENTS ON MODELLING	MAX IN[FT]	I-Ni BOND LENGTH/CHANGE
Bulk NiI_2	excellent similarity to experimental spectrum.	R = 4.3 Å	2.78 Å
Surface NiI_2	Very good match of all features	4.5	+ 0.09 Å
c(2x2)	Reasonable match of 3 main peaks	4.8	+ 0.24
c(2x8)	1st maximum broadened as measured, but not good fit between peaks 2 and 3.	4.6	+ 0.15
(2x3)	Not a good match	4.8	+ 0.23

In most cases, the matches to the corresponding experimental spectra were very good, and when the fit was poor it was most likely due to poor experimental data - for example, the derived X(k) for c(2x8) I-Ni(100), never goes negative between the middle and last peaks (see Figure 6.07(a)), probably mainly due to an imperfect μo estimation. The systematic errors are significant in all cases, particularly for the c(2x2) structure, the 2.78 Å bond length, being predicted as 3.02 Å! For iodine atoms in hollow sites in this $\theta = {}^{1}/_{2}$ overlayer, the EXAFS is dominated by the nearest nickel shell, such that the situation is similar to that in section 6.06 and Figure 6.14 - in the case of the c(2x2) structure the main peak occurs at the expected R-value, whereas that for the bulk nickel iodide structure is displaced due to the interfering iodine shell (and the short data range), such that there appears to be a significant difference in the bond lengths in these two structures.

There is clearly another problem, since the results in Table 6.01, are all bond length contractions relative to bulk nickel iodide, whereas Table 6.04 predicts apparent expansions. One possibility is that the bond lengths in the surface structures are very much smaller than that in bulk nickel iodide, such that even with the introduction of apparent expansions, bond length contractions are still derived. This is unlikely. Since the atomic phase shifts are not correct, the zero intercept criterion is meaningless, and the gradient of the phase function difference is not equal to the bond length change. To get zero intercepts in the phase function differences, large positive ΔEo's are needed - for example, for the c(2x8) dataset number 802, the Eo point is 6 eV above the edge, compared to a point 4 eV below the edge in the reference compound, the derived bond length being 0.09 Å shorter than 2.78 Å, (see Table 6.01). It has been noted that changes in the k-scale origin of only

± 5 eV can cause significant shifts (ie ± 0.05 Å) in the derived nearest neighbour distance[16]. The situation can be described as follows: if the Eo point is chosen at a higher energy, then the EXAFS peaks move down to lower k-values, especially for the low k data, thus stretching out the EXAFS and making it appear to represent a shorter bond length.

It can be concluded, therefore, that the negative bond length contractions deduced by the Fourier-filtering and phase-function-comparison method are probably due to the large arbitrary ΔEo's needed to obtain the (meaningless) zero intercepts.

6.08 Review of SEXAFS Publications for Iodine Overlayers

Publications of SEXAFS work for iodine adsorbed onto single crystal substrates, exist for the following structures:

θ = 1/3, (√3x√3) R30° I-Ag(111); bulk AgI as reference compound[15]

θ = 1/3, (√3x√3) R30° I-Cu(111); bulk Cu I model[15,17]

θ = 1/2, c(2x2) I-Cu(110) ; bulk Cu I model[15]

θ = 1/4, p(2x2) I-Cu(100) ; bulk Cu I model[17]

It is of interest to check whether the analyses of SEXAFS spectra of these structures can yield accurate answers, since there are the potential problems due to the short data range and the high iodine backscattering factor. Since the reference compounds are tetratedrally co-ordinated structures with the iodine atoms surrounded by metal ions[18] the EXAFS spectra can be shown to be dominated by the first shell, the potentially troublesome iodine shell giving only a minor effect, such that the Fourier transform is able to correctly separate out these shells, enabling the I-Cu or I-Ag atomic phase shifts to be accurately determined. The above surface structures are also quite suitable for study via SEXAFS, since the low iodine coverages give rise to large I-I separations, enabling the I-metal bond lengths to be reliably determined.

The Fourier transform of one of the c(2x2) I-Cu(110) spectra (Figure 3(b),[15]) contains twin peaks at R ≈ 1.5 and 2.5 Å and is interpreted by Citrin et al[15], as being due to the 'Ramsauer-Townsend effect', hence proving that the nearest shell contains iodine atoms at r ≈ 2.7 Å and thus proving the existence of molecularly adsorbed iodine, the coverage being θ ≈ 1. Such a speculation has not been followed up since such a structure is thought to be unlikely - iodine molecules lying flat on the Cu(100) surface are simply too large to pack into the c(2x2) layer. Figure 6.02-6.08(b) show that low-R peaks can exist when the first shell is a light atom, such peaks simply being due to the short k-ranges, and the imperfect μo estimations. Indeed a model EXAFS calculation for such a c(2x2) overlayer of iodine molecules does not produce twin peaks in the Fourier transform modulus. The iodine backscattering factor, F(k), continuously decreases in value, up to k ≈ 7.5 $Å^{-1}$ (Figure 2.09[3]), such that a Fourier transform of the I-I EXAFS up to k ≈ 8.5 $Å^{-1}$, does not produce two peaks; only by simulating data up to k ≈ 15 $Å^{-1}$ and including this in this transform, does the 'Ramsauer-Townsend effect' appear, in which the low R peak has about half the amplitude of the main peak and decays gradually towards zero as k approaches 0 $Å^{-1}$, such a structure being characteristic of 'Ramsauer-Townsend peaks'.

An example of such a double peak appears in the Fourier transform modulus of an I-Ag SEXAFS spectrum - see Figure 1 in reference[15]. Again, it is hard to understand how this can be due to 'Ramsauer-Townsend effect', since the silver backscattering factor and phase shift are approximately linear functions up to k ≈ 7 $Å^{-1}$[3], and the SEXAFS spectra ends at k ≈ 7.5 $Å^{-1}$; a spectrum ending between 10 and 15 $Å^{-1}$ would be required to produce double peaks in the transform modulus.

Also in SEXAFS studies, there is sometimes the tendency to interpret high R peaks as being due to more distant shells of atoms, even when these peaks are smaller than the 'noise', such is the desire to link the 'frequency' spectrum with the radial distribution function.

6.09 References

1. If the adsorbate layer is as postulated in Figure 4.06, then it is not surprising that the EXAFS of the nearest shell cannot be isolated (and hence the phase function cannot be obtained), since the next shell of nickel atoms is sufficiently near to cause problems. EXAFS studies have severe limitations when applied to disordered systems, as explained in reference 2.

2. P Eisenberger, G S Brown, Solid State Communications 29, p 481, 1979:
'The study of disordered systems by EXAFS: limitations'.

3. Boon-Keng Teo and P A Lee, Journal of the American Chemical Society 101:11, May 1979, p 2815:
'Ab Initio Calculations of Amplitude and Phase Functions in EXAFS Spectroscopy'.

4. J Stöhr and R Jaeger, Surface Science 134 (1983) p 813:
'Structure of Ag on Si (111) 7x7 by SEXAFS'
- In this work the phase shift derived from a silver foil is found to be very similar to that calculated by Teo and Lee[3].

5. P A Lee, P H Citrin, P Eisenberger and B M Mincaid
Reviews of Modern Physics 53 number 4 part 1, October 1981, p 769:
"EXAFS - its strengths and limitations as a structural tool".

6. E A Stern, D E Sayers and F W Lytle, Phys Rev B11(12), June 1975, p 4836:
'EXAFS technique III - determination of physical parameters'.

7. P A Lee and G Beni, Phys Rev B15(6), March 1977, p 2862:
'New method for calculation of atomic phase shifts: application to EXAFS in molecules and crystals'.

8. M P Seah and W A Dench, NPL report, Chem 82, April 1978:
'Standard data base for electron inelastic mean free paths'.
- In the energy range k = 3.8 to 15.0 $\mathring{A}^{-1}$, λ_{imfp} increases approximately linearly from 3.8 to 15.0 $\mathring{A}$.

9. B A Bunker and E A Stern, Phys Rev B27(2), January 1983, p 1017:
'Phase factor in EXAFS'.
p 1020 states: 'two phases can be made to agree if... experimental phase is recalculated by changing its Eo origin to a more negative value ... shift in Eo introduced by breakdown of small atom approximation ... is - 13 eV'.

10. L I Schiff, 'Quantum Mechanics', Internation Student Edition, 2nd edition, McGraw-Hill, 1955:
Chapter V: Continuous Eigenvalues: Collision Theory.

11. E Hecht and A Zajac, 'Optics', Addison-Wesley, 1969:
p 202: Addition of waves of different frequency.

12. G Martens, P Rabe, N Schwentner and A Werner, Phys Rev Lett 39(22), November 1977, p 1411:
'EXAFS beats: A new method to determine differences in bond lengths'.

13. S Ainsworth and D P Woodruff,
'Multiple Bondlengths and Short Data Ranges in SEXAFS and EXAFS'
to be published Solid State Communications.

14. A Puschmann and J Haase, Surf Sci 144(1984), p 559:
'Surface EXAFS of the (2x1) oxygen adlayer on Ag(110)'
- 'Ag atoms in both the first and second layers contribute to the measured bondlength which then has to take a value between 2.06 and 2.17 Å'.

15. P H Citrin, P Eisenberger and R C Hewitt, Surf Sci 89(1979), p 28:
'SEXAFS studies of iodine adsorbed on single crystal substrates'.

16. A P Hitchcock and C H Teng, Surf Sci 149(1985) p 558:
'Extended energy loss fine structure in reflection energy loss spectra of Cu and Ni'.

17. P H Citrin, P Eisenberger and R C Hewitt, Phys Rev Lett 45(24), December 1980, p 1948:
'Adsorption sites and bond lengths of iodine on Cu(111) and Cu(100) from SEXAFS'.
Errata: Phys Rev Lett 47(21), November 1981, p 1567.

18. R W G Wyckoff, 'Crystal Structures', 2nd edition, volume 1, 1965:
p 108: Tetrahedrally coordinated structures
III, c1: The zinc sulphide arrangement.

CHAPTER 7

MULTI-SHELL MODELLING ANALYSIS METHOD ILLUSTRATED BY APPLICATION TO THE I-Ni (100) STRUCTURES

7.01 OVERVIEW

In this chapter, a multi-shell modelling analysis method is described, and is applied to the deduction of the structures present in the surface iodide, and in the c(2x2), c(2x8), and c(2x3) iodine overlayers on Ni (100). This serves as an illustration of the technique, as could be applied to to any EXAFS analysis for a structural derivation.

The basic modelling approach is as follows:-

(i) Measure the EXAFS or the SEXAFS from a compound of known structure - the model compound.

(ii) Theoretically calculate the atomic phase shifts for this compound, using a muffin-tin potential model of the solid.

(iii) Theoretically calculate the EXAFS from the known structure and the calculated phase-shifts.

(iv) If this calculation cannot be made to match the experimental EXAFS, iterating various non-structural parameters, then the phase-shifts are not correct.

(v) Iterate the phase-shifts until the match is as close as can be obtained, at which point the phase-shifts can be regarded as correct.

(vi) Set up a guessed structure, corresponding to a spectrum, and calculate the EXAFS using the above atomic phase-shifts, allowing Eo to vary.

(vii) Allow the structural parameters to vary to achieve a match.

(viii) If this fit is better than for any other postulated structure, if the structure is still a real geometrical possibility, and if the non-structural parameters are physically reasonable, then the structure can be said to be derived.

7.02 The Model Compound and the Derivation of the Atomic Phase-Shifts

In order to derive the bond lengths in a set of unknown structures, in this example various I-Ni (100) structures, the atomic phase-shifts, ie those for a central iodine atom (with a core hole), and backscattering nickel and iodine atoms, need to be derived from the EXAFS of a model compound, eg bulk nickel iodide (NiI_2).

Bulk NiI_2 has the cadmium chloride structure[1], in which the iodine atoms lie in hexagonal close packed layers, laying on top of each other to form a cubic close packing of iodine atoms; the smaller nickel atoms are hexagonally close packed in layers between every second iodine layer - Figure 4.03(a, b). Each iodine atom has 6I neighbours in its own hcp layer at distances of 3.89 Å, 3I atoms in the layer above and 3I in the layer below all at 3.97 Å, the nearest neighbours being 3 Ni atoms at 2.78 Å, and there being 3 Ni atoms in the same interlayer at 4.78 Å; there are no other atoms within 5 Å - Figure 4.03(c).

The atomic phase-shifts have been obtained using the Daresbury computer program 'MUFFPOT'[2, 3]. This program requires various inputs:-

(i) The crystal structure eg, bulk NiI_2;

(ii) the atomic wavefunctions (in Clementi format) of the central and backscattering atoms;

(iii) the Madelung correction factor for each atom - zero for elements and covalent compounds; a number equal to the atomic valency in ionic compounds;

(iv) the muffin-tin radius of each atom.

Since in the EXAFS process, a core hole is created in the central atom, the electronic structure resembles that of the next atom in the periodic table, thus for the I L_{III} EXAFS of bulk NiI_2, Xenon was used to represent a singly ionised iodine atom.

The theoretically calculated atomic phase-shifts then need to be checked for reliability. This is one of the uses of the program 'EXCURVE'[4, 5]. The atomic phase-shifts are each calculated as the individual l-components (l=0 to 13) as functions of photo-electron energy, E. Within 'EXCURVE' these phase-shifts are multiplied by (A + BE), where A ≈ 1.000, B ≈ 0.005, E in eV, such that the EXAFS calculated using these iterated phase-shifts and the known structure of a model compound, match an experimentally measured EXAFS spectrum. Iterating to the bulk NiI_2 dataset 834, has produced the atomic phase-shifts for the central iodine ion, and backscattering nickel and iodine atoms, labelled CAI, BSN, BSI in this thesis - Figure 7.01.

In all uses of the program, there are a number of variable parameters:-

(i) Eo, the energy in eV of photoelectrons at the absorption edge - in general, equal to the Fermi energy, E_F. Eo can be varied if the atomic phase-shifts are inexact. Eo is typically a few eV.

(ii) VPI, the constant imaginary potential used to describe the finite lifetime of the photoelectron; in other

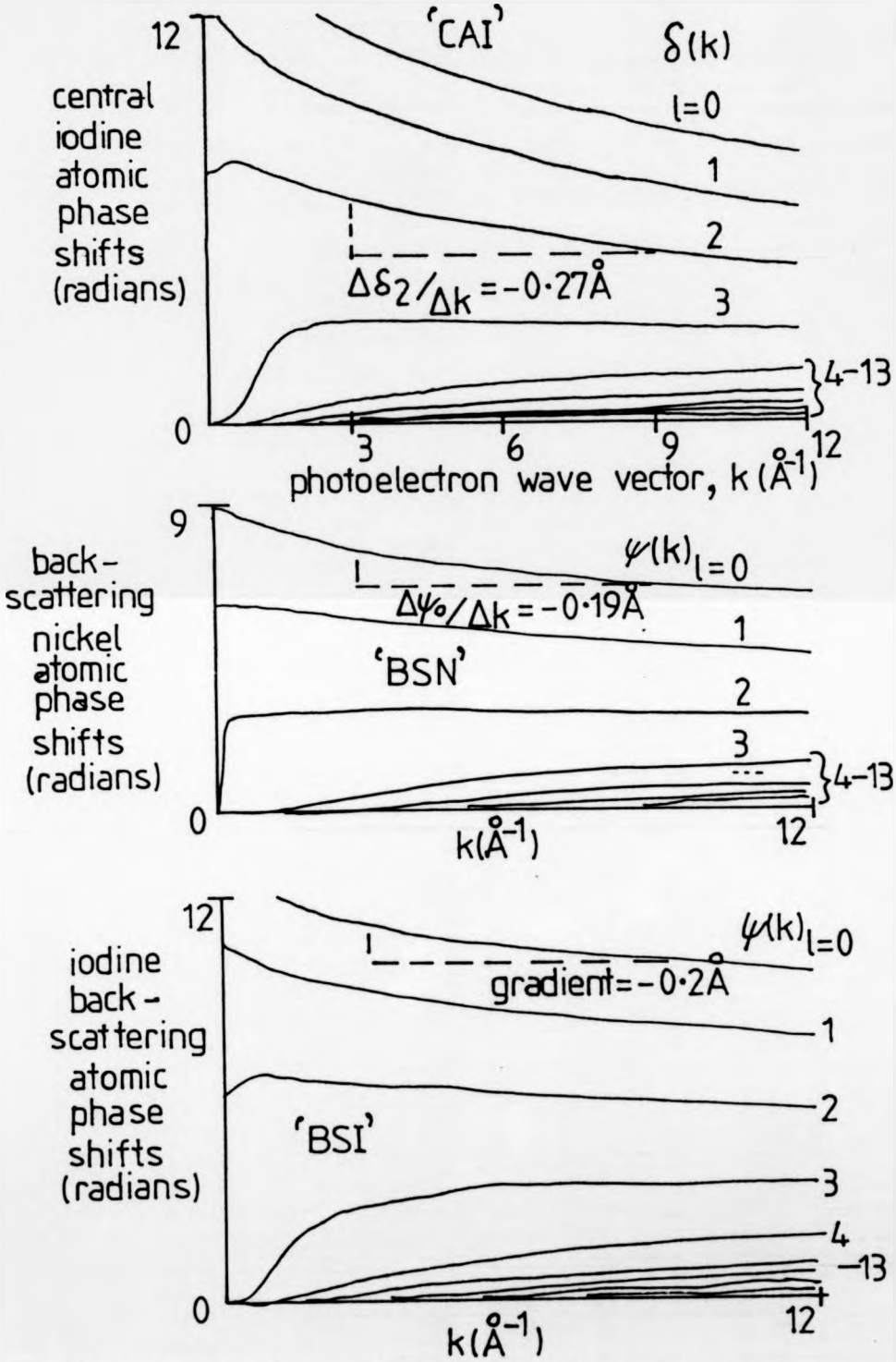

Fig.7·01: Atomic phase shifts of iodine L_{III} photo-electron.

words a mean free path that is proportional to k. VPI can have values between - 1 and - 5 eV; - 4 eV corresponds to a mean free path of 4 Å for photoelectrons, $k \approx 6$ Å^{-1}.

(iii) AFAC, the energy-independent amplitude factor used to account for the reduction in the EXAFS amplitude due to multiple excitations, shake-up in the photo-ionisation process, and Auger emission[6]. Allowed values range from 0.3 to 1.0.

The program also requires estimations of the Debye-Waller factors. In all the work described in this thesis, the Debye-Waller factors were fixed: $2\sigma_1'^2 = 0.01$ Å^2 ($\sigma_1' \approx 0.7$ Å), $2\sigma_n'^2 = 0.03$ Å^2, n = 2, 3 ... ($\sigma_n' \approx 0.12$ Å), these being the accepted values[7-9]. Accounting for correlated vibrations has the effect of reducing the EXAFS contributions from more distant shells relative to the nearest shell.

The second use of EXCURVE is to deduce unknown structures. A structure is postulated and the EXAFS is calculated for each shell of atoms, the total EXAFS being the sum of these contributions. Since the EXAFS magnitude falls of rapidly with distance, a definition of all the shells within r = 5 Å is adequate. Figure 7.02 shows the result of such a calculation and comparison with a measured spectrum. The experimental EXAFS has been obtained from dataset 833, having gone through the steps of energy calibration, background subtraction and μ_0 estimation. Eo has been optimised, ie a photoelectron energy of 6.3 eV at the absorption edge has the effect of 'lining-up' the experimental and theoretical spectra. It is important to comment at this point, that this Eo of + 6.3 eV corresponds to an energy-zero that is 6.3 eV below the edge within the notation introduced in Chapter 5 (the Fourier-filtered single-shell analysis method). The two other variables, VPI and

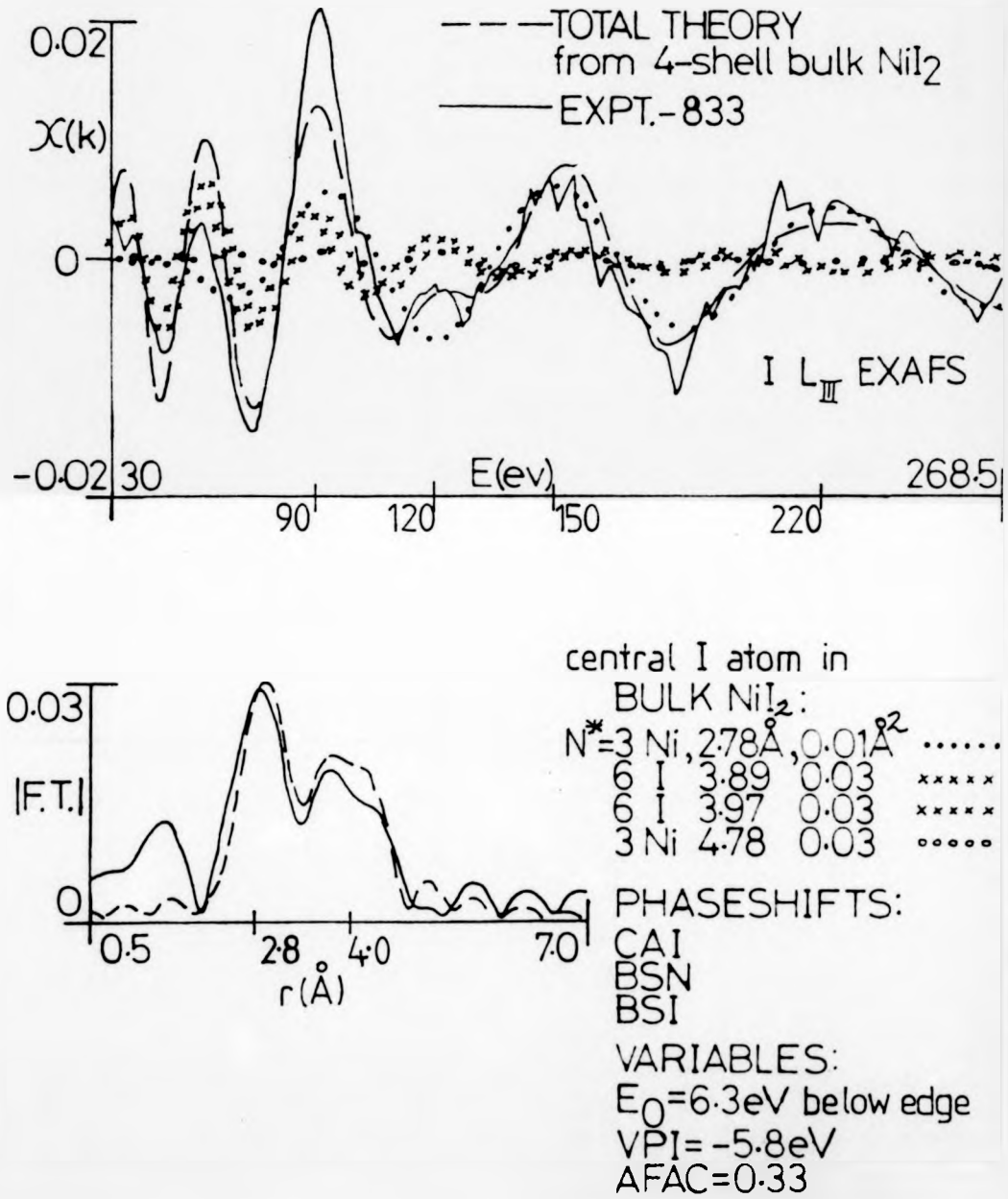

Fig. 7·02: χ(k) and Fourier transform modulus for bulk NiI_2.

AFAC, have been adjusted to optimise the match (Figure 7.02) and remain physically sensible. Whilst the fit is very good, it is not quite optimised, since the atomic phase-shifts were obtained from a different bulk NiI_2, dataset - 834. The phase-shifts were allowed to vary to optimise to dataset 833, these being named EXOUTB0, EXOUTB1, and EXOUTB2, for central iodide, backscattering nickel, and backscattering iodine, respectively. They differ from CAI, BSN and BSI, below 60 eV where the extraction of the EXAFS function is unreliable, but this is unimportant since single scattering theory does not apply at these low energies.

The differences in the two sets of phase-shifts give an indication of their uncertainty. Using, as input to EXCURVE, the bulk NiI_2 structure, EXOUTB0, 1 and 2, and the dataset 833, and allowing the structure to vary (along with Eo, AFAC and VPI) caused the following changes to be made:-

$\Delta r_1 = + 0.01$ Å; $\Delta r_2 = - 0.04$ Å, $\Delta r_3 = - 0.04$ Å.

It therefore appears that such phase-shifts can be used to analyse the spectra of unknown structures with accuracies typical of these reported using the Fourier-filtering approach, one publication [10], quoting a second nearest neighbour determination. Eo, VPI, and AFAC were found to differ by less than 10% (0.3 eV, 0.5 eV, and 0.03 respectively), suggesting that such parameters can also be accurately determined.

The multi-shell modelling method is useful for showing the individual shell contributions to the total EXAFS. For the example of bulk NiI_2, the three main peaks at 90, 150 and 220 eV (Figure 7.03) can be seen to be derived mainly from the nearest nickel shell, whilst the iodine shells cause the 90 eV peak to have a (previously inexplicable) large amplitude, and give rise to the 'mini-peak' at 120 eV. The more distant nickel shell contributes very little.

7.03 The Derivation of an Unknown Structure: Surface Nickel Iodide

Quite a bit is known about the surface iodide structure from LEED and AES work, the postulated structure being shown in Figure 4.04. This structure ($\beta = 61^{o}$, $b_1 = 3.9$ Å, $b_2 = 4.0$ Å) was used as a starting point, the radial distribution function around an iodine atom being given in Table 7.01:-

Shell 1 = 4 N_i atoms	at 2.78 Å,	Debye-Waller factor = 0.01 Å^2
2 = 4 I	4.01	0.03
3 = 2 I	3.89	0.03
4 = 3 I	3.97	0.03
5 = 3 N_i	4.78	0.03

TABLE 7.01: THE POSTULATED STRUCTURE OF SURFACE NICKEL IODIDE

Iodine atoms in the layer next to vacuum, and that next to the substrate have slightly different environments, such that the above distribution function is an average; for example, in the top layer, each iodine has three nickel nearest neighbours, whereas for the layer beneath, each iodine atom is also bonded to the N_i (100) surface, with an average co-ordination of around two (equal numbers of atoms in hollow, bridge and atop sites), thus having a co-ordination number of five, making the grand average co-ordination number to be four.

Figure 7.03 shows the results from EXCURVE, the structural parameters (r_1 to r_5) having been allowed to vary, along with the non-structural ones (Eo, VPI, and AFAC). The experiment dataset, 794, was taken with the ‹100› vector of the N_i (100) surface being horizontal, with the plane polarized X-ray beam being incident normally to this surface, thus the shell description of the

SURACE NiI_2-Ni{100}
derived structure:

N*	atomic-type	radial distance(Å)	shift from model(Å)
4·0	Ni	2·77	−0·01
4·6	I	3·99	−0·02
2·3	I	3·93	+0·04
3·0	I	3·94	−0·03
3·0	Ni	4·92	+0·14

E_o = 4·0eV below edge, VPI=−5·2eV, AFAC=0·33
atomic phase shifts: CAI, BSN, BSI

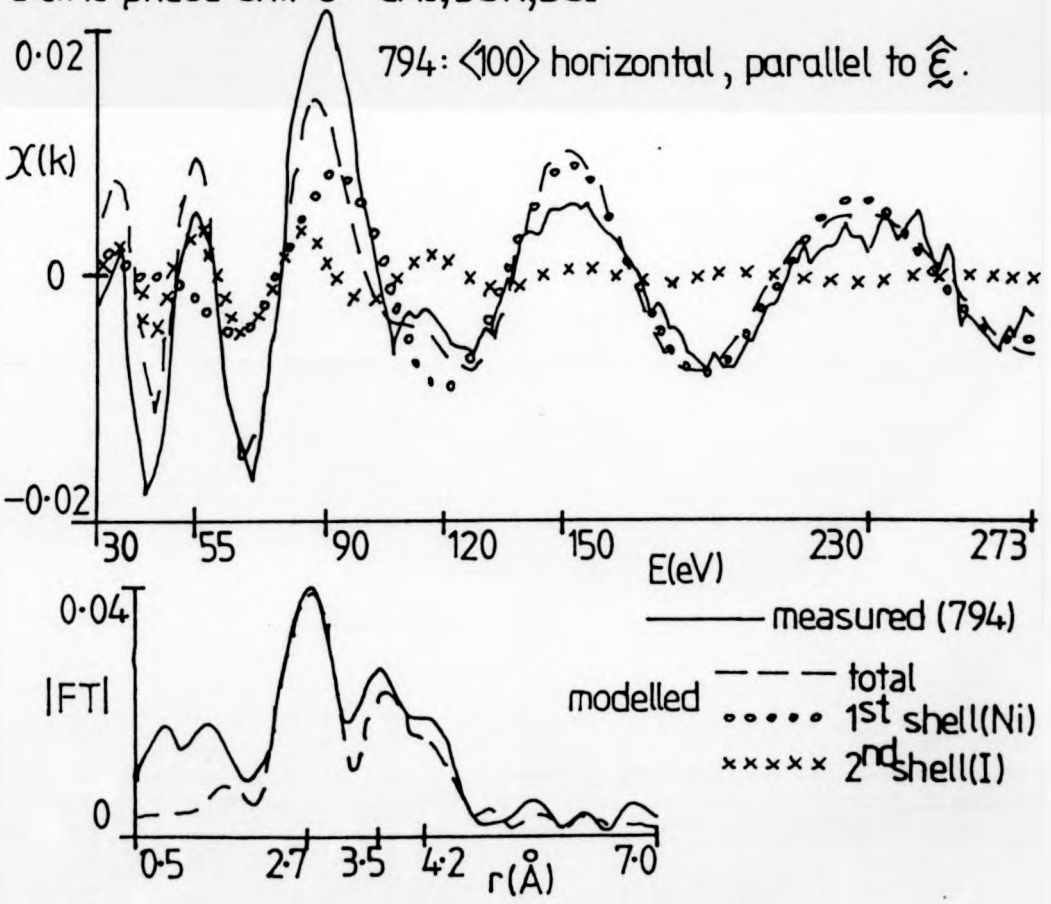

Fig. 7·03: Measured and optimised modelled spectra for surface NiI_2-Ni{100}.

postulated structure is based upon the effective co-ordination numbers for the appropriate geometry, the L_{III} edge equation (Equation 2.18) having been used for such a calculation. The good fit between theory and experiment confirms that the postulated structure is almost certainly correct, the only significant change needed being Δr_s = + 0.14 Å, but since this shell contributes very little to the EXAFS, such a displacement need not be a genuine structural change. It is re-assuring that the parameters, AFAC and VPI are very similar to those in the bulk NiI_2 iterations, and the very similar Eo suggests little chemical difference between the iodine atoms in each of the two structures.

The three iodine shells are not resolvable, therefore it is not possible to conclude that any I-I spacings are different from those in the postulated structure. The observed change in the I-N_i bond length is - 0.01 Å, which is probably not significant. There is no quantitative way of estimating the uncertainties in the derived values (one could vary parameters and observe when the fit becomes visually unacceptable), hence it is necessary to analyse many spectra and to look at the spread of values obtained.

A surface EXAFS spectrum taken from a surface nickel iodide sample, with the electric vector at 45° to the horizontal ‹100› vector is shown in Figure 7.04, along with the structural optimisation. Such a spectrum (823) is typical of those taken at this orientation, the iodine mini-peak being shifted to an energy greater than 120 eV - since more weighting is given to I-I scattering across planes (compare the effective numbers of atoms per shell in Figures 7.03 and 7.04), this suggests that the layer spacing is slightly less than that postulated.

SURFACE NiI_2 – Ni{100}

N^* = 4·0	Ni atoms at	r = 2·777 Å	adjustment = −0·003 Å
3·5	I	3·95	−0·06
1·7	I	3·887	−0·003
3·2	I	3·93	−0·04
3·0	Ni	4·72	−0·06

E_o = 2·7eV below edge , VPI = −4·0eV, AFAC = 0·34

atomic phase shifts = CAI, BSN, BSI

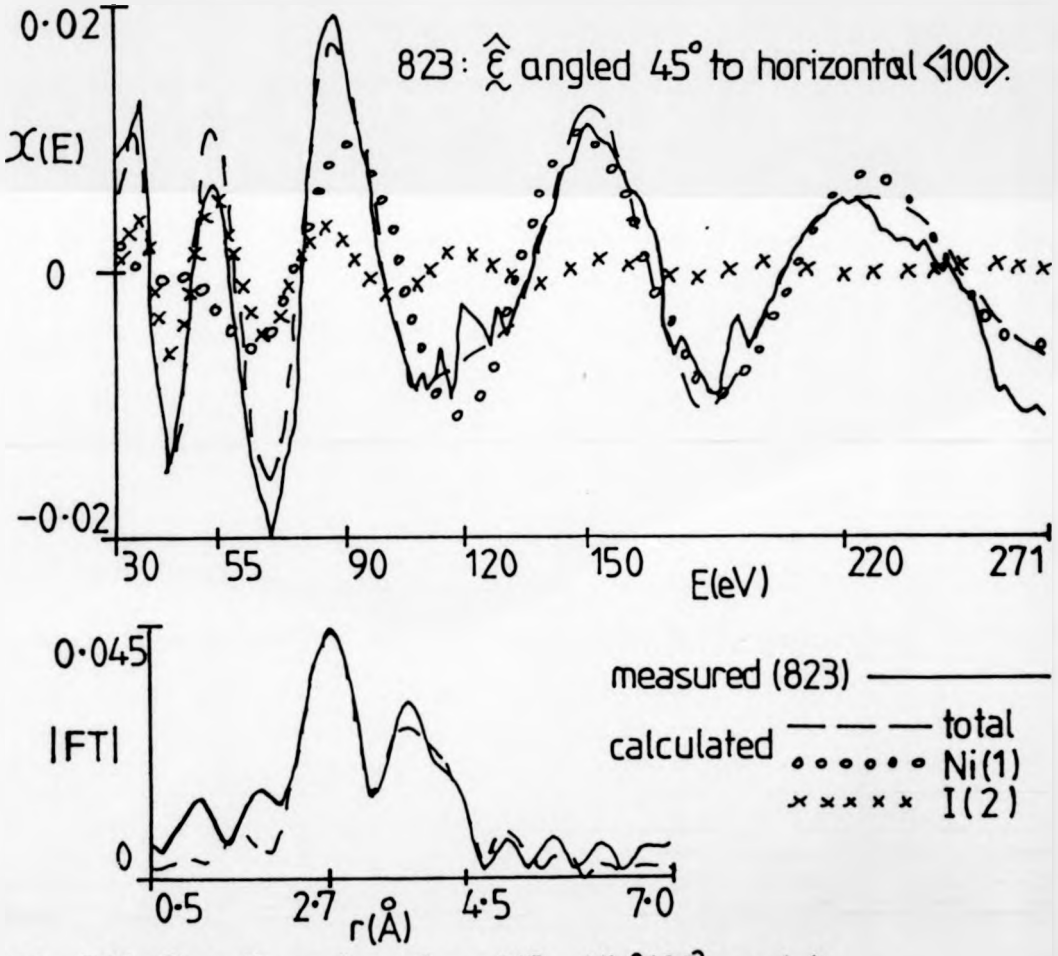

Fig. 7·04: Iteration of surface NiI_2 – Ni{100} model.

Results for all the analyseable SEXAFS spectra of the surface nickel iodide structure are given in Table 7.02, along with the results for other structures.

Other postulated structures were used to attempt to reproduce the surface nickel iodide spectra; bulk NiI_2 and distorted bulk NiI_2 ($\beta = 61^{o}$) were found to give poorer (but still quite reasonable) fits, and again showed no major changes in the I-Ni spacing.

With a normal incidence X-ray beam, and the surface nickel iodide - Ni (100) orientated with the <110> vector horizontal, an inexplicably large EXAFS amplitude was obtained. Comparison of the VPI and AFAC parameters (Table 7.02) suggest that the crystal movement may have brought a region of c(2x2) I-Ni (100), (which can co-exist with surface nickel iodide at room temperature), into the X-ray beam.

7.04 C(2x2) I-Ni (100): Structural Derivation

The $\theta = 1/2$ iodine overlayer on Ni (100) is characterised by a c(2x2) LEED pattern, hence the iodine overlayer consists of a square mesh of iodine atoms, of side $\sqrt{2}$ times the square mesh side of the Ni (100) surface, the square being rotated 45^{o} relative to the substrate square. Unknown parameters are the positioning of this overlayer onto the substrate, (and hence the adsorption site), and the height above the top substrate layer (hence the bond lengths). EXAFS analysis is particularly sensitive to these parameters.

Figure 4.05 shows the c(2x2) I-Ni ($\bar{1}$00) structure, with the iodine atoms in hollow adsorption sites; also shown is the radial distribution fuction around a central iodine atom. The radial distribution functions for hollow, bridge, and atop adsorption sites are given in Table 7.03, assuming that the I-Ni bond distance is 2.78 Å.

Table. 7·02 : I-Ni{100} multi-shell modelling results

I-Ni structure and orientation	SEXAFS spectrum	E_o point (eV) rel. to edge	VPI (eV)	AFAC	bond length /change (Å)	derived I-I distance (Å)	comments
bulk NiI_2	834	6·0 below	−6·3	0·36	2·78		– CAI, BSN, BSI phase shifts
	833	6 3 below	−5·8	0·33	2·78		– EXOUTB0,1,2 derived
surface NiI_2-Ni{100}							
⟨100⟩ horizontal, $\tilde{\varepsilon}$ at 45°	823	3 below	−4	0·34	−0·003	3·93	CAI, BSN, I used in analyses
" " , normal incidence	794	4 below	−5	0·33	−0·01	3·96	
" " "	796	3·5 below	−5·6	0·30	−0·02	3·94	– data ends 240eV above edge
⟨110⟩ horiz^{l} " "	797	4 below	−8	0·48	−0·03	3·95	N_1^* = 6·0
" " " "	798	3·5 below	−7	0·49	−0·02	3·94	
θ = ½ c(2×2)I-Ni{100} I's in hollows							
⟨100⟩ horiz^{l}, $\tilde{\varepsilon}$ at 45°	829	5 above	−6	0·37	−0·01	3·32	– EXOUTB0,1,2
" "	"	6 above	−5	0·42	−0·003	3·37	CAI, BSN, I used
" "	830	8 above	−7	0·40	±0·00	3·42	"
" , normal incidence	831	5 above	−7	0·38	−0·02	3·32	"
" "	817	7 above	−7	0·49	+0·02	3·37	– EXOUTB0 1 2
θ = ⅜ c(2×8)I-Ni{100}							
⟨100⟩ horiz^{l}, normal incidence	803	3 above	−4	0·38	−0·07	4·10	CAI, BSN, I {hollow/mid/
" "	811	3 above	−6	0·62	−0·05	4·16	EXOUTB0,12} bridge
" "	"	6 above	−1	0·34	−0·01	4·37	" hollow/bridge
θ = ⅓ (2×3)I-Ni{100}							
⟨100⟩ horiz^{l}, normal incidence	821	4 above	−2	0·43	−0·01	4·35	CAI, BSN, I hollow/bridge
" "	820	4 above	−5	0·37	+0·006	4·48	EXOUTB0,12 {hollow/mid/
" "	"	1 above	−6	0·42	−0·01	4·08	" } bridge

Note: I-I spacings can be shown to be 3·52, 4·13 and 4·50Å for θ = ½, ⅜ and ⅓.

I-site	shell			r(Å)	$2\sigma^2$(Å^2)
hollow	1st	4	Ni atoms	2·78	0·01
	2nd	4	I	3·52	0·03
	etc.	1	Ni	3·91	"
		4	Ni	4·64	"
		8	Ni	4·98	"
		4	I	4·98	"
bridge		2	Ni	2·78	0·01
		4	I	3·52	0·03
		4	Ni	3·73	"
		2	Ni	4·43	"
		2	Ni	4·49	"
		4	I	4·98	"
atop		1	Ni	2·78	0·01
		4	I	3·52	0·03
		4	Ni	3·73	"
		4	Ni	4·49	"
		4	Ni	4·87	"
		4	I	4·98	"

Table 7·03 : Radial distribution functions of I atoms in $\theta=1/2$ c(2×2)I-Ni{100} for 3 adatom sites.

Each of these structures was used as a basis for an EXAFS calculation using EXCURVE, with the non-structural parameters being allowed to vary to attempt to match each of these theoretical calculations with a measured SEXAFS spectrum (dataset 829), the results being shown in Figure 7.05. Looking at the $\chi(k)$ spectra, it can be seen that only the hollow site gives a reasonable fit - in such a site the high co-ordination number causes the EXAFS to be a single oscillation arising from the I-N_i distance. In the other two sites, higher 'frequency' oscillations show up due to the increasing relative effects of the more distant shells.

The bridge and atop sites can therefore be ruled out, since these sites contain shells of atoms that produce EXAFS oscillations that do not appear in the measured spectra, this adsorption site determination being similar to those based upon the measurements of second shell distances within Fourier-filtering analyses[10, 11].

The Fourier transform magnitudes and the AFAC values also show that the hollow site is the only likely candidate. For the bridge and atop sites, the main peak due to the nearest nickel shell is smaller than that observed, despite AFAC being adjusted to 0.54 and 0.81, respectively. The previous consistent AFAC values of between 0.3 and 0.5 for bulk N_iI_2, the surface nickel iodine and the $\theta = 1/2$ hollow-site structure, suggest that the high values have arisen from an attempt by the program to make the EXAFS from two and one nickel atoms appear like that from four atoms. Such a procedure is analogous to site determinations via the absolute amplitudes of the EXAFS spectra of surface structures compared to that of a model compound[10, 12].

In order to make the site determination more convincing, each of the postulated structures was allowed to vary to attempt to match dataset 829. Starting with the hollow site structure, a very

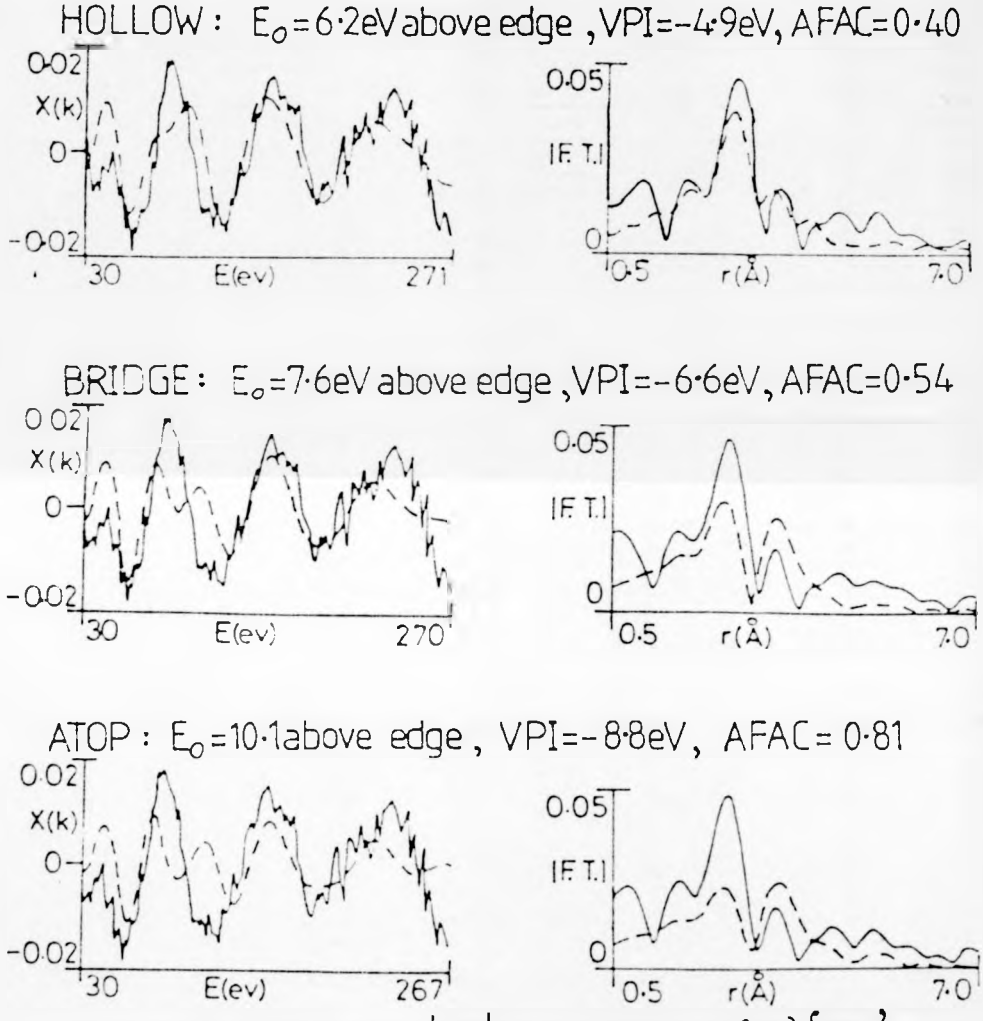

Fig. 7·05 : Adsorption site determination via SEXAFS

good match is obtained - Figure 7.06 - for only minor adjustments of the shell distances, the one exception being the nearest iodine shell. Figure 7.07 shows that the total EXAFS is built up almost entirely from the nearest nickel shell, the nearest iodine shell contributing largely to the peak at 50 eV - both the μ_o estimations and the atomic phase-shifts are very unreliable at energies below 70 eV, and hence it is not surprising that the optimisation of a parameter (the r_2 value) to this one feature (the 50 eV peak), gives an inaccurate result. Also, since the Eo value optimisation tends to be dominated by the largest features in the EXAFS, these being the three oscillations arising from the nickel shell, there may well be an Eo offset remaining for the iodine shell, since Eo adjustments should be made independently for each shell[13]. The single Eo adjustment made using the multi-shell modelling method, therefore limits the potential accuracy for the distance determinations of the more distant shells, but this should not be important since an error in Eo of 5 eV should not produce errors larger than $\Delta r = 0.05$ Å. Indeed even if the uncertainty, in the I-I spacing is 0.20 Å, it should still be possible to identify whether a structure is $\theta = 1/2$, $\theta = 3/8$, or $\theta = 1/3$ I-N_i (100), by an analysis of its SEXAFS spectrum, since the I-I spacings in these c(2x2), c(2x8) and (2x3) overlayers are very different: 3.52, 4.13 and 4.50 Å, respectively.

A poorer fit is obtained from the bridge-site model - Figure 7.08 - and a number of indicators suggest that this structure is not correct: the AFAC value needs to be 0.64 (approximately twice the value of the hollow site AFAC); and some of the shells have moved by large distances in order to supply contributions that make the total EXAFS appear as the experimentally measured spectrum - Figure 7.09. Since such a structure cannot in reality exist (realistically sized atoms cannot be packed into such an arrangement of shells) it must be

iterated from c(2×2) hollow — — — —

4·4 Ni atoms at	2·77Å	change = −0·01Å
3·7 I	3·28	−0·24
1·2 Ni	3·83	−0·08
4·6 Ni	4·73	+0·09
8·2 Ni	5·06	+0·08
3·7 I	5·19	+0·21

phase shifts = exoutb0,1,2

$E_o = -4.6$eV VPI = −5·9eV AFAC = 0·37

to match experimental dataset 829 ———

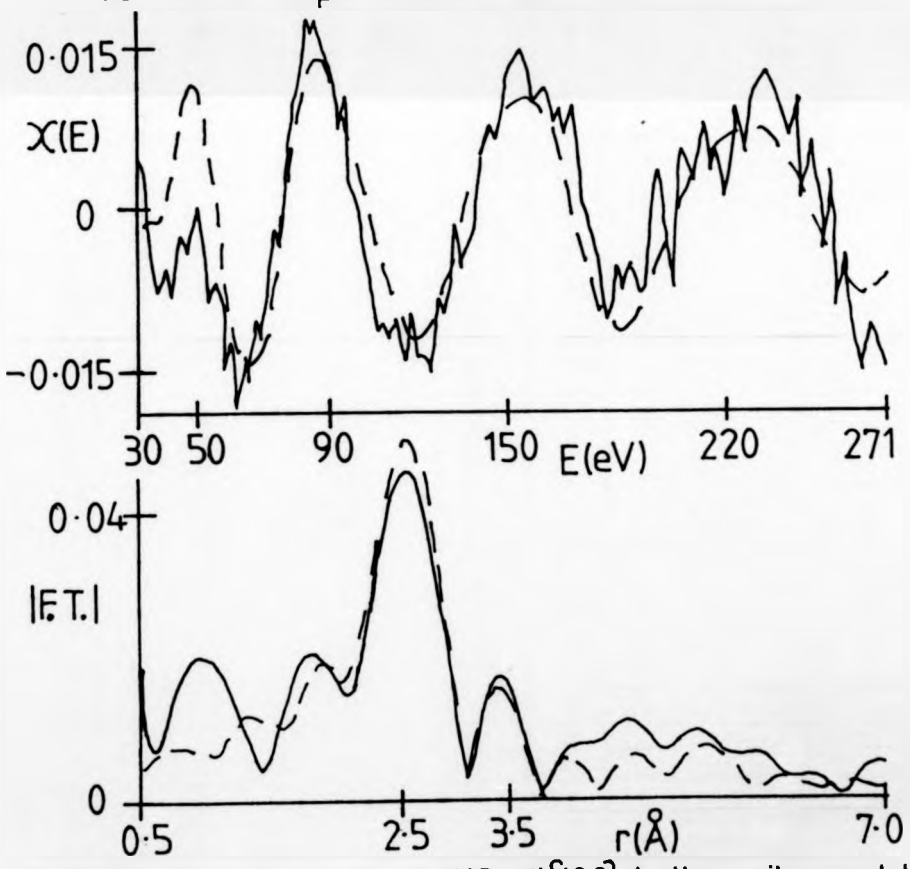

Fig. 7·06: Iteration of c(2×2)I-Ni{100} hollow site model.

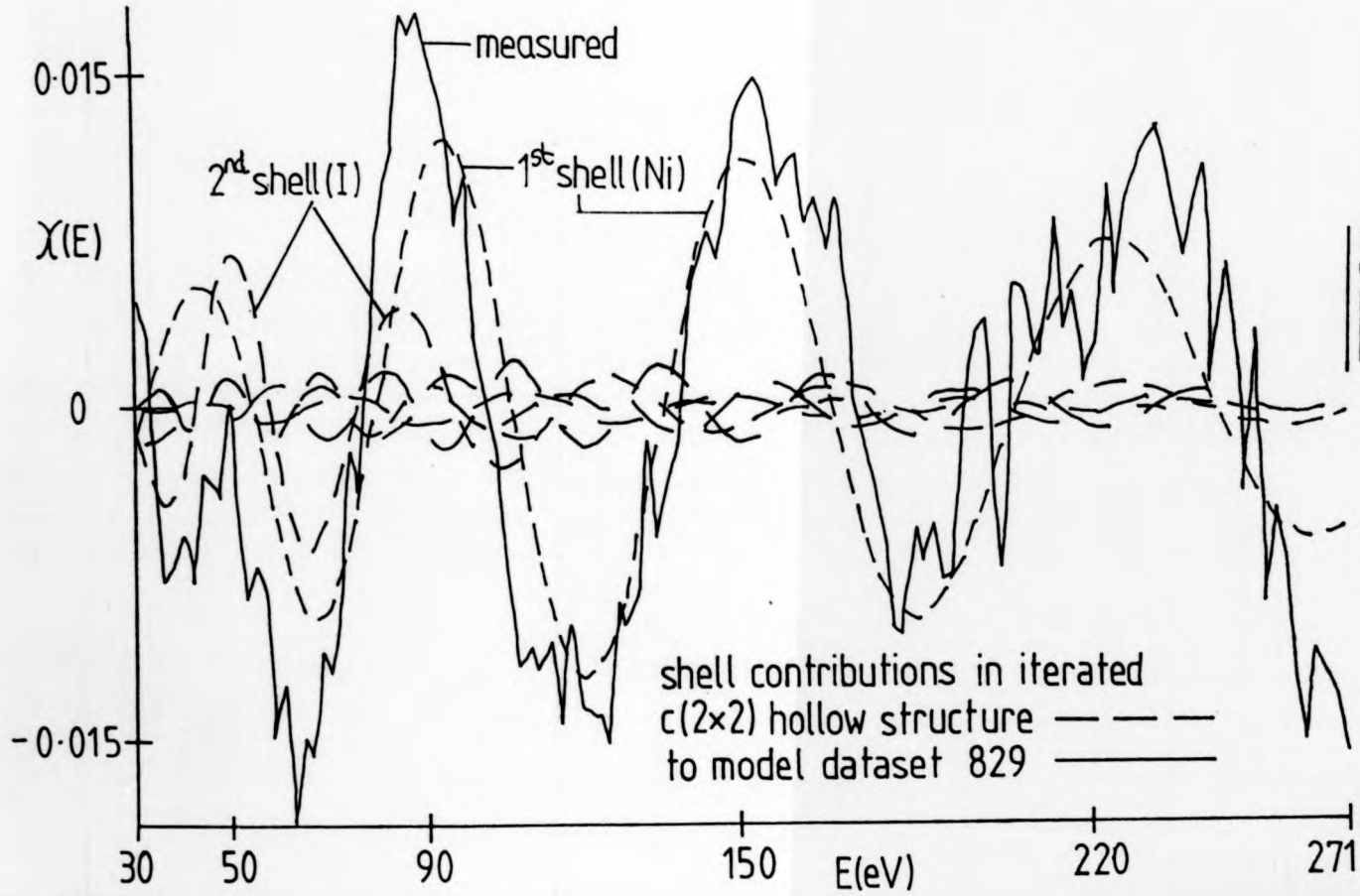
measured
0·015
2nd shell (I)
1st shell (Ni)
χ(E)
0
-0·015
shell contributions in iterated
c(2×2) hollow structure — — —
to model dataset 829 ———
30
50
90
150
E(eV)
220
271

Fig. 7·07

Fig. 7·08.

— — — — c(2×2)-bridge structure iterated

E_0=−7·5eV VPI=−5·4eV AFAC=0·64

shell 1 =	2·2 Ni atoms at	2·79Å	movement=+0·01Å
2	3·7 I	3·53	+0·01
3	4·4 Ni	3·56	−0·17
4	2·0 Ni	4·25	−0·18
5	2·2 Ni	5·14	+0·65
6	3·7 I	4·79	−0·19

atomic phase shifts = EXOUTB0,1,2

iterated to dataset 829 ————

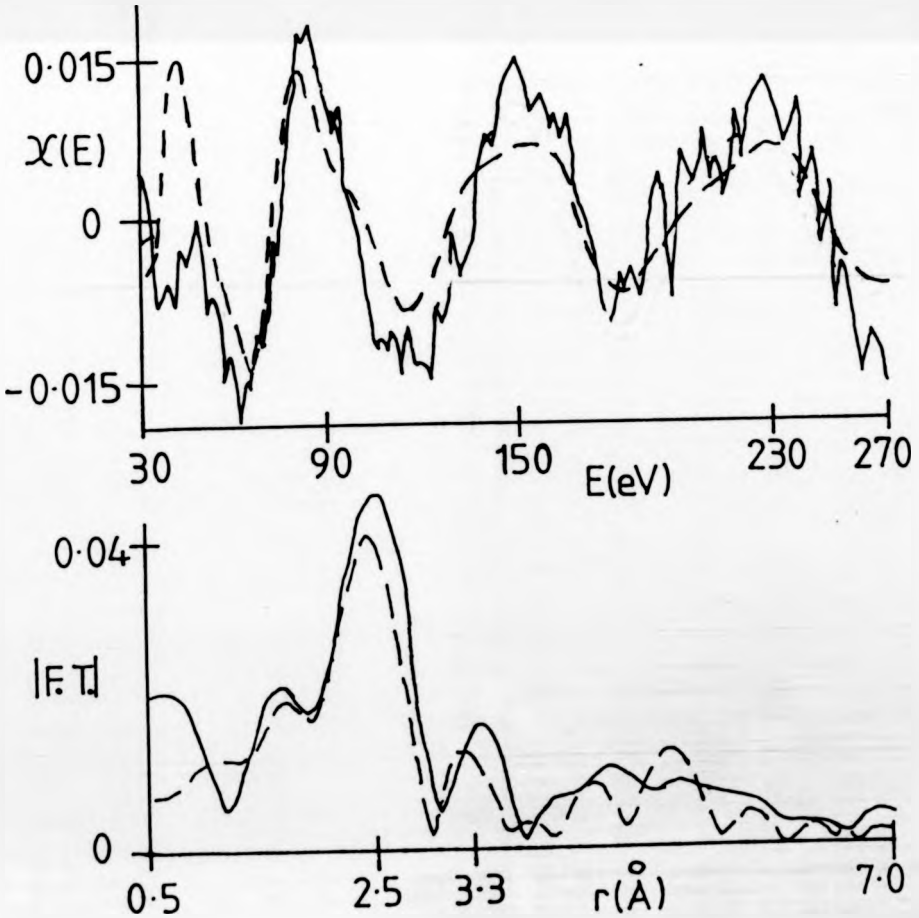

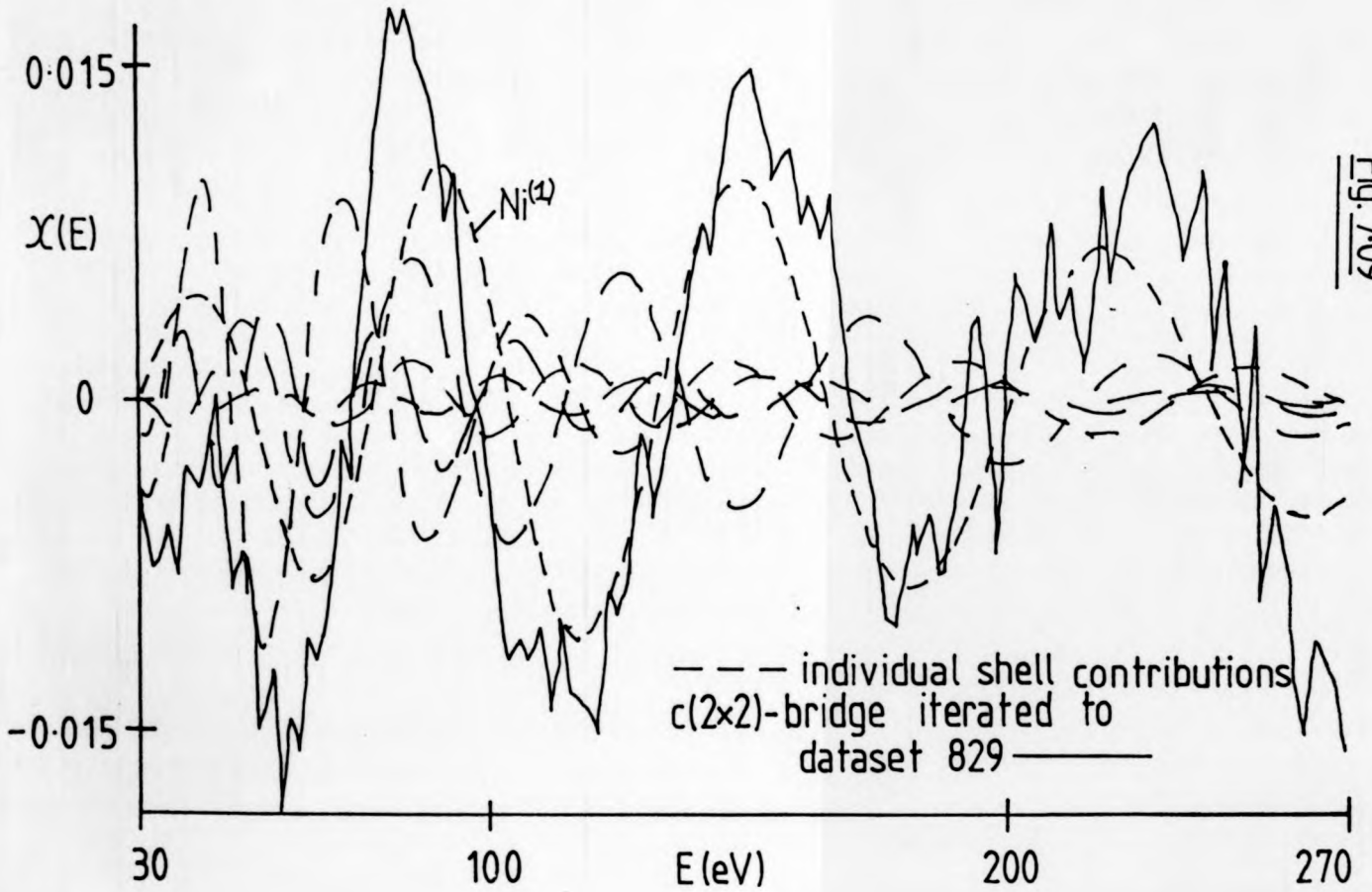
0·015
χ(E)
0
-0·015
Ni(1)
— — — individual shell contributions
c(2×2)-bridge iterated to
dataset 829 ———
30
100
E(eV)
200
270

Fig. 7·09

discounted. For the atop site, an even poorer match is reached (Figure 7.10), the amplitudes not matching despite AFAC being 1.0 (the computer software does not allow a higher value), and the shells having major adjustments to build up the total EXAFS (Figure 7.11) in a purely arbitrary fashion.

A number of other starting structures, such as the surface nickel iodide structure, were also investigated, but these were all found to give worse fits. The results for the hollow site iterations to various experimentally measured spectra are shown in Table 7.02, there being no measurable change in the I-N_i bond length of 2.78 Å, but the ΔE_o values being around + 10 eV relative to bulk nickel iodide.

The ΔE_o optimisation in this multi-shell modelling approach is analogous to that in the Fourier-filtering method and similar ΔE_o values result (compare Tables 7.02 and 6.01).

Notice in the Fourier transform modulus of the c(2x2) dataset 829, that the main peak lies at $r \approx 2.5$ Å, (Figures 7.06, 7.08 and 7.10 all show the same experimental functions), whearas for the bulk and surface nickel iodide structures the I-N_i peaks lie at $r \approx 2.7$ Å. An analysis based on the positions of these peaks would therefore predict a shorter bond length in the c(2x2) structures; the multi-shell modelling technique is not susceptible to such errors.

7.05 C(2x8) I-N_i (100): Structural Derivation

For an iodine coverage of $\theta = 3/8$, a c(2x3) LEED pattern can be observed, one consistent overlayer on the N_i (100) surface being shown in Figure 4.02(b) and Figure 4.06(a), the radial distribution function of neighbours around a central iodine atom being fairly complex due to the mixture of hollow and near bridge sites - Figure 4.06(b). Movement of the overlayer mesh in the <100> direction for which expansion occurs would give a different mixture of hollow and

Fig. 7·10

solution derived from c(2×2) atop — — —
E_o = −10·0eV VPI = −6·0eV AFAC = 1·00
N*1 = 1·2Ni r1 = 2·81Å shift = +0·03Å

2	3·7 I	3·58	+0·06
3	4·1Ni	3·59	−0·14
4	3·9Ni	4·33	−0·16
5	4·4Ni	4·71	−0·16
6	3·7 I	4·79	−0·19

phase shifts = EXOUTB 0,1,2
iterated to dataset 829 ————

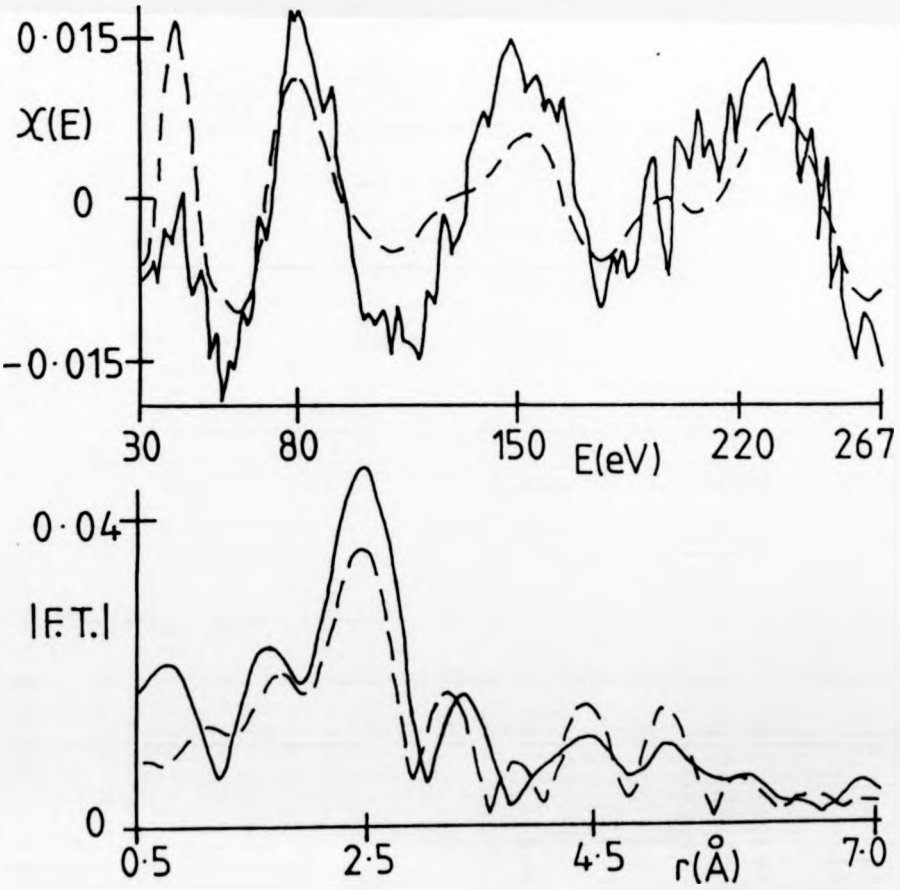

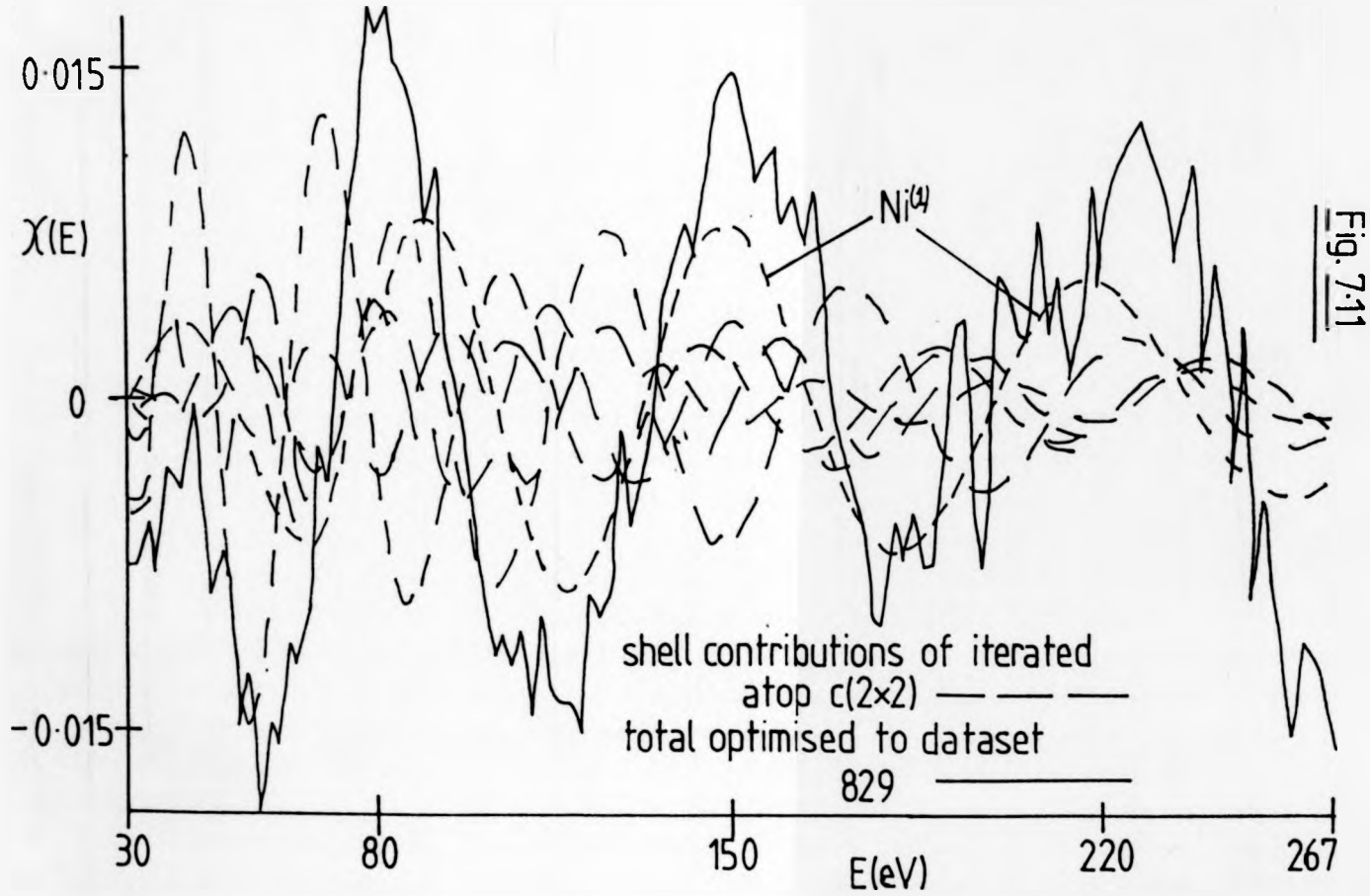
0·015
χ(E)
0
-0·015
Ni(4)
shell contributions of iterated
atop c(2×2) — — —
total optimised to dataset
829 ——
30
80
150
220
267
E(eV)

Fig. 7·11

bridge sites; movement in the other <100> direction is thought unlikely - such differences in radial distribution functions should show up in the iodine EXAFS.

The EXAFS was calculated from a starting structure, consisting of iodine atoms in equal numbers of hollow and bridge sites on the N_i (100) surface, with the I-I distances corresponding to a coverage, θ = 1/2, the effective numbers of atoms per shell being calculated for a normal incidence X-ray beam, the central I radial distribution function therefore being: 2.7 nickel atoms at a distance, r = 2.78 Å, with a Debye-Waller factor, 2 σ^2 = 0.01 Å^2; 1.9 N_i at 3.73 Å; 1.0 N_i at 4.49; 4.6 I at 4.13; 1.7 N_i at 4.64; and 2.3 I at 4.98 Å; all these shells having a Debye-Waller factor of 0.03 Å^2. The atomic phase-shifts EXOUTBO, 1 and 2 were used. The fit to a measured spectrum (811) could be improved slightly by allowing the r-values to vary as well as the non-structural parameters - see Figure 7.12 - there being no significant change in the I-N_i bond length, and the AFAC value being quite reasonable.

A slightly different starting structure involving hollow, bridge and midway between hollow and bridge adsorption sites (2.3 N_i 2.78 Å 0.01 A^2; 0.6 N_i 3.219, 1.3 N_i 3.73, 0.2 N_i 3.91; 4.6 I 4.13; 0.7 N_i 4.32; 1.3 N_i 4.49; 0.3 N_i 4.52 and 2.3 I at 4.98 Å; all with Deby-Waller factor 0.03 Å^2) gives the iterated fit shown in Figure 7.13, this being only slightly worse than the match shown in Figure 7.12 (in terms of the sum of the squares of the differences between theory and experiment), and indicating a shortening of the I-N_i bond length by 0.05 Å. The less consistent AFAC of 0.62 suggests that this model is not as good, but due to the rather poor quality of the measured spectrum (by bulk EXAFS standards) it is not possible to make a definitive structural derivation. The results indicate that the mixture of hollow and bridge sites gives approximately the

E_o=6·0eV above edge, VPI=−1·2eV, AFAC=0·34,

N*	Atomic type	r-value(Å)	displacement(Å)
2·7	Ni	2·77	−0·01
1·9	Ni	3·61	−0·12
1·0	Ni	4·40	−0·10
4·6	I	4·37	+0·24
1·7	Ni	4·40	−0·16
2·3	I	4·79	−0·19

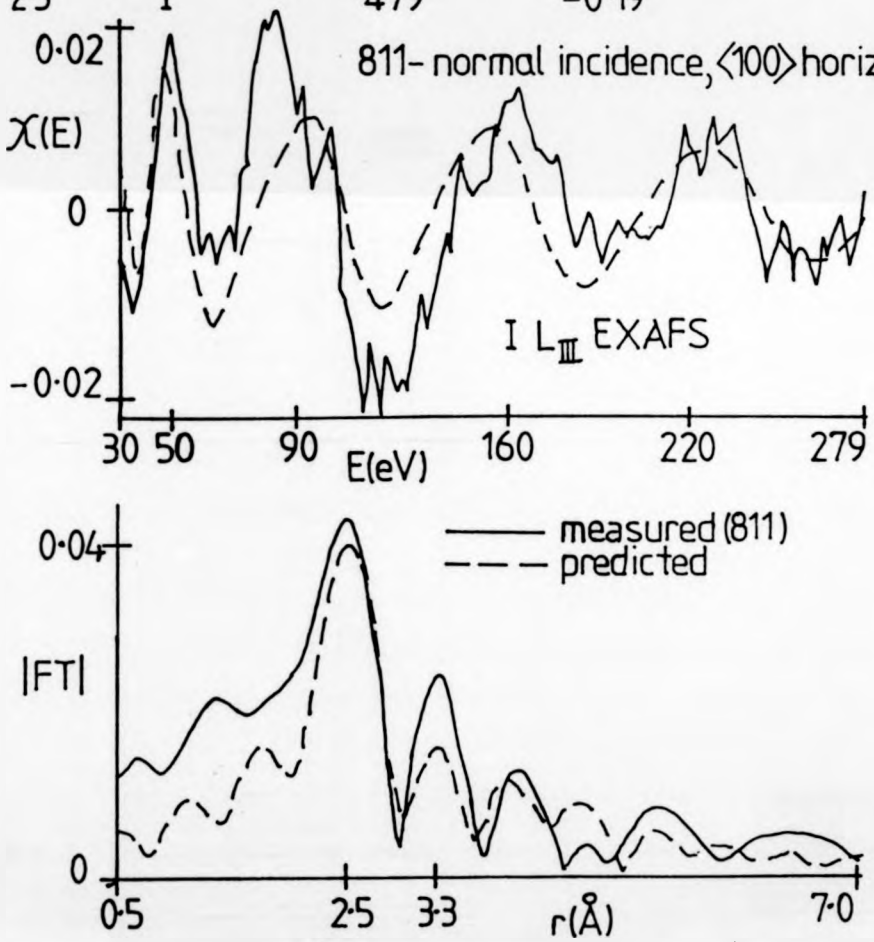

Fig. 7·12: Optimised ~~θ=3/8~~ c(2×8)I-Ni{100} hollow/bridge model.

Fig.7·13 : $\theta = 3/8$ structure derived from hollow/mid/bridge model.

N^{*} = 2·3 Ni atoms, r = 2·73Å, shift = −0·05Å

0·6	Ni	3·53	+0·14
1·3	Ni	3·53	−0·20
0·2	Ni	4·06	+0·15
4·6	I	4·16	+0·03
0·7	Ni	4·11	−0·21
1·3	Ni	4·26	−0·23
0·3	N	4·515	−0·005
2·3	I	4·77	−0·21

E_o = 2·8eV above edge , VPI = −5·9eV , AFAC = 0·62

atomic phase shifts = EXOUTB0,1,2

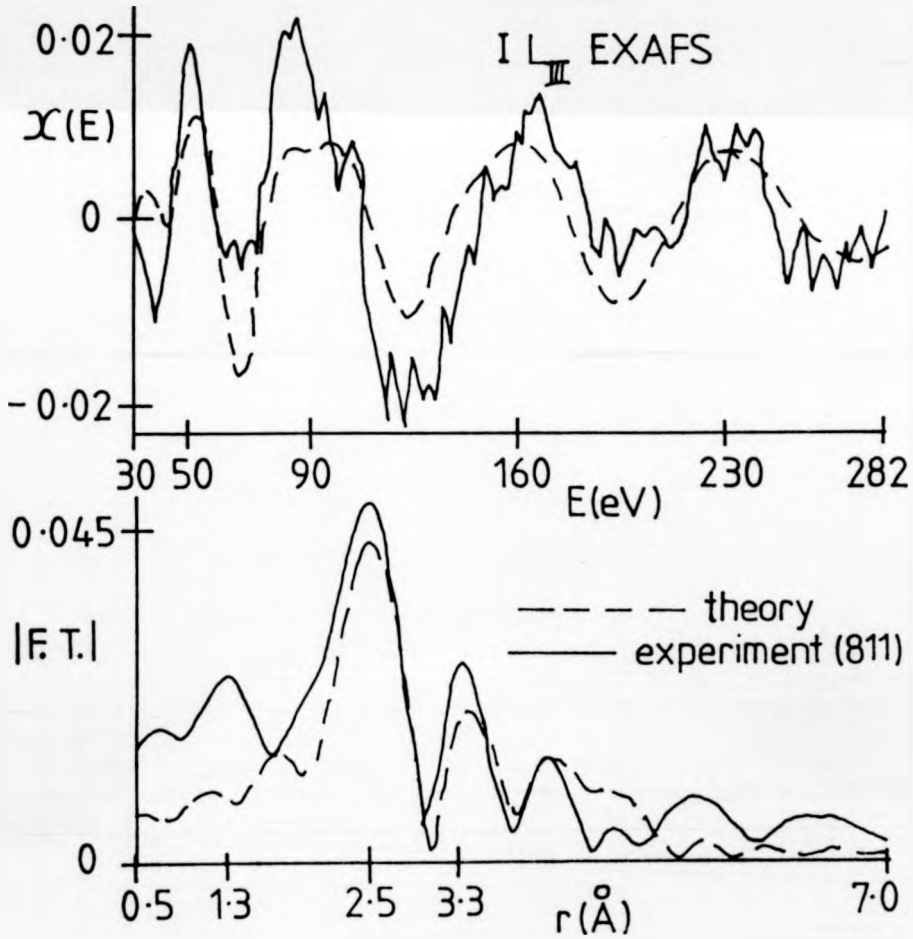

correct effective co-ordination number, that the suggested I-I distances are about right, and that the I-N_i bond length may be a little shorter than in bulk N_iI_2.

7.06 $\Theta = 1/2$, (2x3) I-N_i (100): Structural Derivation

The postulated bridge/hollow site structure of Figure 4.07 was used as the basis of an EXAFS calculation, the result being shown in Figure 7.14, where a comparison is given with one of the two available spectra measured from the c(2x3) I-N_i (100) surface structure. The effective numbers of atoms in each shell used in the calculation are those appropriate to a normally incident X-ray beam, the polarization direction being parallel to the horizontal <100> vector of the N_i (100) surface; Eo, VPI and AFAC have been optimised. The main mismatches are the 150 eV peak in $\chi(E)$ and the r = 1.3 Å peak in the Fourier transform modulus, which are thought to be due to the impossibility of obtaining an exact μo estimation with the poor quality experimental data.

Allowing the structural parameters also to vary, achieved the slightly better match of Figure 7.15 there being an insignificant change in the I-N_i bond length (- 2.79 Å), the estimated effective co-ordination number being approximately correct (the AFAC value of 0.37 being consistent), and the structure being quite likely to be correct (no drastic changes in any of the shell distances). Another likely structure is one in which there is a movement of the iodine atoms, in the direction of the expansion shown in Figure 4.07(a), such that the iodine atoms all lie in equivalent sites part way between bridge and hollow sites. Such a model was found to give a slightly poorer match to the experimental data, with a derived I-N_i bond distance of 2.77 Å, and an AFAC value of 0.42 (the effective co-ordination number is smaller in this model).

— — — e.x.a.f.s. from postulated $\theta = 1/3$ structure:
shell 1 = 2·7Ni r1 = 2·78Å D.W.1 = 0·01Å²
2 1·9Ni 3·73
3 1·0Ni 4·49
4 4·6 I 4·50
5 1·7Ni 4·64
6 2·3I 4·98
} D.W.'s = 0·03
iterated parameters:
E_0 = 3·8eV above edge AFAC = 0·35 VPI = −5·1eV
phase shifts = exoutb0,1,2

——— e.x.a.f.s. from experimental dataset 820

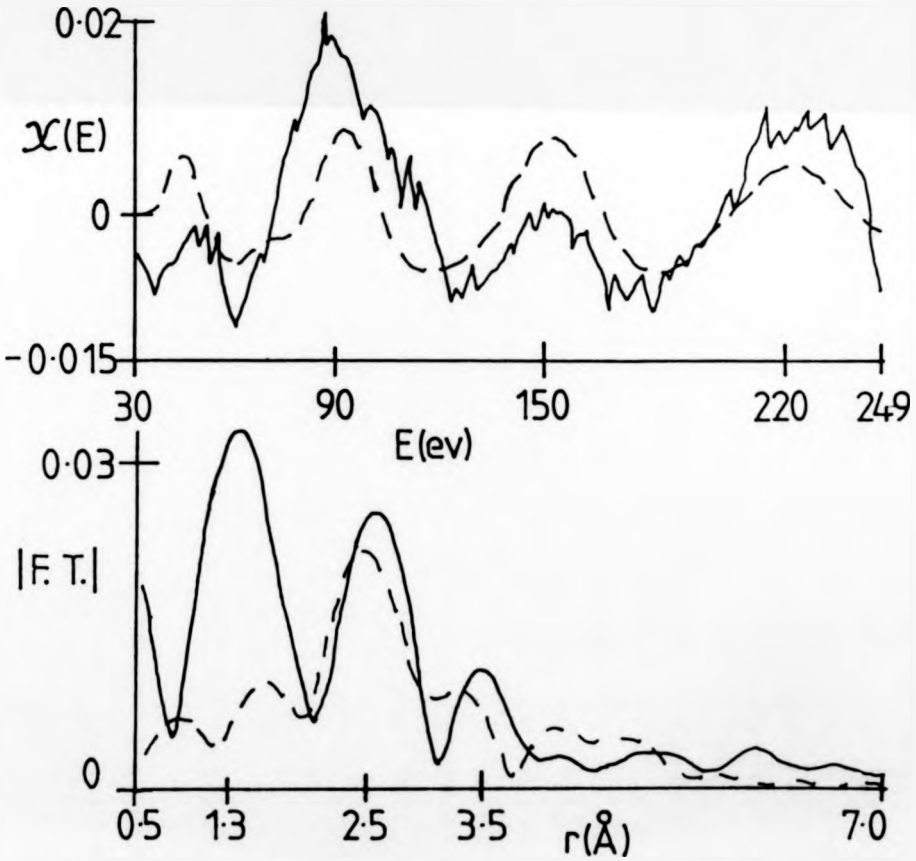

Fig.7·14: EXAFS of (2×3)I-Ni{100} and of hollow/bridge model.

Fig. 7·15:

structural iteration of $\theta = 1/3$ I – Ni{100}:

N^*		r	Δr
2·7	Ni	2·786Å	+0·006Å
1·9	Ni	3·66	−0·07
1·0	Ni	4·39	−0·10
4·6	I	4·48	−0·02
1·7	Ni	4·39	−0·25
2·3	I	4·90	−0·08

$E_o = 3·6$eV above edge, VPI = −5·0eV, AFAC = 0·37

atomic phase shifts = exoutb0,1,2

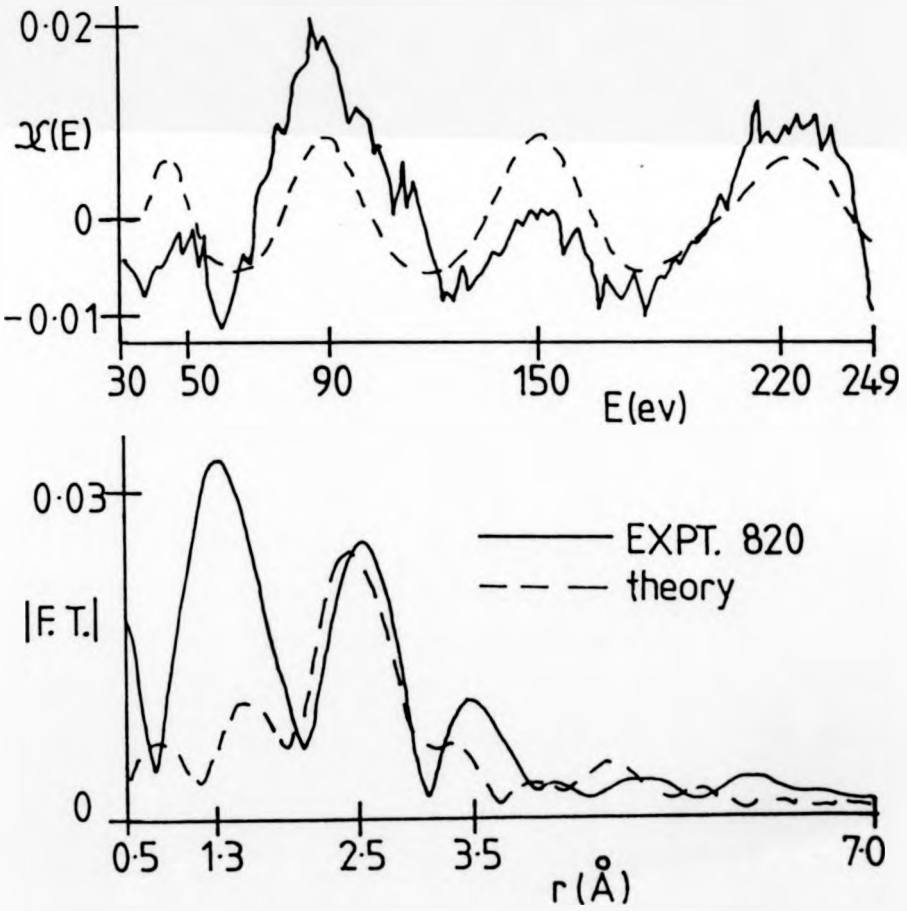

Models based upon bridge or atop adatom sites were found to be unsuitable, it not being possible to obtain EXAFS spectra that matched those measured.

It seems that the I–N_i bond length is almost certainly effectively unchanged from the value of 2.78 Å, and that the iodine overlayer shown in Figure 4.07(a) is a very good estimate of the actual structure, the adatoms being in hollow and bridge sites, or in sites someway between the two.

7.07 Reliability of Structural Derivations

For each result to be reliable, the calculated EXAFS for the derived structure must clearly match the measured spectrum, no other structures should give anywhere near as good a simulation in order to avoid ambiguity, and all the iterated parameters must be physically reasonable. Such structural derivations are therefore similar to those obtained via LEEDS studies. In order to quote an uncertainty in a parameter such as the bond length it is necessary to vary this parameter until the match between theory and experiment becomes unacceptable; a less subjective method is to quote the standard deviation amongst a set of values derived from different spectra of the same structure (taken at different orientations for example).

For surface N_iI_2 and c(2x2) I–N_i (100), the matches are excellent, the surface nickel iodide structure as determined by LEED being confirmed, and the hollow adsorption site for the $\theta = 1/2$ overlayer being deduced. The values of VPI remained reasonable for all solutions: – 4 to – 8 eV for bulk N_iI_2, surface N_iI_2 and

c(2x2) I-N_i (100); and - 2 to - 6 eV for the $\theta = 3/8$ and $\theta = 1/3$ overlayers - these values correspond to the expected electron mean free paths of a few Å at the photo-electron energies involved. AFAC values, whilst being low, remain in the range 0.30 to 0.49 for bulk N_iI_2, surface N_iI_2 and c(2x2) I-N_i (100), and 0.3 to 0.6 for the lower coverage adlayers.

Measured spectra of $\theta = 3/8$ and $1/3$ structures could best be reproduced by hollow and bridge adatom site models, although models containing iodine atoms in just hollow or only bridge sites also gave reasonable matches, so these structures could not be deduced with absolute certainty. However, whichever model was used, the I-N_i bond length remained effectively the same as the 2.78 Å in bulk N_iI_2, there also being no change in this value for the surface N_iI_2 and $\theta = 1/2$ structures.

The meanings of these results in terms of surface chemistry, are discussed in detail in Chapter 9.

7.08 References

1. R W G Wyckoff 'Crystal Structures' volume 1, second edition, 1965. p 270:
   The cadmium chloride ($CdCl_2$) arrangement.
2. E Pantos. Nuclear Instruments and Methods 208, 1983, p 449.
3. E Pantos 'The SRS Program Library' available from SERC, Daresbury Laboratory, Warrington.
4. S J Gurman, D L technical memorandum 21T, April 1980.
   'Notes on the EXAFS programs at the DL'
   - gives the basic theory plus program listings.
5. G P Diakun, G N Greaves, S S Hasnain, P D Quinn,
   DL tm 38 E, January 1984: 'X-ray absorption spectroscopy'
   - notes on how to run :
   'EXBACK' - background subtraction and μo estimation via polynomials
   and 'EXCURVE'.
6. E A Stern B A Bunker and S M Heald, Phys. Rev B21(12), June 1980, p 5521,
   'Many body effects on EXAFS amplitudes'.
7. P A Lee, P H Citrin, P Eisenberger and B M Kincaid, Reviews of Modern Physics 53, number 4, part 1, p 769, October 1981:
   'EXAFS - its strengths and limitations as a structural tool'.
8. E A Stern D E Sayers, and F W Lytle, Phys Rev B11(12), June 1975, p 4836
   'EXAFS technique III - determination of physical parameters'.
9. P A Lee and G Beni, Phys Rev B15(6), March 1977, p 2862
   'New method for calculation of atomic phase-shifts: application to EXAFS in molecules and crystals'.

10. Accuracies of ± 0.02 Å in the bond length, and ± 0.10 Å in the second nearest neighbour are typically reported, eg:
S Brennan, J Stöhr, and R Jaeger, Phys Rev B24(8), October 1981, p 4871
'Structure determination of c(2x2)S on N_i (100) using polarization-dependent SEXAFS'.

11. S M Brennan, 'Surface EXAFS of sulphur on nickel'.
Stanford Synchrotron Radiation Laboratory, report 82/03, June 1982.

12. P H Citrin, P Eisenberger, R C Hewitt, Surf Sci 89, 1979, p 28.
'SEXAFS studies of iodine adsorbed on single crystal substrates'.

13. B A Bunker and E A Stern, Phys Rev B27(2), January 1983, p 1017.
'Phase factor in EXAFS'.

CHAPTER 8

SEXAFS of Cl-Cu{111} STRUCTURES

8.01 Overview

In this chapter, a description is given of the SEXAFS data collection from two surface structures formed by the dissociative adsorption of chlorine onto the Cu(111) single crystal face - the $\theta = {}^{1}/_{3}$, $(\sqrt{3} \times \sqrt{3})$ R30° and the $\theta = 0.45$, $(6\sqrt{3} \times 6\sqrt{3})$ R30° structures described in chapter 4 - and from a bulk CuCl sample acting as a reference compound. An outline is given of some of the procedures adopted to obtain data of the necessary quality.

Analyses using the fourier-filtering single shell approach show that for the $\theta = {}^{1}/_{3}$ overlayer, the chlorine adatoms reside in hollow sites (co-ordination number of 3), the Cl-Cu bond length being approximately 2.39 Å - significantly larger than the 2.34 Å occurring in bulk CuCl. The multi shell modelling approach gives the same conclusions, within the large uncertainties, that arise mainly from the short k-ranges of the datasets.

A major problem is observed: the estimation of μ_o when the data ends at a lowish k-value where the EXAFS amplitude is significantly large. For surface EXAFS spectra, a spline is shown to give better background estimations than a polynomial algorithm. This μo problem explains why a previous SEXAFS publication gives an incorrect structural derivation of the surface NiI_2-Ni(100) structure.

8.02 Data Collection

Work at Daresbury during May and September 1984 by the Warwick University group (C Riley, M Crapper, S Ainsworth plus R G Jones of Nottingham University), set out to measure chlorine SEXAFS spectra from the two Cl-Cu(11) surface structures, and from bulk CuCl. Measurements of the X-ray absorption coefficient were made around the chlorine K-edge energy of 2823 eV, there being no copper edges anywhere near this energy range (the copper L_I edge is at

1096 eV, and the K-edge at 8979 eV). The only problem that was anticipated was the low signal (ie edge jump and EXAFS oscillations), compared to the background (the extrapolation of the pre-edge absorption), due to the small absorption coefficient of chlorine, a light element (atomic number 17).

Poor alignment of the pre-mirror and monochromator for the first experiments caused oscillations to remain in the normalised background (see Section 3.08 for an explanation of the exceptionally high signal: noise required for good quality data), that were larger than the EXAFS oscillations in spectra taken from surface structures. The vastly larger signal from the bulk CuCl sample, enabled the EXAFS to be clearly visible - Figure 8.01(a).

Prior to the second set of measurements, the optical components of the beam-line at Daresbury, were correctly aligned, enabling reasonable quality spectra to be taken - EXAFS oscillations just visible above the 'noise'.

A variety of detection techniques were tried in order to enhance the surface sensitivity of the measurement, and hence to improve the signal-to-noise ratio of the data. An electron energy analyser (CHA) set to the energy of the KLL chlorine Auger electrons (2384 eV), recorded SEXAFS spectra that show increases in signal of 30% on passing the 2823 eV point. Unfortunately the signal was so small (due to the difficulty in getting the X-ray beam to hit the sample at the focal point of the electron analyser, which has a high spatial sensitivity and small range of acceptance angles), that the random fluctuation in signal from one energy value to the next was much larger than the EXAFS amplitude! Detecting the LMM Auger electrons (the analyser having a window around 100 eV), showed an improvement in signal: noise ratio, despite the reduction in surface sensitivity causing the edge: background ratio to be 17%. In fact

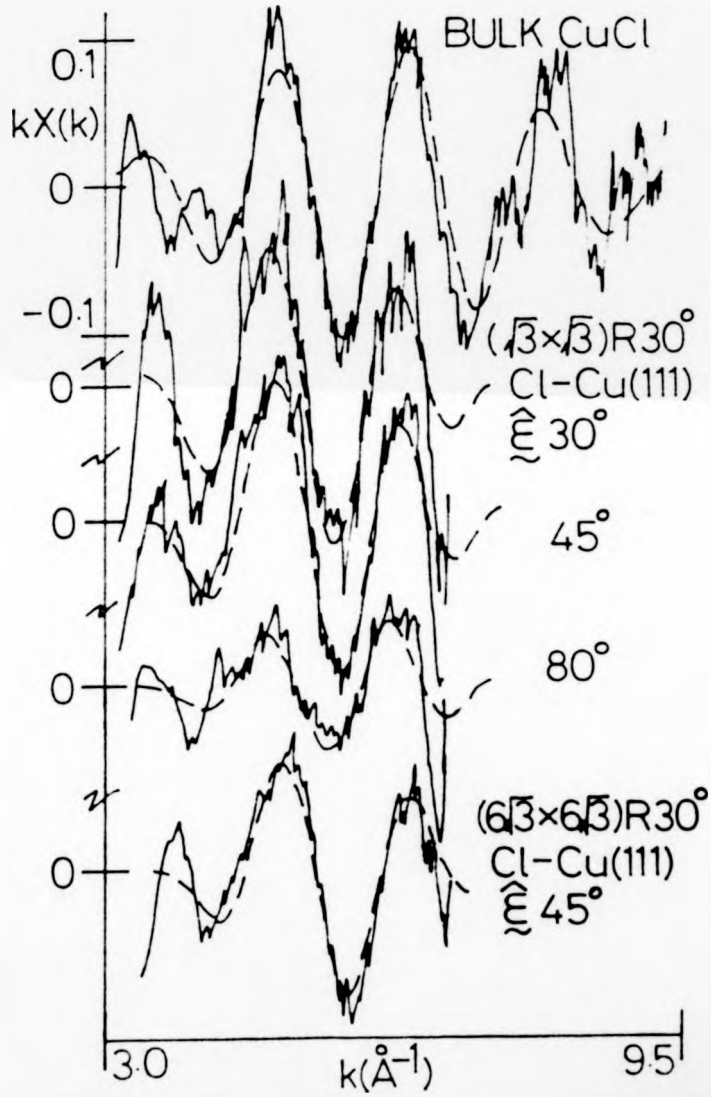

Fig. 8·01 : Total and filtered EXAFS for Cl- Cu structures.

the best signal: noise (ie. the clearest EXAFS) was obtained by measuring the crystal current (equivalent to the total electron yield) as a function of the X-ray energy. The much larger signals enabled the EXAFS oscillations to be just recognisable after one scan above the chlorine K-edge, despite the edge jump being only 1% of the background absorption.

Adding together (taking care to align the edge jumps and hence the energy scales) about a dozen of the best spectra for a given surface structure and a given angle of X-ray incidence, produced spectra of sufficient quality to be analysed - Figure 8.01(b) - (e). Unfortunately, the monochromator performed so well that it transmitted significant amounts of the third-harmonic X-ray - the Ge(111) crystals cannot reflect the second harmonic. Therefore, with the crystals set to transmit $h\nu_1$ = 3,000 eV (ie just 180 eV into the chlorine K-edge EXAFS region), a large edge jump due to the $h\nu_3$ = 9,000 eV X-rays exciting the copper K-shell, obscured any further chlorine EXAFS. The data range is therefore limited to below k = 7 $\AA^{-1}$ for the ($\sqrt{3}$ x $\sqrt{3}$) R30^o and (6 $\sqrt{3}$ x 6 $\sqrt{3}$) R30^o Cl-Cu(111) structures.

8.03 Analysis Using the Fourier-filtering Single-shell Method

Background subtractions (ie extrapolations of the pre-edge absorption coefficients), μo estimations, E_o estimation in the bulk CuCl EXAFS, and ΔE_o estimations in the spectra of the surface structures, were performed in the manner described in Chapter 5. The resulting kX(k) spectra are shown in Figure 8.01.

Figure 8.02(a) shows the Fourier transform of the bulk CuCl EXAFS, E_o having been set to 12 eV below the edge to cause the modulus and the imaginary component to have coincident maxima at R ≈ 4.1 $\AA$. Also shown is the windowed modulus, illustrating the Cl-Cu peak can clearly be isolated, enabling the inverse Fourier

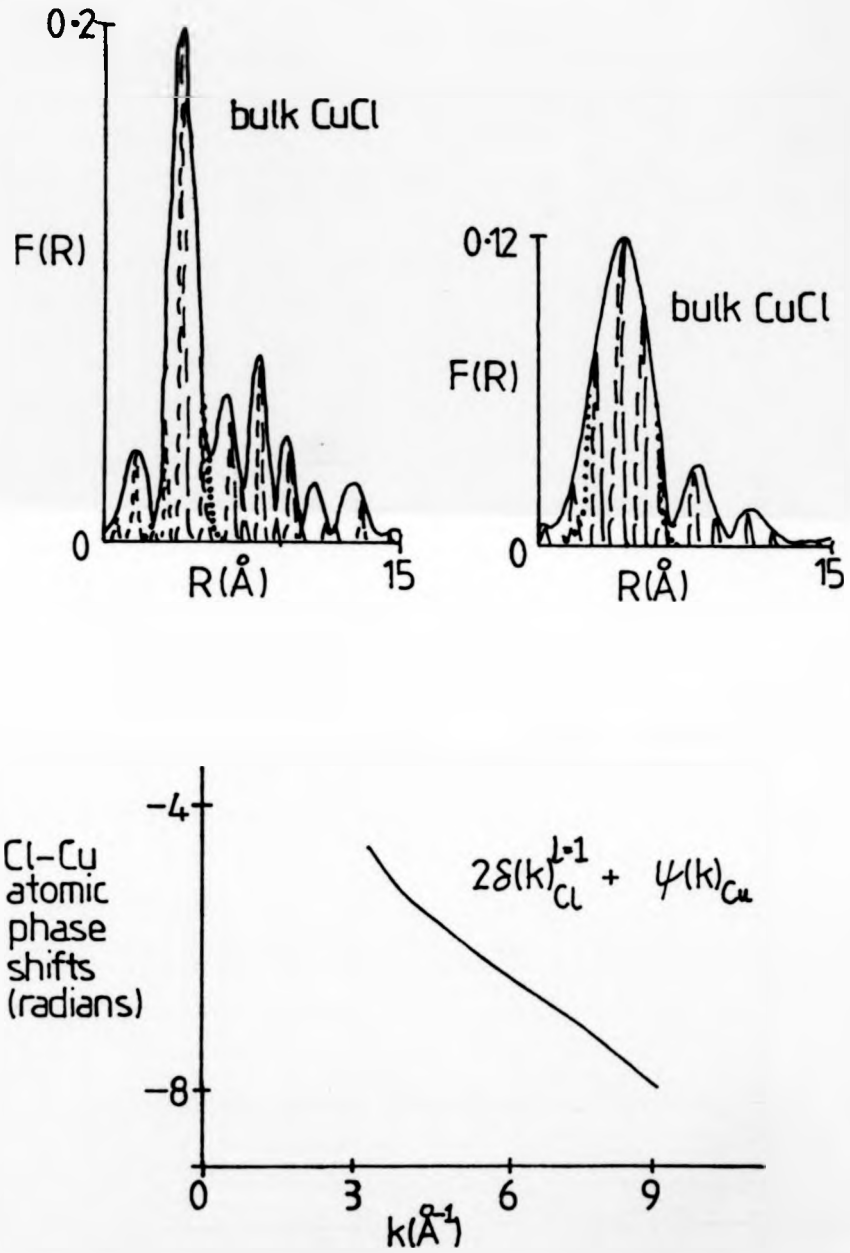

Fig.8·02: Fourier transforms and phase shifts derived from bulk CuCl EXAFS.

transform to give a good reproduction of the EXAFS due to this single nearest shell - shown in Figure 8.01(a), overlaid upon the raw EXAFS. The phase function was obtained from this back transform, and 2kr ($r = 2.34$ Å[1]) was subtracted to give the sum of the central chlorine ion and backscattering copper atom phase shifts - Figure 8.02(b) - these having a gradient in k-space of - 0.6 Å, equal to the theoretical prediction[2]. It is these phase shifts, within a restricted k-range that were used in the bond distance determinations of the surface structures.

In order to check the feasibility of an analysis of the short k-range available for the surface structures, the bulk CuCl spectrum was truncated at $k = 7$ Å^{-1} and treated as an 'unknown compound spectrum'. The main effect on the Fourier transform (Figure 8.02(c)) is a broadening of the main peak - the FWHM being approximately 3 Å in R-space, obscuring a couple of previously resolvable peaks. This necessitated the use of a wide window function prior to the inverse transform. The derived phase function was found to differ in gradient by only 0.03 Å compared to that from the whole k-range, suggesting $\Delta r_1 = 0.015$ Å. Such an error is within the limits of the typical accuracy of a SEXAFS analysis such that if the X(k) functions can be obtained, then reasonably accurate results should be obtainable. If the chlorine atoms do lie in hollow sites as postulated (Figure 4.09) for the $\theta = {}^1/_3$ structure, then interference from higher shells (a problem in the analyses of the short data ranges of the I-Ni(100) spectra) should not be too important.

The raw EXAFS datasets are shown in Figure 8.01(b)-(e), the Fourier transforms in Figure 8.03(a)-(d), the filtered EXAFS again in Figure 8.01(b)-(e), and the differences between the phase functions of these unknown structures and that of bulk CuCl in Figure 8.04(a)-(d). The results are summarised in Table 8.01, (which also includes the results from a multi-shell modelling analysis to be

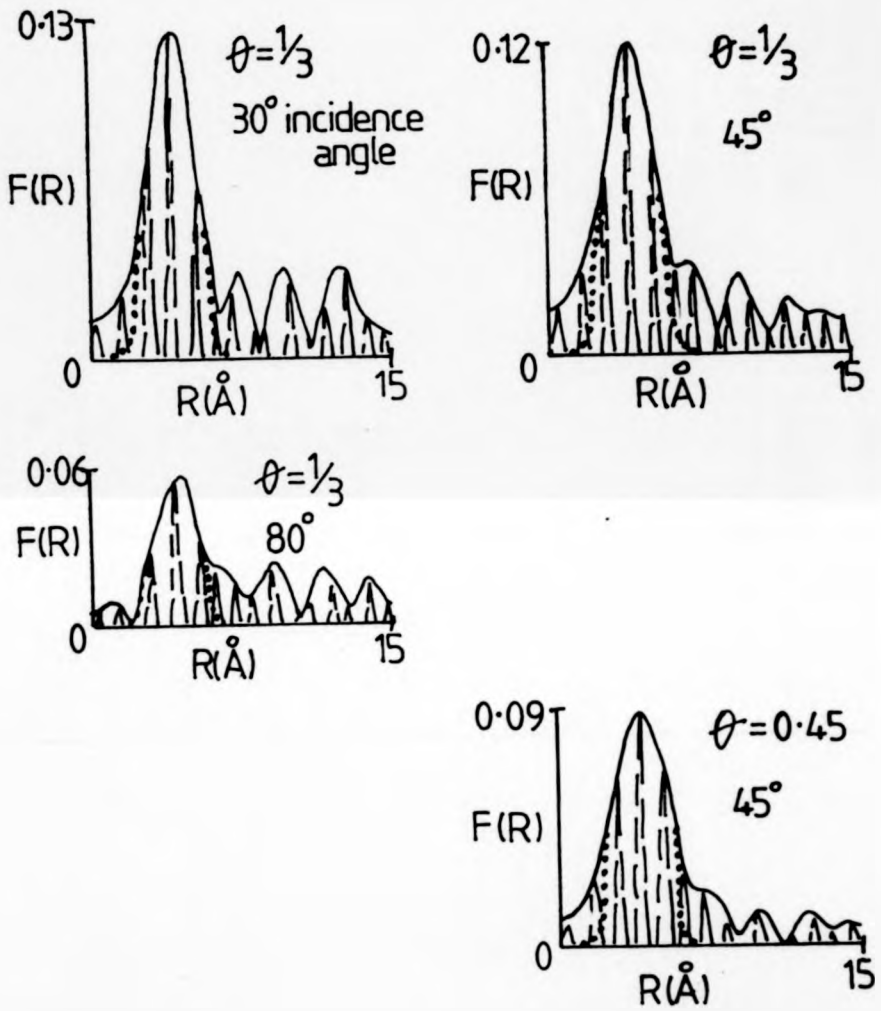

Fig.8·03: Fourier transforms of Cl–Cu{111} EXAFS.

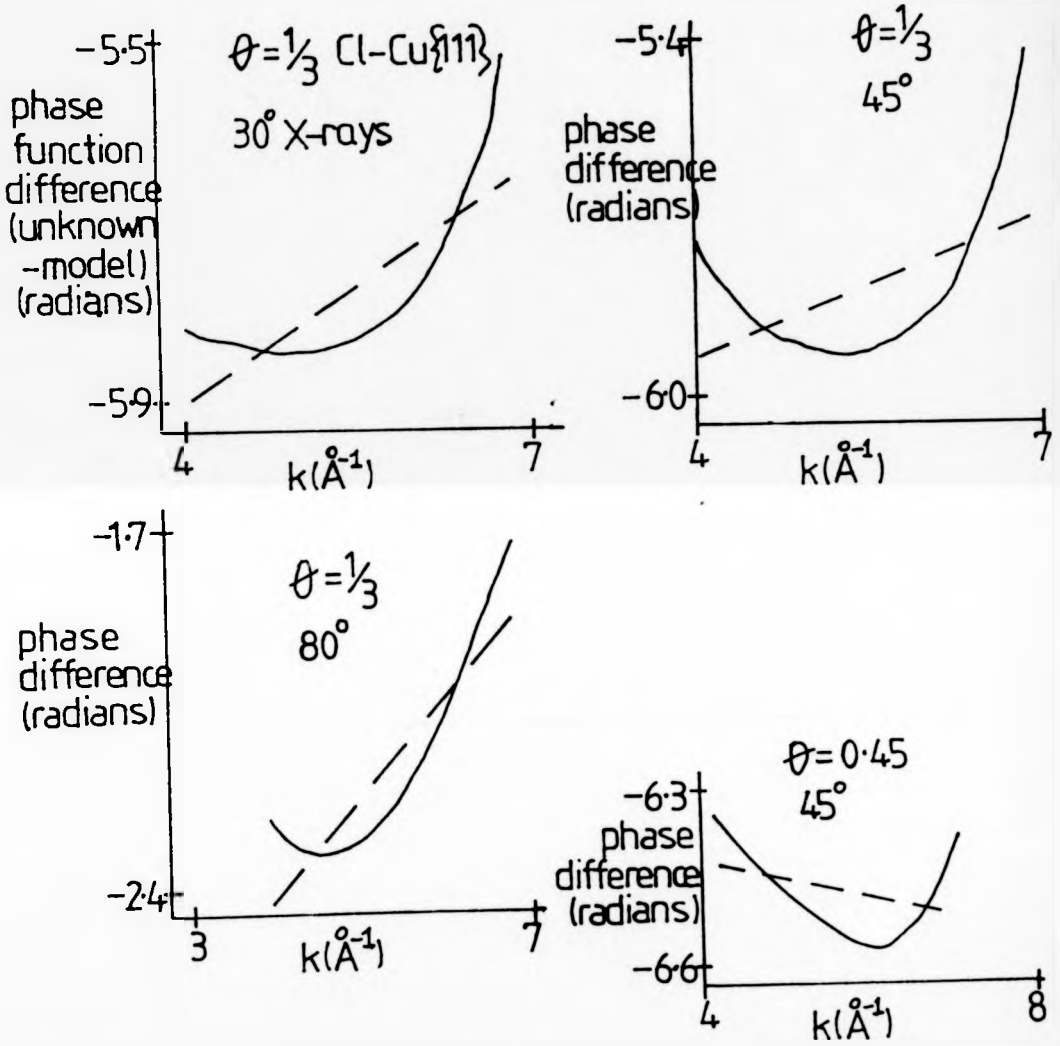

Fig. 8·04: Phase function unknown - model Cl-Cu compound.

described later in this chapter). The ΔE_o values were chosen to set the intercepts of the phase function differences to effectively zero radians, and it is re-assuring that Figure 8.03 shows the expected alignments of the peaks in the moduli and imaginary components.

The EXAFS above a K-edge of an adatom is particularly suitable for the identification of the adsorption site of that adatom, because of the strong directionality in the emission of the photo-electron, and hence the large variation in the EXAFS amplitude with the incidence angle[3-6].

The solid lines in Figure 8.05 show the calculated variations in the EXAFS amplitude as a function of the X-ray incidence angle, α, for three chlorine adsorption sites on Cu(111): atop, bridge and hollow. The atop site gives the most variation: at normal incidence ($\alpha = 90^o$) the electric vector lies parallel to the surface, and there is zero probability of the photo-electron being emitted at 90^o to this direction, hence the first shell EXAFS amplitude is zero; whereas for glancing incidence, the effective co-ordination number becomes large (see Equation 2.10). There should be no variation in the EXAFS amplitude as the crystal is rotated about an axis lying normal to the surface. From the EXAFS amplitudes measured at three incidence angles - 30^o, 45^o and 80^o - for the $\theta = {}^1/_3$ structure (shown as the crosses in Figure 8.05), the atop site can definitely be ruled out, but it is not possible to distinguish between the bridge and hollow sites.

As mentioned in section 4.04, the $\theta = 0.45$ structure can be thought of as a compression of the $\theta = {}^1/_3$ overlayer, and if the chlorine adatoms reside in hollow sites in the $\theta = {}^1/_3$ structure, then some would be moved towards bridge or atop sites during the compression, causing a decrease in the effective co-ordination number. For SEXAFS spectra taken at the X-ray incidence angle,

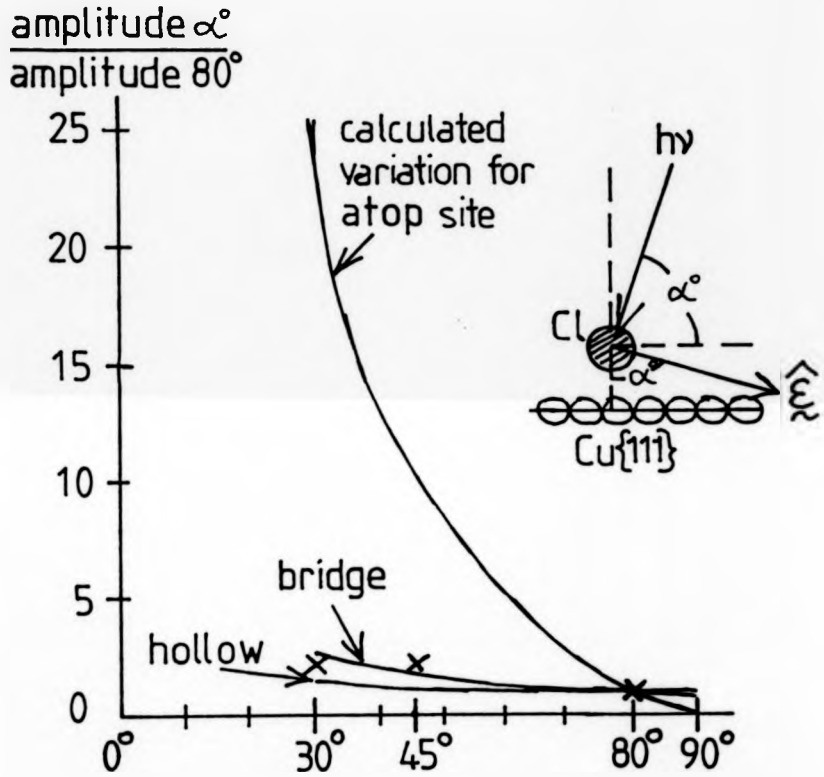

Fig.8·05 : Cl adatom site determination via polarisation-dependent SEXAFS amplitude.

x : measured amplitudes normalised to that at 80°.

BULK CuCl (dataset 1905)

Fourier filtering method

E_o=12eV below edge, |FT| peak at R=4·1Å, $A(k)^{max.}$=0·10, phase shifts=-0·6Å gradient

Multi shell method

E_o=13eV below edge, VPI=-5eV, AFAC=0·30, phase shifts=PHSCL, EXOUTA1,2

$(\sqrt{3}\times\sqrt{3})R30°$ Cl-Cu{111}, $\theta=\frac{1}{3}$

		Fourier filtering results			Multi shell results					
dataset:	X-ray incidence:	E_o(eV below edge):	Δr_1(Å):	$A_1(k)^{max.}$:	E_o(eV below edge):	VPI(eV):	AFAC:	Δr_1(Å):	Cl-Cl(Å):	μ_o:
3093	30° (near glancing)	7	+0·04(±0·04)	0·11	11	-1·6	0·40	+0·01	4·26	polynomial
CL45AD	45°	7	+0·04(±0·06)	0·11	10	-2	0·30	+0·04	4·26	spline
"	"				* 10	-2	0·30	+0·05	4·30	spline
3115	80° (near normal)	9	+0·09(±0·06)	0·05	10	-7	0·35	+0·04	4·41 †	polynomial #
$(6\sqrt{3}\times6\sqrt{3})R30°$ Cl-Cu{111}, $\theta=0·45$										
3081	45°	14	-0·02(±0·04)	0·09	13	-7	0·40	0·000	4·04	spline
					12	-5	0·40	+0·05	3·94	polynomial

TABLE 8·01: Results of SEXAFS analyses of Cl-Cu{111} structures; bulk CuCl reference compound

* : Low-k peak (below 70eV) excluded in analysis

\# : Splines or polynomials used for μ_o's in multi-shell analyses; splines in Fourier method

† : Expected Cl-Cl spacings = 4·43Å for $\theta=\frac{1}{3}$ hcp overlayer on Cu{111}
3·81Å " " 0·45 " " " "

$\alpha = 45^{o}$, the EXAFS amplitudes are 0.11 for the $\theta = {}^{1}/_{3}$ overlayer, and 0.09 for $\theta = 0.45$, these values being compatible with the postulated hollow sites for the $\theta = {}^{1}/_{3}$ structure, and the mixture of sites for the 'compression structure'

The results suggest a Cl-Cu bond length of around 2.38 $\mathring{A}$ in the $\theta = {}^{1}/_{3}$ structure and 2.32 $\mathring{A}$ in the $\theta = 0.45$ overlayer, compared to 2.34 $\mathring{A}$ in bulk CuCl.

8.04 Multi-shell Modelling Analysis

The first step in any multi-shell modelling analysis is to derive the appropriate atomic phase-shifts from the EXAFS spectrum of a model compound. The bulk CuCl structure, shown in Figure 4.11[1], was used as a basis of a theoretical EXAFS calculation, using the neutral chlorine atomic phase-shift, PHSCL, available in the Daresbury library, to represent the central and backscattering chlorine atomic phase-shifts, and using the backscattering nickel phase-shifts, BSN, derived from the EXAFS of bulk NiI_2 (see Section 7.02) as an approximation for the copper backscattering phase shift (these two elements are adjacent in the Periodic Table, hence their atomic phase shifts should be similar). Leaving PHSCL fixed for the central phase-shift, and allowing the program EXCURVE to vary the other two phase-shifts and the non-structural parameters, to obtain a match to the measured spectrum, dataset number 1905, derived the phase-shifts EXOUTA1 for the backscattering copper, and EXOUTA2 for the backscattering chlorine atoms. The theory and experiment comparison is shown in Figure 8.06, and the derived phase-shifts in Figure 8.07.

Notice in Figure 8.06 that the value of E_o is consistent with that derived using the criterion described previously when using the Fourier-filtering single shell approach, and that the values of AFAC (= 0.30) and VPI are consistent with the iodine-nickel studies. The only serious mismatch is that the experimentally measured spectrum has a small peak before the 250 eV peak, which is now

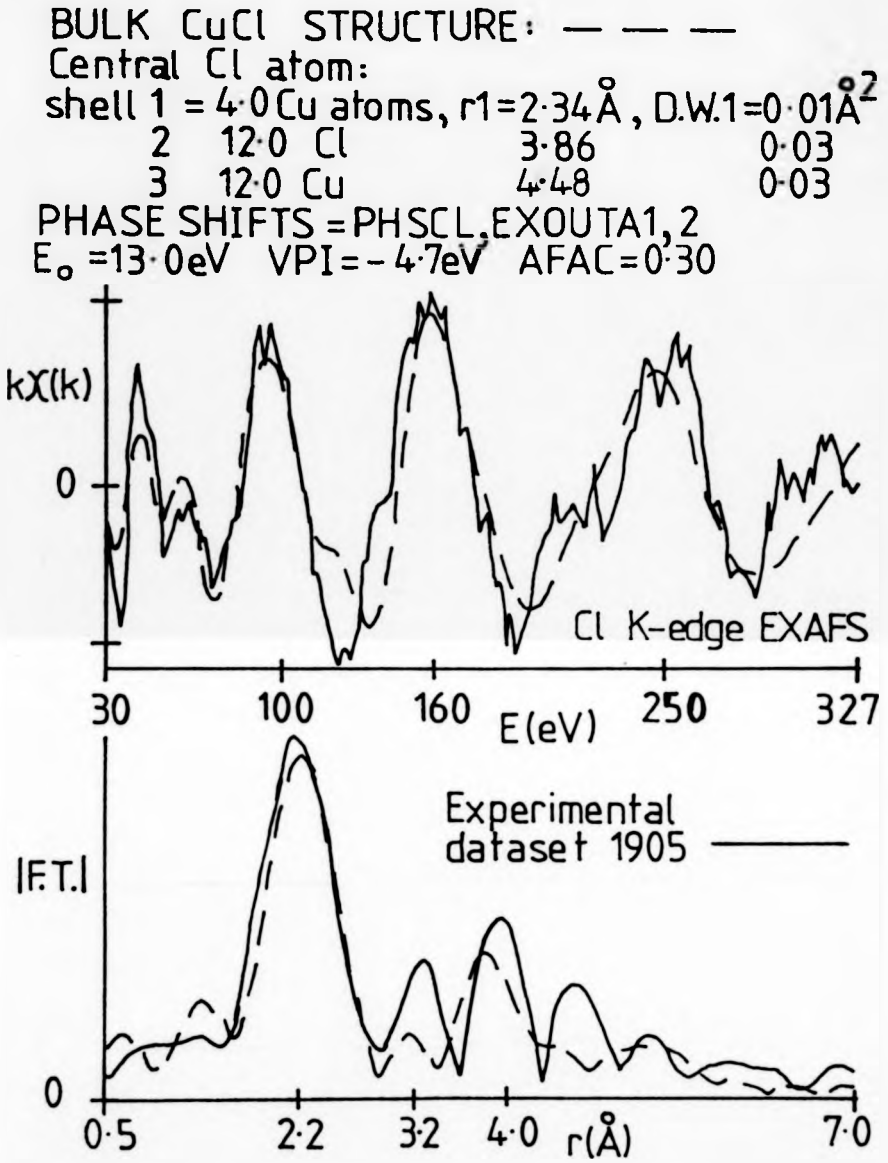

Fig. 8·06: Measured and modelled EXAFS spectra and Fourier transform moduli – bulk CuCl.

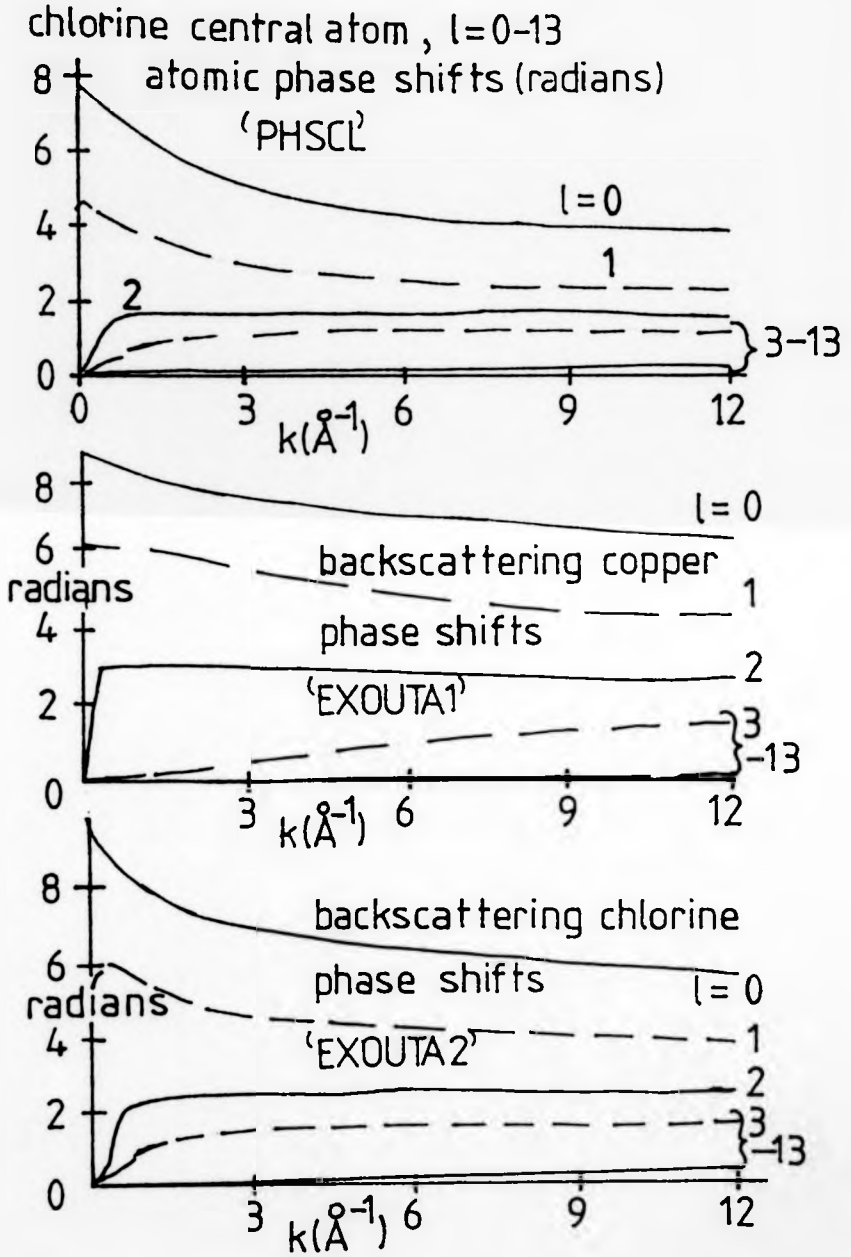

Fig. 8.07: Cl-Cu phase shifts derived from Cl K-edge EXAFS of bulk CuCl (1905).

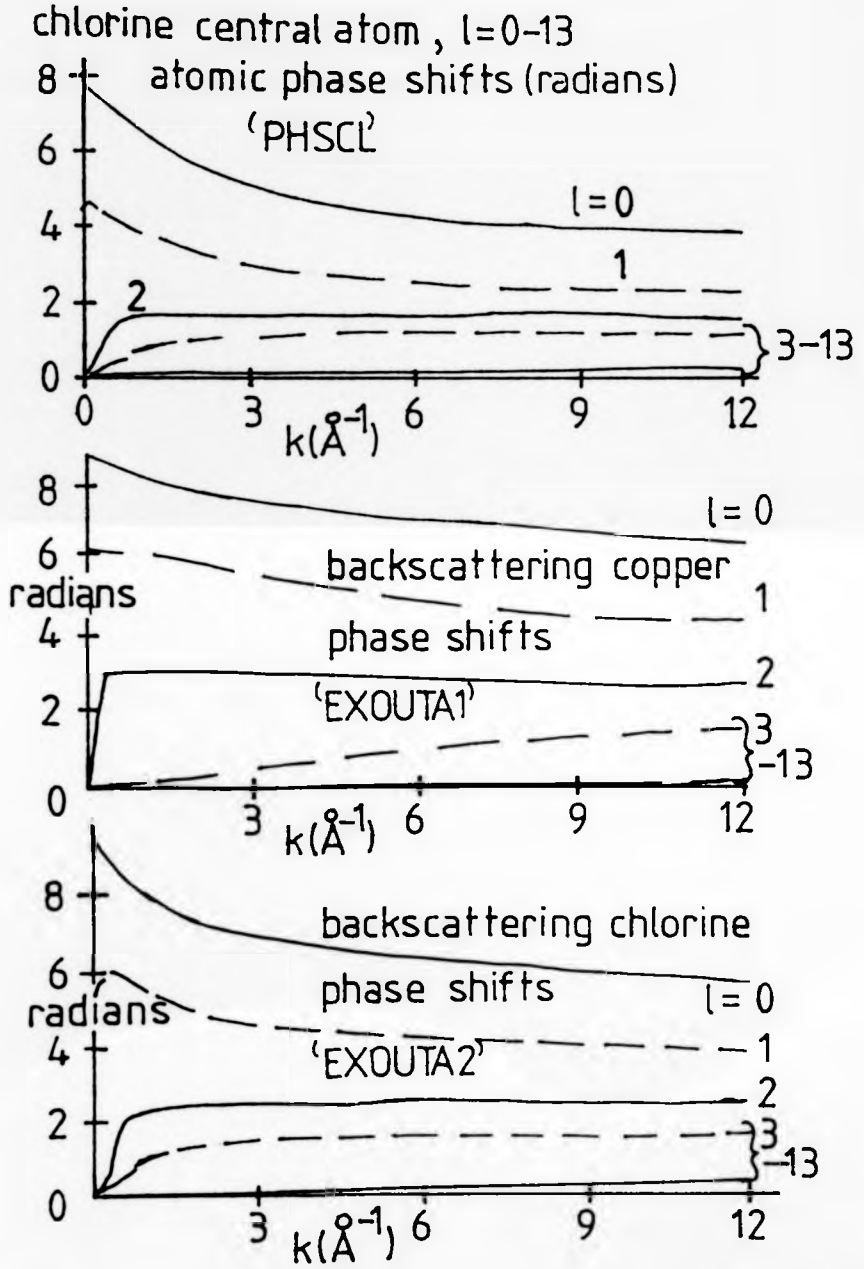

Fig. 8.07: Cl-Cu phase shifts derived from Cl K-edge EXAFS of bulk CuCl (1905).

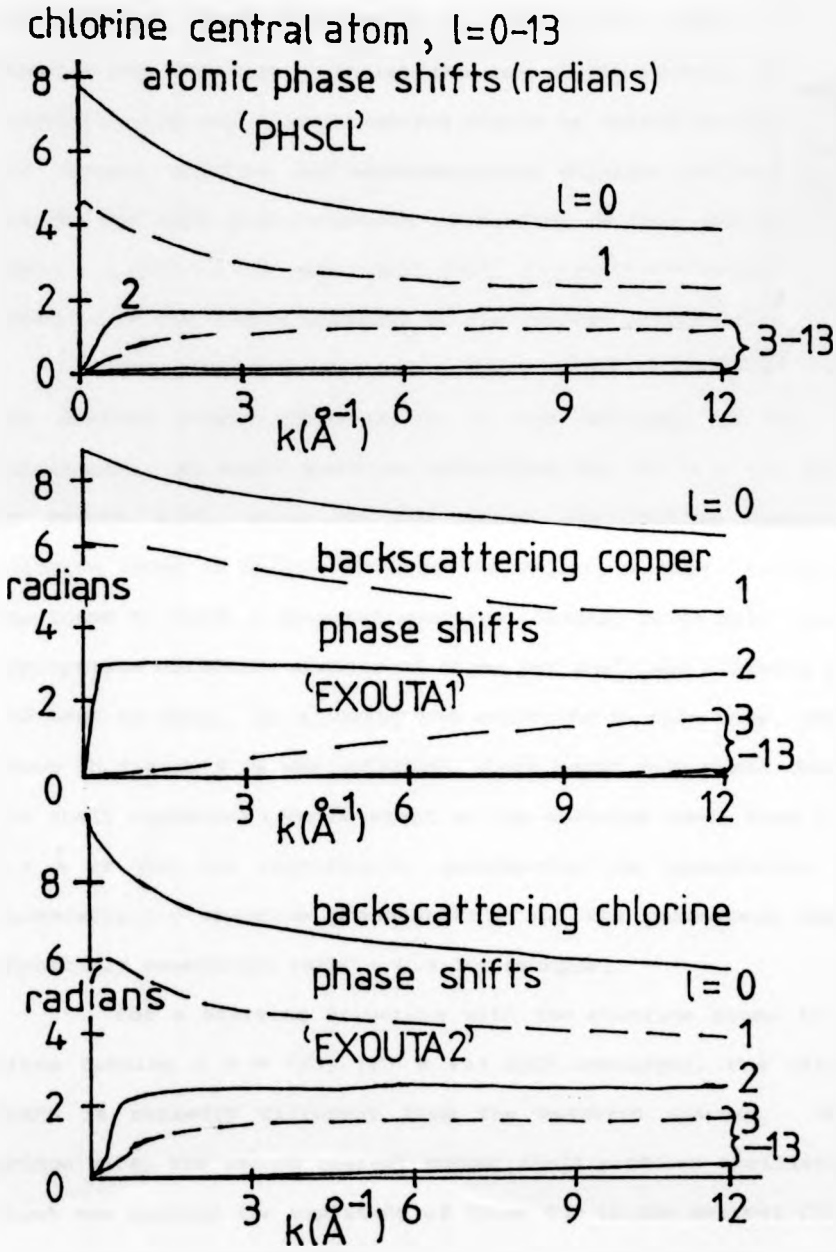

Fig. 8.07: Cl-Cu phase shifts derived from Cl K-edge EXAFS of bulk CuCl (1905).

believed to be a spurious edge jump introduced by the detection system to monitor the electron yield. This feature is not matched by the modelled EXAFS and hopefully should not affect the derived phase-shifts too much. Whilst the sum of the central chlorine and backscattering copper phase-shifts should be fairly accurate, that of the central chlorine and backscattering chlorine is very uncertain due to the weak photo-electron scattering of this nearest chlorine shell - a plot of the individual shell contributions showed the total EXAFS to be due almost entirely to the nearest copper shell.

The next step in a multi-shell modelling analysis is to use the derived atomic phase-shifts in the analyses of the unknown structures. An EXAFS spectrum calculated for the $\theta = {}^{1}/_{3}$ structure of Figure 4.09, given as the radial distribution function for chlorine atoms in hollow sites on the Cu{111} surface, in Table 8.02 was found to match a measured spectrum (CL45AD) quite well, using the appropriate effective numbers of atoms per shell and allowing E_O VPI, and AFAC to vary. On allowing the structure to also vary, the match shown in Figure 8.08 was obtained, there being only small changes in the shell distances (the movement of the chlorine shell from 4.4 Å to 4.3 Å is not too significant, considering the uncertainty in the backscattering chlorine phase-shift), and the parameters remaining physically reasonable (AFAC = 0.3 for example).

For a starting structure with the chlorine atoms in bridge sites forming a $\theta = {}^{1}/_{3}$, $(\sqrt{3} \times \sqrt{3})$ R30° overlayer, the calculated EXAFS is markedly different from the measured spectra. For the bridge site, the second nearest copper shell produces oscillations of about one quarter the amplitude of those due to the nearest shell, of a 'frequency' corresponding to $r_2 = 2.96$ Å - such an effect is not

Cu shells around central Cl:

hollow: 3 Cu neighbours at 2·34Å (top Cu{111} layer)
3 Cu " " " 3·47 " "
1 Cu at 3·90* or 3 Cu at 4·17† (layer below)

bridge:
2 Cu 2·34Å (top layer)
2 Cu 2·96 " "
4 Cu 3·59 " "

atop:
1 Cu 2·34 (top layer)
6 Cu 3·47 " "

Cl shells:

$\theta = \frac{1}{3}, (\sqrt{3} \times \sqrt{3})R30°$ Cl-Cu{111}: 6 Cl 4·43Å

$\theta = 0{\cdot}45$, $(6\sqrt{3} \times 6\sqrt{3})R30°$: 6 Cl 3·81

Table 8·02: Local enviroments of Cl adatoms in Cl-Cu{111} structures

Calculations based on unreconstructed Cu{111} and Cl-Cu bond lengths of 2·34Å.
Expected Debye-Waller factors: 0·01Å^2 for nearest Cu atoms; 0·03Å^2 for others.
There are 2 types of hollow site: hcp or 'aba....' (*) and fcc / 'abc....' type packing (†).

Iteration of hollow site model to SEXAFS spectrum of $\theta = 1/3$ $(\sqrt{3}\times\sqrt{3})R30°$ Cl–Cu{111}

N^{*} = 3·5 Cu atoms at 2·38Å , shift = +0·04Å

3·0 Cu	3·46	−0·01
2·8 Cu	3·90	−0·27
5·0 Cl	4·26	−0·17

E_o = 10·1eV below edge , VPI = −2·0eV, AFAC = 0·30

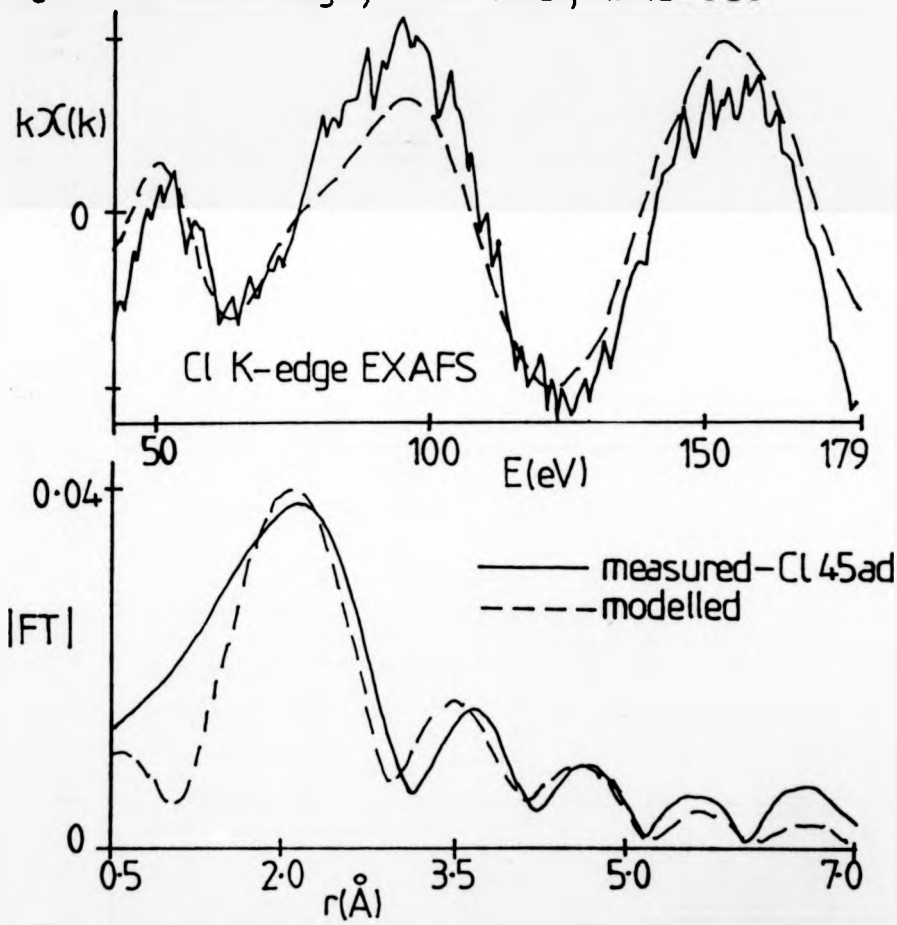

Fig. 8·08 : SEXAFS structural derivation of $\theta = 1/3$, $(\sqrt{3}\times\sqrt{3})R30°$ Cl–Cu{111}, based on hollow adatom sites.

seen in the measured spectra which consist of a single oscillation derived from $r_1 \approx 2.34$ Å. The required AFAC value of 0.46 suggests that the bridge site is not correct.

The atop site appears to be even less likely (this site is also ruled out on the basis of the polarisation dependent EXAFS amplitude). At normal incidence the EXAFS contribution of the first shell (ie the one copper atom directly below the chlorine atom) is zero, such that the EXAFS is derived from the second shell of six copper atoms at 3.47 Å. At 30° incidence angle, the first and second shells should be roughly equivalent in their contributions, each being of clearly different 'frequencies' - the measured spectra show no such features. Again the AFAC values of around 0.48, suggest the effective co-oridination number is too small.

Results for the three angles of incidence-30°, 45°, and 80° - on the $\theta = 1/3$ structure, are given in Table 8.01.

The $\theta = 0.45$ structure given in Figure 4.10 and defined in Table 8.02 (a mixture of 2 hollow: 1 bridge: 1 atop sites), was used to calculate the EXAFS, and was compared to the one available spectrum - dataset 3081 - taken at an X-ray incidence, $\alpha = 45°$. The iterated solution is shown in Figure 8.09, the chlorine-chlorine distance of 4.0 Å being not too far from the 3.8 Å required for a top layer of coverage $\theta = 0.45$, and the AFAC value (0.40) confirming that the postulated average effective co-ordination number is roughly correct (if the mixture is weighted more in favour of atop sites, than there is a descrepancy in AFAC values).

Bond lengths appear to be 2.38 and 2.34-2.39 Å in the $\theta = 1/3$ and 0.45 overlayers, respectively.

8.05 The Estimation of μ_o by a Spline or Polynomial Through μ

Analysing the $\theta = 0.45$ structure by the multi-shell modelling method, was found to produce significantly different

$(6\sqrt{3}\times 6\sqrt{3})R30^{\circ}$ iterated E.X.A.F.S. — — —

3·5 Cu atoms at	2·34Å	, shift=0·000Å
1·0 Cu	2·51	0·002
3·0 Cu	3·44	−0·03
1·0 Cu	3·53	−0·06
4·0 Cl	4·04	+0·23

E_o=13eV below edge , VPI=−7·0eV, AFAC=0·40

Atomic phase shifts = phscl, exouta1, 2

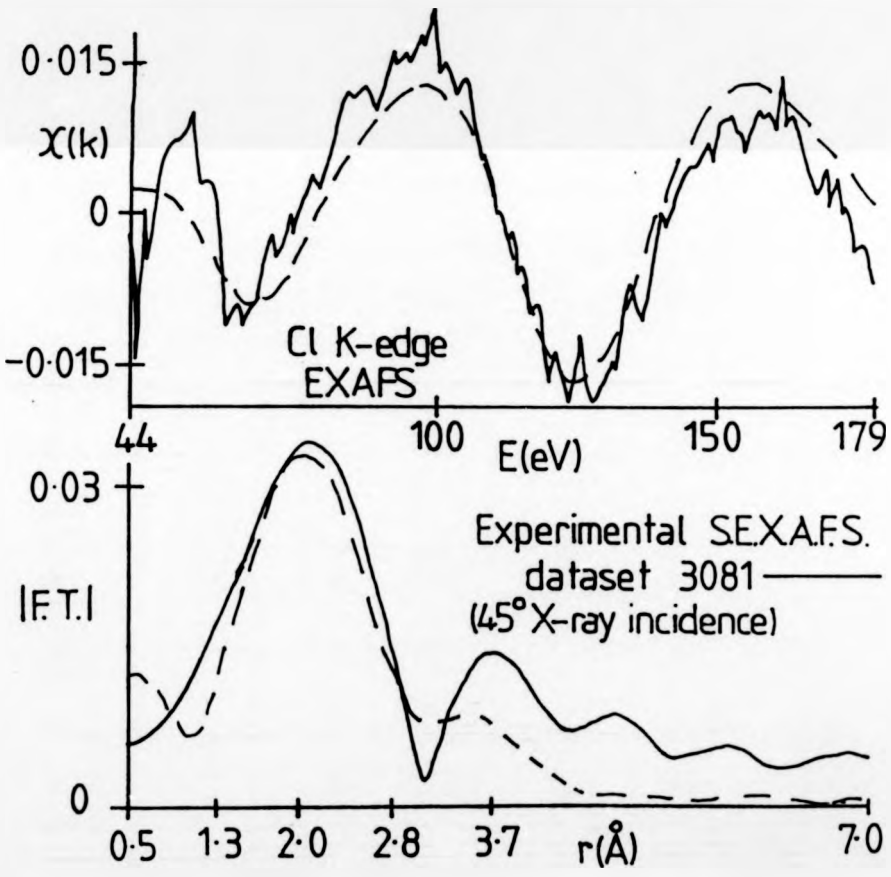

Fig. 8·09: Measured and modelled EXAFS spectra and Fourier transform moduli - β=0·45 Cl-Cu{111}

results for the bond length, depending upon whether a spline or a polynomial was used to estimate μo (see Table 8.01). In order to test which method produces the best μo estimation and hence the most reliable bond length determination, studies were made using the bulk CuCl spectrum 1905.

The Daresbury program EXBACK was written for bulk EXAFS data analysis. Since bulk EXAFS spectra are usually measured by the transmission of X-rays through a thin foil, the extrapolated pre-edge background and μo (the smooth atomic absorption coefficient), are seen to fall gradually with the X-ray energy and can be well represented by simple polynomial functions. For surface EXAFS work, there are many measurements convoluted within the estimation of μ (the EXAFS containing absorption coefficient), causing the simple curvature to be lost, such that the signal that represents μ can rise, fall or contain maxima or minima above the edge jump; a polynomial may not give a good μ_o estimation in such cases. One of the main problems in surface EXAFS work is that the data often ends at a fairly low k-value where the EXAFS has significant amplitude, which may also cause problems in the μo estimation.

The measured absorption coefficient of bulk CuCl is shown as the solid line in Figure 8.10(a), with the estimation of the atomic coefficient between N3 and N4 as the dashed line. In this case a polynomial of order 5 was found to produce the best μo estimation - the program EXBACK thus represented μo by $(A + BE + CE^2 + DE^3 + FE^4 + GE^5)$, and varied A, B, C, D, E, F and G to minimise the sum of the squares of the differences between μ and μo at each energy datum. The resulting $(\mu-\mu o)/\mu o$ converted to a function of k, and multiplied by k, is shown as the solid line in Figure 8.11, ending at $k \approx 9$ $\AA^{-1}$.

Figure 8.10(b) shows the same μ-data truncated at $h\nu$ = 3,000 eV (the solid line), the best μo estimation again being

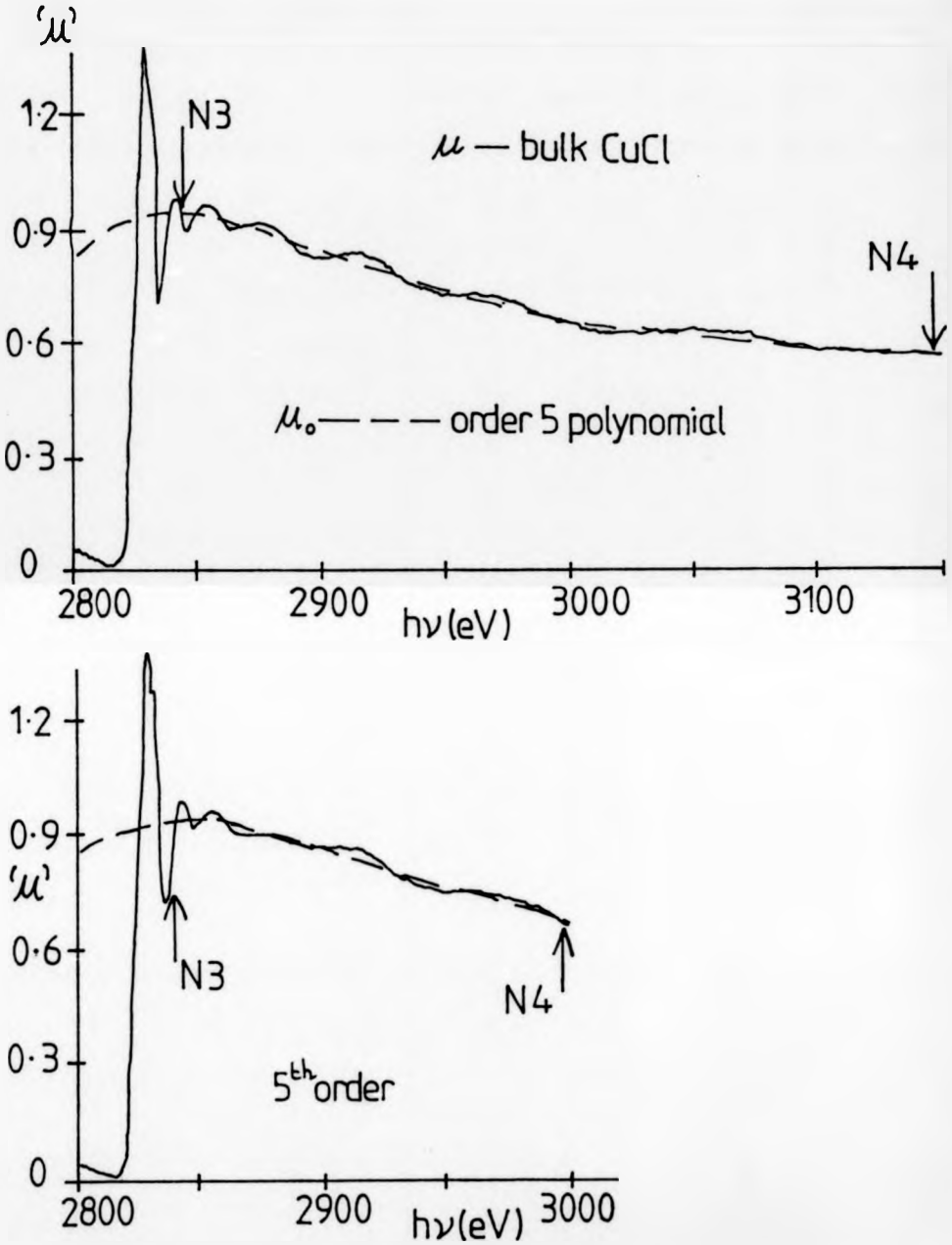

Fig. 8·10: Polynomial μ_0's for extensive and truncated spectra.

for order 5, shown by the dashed line. N3 is a critical parameter affecting the μo estimation near the edge - it was chosen to produce a μo that matched that of Figure 8.10(a) as closely as possible. The kX(k) obtained from this shorter data range is shown as the dashed line in Figure 8.11. It can be seen in both spectra that the polynomial method has a tendency to distort the data just before the highest energy point, such that the short data range spectrum deviates significantly at $k \leq 7$ Å^{-1}. Since the 'frequency' of the last peak is significantly distorted, a derivation of the atomic phase-shifts or of the bond length for an unknown structure, would be in error. Of course for surface EXAPS which does end at such k-values there is no way of knowing the extent of the distortion or of the error introduced, but it could easily lead to a false bond length derivation with an error of several hundreths of angstroms.

The errors that can be introduced by the polynomial μo could explain why the surface iodide structural derivation in a recent publication[7] differs from that presented in this thesis, as indeed some of the characteristics seen in Figure 8.11 are apparent in the publication both for the bulk and the surface nickel iodide datasets, (namely Figures 2(a), and Figure 3 'B' and 'S')[7].

Now consider the same test applied to the spline routine. The computer programs written at Warwick adopt an approach that is more suitable to the analysis of surface EXAPS datasets. Firstly a least squares straight line is fitted to the μ data between two energy values, E_1 and E_2, chosen to cover the range of the EXAPS oscillations - Figure 8.12(a) shows such a procedure applied again to bulk CuCl. The background absorption is then approximated by another straight line, parallel to this line and passing through the base of the edge (for bulk EXAPS type data this becomes negative, and whilst this is physically impossible, the mathematics is valid) - the atomic

Fig.8·11 : kχ(k)'s derived using polynomial μ_0's

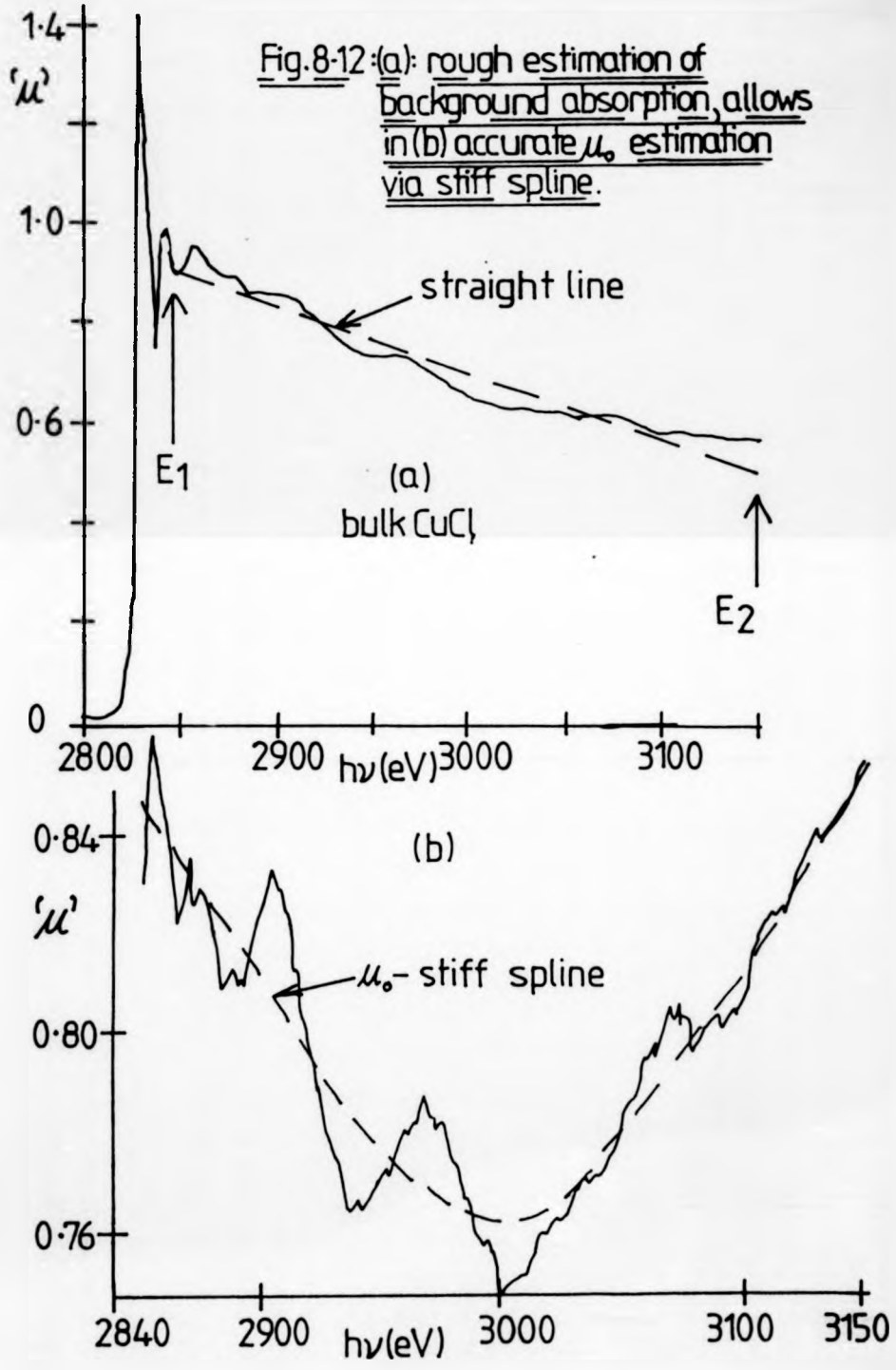

Fig. 8-12: (a): rough estimation of background absorption, allows in (b) accurate μ_0 estimation via stiff spline.

cross section is therefore estimated as being a constant value. The background subtracted absorption coefficient can then be displayed to see the EXAFS in much greater detail - the solid line in Figure 8.12(b) for example. The next procedure is to fit a stiff spline to this data to represent μo.

The cubic spline is characterised by two parameters: the width of a feature (expressed as the number of data points or in this case, the energy range) to which the curvature of the spline can respond; and the amplitude of a feature that the spline interprets as the signal rather than the 'noise'. The 'stiffness' of the spline is, roughly speaking, a product of these two terms.

The spline program is based upon one written to smooth Auger spectra[8], for which application, the breadth term being set to the width of the Auger peak, and the height term to the amplitude of the Auger peak. By analogy, the spline could be used to obtain a smoothed μ function. Alternatively, by increasing the stiffness parameter, the spline is unable to follow the EXAFS oscillations, and instead follows the much broader curvature, hence can be used to estimate μo, as illustrated by the dashed line in Figure 8.12(b). The resulting kX(k) is shown as the solid line in Figure 8.14. Notice that the spline-μo produces EXAFS oscillations of larger amplitude than the polynomial-μo (refer back to Figure 8.11), which is a result of the tendency of the polynomial to follow the μ-data too closely (particularly near the end of a dataset).

The background subtraction of the bulk CuCl spectrum terminated at 3000 eV is shown as the solid line in Figure 8.13, with the μo estimation via a stiff spline being shown as the dashed time. The resulting kX(k) is shown as the dashed line in Figure 8.14, where

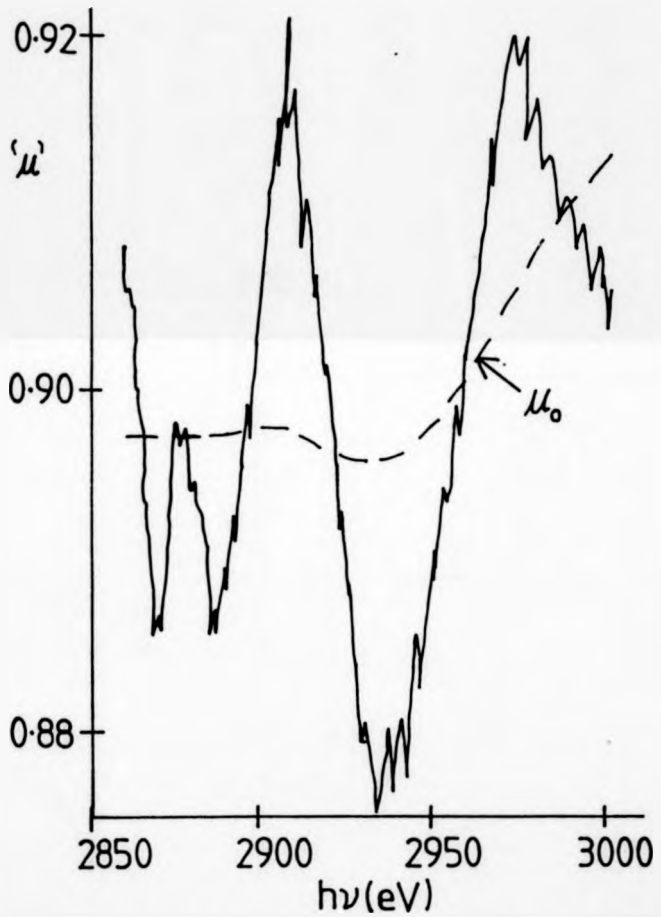

Fig.8·13 : Stiff spline estimation of μ_0 for limited μ data.

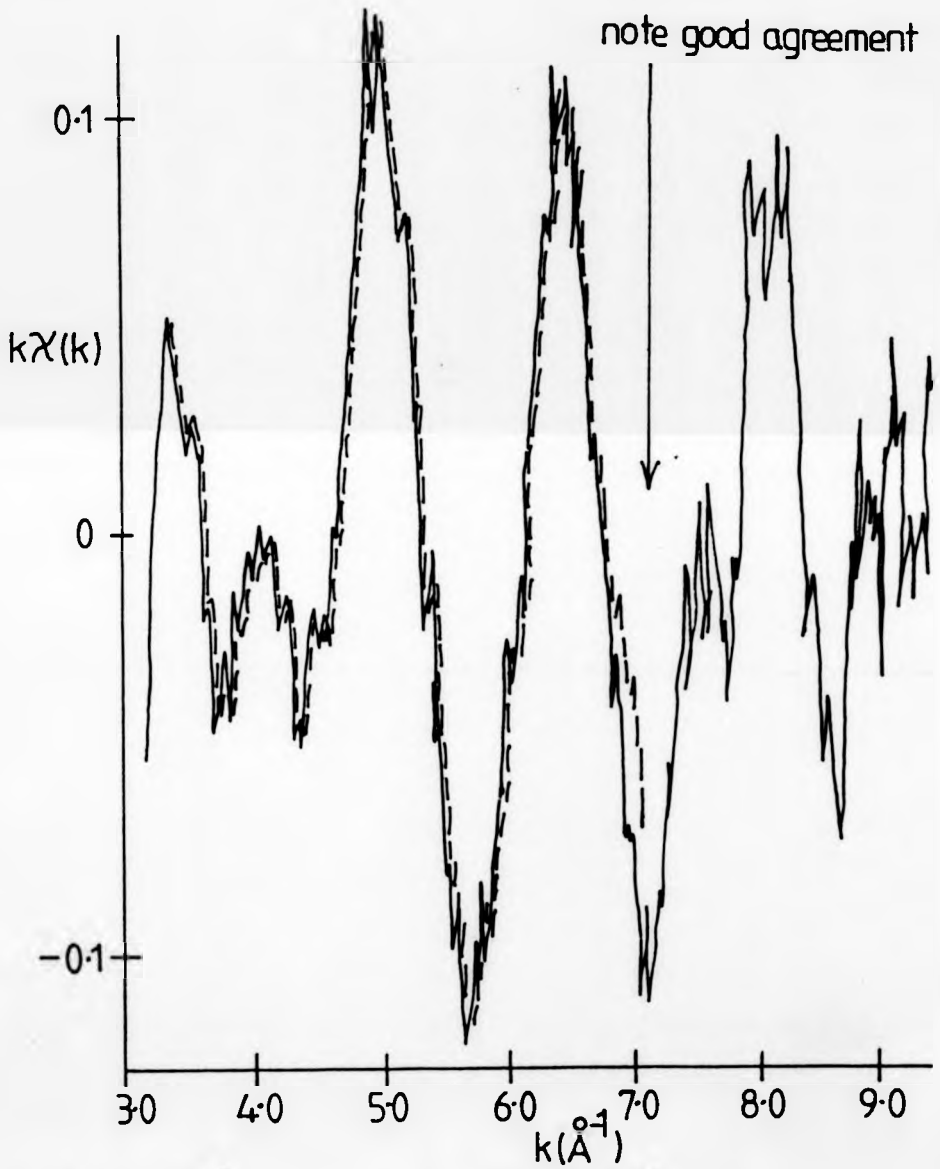

Fig.8·14: kχ(k)'s derived using stiff spline μ_0's.

it can be seen to be 'correct' over nearly the whole of the k-range, there just being a very slight deviation at $k \leq 7$ Å^{-1}. This demonstrates that a spline is a better method for obtaining μo, compared to a polynomial, for this SEXAFS spectrum.

8.06 Reliability of Cl–Cu Bond Length Results

It appears from the Fourier-filtering analyses of the spectra of the $\theta = {}^{1}/_{3}$, Cl–Cu(111) structure, that the Cl–Cu bond length is 2.40 (± 0.03) Å. whilst the multi-shell results indicate a value around 2.37 Å using a polynomial μo, and 2.39 Å using a spline, the latter of the two being more reliable on the basis of the discussion in section 8.05. It seems reasonable, therefore, to quote a result for the Cl–Cu bond length of 2.40 (± 0.03) Å, thus proving a significant difference to the 2.34 Å occuring in bulk CuCl, and being consistent with the determined bond lengths for chlorine adatoms on the Cu(100) surface[9, 10].

For the $\theta = 0.45$ structure, there is unfortunately only one suitable spectrum, which the Fourier-filtering analysis predicts a bond length of 2.32(± 0.04) Å, and the multi-shell analysis gives 2.34 Å using the spline routine to determine μo. Since there is only one spectrum, the result has a large uncertainty ($\geq$ 0.04 Å), but suggests that in this (6 $\sqrt{3}$ x 6 $\sqrt{3}$) R30° Cl–Cu(111) structure, the Cl–Cu bond length is essentially the same as it is in bulk CuCl, ie 2.34 Å.

More work needs to be done in obtaining good-quality spectra to higher k-ranges in order to improve the accuracy and reliability of these Cl–Cu bond lengths.

Interpretations of the bond lengths are given in chapter 9.

8.07 References

1. R W G Wyckoff, 'Crystal Structures', volume 1, second edition 1965, p 108: Tetrahedrally Co-ordinated Structures, including CuCl.

2. B K Teo and P A Lee, Journal of American Chemical Society, Vol 101, number 11, May 1979, p 2815 'Ab initio calculations of amplitude and phase functions for EXAFS spectroscopy'.

3. S Brennan, J Stöhr, and R Jaeger, Phys Rev B24(8), October 1981, p 4871
'Structure determination of c(2x2) S on Ni(100) using polarisation-dependent SEXAFS'.

4. J Stohr, R Jaeger and T Kendelewicz, Phys Rev Lett 49(2), July 1982, p 142:
'Structure of p(2x2) and c(2x2) O on Ni(100): A SEXAFS study.

5. J Stohr, L I Johansson, S Brennan, M Hecht and J N Miller
Phys Rev B22(8), October 1980, p 4052:
'SEXAFS study of oxygen interaction with Al(111) surfaces'.

6. A Puschmann and J Hasse, Surf Sci 144 (1984), p 559:
'Surface EXAFS of the (2x1) oxygen adlayer on Ag(110)'.

7. R G Jones, S Ainsworth, M D Crapper, C Somerton, D P Woodruff, R S Brooks, J C Campuzano, D A King, G M Lamble and M Prutton.
Surf Sci 152/153 (1985) p 443
'A Surface EXAFS study of a surface iodide phase on Ni(100)'.

8. The original program was written by M Prutton, Physics Department, York University.

9. P H Citrin, D R Hamann, L F Mattheis and J E Rowe, Phys Rev Lett 49(23), December 1982, p 1712: 'Geometry and Electronic Structure of Cl on the Cu(100) Surface'.
- Cl–Cu bond length = 2.37(± 0.02) Å.

10. F Jona, D Westphal, A Goldman and P M Marcus, Journal of Physics C (Solid State Physics) 16, (1983), p 3001: 'LEED Structure Determination of Cl on Cu(100)'.
- Cl–Cu bond length = 2.41(± 0.02) Å.

CHAPTER 9

CONCLUSIONS

9.01 Overview

In this chapter, the results from the SEXAFS structural investigations of iodine adsorption onto Ni(100) and chlorine adsorption onto Cu(111), are summarised. Studies of such varying coverages, which for the I-Ni(100) system ranges up to a 'corrosion layer', are useful in elucidating the nature of the chemical bonding and the ways in which the chemistry of the system varies: at very low coverage there is effectively a single adatom bonded to the clean metal surface, whereas in the surface nickel iodide - Ni(100) structure, half of the iodine atoms are in similar environments to those iodine atoms within bulk nickel iodine. As well as confirming postulated structures, the SEXAFS results give the changes in bond lengths sufficiently accurately to determine any changes in 'chemistry'. An attempt is also made, in this chapter, to draw some conclusions from the changes in E_o points between structures.

The results in this thesis are compared with other results available for chlorine and iodine overlayers on single crystal faces of transition metals (LEED results as well as SEXAFS work), and comments are made on the present understanding of surface chemical bonding.

9.02 The Structures

Consider, first of all, the I-Ni(100) phases. If the nickel (100) surface could be regarded as perfectly flat, then an individual iodine atom would have no preference for any position in the two-dimensional plane of the surface; there would be potential barriers preventing the adatom-surface distance becoming too small, and preventing the adatom from desorbing. If this were the case, then the highest posible iodine coverage would be reached when the adatoms themselves were compressed together as tightly as possible in a hexagonal close packed layer, somewhere around a coverage $\theta \geq 1/2$.

Such a structure is not observed; instead at $\theta = {}^{1}/_{2}$ there is a c(2x2) LEED pattern, the SEXAFS showing that the adatoms lie in hollow sites. This is clear evidence that the geometry of the iodine layer is influenced by the atomic layout of the top Ni(100) layer. It is this influence that causes the overlayer to remain commensurate with the surface along one <100> direction, as the coverage falls, the expansion being along the other perpendicular <100> vector. (Neither of the <100> directions is favoured, such that domains exist, each having expansion along a random <100> vector.)

Since the iodine atoms sit in hollow sites in the c(2x2) overlayer, the total energy of the system must be minimised here, compared to other possible adsorption sites such as bridge or atop - this may be due to the largest co-ordination number (four, as opposed to two or one) producing the greatest binding energy; due to the adatoms minimising their distance from the bulk metal (as could be understood by a charge - image charge attraction); or due to the effective screening by the nickel atoms of iodine-iodine repulsions. The observed one-dimensional expansion of the overlayer can be reconciled with this preference. I-I repulsions alone would tend to give rise to a two-dimensional expansion of the overlayer as iodine atoms were removed maximising the I-I spacings at all coverages, but, for the I-Ni(100) system, such an expansion (starting from the c(2x2) overlayer with the adatoms in hollow sites) would entail some adatoms moving up over 'the tops of hills'; for the observed <100> expansion adatoms need only move over 'saddles', this being a lower energy route.

For the two other coverages studied ($\theta = {}^{3}/_{8}$, and $\theta = {}^{1}/_{3}$) SEXAFS analyses show that the iodine atoms tend to minimise their distance from the metallic bulk (ie maximise their co-ordination number).

Although not as great as the iodine–nickel attraction, the iodine–iodine repulsions are also important, giving rise to the overlayer expansion (for a given iodine atom, the repulsive energy due to all the other adatoms in the overlayer, must be less than the binding energy due to the bulk metal, otherwise a stable structure could not exist). These forces fall as the iodine–iodine separations increase, such that at coverages much less than $\theta = {}^1/_3$ (when the iodine–iodine separations are much greater than 4.50 Å) an individual iodine atom could be moved from one hollow site to an adjacent one, without significantly increasing the total energy, thus the overlayer would tend to be disordered, the iodine–iodine spacings being somewhere near maximisation. Such disordering is observed, but no adatom site determination has been made at these low coverages.

Heating the nickel crystal in a relatively high pressure of iodine, allows iodine atoms to diffuse into the nickel, forming a layer of NiI_2. This surface nickel iodide appears (from SEXAFS and LEED) to have a very similar structure to a slice of bulk nickel iodide, suggesting that the high stability of this chemical compound determines the structure of the iodine and nickel atoms – the underlying Ni(100) causes only minor distortions and is itself believed to be undistorted.

The $(\sqrt{3} \times \sqrt{3})$ R30° Cl–Cu(111) structure for a chlorine coverage, $\theta = {}^1/_3$, appears to consist of chlorine adatoms lying in hollow sites (threefold for this surface of the face centred cubic crystal); and the $\theta = 0.45$ structure of similarly hexagonally close packed adatoms, also appears to have the maximum possible average co–ordination number. These observations of electro–negative atoms residing in hollow sites of maximum co–ordination number on metal surfaces are typical results [1–6] – see Table 9.01.

X-M STRUCTURE	X Co-ordⁿ / Adⁿ site	Bond length (Å)	Method	Ref.
bulk CuI	4	2·617		
$\theta=\frac{1}{3}$, $(\sqrt{3}\times\sqrt{3})R30°$ I-Cu{111}	3 / hollow	+0·04(±0·02)	SEXAFS	[1]
" "	3 / hollow	+0·07(±0·02)	"	[2]
$\theta=\frac{1}{4}$, p(2×2) I-Cu{100}	4 / hollow	+0·07(±0·02)	"	[1]
bulk AgI	4	2·803		[2,3,4]
AgI molecule	1	2·54		[4]
$[Ag_4I_4]$		2·85		"
$(\sqrt{3}\times\sqrt{3})R30°$ I-Ag{111}, $\theta=\frac{1}{3}$	3 / hollow	+0·07(±0·03)*	SEXAFS	[2]
$c(\sqrt{3}\times\sqrt{3})R30°$ I-Ag{111}	?	2·80	LEED	[4]
I-Ag{111} structure		+0·00(±0·14)*†	"	[3]
bulk NiI_2	3	2·78	SEXAFS	[thesis]
$\theta=\frac{1}{3}$ (2×3) I-Ni{100}	4,2 / hollow, bridge	+0·00(±0·02)	"	"
$\frac{3}{8}$ c(2×8) "	4,2 / hollow, near bd	−0·01(±0·02)	"	"
$\frac{1}{2}$ c(2×2) "	4 / hollow	+0·00(±0·02)	"	"
surface NiI_2-Ni{100}	~4	−0·01 (±0·02)	"	"
bulk γ-NiS	4	2·18		[5]
" Ni_3S_2		2·28		"
" NiS_2		2·34		"
" α-NiS		2·38		"
c(2×2)S-Ni{100}	4 / hollow	2·18(±0·06)	LEED	"
c(2×2)S-Ni{110}	4	2·17(±0·10)	"	"
p(2×2)S-Ni{111}	3 / hollow	2·02(±0·06)	"	"
O,S,Se,Te on Ni,Cu,Ag{111},{100}	'expected' hollows	—	LEED	[6]
bulk CuCl	4	2·34		
$\theta=\frac{1}{2}$, c(2×2)Cl-Cu{100}	4 / hollow	+0·03(±0·02)	SEXAFS	[12]
" " "	4 / hollow	+0·07(±0·02)	LEED	[13]
$\theta=\frac{1}{3}$, $(\sqrt{3}\times\sqrt{3})R30°$ Cl-Cu{111}	3 / hollow	+0·06(±0·03)	SEXAFS	[thesis]
0·45{$6\sqrt{3}\times6\sqrt{3}$}R30° Cl-Cu{111}	max^m coord^n no.	−0·01 (±0·04)	"	"

TABLE 9·01: Bond lengths and adatom sites for electronegative adsorbates (X) on metal substrates (M)

* bond length change relative to bulk AgI.

~ although LEED cannot deduce bond lengths accurately enough to determine changes in chemistry, results are quoted for completeness.

9.03 E_o Changes

Firstly, consider what is known about the relationship between the ΔE_o value and the difference in chemistry between the unknown and reference compounds. It is shown in Section 5.08, that the central atomic phase-shift of Ca^{2+} can be made to appear equivalent to that of neutral Ca, by setting the E_o point a further 10 eV below the edge. As a rough general guide, therefore, if the E_o value is 5 eV further below the edge in the unknown compound, then the central atom is one electronic charge more positive than in the model compound.

This agrees in magnitude with the figure quoted by Bunker and Heald[7], however it is of the opposite sign! Comparing the atomic phase-shifts of the EXAFS spectra of the tetrahedrally co-ordinated semiconductors CuBr, ZnSe, GaAs, and Ge, for central atoms of Cu, Zn, Ga, Ge, As, Se or Br, it was shown[7] that the E_o point had to be chosen further below the edge as the central atom became more negatively charged (in CuBr, Cu has a charge of approximately + 0.74 electronic units; in germanium, each Ge atom is neutral; in CuBr, the Br has a charge of - 0.74 e), this amount being approximately 5 eV per electron charge transfer. The explanation for this[7] is that if the central atom is positively charged, then at the absorption threshold, the photo-electron is held in a localised state, requiring X-rays several eV above the edge to produce a photo-electron that can propogate from the atom and therefore contribute to the EXAFS - the E_o point is therefore several eV above the edge. For a neutral or negatively charged absorbing atom, any photo-electron would be able to propogate outwards, the E_o point therefore being at the edge itself.

However, for Cu and Zn central atoms within CuBr and ZnSe, the ΔE_o values do not show the some trend, but deviate by up to 5 eV

- this is interpreted as being due to charge transfer occuring after excitation[7].

Results for the EXAFS phase functions for the second shells (eg As-As photo-electron scattering in GaAs), show no variations in E_o values through the range from Ga to Br - this is interpreted as being due to the fact that the central and backscattering atoms are equally charged[7] - (this explanation is not easy to understand, when it is generally believed that it is the central atom phase-shifts that vary with charge state, whilst the backscattering phase-shifts are relatively independent of chemistry).

There are clearly many parameters affecting ΔE_o values, preventing simple interpretations; the majority of SEXAFS publications do not quote ΔE_o values. A ΔE_o value of 1.0 eV is found to be sufficient to make the central sulphur and backscattering nickel atomic phase-shifts equal in c(2x2) S - Ni(100) and bulk NiS[8] and - 2.0 eV for O-Ni scattering for a structure formed by the adsorption of oxygen onto Ni(100), compared to the model compound NiO[9].

The E_o trends for the structures described in this thesis are given in Figure 9.01(a). For bulk NiI_2, the E_o point is about 6 eV below the edge. For bulk CuCl it is 12 eV below the edge (with E_o at the edge, there was a maximum in the imaginary component of the Fourier transform, at a slightly higher R value than the maximum in the modulus, and these could be made to coincide by choosing E_o = 12 eV below the edge ; to move the nearest lower maximum of the imaginary component into coincidence, an E_o point several tens of eV above the edge was needed, which is physically unreasonable). The fact that the photo-electrons have a few eV energy at the absorption threshold is understood by a Fermi level argument (see Section 5.03, and Figure 5.04), and the larger energy in the case of the chlorine

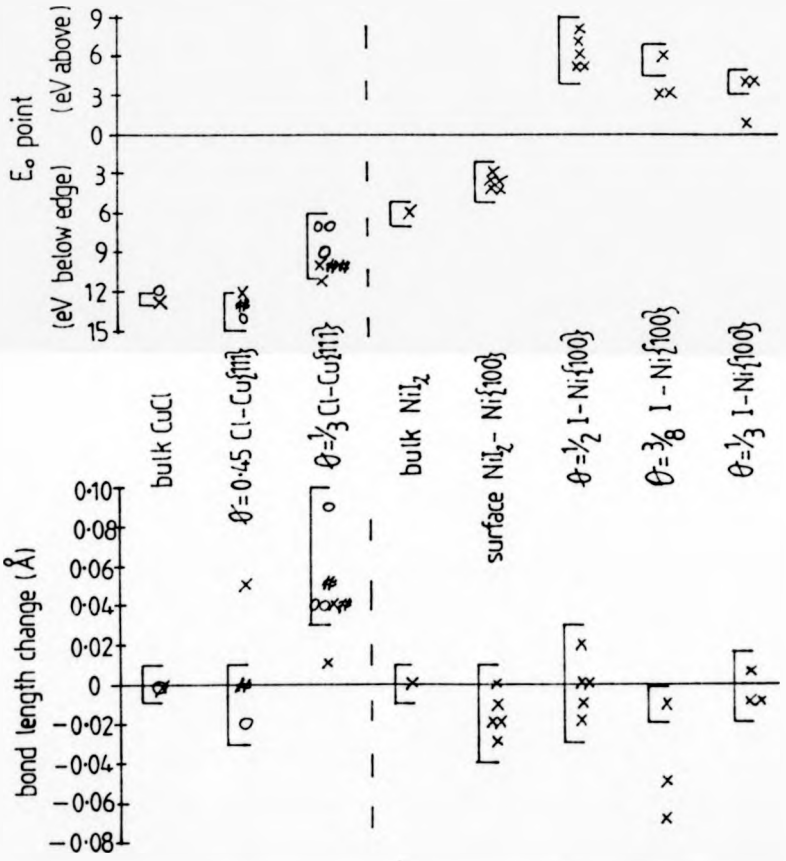

Fig. 9·01: I-Ni and Cl-Cu bonding parameters in I-Ni{100} and Cl-Cu{111} structures compared to bulk NiI_2 and CuCl.

SEXAFS analyses: × multi shell method (polynomial μ_0)
" " " (spline μ_0)
o Fourier filtering method (spline μ_0)

Error bars ⊏: ±1eV for E_0 points; ±0·01Å for bond lengths, excuding polynomial-μ_0 Cl-Cu results (unreliable due to short k-ranges), and hollow/mid/bridge models $\theta=\frac{3}{8}$ and $\frac{1}{3}$ I-Ni results (less likely than hollow/bridge models).

central atom may be derived in part from the greater negative charge on this atom (CuCl is 26% ionic, NiI_2 only 12%). It is the ΔE_o value between the unknown and model compound, that is important in the analysis procedure to derive any change in the bond lengths, the ΔE_o value being most reliably determined using the zero intercept phase function difference Criterion, used in the analyses presented in this thesis, and mentioned elsewhere[7]. For surface NiI_2: Ni(100), ΔE_o is onbly 2-3 eV relative to bulk NiI_2, confirming that the two iodides are chemically very similar. Whilst the θ = 0.45 cl-Cu(111) E_o point is effectively the same as in bulk CuCl, the θ = $^1/_3$ overlayer has its E_o point 3 eV higher at 9 eV below the edge, which is not an untypically large shift. For the low coverage I-Ni(100) structures, the shifts in the E_o points relative to bulk NiI_2, are quite large: 12 eV for the c(2x2) I overlayer, the E_o point being 6 eV above the edge.

It is not easy to understand such larger E_o shifts. Interpretation purely in terms of the ΔE_o value being required to make the central atomic phase-shifts appear equal (as set out in Section 5.08 and Figure 5.08), suggests that whilst the central iodine atom is nearly neutral in bulk NiI_2, it is more than doubly negatively charged in the θ = $^1/_2$ overlayer. This is clearly not the case - the small work function change caused by the adsorption of iodine onto nickel, suggests that the iodine overlayer is not far off being neutral. It could well be that charge transfer effects are taking place after excitation in the surface structures but not in the bulk compound, and this is not surprising since the bulk compound is a covalently bonded insulator, whereas the surface structures consist of fractional monolayers of iodine on top of a metal (containing conduction electrons).

In bulk NiI_2, X-ray excitation leaves the absorbing iodine atom positively charged, the central atom phase-shifts being that of a photo-electron leaving the potential of the central I^+. For I-Ni(100) structures, each ionised iodine can quickly be retored to neutrality by the transfer of a conduciton electron from the metal, such that the central atom phase-shift is that for a neutral central iodine atom, the charge transfer being effectively instantaneous with regards to the low and intermediate k-valued photo-electrons, giving rise to the measured EXAFS spectra. The E_o shifts of around 9 eV are not too inconsistent with the transfer of one electronic unit of charge, the direction of the shift being consistent with that described in Section 5.08, ie the central I atoms in the I-Ni(100) structures each appear to be one electronic unit more negative than those I atoms in bulk NiI, when the EXAFS spectra are compared.

It is thought[10], that there is less competition for the metallic bonding electrons at low I coverages, leading to stronger I-Ni bonds. There is no indication in the E_o values that the iodine adlayers become more negatively charged as the I coverage falls (indeed the trend is for the E_o point to fall to lower energies, suggesting a less negative overlayer, as the I coverage falls from $\theta = {}^1/_2$ through $\theta = {}^3/_8$, to $\theta = {}^1/_3$), such that if a greater charge is involved in the bond at lower coverages, then this bond must remain predominantly covalent, the iodine atom being only charged to approximately - 0.1 electronic units.

9.04 Bond Length Changes

The changes in I-Ni and Cl-Cu bond lengths that can detected in the SEXAFS analyses of the I-Ni(100) and Cl-Cu(111) structures relative to bulk $Ni-I_2$ and bulk CuCl, are summarised in Figure 9.01(b).

A variety of theories have been put forward to predict differences in the same atom pair bond lengths in two compounds, but as yet no 'universally valid' explanation exists. The parameters affecting bond length are thought to include the bond type (covalent or ionic), bond strength, co-ordination number, and the orienation of the bonds.

One hypothesis states that if the local geometry around an atom is similar in two compounds, then the bond length is similar[5]. For c(2x2) overlayers of S on Ni(100) and (110), the S-Ni bonding geometry is very similar to that in mullite (γ - NiS), and the S-Ni bond lengths are all approximately 2.18 Å (see Table 9.01[5]). The bond lengths in other bulk compounds - Ni_3S_2, NiS_2 and α-NiS - are significantly larger, and that in p(2x2)S-Ni(111) shows a marked contraction, compared to all the bulk compounds[5]. The Ag-I bond lengths in c($\sqrt{3}$ x $\sqrt{3}$) R30° I-Ag(111) are bulk AgI, which have fairly similar local structures around the iodine atoms, are reported[4] to be effectely the same value, ie 2.80 Å, whereas the bond lengths in the very differently arranged AgI molecule and $[Ag_4I_6]$ radical are quite different.

It is thought that the bond length is different for different bond orientations, and different co-ordination number, but it remains impossible to predict even the sign of the difference, let alone its value. On reducing the co-ordination number from 4 to 3, the S-Ni bond length is reduced from 2.18 to 2.02 Å (see Table 9.01[5]), which can be explained[5, 11] by assuming that the total charge transfer to the electronegative species is independent of the

co-ordination number, such that in the first structure this constant total charge is shared by 4 metallic atoms, whereas in the second structure it is shared by only 3, each individual bond therefore being stronger and hence shorter in the lower co-ordination structure.

When such a theory is applied to the I-M(metal) bond lengths within bulk AgI and bulk CuI (in which the I co-ordination numbers are 4), compared to those in the ($\sqrt{3}$ x $\sqrt{3}$) R30° I structures on Ag(111) and Cu(111) in which the co-ordination numbers are 3), it predicts the opposite trend to that observed, the measurements indicating that the I-M bond lengths are around 0.07 Å <u>larger</u> in the surface structures compared to the bulk compounds[1, 2]. An alternative theory is put forward to explain these results[11] - bulk AgI and CuI are tetrahedrally co-ordinated structures in which the four I-M bonds are spaced as far apart as is possible (109°), whereas for the three-fold co-ordination of the I atoms on the metal(111) surfaces, the three I-M bonds are all constrained within a limited solid angle (they are all directed downwards towards to surface being about 60° apart), these strained bonds therefore being weaker and hence longer.

The changes in the I-Ni and Cl-Cu bond lengths that can be detected in the SEXAFS analyses of the I-Ni(10) and Cl-Cu(111) structures, relative to bulk NiI_2 and bulk CuCl, are summarised in Figure 9.01(b), and included in Table 9.01.

The increased Cl-Cu bond length for Cl atoms in hollow sites on the Cu(111) surface compared to bulk CuCl, is consistent with the similarly larger bond length for Cl atoms in hollow sites on Cu(100)[12, 13], and tends to support the theory that if the bonds are geometrically restricted then they are weaker, and therefore longer.

Negligible I-Ni bond length differences for the I-Ni(100) structures, including the surface NiI_2 on Ni(100), compared to bulk NiI_2, may be explained by the fact that in bulk NiI_2, the I-Ni bonds are constrained to within a similarly small solid angle (see Figure 4.03(a)) as they are in the surface structures, giving rise to similar bond characteristics.

As the I coverage is reduced from the $\theta = {}^1/_2$, c(2x2) I overlayer, through the variable coverage phases, the I binding energy increases, it being thought[10], that approximately half this increase comes from the reduction in the through space I-I repulsion, the other half coming from an increase in the I-Ni bond strength (equivalent to a reduction in the effective through metal I-I repulsion) as the I-I spacing increases. No shortening of the I-Ni bond length is observed as the I coverage falls, hence the theory of the strengthening I-Ni bond cannot be confirmed from the bond length data.

9.05 Concluding Remarks

At the present date, in surface science, it is clear that there is little understanding of the bond length variations between adsorbate structures on single crystal surfaces and bulk compounds, although results are beginning to be accumulated for chemisorption on metal surfaces[14], and much work has been done to try to understand structural chemistry[15]. It is hoped that the results presented in this thesis will make their small contribution to surface science studies.

9.06 References

1. P H Citrin, P Eisenberger and R C Hewitt, Phys Rev Lett 45(24), December 1980, p 1948:
'Absorption sites and bond lengths of I_2 on Cu(111) and Cu(100) from SEXAFS'.

2. P H Citrin, P Eisenberger and R C Hewitt, Surf Sci 89(1979) p 28:
'SEXAFS studies of I_2 adsorbed on single crystal substrates'.

3. F Forstmann, W Berndt and P Büttner, Phys Rev Lett 30(1973) p 17:
'Determination of the adsorption site by LEED for iodine on silver (111)'.

4. 'The Nature of the Surface Chemical Bond', edited by T N Rhodin and G Ertl, North Holland Publishing Company, 1979'.

5. J E Demuth, D W Jepsen, P M Marcus, Phys Rev Lett 32(21), p 1182, May 1974:
'Crystallographic dependence of chemisorption bonding for sulphur on (001), (110) and (111) nickel'.

6. F Jona, J Phys C11(21), November 1978, p 4271:
Review Article: 'LEED Crystallography'.

7. B A Bunker and E A Stern, Phys Rev B27(2), January 1983, p 1017:
'Phase factor in EXAFS'.

8. S M Brennan, Stanford Synchrotion Radiation Laboratory, report 82/03, June 1982:
'Surface EXAFS of sulphur on nickel'.

9. J Stöhr, SSRL report 80/07, December 1980,
'EXAFS and Surface EXAFS: Principles, Analysis and Applications'

10. D P Woodruff, Applications of Surface Science 22/23(1985), p 459:
'Geometrical and Electronic Structure of Multiple Surface Phases: Iodine on Ni(100)'.

11. P Eisenberger, P H Citrin, R Hewitt and B Kincaid,
CRC Critical Reviews in Solid State and Materials Sciences, May 1981, p 191:
- this publication contains a review of I-Ag(111) and I-Cu(111) SEXAFS.

12. P H Citrin, D R Hamann, L F Mattheiss and J E Rowe, Phys Rev Lett 49(23), December 1982, p 1712:
'Geometry and electronic structure of Cl on the Cu(001) surface'.

13. F Jona, D Westphal, A Goldmann and P M Marcus,
Journal of Physics C (Solid State Physics) 16, (1983), p 3001:
'LEED structure determination of Cl on Cu(100)'.

14. K A R Mitchell, Surf Sci 149 (1985), p 83:
'Analysis of surface bond lengths reported for chemisorption on metal surfaces'.

15. L Pauling
'Nature of the Chemical Bond, and the structure of molecules and crystals: An Introduction to Modern Structural Chemistry'
3rd eidtion, 1960, Cornell University Press.